

Advanced computational methods in identification of thermo-acoustic systems

A thesis accepted by the Faculty of Aerospace Engineering and Geodesy of the
Universität Stuttgart in partial fulfilment of the requirements for the degree of
Doctor of Engineering Sciences (Dr.-Ing.)

by

Dipl.-Ing. Krzysztof Kostrzewa

born in Poznan

Main referee: Prof. Dr.-Ing. Manfred Aigner

Co-referee: Prof. Dr.-Ing. Franz Joos

Date of defence: 17th Dezember 2010

Institute of Combustion Technology for Aerospace Engineering
University of Stuttgart

2011

Acknowledgments

This thesis emerged from the studies I conducted during my employment with the Institute of Combustion Technology (VT) at DLR in Stuttgart between 2003 and 2007. It is the result of an applied research, which had many contributors to its success.

First of all, I would like to acknowledge the support and help of numerous people, without whom this thesis would not have been ever possible:

My warmest thanks to Siemens AG from Mülheim an der Ruhr and DLR from Stuttgart for providing the funding and equipment to undertake this project. Especially I would like to mention here Dr. -Ing. Michael Huth and Dr. -Ing. Werner Krebs from Siemens AG, Prof. Dr. -Ing. Manfred Aigner and Dr. -Ing. habil. Berthold Noll from DLR who provided invaluable information and advices, which helped steer the project in a direction leading to its successful conclusion.

Furthermore, I would like to thank to my supervisors: Dr. -Ing. Joachim Lepers, Dr. -Ing. Sven Bethke and Dipl. -Ing. Peter Kaufmann from Siemens with whom I was honored to work. Their positive attitudes and useful advises kept the project moving forward even when the outlook seemed grim. I appreciate their personal character and expertise that provided the insight to overcome the many issues encountered in this project.

Thanks also to Prof. Wolfgang Polifke and Dr. -Ing. Andreas Huber from TU München for all their advices and assistance with regard to system identification. I also highly appreciate the possibility to work with the Acoustic Postprocessor developed at TU München.

Many thanks go out to all persons I have had the privilege of getting to know during my time at DLR and Siemens. Especially, I would like to thank Dipl. -Ing. Axel Widenhorn from DLR for his great assistance during this project. He was an invaluable source for almost any questions regarding acoustic boundary conditions.

Finally, I would like to thank my entire family. My parents and wife have always supported my endeavors. They have been always a great source of my motivations and inspirations. Through often-difficult situations, my wife provided me a good home environment and an understanding for me.

Contents

LIST OF FIGURES	V
LIST OF TABLES	XIII
NOMENCLATURE.....	XV
ZUSAMMENFASSUNG	XXI
SUMMARY	XXIII
1 INTRODUCTION.....	1
1.1 RESEARCH OBJECTIVE	4
1.2 LITERATURE OVERVIEW.....	5
1.3 THESIS OUTLINE.....	7
2 THERMO-ACOUSTICALLY INDUCED COMBUSTION INSTABILITIES.....	11
2.1 MECHANISM OF COMBUSTION INSTABILITIES.....	11
2.1.1 Rayleigh's Criterion	12
2.2 THERMO-ACOUSTIC INSTABILITIES SOLUTIONS METHOD	13
2.2.1 Passive means.....	13
2.2.2 Active means.....	14
3 ACOUSTIC MODELING	15
3.1 THEORY AND BASIC CONCEPTS.....	15
3.1.1 Wave equation	15
3.1.2 Validity of linearity assumptions in thermo-acoustics	18
3.1.3 Solution methods	19
3.1.3.1 One-dimensional acoustic wave propagation.....	19
3.1.3.2 Acoustic damping.....	21
3.1.3.3 Acoustic Impedance.....	23
3.2 ONE-DIMENSIONAL ACOUSTIC NETWORK MODELS.....	24
3.2.1 Transfer matrix method.....	25
3.2.1.1 Straight duct element.....	26

3.2.1.4	<i>Feedback mechanism in combustion systems</i>	30
3.2.1.5	<i>Characterization of acoustic stability</i>	32
3.2.1.6	<i>Limitation of the one-dimensional acoustic network codes</i>	34
4	MODELING OF TURBULENT REACTIVE AND NON-REACTIVE FLOWS	
	USING CFD	37
4.1	<i>THEORY AND NUMERICAL MODELING OF TURBULENCE</i>	37
4.1.1	<i>Numerical simulation of turbulence</i>	38
4.1.2	<i>RANS modeling</i>	39
4.1.2.1	<i>Classical turbulence models for unclosed terms</i>	41
4.1.3	<i>Unsteady RANS modeling</i>	43
4.1.3.1	<i>CFL requirement</i>	44
4.2	<i>COMBUSTION MODELING</i>	45
4.2.1	<i>Turbulent premixed flames</i>	46
4.2.2	<i>Combustion models</i>	47
5	NUMERICAL SYSTEM IDENTIFICATION OF THERMO-ACOUSTIC ELEMENTS	51
5.1	<i>FUNDAMENTALS OF NUMERICAL SYSTEM IDENTIFICATION</i>	51
5.1.1	<i>Characterization of discrete time systems</i>	52
5.1.2	<i>Linear Time Invariant (LTI) Systems</i>	53
5.1.3	<i>Frequency response of LTI systems</i>	54
5.1.3.1	<i>z-Transformation</i>	54
5.1.3.2	<i>Inverse z-Transformation</i>	55
5.2	<i>MODELS OF LTI SYSTEMS</i>	55
5.3	<i>WIENER-HOPF EQUATION</i>	56
5.3.1	<i>Auto-correlation matrix</i>	57
5.3.2	<i>Cross-correlation vector</i>	58
5.4	<i>RECONSTRUCTION OF THERMO-ACOUSTIC ELEMENTS BY MEANS OF CFD/SI</i>	58
5.4.1	<i>Acoustic boundary conditions</i>	59
5.4.2	<i>Forcing signals</i>	61
5.4.2.1	<i>Harmonic function</i>	61
5.4.2.2	<i>White noise</i>	62
5.4.3	<i>Causality and choice of variables</i>	62
5.4.4	<i>Location of the reference planes</i>	64
5.4.5	<i>Extraction of time series</i>	65
5.4.6	<i>Acoustic variables p' and u' and normalization</i>	66
5.4.7	<i>Optimal setting for numerical system identifications</i>	66

5.4.7.1	Filter order L and jump factor m	67
5.4.7.2	Sampling and frequency increment	69
5.4.7.3	First approximation for a value of L	69
5.4.7.4	Optimal settings for L and m	70
6	DUCT WITH A SUDDEN CHANGE OF DIMENSION.....	73
6.1	ANALYTICAL MODEL FOR A SUDDEN CHANGE OF DIMENSION	73
6.2	CFD COUPLED WITH SYSTEM IDENTIFICATION (CFD/SI)	74
6.2.1	Boundary conditions and CFD model	75
6.2.2	Steady state solution	76
6.3	VALIDATION OF CFD/SI WITH MEASUREMENTS, FEM AND ANALYTICAL MODEL	77
6.4	OPTIMAL VALUES OF L AND M FOR CFD/SI	80
6.5	SENSITIVITY STUDY	80
6.5.1	Spatial discretization dx	80
6.5.2	Time discretization dt	82
6.5.3	Time scheme variations	85
7	TRUNCATED TEARDROP SPECIMEN.....	89
7.1	CFD/SI APPROACH TO RECONSTRUCT ACOUSTIC TRANSFER MATRICES.....	90
7.1.1	CFD model and Boundary Condition	90
7.1.2	Steady state flow field	92
7.2	ACOUSTIC TRANSFER MATRIX BY MEANS OF CFD/SI AND ONE-DIMENSIONAL ACOUSTIC MODELING.....	93
7.3	OPTIMAL VALUES OF L AND M	95
7.4	ACOUSTIC REFLECTIVITY AT BOUNDARIES.....	96
7.5	IMPEDANCE CALCULATION.....	98
8	ATMOSPHERIC TEST RIG WITH A GENERIC BURNER	103
8.1	TEST RIG DESCRIPTION	103
8.2	URANS MODELING.....	105
8.3	RANS SOLUTIONS.....	107
8.4	VALIDATION OF THE FLAME TRANSFER FUNCTION CALCULATION	108
8.5	CFD/SI VS. TIME LAG APPROACH.....	110
8.6	CFD/SI VS. HARMONIC FORCING	111
8.7	SENSITIVITY STUDY	113
8.7.1	Combustion modeling.....	113
8.7.2	Boundary conditions.....	117
8.7.2.1	Harmonic excitation at 60 Hz	119

8.7.3	<i>Time resolution</i>	122
9	INDUSTRIAL TEST RIG WITH A GENERIC BURNER AT ELEVATED PRESSURE	125
9.1	<i>URANS MODELING</i>	126
9.1.1	<i>Steady State Solution</i>	128
9.2	<i>RECONSTRUCTION OF FLAME TRANSFER FUNCTION</i>	129
9.3	<i>EXPERIMENTAL PRESSURE SPECTRUM MEASUREMENTS VS. STABILITY PREDICTION BASED ON A ONE-DIMENSIONAL ACOUSTIC NETWORK CODE</i>	130
9.3.1	<i>CFD/SI vs. time lag approach</i>	131
9.3.2	<i>Stability prediction based on CFD-based transfer functions</i>	132
10	SAS BASED FORCED RESPONSE OF AN ATMOSPHERIC TEST RIG WITH A GENERIC BURNER	137
10.1	<i>SAS MODELING</i>	137
10.2	<i>SAS BASED SPACE AND TIME-RESOLVED FLOW FIELD</i>	139
10.3	<i>SAS WITH A HARMONIC FORCING</i>	142
11	SAS OF INDUSTRIAL TEST RIG AT ELEVATED PRESSURE	147
11.1	<i>SAS MODELING</i>	147
11.2	<i>SAS SPACE AND TIME-RESOLVED FLOW FIELD</i>	149
12	SIMULATION OF SELF-EXCITED OSCILLATIONS	155
12.1	<i>URANS CALCULATION OF SELF-EXCITED OSCILLATIONS</i>	156
12.2	<i>VALIDATION OF CFD-BASED ACOUSTIC MODES BY MEANS OF A ONE-DIMENSIONAL ACOUSTIC CODE</i>	158
13	CONCLUSIONS AND RECOMMENDATIONS	161
A	TURBULENCE MODELS	165
B	TIME DISCRETIZATION	166
C	ANALYTICAL TIME LAG MODELS	167
D	SOLUTION ERROR ANALYSIS	169
E	APPROXIMATION OF IMPEDANCE BOUNDARY CONDITIONS	171
F	HPC - COMPUTATIONAL RESOURCES	172
	LITERATURE	175

List of Figures

Fig. 1.1	Cross section of the SGT6-6000G gas turbine.....	1
Fig. 1.2	NACOR Project - competence circle	2
Fig. 2.1	A schematic of the feedback loop responsible for combustion instabilities [5][84].....	12
Fig. 3.1	Acoustic wavelength in a mixture of burnt gasses as a function of temperature and frequency	19
Fig. 3.2	Sound waves traveling in a tube	20
Fig. 3.3	Damping coefficient as a function of Mach number: red circles – thermo-viscous effects, dark blue circles turbulence effects, green circle – sum of two effects	23
Fig. 3.4	An example of one-dimensional acoustic network model of a premixed burner...25	
Fig. 3.5	Symbolic conventions for a straight duct element	27
Fig. 3.6	The acoustic wave propagation in connected ducts	28
Fig. 3.7	Flame element: acoustic jump condition	29
Fig. 3.8	Simple acoustic model with a flame	30
Fig. 3.9	A sketch of a generic partially premixed system.....	31
Fig. 3.10	The eigenfrequency of the simple model: green triangle - interaction index $n=0.5$, red rectangular $n=1,5$	34
Fig. 4.1	Arbitrary variable in a turbulent flow solved by DNS, LES and RANS.....	38
Fig. 4.2	Periodic oscillation with superimposed turbulent fluctuations	43
Fig. 4.3	Borghi turbulent combustion diagram [40].....	46
Fig. 5.1	Block representation of an arbitrary system [95]	52
Fig. 5.2	The system of interest: a thermo-acoustic element and reference planes [50]	59
Fig. 5.3	Tube and wave propagation [46].....	63

Fig. 5.4	Location of the reference planes and the boundary of the black box [50].....	64
Fig. 5.5	Acoustic transfer matrix of a sudden change of dimensions for the transfer matrix element T_{11} : analytical solution (red rectangular) and CFD/SI for different length of L: L=10 (green circle) and L=20 (blue triangle)	68
Fig. 5.6	Correlation between L , m and τ_{mem} for a given filter [50].....	68
Fig. 5.7	The least square error as a function of L for a prototype burner	71
Fig. 5.8	Relative quadratic difference of the transfer matrix element T_{11} of the truncated teardrop for a variation of m values.....	72
Fig. 6.1	Geometry of a sudden change of dimension [50].....	73
Fig. 6.2	Acoustic element represented by the generalized CFD setup	74
Fig. 6.3	Simplified CFD model of a sudden change of dimensions.....	75
Fig. 6.4	Local axial velocity and pressure distributions.....	76
Fig. 6.5	Acoustic Transfer Matrix: Normalized Amplitude: red rectangular – analytical model, blue rectangular – FEM, grey rectangular – measurements, green rectangular – CFD/SI	78
Fig. 6.6	Acoustic Transfer Matrix: Phase: red triangle – theory, blue triangle – FEM, grey triangle measurements, green triangle – CFD/SI.....	79
Fig. 6.7	The Relative quadratic difference of the element T_{11} as a function of L and m	80
Fig. 6.8	Spatial discretization dx variations: Normalized amplitude: green diamond – 11000 nodes, red diamond – 23000 nodes, yellow diamond 41000, grey diamond – measurements.....	81
Fig. 6.9	Spatial discretization dx variations: Phase: green diamond – 11000 nodes, red diamond – 23000 nodes, yellow diamond 41000, grey diamond – measurements	82
Fig. 6.10	Relative truncation errors as a function of number of time steps N [24]: red rectangular – relative time derivative error, green triangle – relative absolute error.....	83
Fig. 6.11	Time discretization dt variations: Normalized Amplitude: green circle – dt=2.5e-5 s, red circle dt=5e-5 s, grey circle – measurements	84

Fig. 6.12	Time discretization dt variations: Phase: green diamond – $dt=2.5e-5$ s, red diamond $dt=5e-5$ s, grey triangle – measurements	84
Fig. 6.13	First and second order truncation errors order as a function of number of time steps N: not filled red rectangular – 1 st order, filled red rectangular – 2 nd order ...	85
Fig. 6.14	Time scheme variations: Normalized Absolute value: green rectangular – 1 st order, orange rectangular – 2 nd order, grey rectangular – measurements	86
Fig. 6.15	Time scheme variations: Phase: green rectangular – 1 st order, orange rectangular – 2 nd order, grey rectangular – measurements	87
Fig. 7.1	Truncated teardrop specimen in position for impedance measurements.....	89
Fig. 7.2	The truncated teardrop element represented by the generalized CFD setup.....	90
Fig. 7.3	BC and CFD model of truncated teardrop specimen	91
Fig. 7.4	Truncated teardrop specimen: normalized pressure and axial velocity distribution at $y=0$ m.....	92
Fig. 7.5	One-dimensional acoustic representation of a truncated teardrop.....	93
Fig. 7.6	Acoustic transfer matrices of the truncated teardrop specimen: normalized absolute value: red triangle – CFD/SI, green rectangular – one dimensional acoustic network model.....	94
Fig. 7.7	Acoustic transfer matrices of the truncated teardrop specimen: phase red triangle – CFD/SI, green rectangular – one dimensional acoustic network model.....	94
Fig. 7.8	The relative quadratic difference of the element T_{11} of the truncated teardrop specimen	95
Fig. 7.9	Acoustic reflectivity vs. acoustic transfer matrices of the truncated teardrop specimen: normalized absolute value: CFD/SI with RBCs - red rectangular, CFD/SI with NRBCs at inlet and outlet-purple rectangular, NRBCs at outlet and RBCs at the inlet- yellow rectangular, TMA modeling - green rectangular	97
Fig. 7.10	Acoustic reflectivity vs. acoustic transfer matrices of the truncated teardrop specimen: phase: CFD/SI with RBCs - red rectangular, CFD/SI with NRBCs at inlet and outlet-purple rectangular, NRBCs at outlet and RBCs at the inlet- yellow rectangular, TMA modeling - green rectangular	98
Fig. 7.11	Reference location for Impedance measurements of the truncated teardrop specimen	99

Fig. 7.12	TMA model with the truncated teardrop specimen represented by the CFD/SI approach.....	99
Fig. 7.13	TMA model of the truncated teardrop specimen.....	100
Fig. 7.14	Normalized Impedance of the truncated teardrop specimen: Amplitude, black circle measurements, red triangle –TMA model, green diamond – TMA model with the truncated teardrop specimen represented by the CFD/SI approach.....	101
Fig. 7.15	Normalized Impedance of the truncated teardrop specimen: Phase, black circle-measurements, red triangle –TMA model, green diamond – TMA model with the truncated teardrop specimen represented by the CFD/SI approach.....	101
Fig. 8.1	Picture of the investigated experimental test rig [74]	103
Fig. 8.2	Sketch of a prototype burner [74]	104
Fig. 8.3	Ten degree segment of URANS model.....	105
Fig. 8.4	Boundary conditions and CFD model of an atmospheric test rig	106
Fig. 8.5	Atmospheric test rig: a - normalized axial velocity distribution, b - normalized static temperature	107
Fig. 8.6	Flame transfer function: normalized amplitude. green and red rectangular – measurements with $P_u=16\%$, blue diamonds – CFD/SI	108
Fig. 8.7	Flame transfer function: phase, green and red rectangular – measurements with $P_u=16\%$, blue diamonds CFD/SI	109
Fig. 8.8	PDF and DF distributions of the atmospheric test rig: green rectangular – PDF (probability density function), red rectangular – DF (distribution function)	110
Fig. 8.9	Flame transfer function: phase: green and red rectangles – measurements with $P_u=16\%$, blue diamonds CFD/SI, yellow triangles – time lag model with $\tau=14.8$ ms based on a RANS simulation	111
Fig. 8.10	Flame transfer function- Normalized amplitude: red triangles – URANS with single sinusoidal excitations, blue diamonds – CFD/SI.....	112
Fig. 8.11	Flame transfer function - phase: red triangles – URANS with.....	112
Fig. 8.12	Normalized molar reaction rate: a) EDM, b) model EDM/FRCH, c) model EDM/FRCH model with five step kinetics.....	114

Fig. 8.13	Normalized reaction rate distribution: blue diamonds - EDM, red rectangular - EDM/FRCH with 5 steps chemistry and green triangle – EDM/FRCH with one step.....	115
Fig. 8.14	Flame transfer function - normalized amplitude: blue diamonds – EDM/FRCH with one step chemistry, crimson rectangular EDM/FRCH with five steps kinetics, green triangle – EDM, green and red rectangles – measurements with $P_u=16\%$	116
Fig. 8.15	Flame Transfer Function. Phase. blue diamonds – EDM/FRCH with one step chemistry, crimson rectangular EDM/FRCH with five steps kinetics, green triangle – EDM, green and red rectangles – measurements with $P_u=16\%$	117
Fig. 8.16	Flame transfer function. normalized amplitude: yellow circle – reflective inlet & outlet, dark blue diamonds reflective inlet & non-reflective outlet, blue triangle – non-reflective inlet & outlet.....	118
Fig. 8.17	Flame transfer function - phase: yellow circle – reflective inlet & outlet, dark blue diamonds reflective inlet & non-reflective outlet, blue triangle – non-reflective inlet & outlet.....	119
Fig. 8.18	Normalized heat release time evaluation at 60 Hz: blue circle – reflective inlet & outlet, red rectangular non-reflective inlet & outlet	120
Fig. 8.19	Normalized pressure time evaluation at 60 Hz: blue circle – reflective inlet & outlet, red rectangular – non- reflective inlet & outlet.....	121
Fig. 8.20	Fast Fourier transform of pressure at the same monitor point: blue circle – reflective inlet & outlet, red circle – non-reflective inlet & outlet	121
Fig. 8.21	Flame transfer function: normalized amplitude: orange circle – $\Delta t = 0.000025$ s, pink triangle – $\Delta t = 0.00005$ s, blue diamonds – $\Delta t = 0.0001$ s	122
Fig. 8.22	Flame transfer function: phase: orange circle – $\Delta t = 0.000025$ s, green triangle – $\Delta t = 0.00005$ s, blue diamonds – $\Delta t = 0.0001$ s	123
Fig. 9.1	An industry test rig with a prototype combustion system	125
Fig. 9.2	CFD boundary conditions for a $1/8^{\text{th}}$ sector model.....	126
Fig. 9.3	Normalized velocity and CH ₄ mass fraction for the main inlet A.....	127
Fig. 9.4	Normalized axial velocity distribution and normalized molar reaction rate distribution at $z=0$ m.....	128

Fig. 9.5	Flame transfer function: normalized amplitude, blue triangle – CFD/SI, green rectangular – harmonic excitation	129
Fig. 9.6	Flame transfer function: phase angle, blue triangle – CFD/SI, green rectangular – harmonic excitation	130
Fig. 9.7	PDF and DF distributions: green rectangular – PDF (probability density function), red rectangular – DF (distribution function).....	131
Fig. 9.8	Flame transfer function: phase: green triangles – time lag model, dark blue triangles – CFD/SI.....	132
Fig. 9.9	TMA model of industrial experimental test rig at elevated pressures.....	133
Fig. 9.10	TMA sensitivity to a small change in the mean time lag value: rectangular - TMA with FTF induced by u' (based on the time lag approach) with different mean time lag values, green diamonds - measurements	134
Fig. 9.11	Predictions and measurements of the stability margin for the considered system: red rectangular - TMA model with FTF induced by u' based on the CFD/SI, blue rectangular - TMA model with FTF's based on the time lag approach, green diamonds - measurements.....	135
Fig. 10.1	SAS geometry and boundary conditions	138
Fig. 10.2	Grid resolution (a), blending factor (b), and CFL number of SAS model (c).....	140
Fig. 10.3	The axial velocity distribution: instantaneous SAS (a), averaged SAS (b), and RANS solution (c)	141
Fig. 10.4	The normalized temperature distribution: instantaneous SAS (a), averaged SAS (b), and RANS solution (c)	141
Fig. 10.5	$Y_{CH_4}=0.003$ iso-surface colored by the normalized axial velocity	142
Fig. 10.6	Flame visualization from [74]: left: quasi-steady flame at about 10 Hz, right: ring vortex structure at about 55 Hz	143
Fig. 10.7	Visualization of ring structures induced by the inlet forcing:Left - LES from [81] at 120 Hz ,Right - SAS at 90 Hz.....	143
Fig. 10.8	CH ₄ iso-surfaces for five phases of a forced cycle at 90 Hz.....	144
Fig. 10.9	Time evaluation of the averaged velocity at the diagonal inlet (red triangles) and the volume integrated heat release (blue triangles).....	145

Fig. 10.10 Prediction and measurement of the phase of flame transfer function: SAS-based phase (dark triangle), CFD/SI (blue rectangular), and measurements (red and green rectangular)	146
Fig. 11.1 SAS boundary specification for the full 360-degree model	147
Fig. 11.2 Grid resolution (a), blending factor (b) and CFL number of the SAS model (c) ..	149
Fig. 11.3 The normalized axial velocity distribution: instantaneous SAS (a), statistically averaged SAS (b), and bottom RANS solution (c).....	150
Fig. 11.4 The normalized temperature distribution: upper left corner – instantaneous SAS, upper right corner averaged SAS and bottom RANS solution	151
Fig. 11.5 Visualization of coherent structures by strain rate invariants colored by the normalized temperature	152
Fig. 12.1 URANS Boundary conditions for a calculation of self-excited oscillations	156
Fig. 12.2 Pressure time evaluation of a monitor point for $dt=0.00005$ s and characteristic phases	157
Fig. 12.3 TMA model of a generic burner	158
Fig. 12.4 TMA perdition vs. URANS computation: red rectangular – TMA prediction, blue triangle – URANS computation.....	160

List of Tables

Tab. 6.1	Numerical models – duct with a sudden change of dimensions.....	75
Tab. 7.1	Numerical models- truncated teardrop specimen	91
Tab. 8.1	Numerical models - Atmospheric Test Rig	106
Tab. 9.1	Numerical models - Industrial Test Rig at elevated pressure.....	127
Tab. 10.1	Numerical models- SAS of an atmospheric test rig	139
Tab. 11.1	Numerical models- SAS of Industrial Test Rig at elevated pressure.....	148
Tab. 12.1	TMA acoustic boundary conditions for a generic burner.....	159

Nomenclature

Roman letters

A	Pre-exponential constant	[1/s]
A	Area	[m ²]
A _{EBU}	Eddy Break-Up coefficient	[-]
B _{EBU}	Eddy Break-Up coefficient	[-]
c	Cross-correlation vector	[-]
c	Speed of sound	[m/s]
c _p	Specific heat at constant pressure	[J/kgK]
c _v	Specific heat at constant volume	[J/kgK]
d	Diameter	[m]
D _k	Molecular diffusivity coefficient of species k	[m ²]
e	Internal energy	[J/kg]
f	upstream traveling wave	[-]
f	Frequency	[Hz]
f _N	Nyquist frequency	[Hz]
F	Transfer Function	[-]
g	downstream traveling wave	[-]
h	Unit impulse	[-]
h _{tot}	Total enthalpy	[J/kg]
k	Turbulence kinetic Energy	[m ² /s ²]
k	wave number (=ω/c)	[rad/m]
k	Amplification index in n-τ model	[-]
k±	modified wave number (=ω/(c±u))	[rad/m]
l _{eff}	Effective length	[m]
l _{red}	Reduced length	[m]
L	Filter order in Wiener-Hopf equation	[-]
L _T	Characteristic turbulence length scale	[m]
L _{flame}	Flame length	[m]
m	Jump factor in Wiener-Hopf equation (dt=mΔt)	[-]
M	Mach number (=u/c)	[-]

n	Mode number	[-]
N	Number of time steps	[-]
P	Pressure	[Pa]
q	Volumetric heat release rate	[W/m ³]
Q	Heat release rate	[W]
r	System response	[-]
R	Acoustic reflection coefficient	[-]
R	Radius for general purposes	[m]
R	Gas constant	[J/kgK]
s	Input signal	[-]
t	time	[s]
t _{chem}	Chemical time scale	[s]
T	Temperature	[K]
T	Time scale	[s]
T	Transfer matrix	[-]
u	Velocity	[m/s]
V	Volume	[m ³]
Y	Mass Fraction of species k	[-]
x,y,z	Cartesian coordinates	[m]
X	White noise	[-]
z	Argument of z-transform	[-]
Z	Acoustic Impedance (=p'/u')	[kg/m ² s]
D	Inlet or outlet diameter	[m]
Z _o	Characteristic acoustic impedance	[kg/m ² s]
Z _{red}	Reduced acoustic Impedance	[-]
St	Strouhal number (=fD/u)	[-]
Pu	Pulsation level	[%]
S	Invariant of strain rate	

Greek letter

α	Area ratio	[-]
Δ	Relative quadratic difference	[-]
Δx	Distance between reference planes	[m]
Δt	Discrete time step in CFD	[s]
β_t	Turbulent damping	[1/s]

β_v	Thermo viscous damping	[1/s]
γ^2	Coherence function	[-]
Γ	Eddy diffusivity	[-]
$\mathbf{\Gamma}$	Auto-correlation matrix	[-]
ε	Time truncation error	[-]
ε	Turbulence eddy dissipation	[m ² /s ²]
η_{Kol}	Kolmogorov length scale	[m]
κ	Thermal diffusivity	[kg/ms]
κ_t	Turbulence diffusivity	[kg/ms]
κ	Ration between specific heat capacities (=c _p /c _v)	[-]
λ	Thermal conductivity	[W/mK]
λ	Acoustic wavelength (=c/f)	[m]
λ	Air factor (=1/φ)	[-]
μ	Dynamic viscosity	[kg/ms]
μ_t	Turbulence viscosity	[kg/ms]
ν	Kinematic viscosity (=μ/ρ)	[m ² /s]
ν	Stoichiometric coefficient	[-]
ρ	Density	[kg/m ³]
τ	Time delay for general purposes	[s]
τ_v	Viscous shear stress	[Pa]
ϕ	Equivalence ratio (=1/λ)	[-]
Φ	Independent variable in CFD problem	[-]
ζ	Pressure loss coefficient	[-]
ω	Angular frequency (=2πf)	[rad/s]
ω_k	Chemical source term for species k	[kg/m ³ s]
ω_i	Imaginary part of angular frequency	[rad/s]
ω_r	Real part of angular frequency	[rad/s]

Mathematical letter

\times	Cross-product
$\det(\mathbf{A})$	Determinant of matrix A
:	Double inner product of two tensors
\tilde{x}	Favre average of a quantity x

x''	Fluctuation corresponding to Favre average of quantity x
x'	Fluctuation corresponding to Reynolds average of quantity x
\hat{x}	Fourier transformation of x
∇	Gradient operator
$\Im(x)$	Imaginary part of x
$i = \sqrt{-1}$	Imaginary unit
\cdot	Inner product
A^{-1}	Inverse of Matrix A
Δ	Laplace operator ($=\nabla\cdot\nabla$)
$\frac{D}{Dt}$	Material derivative
O	Order
$\frac{\partial}{\partial t}$	Partial derivative
PDF(x)	Probability density function of x
DF(x)	Probability distribution function of x
$\Re(x)$	Real part of x
\bar{x}	Reynolds average of a quantity x
Σ	Summation

Abbreviations

CFD	Computational Fluid Dynamics
CFL	Courant-Freidricks-Levy number
CPU	Central Processing Unit
CTA	Constant Temperature Anemometry
CV	Control Volume
DNS	Direct Numerical Simulation
DF	Probability Distribution Function
FFT	Fast Fourier Transform
FTF	Flame Transfer Function
GR	Growth Rate of unstable Frequencies
LES	Large Eddy Simulation
NS	Navier-Stokes
PDF	Probability Density Function
RANS	Reynolds averaged Navier-Stokes
SAS	Scale Adaptive Simulation

URANS	Unsteady Reynolds averaged Navier-Stokes
STP	Standard Temperature and Pressure
TMA	Thermoacoustic Stability Code developed at Siemens
SI	System Identification
DES	Detached Eddy Simulation
SST	Shear Stress Transport Model
EDM	Eddy Dissipation Model
FRCH	Finite Rate Chemistry Model
LTI	Linear Time invariant
SISO	Single Input – Single Output
MIMO	Multi Input – Multi Output
ARX	AutoRegressive model with eXternal input
FIR	Finite Impulse Response
LODI	Navier-Stokes characteristic boundary conditions (NSCBC) including viscous and diffusion terms under the locally one-dimensional inviscid (LODI) assumptions
RBC	Reflective Boundary Condition
NRBC	Acoustic Non-Reflective Boundary Condition

Zusammenfassung

Der Einsatz von fossilen Brennstoffen zur Energieerzeugung hat einen signifikanten Einfluss auf die Umwelt, denn sogar das Verbrennen von Erdgas – weitläufig als die sauberste aller verfügbaren fossiler Energiequellen betrachtet – ist im Allgemeinen mit Emissionen vieler Luftschadstoffe verbunden. In den letzten Jahrzehnten wurden zusätzliche Umweltregulierungen eingeführt, um die Emissionen von Gasturbinen zu reduzieren. Im Mittelpunkt des Interesses stand dabei die Reduktion von Stickoxiden (NO_x) auf akzeptable Werte. Erreicht wurde diese Reduktion teilweise durch den Einsatz einer mager vorgemischten Flamme gegenüber der standardmäßigen Diffusionsflamme. Der wesentliche Nachteil dieser Verbrennungskonzepte besteht in ihrer Anfälligkeit gegenüber thermo-akustisch induzierten Schwingungen, die als Ergebnis des komplexen Rückkoppelungsmechanismus zwischen Druck- und Wärmefreisetzungsschwankungen induziert werden und unter bestimmten Betriebsbedingungen zu unkontrolliert hohen Druckamplituden im Inneren der Brennkammer führen können.

Um die lineare Stabilität des teilweise vorgemischten Verbrennungssystems von industriellen Gasturbinen vorhersagen zu können, braucht man eine detaillierte Beschreibung der akustischen Charakteristik jeder der Hauptkomponenten. Veränderungen im Verbrennungsprozess von Gasturbinen zur Reduktion der Emissionen kann zu großen Amplituden der Druckschwingungen, verbunden mit einer Kopplung zwischen den natürlichen akustischen Moden des Brenners und der transienten Wärmefreisetzung der Flamme führen. Detaillierte eindimensionale akustische Modelle müssen daher aufgesetzt werden, um gesamte Verbrennungssysteme nachbilden zu können und bestehen aus Leitungen, Diffusoren, Verbindungen und einem Flammelement. Es sind zeitlich verzögerte Elemente nötig, um Interaktionen zwischen Akustik und transienter Wärmefreisetzung zu beschreiben und um die Stabilität des Systems unter Verwendung der linearen Stabilitätstheorie zu untersuchen. Das Hauptziel dieser Arbeit war die Entwicklung und Validierung technisch relevanter Werkzeuge, um die Folgen von Verbrennungsinstabilitäten zu vermeiden.

Aus Sicht der akustischen Modellierung können die Elemente des Verbrennungssystems entweder durch akustische Übertragungsmatrizen oder Flammenübertragungsfunktionen charakterisiert werden. Die Beschreibung des Brenners und der Flamme sind von besonderer Bedeutung. In der vorliegenden Studie wurden das akustische Übertragungsverhalten einer abrupten Querschnittsänderung, einer abgeschnittenen "Tränentropfenprobe", eines atmosphärischen Drallbrenners, sowie eines Prototyps eines industriellen Brenners bei höheren Drücken unter Verwendung transienter Strömungssimulation und Systemidentifikation berechnet. Ein leicht verständlicher Prozess zur Berechnung von solchen Übertragungsverhalten wurde dargestellt. Wann immer möglich wurden die Ergebnisse validiert und mit experimentellen und theoretischen Daten verglichen.

Im vorliegenden Falle eines Industriebrennerprototypen bei hohen Drücken wurde nachgewiesen, dass es durch den Einsatz von CFD-basierenden Flammentransferfunktionen möglich ist, die Vorhersage der gesamten Stabilität des Verbrennungssystems zu verbessern.

Zusätzlich zu diesen Berechnungen wurden LES-ähnliche Berechnungen eines atmosphärischen Drallbrenners und eines Prototyps eines industriellen Brenners bei höheren Drücken durchgeführt, um die Flammen- und Strömungsdynamik zu bestimmen, welche möglicherweise für die Stabilität des gesamten Verbrennungssystems verantwortlich sein könnten. Im Falle eines atmosphärischen Drallbrenners wurde die über LES berechnete Strömung bei diskreten Frequenzen angeregt, um die Entwicklung von kohärenten Strukturen in der Brennkammer sichtbar zu machen. Ähnlich den Experimenten wurde die Entwicklung von kohärenten Strukturen bestimmt. Die numerischen Visualisierungen wurden mit den experimentellen Ergebnissen verglichen.

Zuletzt wurde eine beispielhafte Berechnung von selbsterregten Schwingungen durchgeführt, um zu demonstrieren, dass kommerzielle CFD-Programme in der Lage sind, diese Art von Instabilitäten zu berücksichtigen. Die instabilen Frequenzen, welche während der Berechnung bestimmt wurden, wurden durch Anwendung eines eindimensionalen akustischen Modells validiert.

Summary

The use of fossil fuels in power generation has a significant impact on the environment. Even the burning of natural gas, considered as the cleanest of all commonly available fossil fuels, is generally associated with emissions of many dangerous air pollutants. In the last decades, additional environmental constraints have been introduced to reduce the emissions from gas turbines. The primary focus has been especially placed on nitrogen oxide (NO_x) to minimize its emissions to acceptable values. This reduction has been partially accomplished by utilizing a lean-premixed flame rather than the standard diffusion type flame. The biggest disadvantage of these combustion systems is that they are very prone to thermo-acoustically induced oscillations as a result of a complex feedback mechanism between pressure and heat release fluctuations, which may lead to uncontrolled high-pressure amplitude oscillations inside the combustor at certain operating conditions.

In order to predict the linear stability of partially premixed combustion systems in industrial-scale gas turbines, a detailed acoustic characteristic for each of the major components is required. Sudden changes in the combustion process of gas turbines in order to reduce emissions may result in large amplitude pressure oscillations associated with a coupling between the natural acoustic modes of the combustor and the unsteady heat release from the flame. Detailed one-dimensional acoustic network models have to be built up to represent entire combustion systems. These models consist of ducts, diffusers, junctions and a flame element. Time delay elements have to be applied to describe properly the interactions between acoustics and heat release fluctuations and to investigate the stability of the system using linear stability theory. The main goal of this work is to develop and to validate technically relevant tools to mitigate the consequence of an occurrence of combustion instabilities.

From the acoustic modeling point of view, the combustion system elements can be characterized either by their acoustic transfer matrices or by flame transfer functions. A description of the burner and flame are of main importance. In this study, acoustic characteristics of a sudden change of area, a truncated teardrop specimen, an atmospheric generic swirl burner, and a prototype industrial burner at elevated pressure have been made by means of unsteady flow simulations and system identification. A comprehensive process for the computation of such CFD/SI based characteristics has been shown. Whenever possible the results have been validated and compared with the experimental and theoretical data. In the case of the prototype industrial burner at elevated pressure it has been demonstrated that using the CFD based flame transfer function it is possible to improve the overall gas turbine combustion system stability prediction.

In addition to these calculations, LES-like computations of an atmospheric swirl burner, and a prototype industrial burner at elevated pressure have been performed. It allows for the determination of flame and flow dynamics, which might drive the stability of the entire combustion system.

In the case of an atmospheric swirl burner, the LES-based flow field has also been forced at discrete frequencies to visualize the development of coherent structures in the combustion chamber. Similarly, to the experiments, the evaluation of coherent structures is captured. The numerical visualizations are then compared with the experimental findings.

Finally, an exemplary calculation of self-excited oscillations has been made in order to demonstrate that commercial CFD codes are able to capture these kinds of instabilities. The unstable frequencies found during the computation have been benchmarked employing one-dimensional acoustic network code.

1 Introduction

The use of fossil fuels in power generation has a significant impact on the environment. Even the burning of natural gas considered as the cleanest of all commonly available fossil fuels, is generally associated with emissions of many air pollutants such as CO_2 , NO_x , UHC and CO [105]. The emission of CO_2 can be directly correlated with the global warming effect whereas a high concentration of nitric oxide can lead to respiratory problems and other serious illnesses [1]. Another serious problem caused by this pollutant is the production of acid rain, which causes major soil damage.

In the last decades, additional environmental constraints have been introduced to reduce the emissions from gas turbines. The primary focus has been especially placed on nitrogen oxide (NO_x) to minimize its emissions to acceptable values. However, flame stabilization mechanisms using piloting, as usually implemented in current designs, creates regions where temperatures are significantly higher than the turbine inlet temperature. These hotter regions are responsible for an additional NO_x formation. Therefore, a change in the combustion process to reduce the flame temperature is required. This reduction has been partially accomplished by utilizing a lean-premixed flame rather than the standard diffusion type flame [103]. A diffusion flame temperature is the highest at positions where air and methane meet each other at stoichiometric proportions ($\Phi \sim 1$).

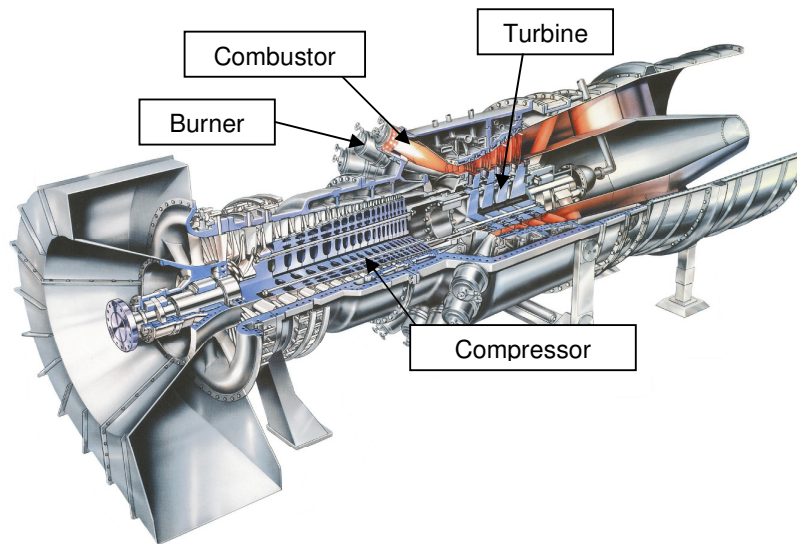


Fig. 1.1 Cross section of the SGT6-6000G gas turbine

As a consequence, the combustion process takes place in a zone at the highest possible temperature, unlike the lean premixed flame that burn at much lower temperatures due to the pre-mixing processes of fuel and air, resulting in a fuel lean mixture ($\Phi < 1$). The fuel mixture must be well premixed to prevent local variations of the fuel-to-air ratio and consequently locally occurring higher temperature regions. This concept is applied to the latest generation of gas turbine combustion systems and is known as lean premixed combustion systems [104].

An example of the latest generation of Siemens SGT6-6000G gas turbines [4] is shown in Fig. 1.1. It has a maximum electrical power output of 266 MW in a single cycle arrangement. In a combined cycle arrangement, the power output increases up to 391 MW. In this case, an overall efficiency of 58.4 % can be achieved. As a gas turbine that is fired with natural gas, NO_x emission below 25 ppm is guaranteed [104].

The use of pre-mixed flames has reduced NO_x emissions to tolerable levels [2]. The disadvantage of these combustion systems is that they are very prone to thermo-acoustically induced oscillations as a result of a complex feedback mechanism between pressure and heat release fluctuations, which may lead to uncontrolled high-pressure amplitude oscillations inside the combustor at certain operating conditions. The resulting mechanical forces can generate high-frequency fatigue stresses on the combustor walls, which significantly reduce the reliability of the gas turbine. Moreover, heat transfer to the liner is driven by the unsteady combustion process, which may lead to locally overheated wall regions.

Under the stringent NO_x emission regulations and operational flexibility requirements, the development of gas turbine combustion systems is limited on the one hand by an overall emission level and on the other hand by thermo-acoustically induced combustion oscillations. Lord Rayleigh in 1878 [30] formulated the fundamental stability criterion for thermo-acoustic oscillations in which he expressed the physical condition that leads to thermo-acoustic stability. Following Rayleigh, many other authors have been studying the interaction of heat and sound resulting in a basic understanding of this condition in simple gas turbine combustion systems [3].

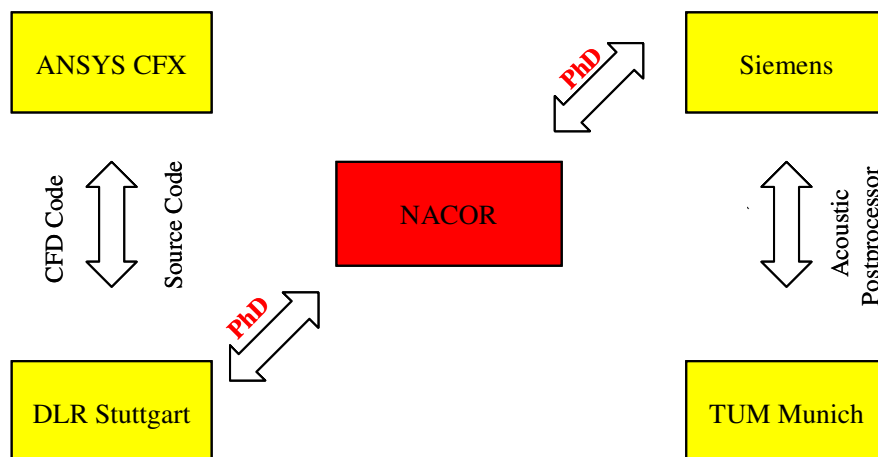


Fig. 1.2 NACOR Project - competence circle

The present work has been done in the frame of the NACOR PROJECT (Setup of a Numerical Test Rig for Mitigation of ALL-Combustor Humming Risks), which was initiated in 2003 for a better understanding and control of the creation of large amplitude oscillations in gas turbine combustors. Collaboration between Siemens AG and DLR (represented by the Institute of Combustion Technology) has been established to understand and characterize the physical nature of thermo-acoustically induced oscillations. To efficiently mitigate the occurrence of these instabilities, the further development and validation of already existing computational tools is needed. Fig. 1.2 shows the interdependence circle of all the institutions involved in the current project. The main project partners are Siemens AG¹, and DLR². Co-partners are TU Munich³ and ANSYS⁴.

Since the development of new combustion systems requires the detailed investigation of thermo-acoustic properties of a given system to better guide an experimental program and to decrease the number of costly engine tests, the main objective of the NACOR Project is to provide a numerical test rig based on time-resolved CFD computations. Using advanced computational methods, that is, URANS⁵, SAS⁶, SI⁷ and TMA⁸ to investigate combustion dynamics and flame/vortex interactions, a relatively low cost verification of various design concepts in terms of the detection and the reduction of combustion instabilities of gas turbines combustion systems can be performed. The main goal is to first of all improve the prediction of stability margins associated with self-excited combustion oscillations with respect to intermediate frequency dynamics (IFD) and secondly to calculate self-excited oscillations directly using impedance boundary conditions. The NACOR project is of an interdisciplinary nature and its success is inherently based on combining advanced state-of-the-art CFD combustion methods and unsteady CFD methods.

Flow fields in modern gas turbine combustors are often inherently unstable, and in many cases steady state computational methods are not capable of predicting the correct properties of the flame. As a result, it is not sufficient to use a steady state approach to determine system dynamics when analyzing combustion systems featuring oscillating flames over a wide range of operating conditions. There are some prominent deficiencies in flame modeling using the time lag approach in TMA models [36]. Therefore, the proper resolution of the dynamical behavior of the system under investigation requires a 3D transient approach. 3D simulations can capture time and space dependent evaluation of 3D aerodynamic design features. CFD based investigations can show the impact of some unstable flow features on the combustion system. The system identification method (SI⁷) coupled with URANS computations, known as CFD/SI [43], can also be used to determine the system dynamics represented by either by acoustic transfer matrix of a flame or flame transfer functions. Alternative methods to analyze combustion systems are SAS computations with a harmonic forcing or direct computations of self-excited oscillations. However, these methods are much more computationally expensive than forced URANS computations because they involve larger computational domains and smaller time steps to enable thermoacoustic instabilities to develop.

¹ Siemens AG, Department of Combustion Technology, Mülheim an der Ruhr

² German Aerospace Agency, Institute of Combustion Technology, Stuttgart

³ Technical University Munich, Institute for Thermodynamics, Garching

⁴ ANSYS GmbH, Otterfing, Germany

⁵ Unsteady Reynolds Averaged Navier Stokes

⁶ Scale Adaptive Simulation – hybrid approach from CFX ANSYS enabling LES-like computations

⁷ System Identification from Control Theory

⁸ Thermoacoustic Stability Code developed at Siemens

1.1 Research objective

The purpose of the present work, carried out in the frame of the NACOR project, is to introduce, test and validate advanced CFD-based computational tools for the identification and detailed characterization of thermo-acoustic systems. One novel contribution of this study is the use of unsteady CFD computations coupled with the system identification method to reconstruct flame transfer functions and acoustic transfer matrices at real operating conditions. By employing these unsteady CFD-based flame responses, it is possible to improve the overall predictability of the one-dimensional acoustic network code (TMA). In addition to this, the further development of TMA with regard to simple one-dimensional acoustic elements such as flame and straight duct elements has been made. All CFD calculations have been conducted using the commercial code ANSYS CFX. The ability to reconstruct the flame transfer function has been further evaluated by utilizing acoustic non-reflective boundary conditions. Whenever possible, the calculated flame transfer functions/acoustic transfer matrices (FTF/ATM) have been validated with existing experimental data

Moreover, the influence of combustion modeling on the CFD/SI method especially with respect to industrial requirements, that is, high pressure levels, cooling flow injections has been investigated in greater detail. Finally, for the first time a validation of this method of a real generic industrial combustor has been performed. In addition to that, LES-like methods has been introduced as a valuable tool that may be employed to determine coherent structures present in the reacting flow field being responsible for flame dynamics.

A further research objective of this study is to utilize URANS methods to perform the computation of self-sustained oscillations. At a given operating condition, the direct interaction between unsteady heat release fluctuations and unsteady velocity fluctuations makes the gas turbine combustion system unstable.

The main objectives of this study can be briefly summarized as follows:

- To calculate and validate acoustic transfer matrices of a sudden change of area dimensions and a truncated teardrop specimen at higher Mach number (~ 0.4) to demonstrate the applicability of the CFD/SI method. To investigate various numerical and physical parameters, that is, time and space resolutions, and acoustic boundary conditions, which may influence the entire identification process. The improvement of single TMA elements using acoustic transfer matrices based on CFD/SI.
- The derivation and detailed validation of CFD/SI based flame transfer functions in order to describe better the relation between velocity and heat release fluctuations compared to a standard time lag approach.
- The improvement of flame responses represented by a 1D flame element by means of the CFD/SI approach, and further improvement in the prediction of thermo-acoustic stability.
- The application and investigation of capabilities of LES-like (SAS) computations to reveal unsteady flow features that may enhance flow dynamics and acoustically induced oscillations.
- The calculation and validation of self-excited oscillations for a generic atmospheric burner by means of URANS and TMA is performed.

The last two are the most demanding in terms of computational expenses. It is necessary to use a very small time step and a 3D geometry when employing SAS computations. For the computation of self-excited dynamics, a further computational penalty is incurred with SAS due to the requirement to extend the computational domain. This extension is needed in order to accurately mimic the acoustic BC.

1.2 Literature overview

In general, there are two key strategies for studying combustion dynamics of thermo-acoustic systems. The first strategy is associated with the self-excitation of combustion modes. In this case, flames themselves strongly interact with acoustic waves. When acoustic pressure fluctuations and heat release fluctuations oscillate in phase then acoustic energy is added to the system, which may become unstable [5]. In some cases, the flows are dominated by their own instability modes, and the feedback loop mechanism cannot be inhibited. The alternative strategy to analyze the dynamics of a system is the forced response approach. However, this approach can be only applied to flows that do not exhibit any self-excited combustion instabilities. Utilizing an additional external forcing in the forced response study could lead to an incorrect understanding with regard to combustion dynamics being already driven by natural unstable modes.

To model and reproduce all the mechanisms that are responsible for combustion driven oscillations, all acoustic relevant components of the combustion systems, starting from the compressor exit up to the turbine inlet, must be included. The pre-dominant source of the acoustic wave is the flame itself. Hence the dynamics of a given combustion system can be characterized mainly by a flame transfer function relating flow variables as a function of frequency [43][59]. Knowing that flame transfer functions, obtained by means of unsteady CFD simulations, describe how a particular thermo-acoustic system behaves, one can combine these with one-dimensional acoustic network codes to determine the overall stability of thermo-acoustics systems [44][96]. This provides an alternative approach to a detailed CFD analysis of a whole system including the upstream and the downstream boundaries of the combustor.

Total mass flow and equivalence ratio fluctuations are the two main factors affecting overall system dynamics. Total mass flow fluctuations can be encountered in fully and partially premixed combustion mode, and are a result of interactions between pressure waves originated in the combustor and the flame front. Equivalence ratio fluctuations occur in partially or fully premixed flames and are a result of differences in acoustic impedance between fuel and air passages. There are also other effects such as hydrodynamic instabilities and coherent flow structures induced by flow acoustic oscillations at the burner mouth that may also be important [97][98].

There are several different means to investigate the thermo-acoustic flame response. Measurements can provide relevant data to reconstruct flame transfer functions, but usually measurement techniques to capture flame dynamics are very complex and limited due to restrictions in optical access. Nevertheless, there are also some good examples of using measurements in the study of flame dynamics. For instance, Lohrmann et al. [74] has performed OH radical concentration measurements and correlated them with a harmonic signal to derive the flame transfer function.

The influence of pressure level on the flame transfer function has been investigated by Freitag et al. [82]. It resulted in determining a power law pressure scaling of the flame transfer function behavior. Auer et al. [99] investigated the impact of air and fuel on flame dynamics. Bellows et al. [83] has also demonstrated that non-linear flame responses can be analyzed by means of experiments. Moreover, Paschereit et al. [81] has used a multi-microphone method to successfully reconstruct the acoustic transfer matrix of a premixed flame.

Flame dynamics can also be analyzed by means of either steady or unsteady simulations. Krebs et al. [36] reconstructed the flame response based on velocity fluctuations using the standard $n-\tau$ formulation derived by Crocco et al. [35]. Crocco proved a general concept that dynamics can be characterized by a global time lag. Similar to Krebs, Flohr et al. [85] employed time lag distributions based on steady CFD computations to derive the acoustic transfer matrix. Other researchers utilized unsteady RANS computations forced at discrete frequencies to determine dynamical flame behavior. Hettel et al. [75][84] succeeded in computing the flame transfer function at discrete frequencies using URANS computations based on single sinusoidal excitations. The idea of extracting dynamical characteristics of a flame from time-dependent simulations and then using this information in linear acoustic analysis has been first introduced by Bohn and Dueker et al. [44] for a turbulent flame and by Krueger et al. [45] for a gas turbine burner. In these studies, the response of the flame to a sudden increase of mass flow rate was determined in a time dependent simulation. The step response was then Laplace-transformed into frequency space, yielding the frequency response function. Moreover, Gentemann and Polifke et al. [43] proposed to employ an alternative computational approach based on System Identification and unsteady URANS computations excited by white noise to investigate flame dynamics for perfectly premixed swirl flames. The reconstructed flame response has been compared to experimental results with satisfactory agreement. In contrast to the Deuker's approach, it has been proposed to determine the impulse response function of a one-port system from unsteady CFD simulation with the random perturbed inlet. Subsequently, the impulse response is z-transformed to obtain the flame transfer function, or with respect to multi-port systems acoustic transfer matrices. Kostrzewa et al. [59] applied the CFD/SI approach successfully to the flame response of a generic gas turbine burner. Recently Huber et al. [96] applied CFD/SI to reconstruct the flame responses to velocity and equivalence ratio fluctuations. Having information of flame dynamics in a form of flame transfer functions, he investigated the impact of fuel supply impedance on the combustion stability of gas turbines. It has been also shown by Polifke et al. [46] that the CFD/SI method can be employed to estimate the acoustic transfer matrix of a simple burner with a flame. A reconstruction of the complete acoustic transfer matrices for a sudden change of area was performed and validated using CFD/SI in [17]. Paschereit and Polifke et al. [42] determined acoustic transfer matrices of a premixed burner getting comparable results with measurement.

Giauque et al. [37] proposed an optional numerical technique using sinusoidal forced LES simulations to evaluate flame dynamics. This computational method offers potentially the most accurate representation in terms of the identification of flame dynamics but it is almost impossible to analyze the dynamics of industrial combustion processes due to very high computational costs.

Following this approach, Truffin et al. [86] studied the unsteady response of partially premixed flame at discrete frequencies. Employing recently developed hybrid models such as Detach Eddy Simulations (DES) and Scale Adaptive Simulations (SAS) seems to be very promising in evaluating unsteady flow features keeping the computational requirement relatively low compared to pure LES computations [65][67][131].

Reliable information about a system dynamic can also be directly obtained from computations of self-excited oscillations. They have a great advantage over the forced response methods since they are able to capture any unstable modes as soon as they are amplified in a manner similar to experiment. However, to be able to perform a combustion simulation of self-excited oscillations, it is very often required that the entire combustion geometry is considered. The geometry should include all inlets and outlets with well-defined acoustic boundary conditions. Due to high computational costs, this approach cannot be widely utilized. Nevertheless, there are some examples using this approach found in literature. The acoustic energy balance and acoustic modes in a turbulent swirled combustor were investigated using LES with well-defined acoustic boundary conditions by Martin et al. [89]. Contrary to Martin's study, URANS computations with the total pressure imposed at inlets and the static pressure at outlets were performed in [88][87] to analyze the self-excited combustion instability encountered in a lab scale, swirl-stabilized combustion system. The total pressure boundary condition enabled flow instabilities to grow and develop with time, which reach a limit cycle after sufficiently long computation time. In addition to this, it is demonstrated in [80] that URANS computation was also able to capture high frequency flow instabilities near an airblast atomizer. There is also ongoing work regarding impedance boundary conditions in CFD, which can be employed to correctly model acoustic boundary conditions of a combustor. Widenhorn et al.[93] and Huber et al. [101] have demonstrated the feasibility of these types of CFD boundary conditions.

1.3 Thesis outline

Chapter 1 introduces the general problems related to thermo-acoustics and emissions from the modern gas turbine combustion system standpoint. The NACOR Project is briefly discussed, and all key research objectives and a literature overview on combustion dynamics studies are presented.

In chapter 2 the theoretical background and some mechanisms leading to combustion driven oscillations are briefly discussed, and the acoustic role of a flame in combustion driven oscillations based on Rayleigh's criterion is also explained.

Chapter 3 provides the fundamentals of acoustic modeling including the wave equation and its solution. Additionally, the one-dimensional approximation is discussed in light of one-dimensional acoustic network codes. This is supplemented by an efficient linear stability analysis, which results in frequencies at which unstable modes are determined. The key element in the stability assessment is a flame element represented by the flame transfer function.

Chapter 4 provides an introduction to turbulence modeling. Energy spectrum and turbulence length scales found in typical turbulent flows are presented. Moreover, turbulence models such as $k-\epsilon$ and SAS utilized in this thesis are outlined.

Since the objective of this thesis is to investigate flame dynamics, it is necessary to give an introduction of turbulent combustion. Reacting flow calculations are always considered under highly turbulent conditions. In this context, the calculation of molar reaction rate using the eddy dissipation concept and the combination of the eddy dissipation model with the finite chemistry model are also explained.

Chapter 5 deals completely with the numerical forced response method and system identification. The background of system identification including essential models, and excitation signals are presented. In addition to this, an optimal setting for the reconstruction of acoustic transfer matrices and flame transfer functions is discussed.

In chapters 6 and 7 the model of a sudden change of area dimensions and a truncated teardrop specimen under non-reacting flow conditions are used to validate the CFD/SI approach for reconstructing acoustic transfer matrices. Acoustic transfer matrices are derived for both cases and the influence of several parameters such as spatial discretization, time discretization, and time scheme on the reconstructed amplitude and phase are examined. The reconstructed acoustic element of the truncated teardrop is then used in a TMA analysis to determine the impedance value at the front of the reference section, and the obtained values are compared with experimental data.

Chapter 8 is devoted to the role of a flame in combustion driven oscillations. The flame response is reconstructed for an atmospheric generic test rig with swirling flow and is analyzed. The flame transfer function is compared with experimental results and with the time lag approach. The results are benchmarked with the flame transfer function derived based on a harmonic forcing at different discrete frequencies. The influence of acoustic boundary conditions, combustion models and time discretization on the amplification behavior of the flame is investigated.

In chapter 9 the CFD/SI procedure is applied to reconstruct the flame transfer function for a generic industrial test rig at elevated pressure. The steps used in assembling the entire one-dimensional system model are described. For two different flame models, a stability analysis is performed using the one-dimensional acoustic code and the model predictions are compared to measurement. The flame response to total volume flow fluctuations in the first model is calculated utilizing the time lag approach, whereas in the second model the flame response to the total volume flow is reconstructed based on CFD/SI.

In Chapters 10 and 11 the reacting flow fields of the atmospheric test rig and the prototype industrial test rig operating at elevated pressures are simulated by means of a SAS turbulence model, and a detailed analysis of coherent structures is carried out. Additionally, in the case of the atmospheric test rig, the numerical findings from the forced SAS computation concerning the existence of ring vortex structures are compared with LES and measurements.

First attempts to calculate self-excited oscillations are given in chapter 12. Making use of the CFD model of the atmospheric test rig, an unsteady RANS calculation is conducted to develop self-excited oscillations within the computational domain.

A total pressure boundary condition at the axial and diagonal inlet and at the outlet a pressure boundary condition are imposed. This set of boundary conditions allows for the interactions between pressure waves being reflected at the outlet and the total pressure at the inlet. Under specific circumstances, these interactions lead to self-excited total mass flow fluctuations within the computational domain. The obtained unsteady pressure signals are analyzed with the help of the Fourier transform to capture unstable frequencies. The TMA model of the used CFD domain is built up and the results from the one-dimensional analysis are compared to each other.

Finally, in chapter 13, conclusions, present issues, and future work including some proposals are summarized.

2 Thermo-acoustically induced combustion instabilities

By all means thermo-acoustic instabilities should be avoided in the design stage of a new combustion system. However, in many practical situations, a detailed understanding of the instability mechanism is very difficult or not possible at all. Full-scale gas turbine combustion systems can be only tested in the field and a small segment of the entire machine in the lab. Due to very high risk caused by combustion dynamics, partial and complete suppressions of all instabilities are a key driving mechanism in gas turbine combustion system development programs. Practical solutions are usually achieved through a trial and error process, which do not include any detailed numerical and experimental descriptions of oscillatory phenomena. In some cases, CFD and other numerical tools can show a direction, in which the current design should be optimized. Sometimes, using simple engineering judgment, one can decrease the risk of instabilities occurring by introducing, for example, asymmetry in the combustion system that prevents a harmonic coupling of sources with the acoustic system. Looking from the system and component level, thermo-acoustic instability is an important design issue in the gas turbine combustion system development. Unfortunately, it is not the only one issue, which designers have to face during the design process. Therefore, a new design is limited to some extent by the changes that can be made in a gas turbine combustion system.

Of course, apart from engineering judgment, detailed and accurate numerical models are required to predict whether a system will be prone to combustion instabilities or stable under challenging operating conditions. Moreover, these models should help to understand the basic physics of instabilities. Many analytical models have been used to date with varying levels of success. Unfortunately, a universal model has not been derived yet, and instability modeling must be conducted on a case-by-case basis.

In the following chapter, a brief overview of the mechanism of combustion instability, thermo-acoustic solution strategies, and means of noise control are presented.

2.1 Mechanism of combustion instabilities

Two different types of combustion instabilities are known to exist in combustion chambers. *Intrinsic instabilities* are due to the combustion process itself, while *system instabilities* involve a coupling between the combustion system and the combustion process. Kailasanath et al. [32] and MacManus et al. [20] discuss the characteristics and consequences of each type of instability. Intrinsic flame instabilities are caused by density variations between products and reactants. Differences in species diffusion rates cause thermo-diffusive instabilities, and reaction rate imbalances between the numerous reacting species can create chemical-kinetic instabilities.

Alternatively, system instabilities can be generated for instance from fluid-dynamic instabilities such as vortex shedding from the inlet of a dump combustor or large-scale coherent structures generated by shear flows. Both mechanisms are described in more detail in [31]. Another system instability, known as a thermo-acoustic instability, involves the coupling of acoustic waves and the unsteady heat release from the flame. This is illustrated in Fig. 2.1.

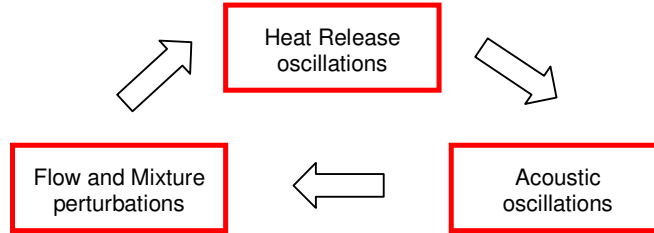


Fig. 2.1 A schematic of the feedback loop responsible for combustion instabilities [5][79]

Combustion instabilities result from a feedback mechanism that can be generally described by the following sequence [5]: (1) a perturbation in flow or thermodynamic variable induces a fluctuation in heat release, (2) the unsteady heat release excites acoustic oscillations that propagate away from the combustion region, (3) the acoustic oscillations excite the flow or thermodynamic variable in (1), thus closing the feedback loop.

2.1.1 Rayleigh's Criterion

The conditions under which the unsteady heat release addition processes amplify acoustic oscillations have been first formulated by Lord Raleigh [30]. Raleigh stated that net energy is added to the acoustic field at a point in space when heat and pressure oscillations are positively correlated in time. Assuming harmonic oscillations, this condition is met when the magnitude of the phase between the unsteady pressure and heat release, θ_{pq} , is less than ninety degrees (i.e. $0 < |\theta_{pq}| < 90$). Conversely, when these oscillations are out of phase (i.e. $90 < |\theta_{pq}| < 180$), the heat oscillations damp the acoustic field.

However, a combustion system in which the unsteady heat release is adding energy to the acoustic field will not necessarily become unstable. That is, a combustion system where $|\theta_{pq}| < 90$ only becomes unstable when the periodic heat release process supplies energy to the acoustic field at a higher rate than the acoustic energy is dissipated and/or transmitted through the combustor's boundaries. The total acoustic energy inside the combustion system can be given in [40] by:

$$\frac{\partial}{\partial t} \int_V \left[\frac{1}{2} \rho_0 u'^2 + \frac{1}{2} \frac{p'^2}{\rho_0 c^2} \right] dV = \frac{\kappa - 1}{\rho_0 c^2} \int_V p' q' dV - \int_S (p' u'_j - u'_j \tau'_{ij}) dS - \int \frac{\partial u'_i}{\partial x_j} \tau'_{ij} dV \quad (2.1)$$

The term on the left hand side of the equation is the rate of the total acoustic energy inside the combustion system. The first term on the right hand side of this equation is acoustic energy generated due to the heat release. The second term on the right hand side is the energy loss at the boundary of the entire combustion system. These conditions are more deeply investigated in [41] resulting in a reformulation of the original Rayleigh criterion. According to [5], the Rayleigh criterion can be expressed as:

$$\frac{\kappa-1}{\rho_0 c^2} \int_V p' q' dV > \int_S p' u' dS \quad (2.2)$$

where p' , u' and q' are the combustor pressure, acoustic velocity oscillations and periodic heat addition processes.. Equation (2.2) simply states that a combustor can become unstable when the net rate of energy addition to the acoustic field exceeds the net rate of damping provided by inherently dissipative processes.

2.2 Control of Thermo-acoustic instabilities

In addition to understanding the physics of combustion instabilities, some research work is also being conducted to control and at least to partially suppress these instabilities. In general, both passive and active means to minimize the effects of self-excited combustion oscillations can be employed. Both control strategies have had some success in controlling and suppressing thermo-acoustic instabilities but no strategy has completely eliminated the problem.

2.2.1 Passive means

Passive control strategies use devices, which are not based on time dependent functions but can be still utilized to eliminate the formation of instabilities. These devices require a thorough understanding of the system dynamics because they cannot respond to any changes.

Knowing the system dynamics, one can remove or damp instabilities by modifying various physical components such as injector geometries, burner outlet geometries, liner designs or other components related to the hardware. These modifications usually affect flow and acoustic conditions strongly and reduce the combustion-induced fluctuations by detuning the flame response and the acoustic resonance of the system. Berenbrink and Hoffmann [18] suggested the modifications of outlet burner boundary conditions to change the system dynamics. Another design option for suppressing the combustion instabilities and extending the quiescent operation range is the design of a multi stage combustion system. This multi stage technology has been introduced in the industrial turbine version of the Rolls-Royce trent combustor [19]. By changing the fuel split between different stages the heat release distribution inside the combustor is directly affected which has an impact on combustion stability.

The second method to passively decrease the combustion dynamics is to increase the damping of the combustion system by placing resonators on the liner.

The most popular type of resonator is the Helmholtz Resonator, in which a small cavity is acoustically connected to the combustion chamber through an orifice. Acoustic resonator can provide effective means for increasing the damping of selected modes. It should be noted that the damping efficiency is limited to a narrow frequency range, so that the acoustic spectrum must be known prior to sizing the resonators.

2.2.2 Active means

Active controls involve time varying actuation of a control parameter to keep a system from becoming unstable. Active controls require both a deep understanding of the system dynamics and identification of a system parameter that controls the system. Several researchers have studied the subject of active control applied to thermo-acoustic systems. MacManus et al. [20] provides reviews of the various control strategies used to date. One of the first who utilized this technique was Heckl et al. [21]. Heckl successfully applied this strategy to the suppression of thermo-acoustic instabilities.

Active control can be categorized as open-loop or closed-loop control. The open loop control strategy is not based on dynamic feedback from the actual system through a sensor, whereas the closed-loop control strategy uses feedback from a sensor. The control strategy used is dependent on the type of instability that one is attempting to control. Herman and Hoffmann et al.

[21]Heckl, M.A., Active control of the noise from a Rijke tube, J. of Sound and Vibration, Vol. 124, 1988, pp.117-133

[22][79] have used the closed-loop control strategy to damp the system dynamics in a full-scale gas turbine combustor. The suppression has achieved by using a multi-channel active instability control system (ACI) with a maximum of 12 control loops, each with an individual sensor and a total number of 24 actuators in the pilot-gas system. The damping process is realized by a modulation of the pilot-gas mass flow out of phase with the heat release fluctuation of the flame.

3 Acoustic Modeling

Clear understanding of the coupling mechanism between acoustic waves and flames has become a key issue in the development of modern combustion systems. Both environmental issues resulting from very strong noise generation, and the destructive interaction between pressure fluctuations and heat release fluctuations in the combustor have to be taken into consideration while designing a new combustion system.

To understand and to describe more deeply the coupling mechanism between acoustic and reacting flows, it is necessary to come back to the roots of theoretical acoustics.

This section provides an introduction to the fundamentals of acoustic modeling and to present the theoretical background for a one-dimensional acoustic network code that can be employed in the prediction of stability margins for thermo-acoustic systems.

3.1 Theory and basic concepts

A sound wave in an elastic medium is originated by a disturbance. This disturbance shifts the molecules with a certain velocity from the balance condition. Once the molecules are displaced from their static position, an internal elastic restoring force coupled with the inertia of the system arises. The molecules are moving back and forth in the direction of wave propagation, producing adjacent regions of compression and rarefaction. This process generates the sound wave. During sound propagation the molecules oscillate around their steady positions but they do not travel. Merely the sound energy is transported with the wave motion without any mass transport [29][33].

In the low frequency limit, for ducts it can be assumed that the sound wave is propagated only in one direction. Variations in pressure $p(x,t)$, velocity $u(x,t)$, and density $\rho(x,t)$ are detected as the sound wave passes through the medium. For an averaged stationary flow, these parameters can be separated into a mean and a fluctuating part. The perturbation value is assumed to be relatively small compared to the mean values in the medium.

In acoustics the most important variables are the fluctuating terms. The fluctuating part of the velocity is called the sound partial velocity and the pressure acoustic pressure. One-dimensional sound wave propagation is completely determined by these values [106][107][108].

3.1.1 Wave equation

The theoretical basis for the derivation the inhomogeneous wave equation for a compressible viscous fluid in the absence of external forces is given by the partial differential transport equations for mass, momentum and energy [7][23], which can be written as follows:

$$\frac{\partial \rho}{\partial t} + \nabla(\rho \mathbf{u}) = 0 \quad (3.1)$$

$$\frac{\partial \mathbf{u}}{\partial t} + \mathbf{u} \nabla \mathbf{u} = -\frac{1}{\rho} \nabla p + \nabla \tau_v \quad (3.2)$$

$$\rho \left(\frac{\partial e}{\partial t} + \nabla(e\mathbf{u}) \right) = -p(\nabla \mathbf{u}) - (\tau_v : \mathbf{u}) + q + \nabla(\lambda \nabla T) \quad (3.3)$$

In Eq. (3.3), the first term on the right hand side represents the reversible rate of internal energy increase per unit volume due to compression, whereas the second term denotes the irreversible rate of internal energy per unit volume by viscous dissipation. In addition to this, the operator $:$ represents the double inner product of two tensor. Thermal heat release per volume due to chemical reactions is denoted by q and heat conduction is modeled by the last term on the right side hand using Fourier's law where λ relates to thermal conductivity.

The propagation of acoustic waves can be entirely described by the above equations when corresponding boundary conditions are provided. However, a direct solution of the above set of equations is far beyond the capacity of current computers. To be able to solve direct this set of non-linear equations, one has to consider different turbulence scales, which then requires a computational grid, which is as small as the smallest turbulence scales and therefore some approximations are required. Assuming that viscous stresses and heat conduction effects are small compared to heat release rate, it is possible to drop out terms. In addition to this, pressure, velocity, density, and thermal heat release rate q can be decomposed into time averaged and fluctuating parts resulting in:

$$p = p_0 + p' \text{ with } \frac{p'}{p_0} \ll 1 \quad (3.4)$$

$$\rho = \rho_0 + \rho' \text{ with } \frac{\rho'}{\rho_0} \ll 1 \quad (3.5)$$

$$\mathbf{u} = \mathbf{u}_0 + \mathbf{u}' \text{ with } \frac{\mathbf{u}'}{\mathbf{u}_0} \ll 1 \quad (3.6)$$

$$q = q_0 + q' \text{ with } \frac{q'}{q_0} \ll 1 \quad (3.7)$$

The time averaged quantities are denoted by the "0" subscript whereas the fluctuating part is indicated by an apostrophe. The derivation of acoustic transport equations for u' and p' can be achieved by firstly introducing the decomposition from Eq. (3.4) to (3.7). Secondly, the transport equation must be time averaged and finally, the time averaged equations can then be subtracted from the instantaneous ones [63].

Considering only low amplitude limits, the acoustic fluctuations are small in amplitude compared to the averaged values. Applying the law of ideal gas, the internal energy term e can be rewritten as [40]:

$$e = c_v T = \frac{c_v p}{R \rho} = \frac{1}{1 - \kappa} \frac{p}{\rho} \quad (3.8)$$

By neglecting higher order terms of the fluctuating quantities, the linearized transport equations for the acoustic pressure and velocity for an inviscid stationary medium ($u_0=0$) then take the form

$$\frac{\partial \mathbf{u}'}{\partial t} = -\frac{1}{\rho_0} \nabla p' \quad (3.9)$$

$$\frac{\partial p'}{\partial t} + \mathbf{u}' \nabla p_0 + \kappa (p_0 \nabla \mathbf{u}') = (\kappa - 1) q \quad (3.10)$$

For low Mach number flows, all terms involving mean flow quantities can be neglected, and additionally the isentropic relation $\kappa p_0 = c_0^2 \rho_0$ where c_0 is the speed of sound can be used. The transport equations (3.10) thus reduce to:

$$\frac{1}{\rho_0 c_0^2} \frac{\partial p'}{\partial t} + \nabla \mathbf{u}' = \frac{(\kappa - 1)}{\rho_0 c_0^2} q' \quad (3.11)$$

Taking the time derivative of Eq. (3.11), the space derivative of Eq. (3.10), and after some algebraic manipulations, one gets the linearized form of acoustic transport equation for low Mach number flows:

$$\frac{\partial^2 p'}{\partial t^2} - c_0^2 \frac{\partial^2 p'}{\partial x^2} = (\kappa - 1) \frac{\partial q'}{\partial t} \quad (3.12)$$

The obtained equation (3.12) is known as the 2^{nd} order wave equation for acoustic pressure with a nonzero right hand side term expressing the effect of heat release fluctuations [6]. Rearranging this equation, one gets:

$$\frac{1}{c_0^2} \frac{\partial^2 p'}{\partial t^2} - \frac{\partial^2 p'}{\partial x^2} = \frac{\partial}{\partial t} \left(\frac{\kappa - 1}{c_0^2} q' \right) \quad (3.13)$$

The heat release rate q' is a thermoacoustic source term and is proportional to an acoustic mass flow source m'_s as follows:

$$m'_s = \frac{\kappa - 1}{c_0^2} q' \quad (3.14)$$

In the absence of combustion and assuming that the flow remains isentropic, i.e., $\partial s / \partial t = 0$, the energy equation (3.3) can be replaced by the isentropic relation. It is also known that pressure is a function of density and entropy and after linearization, one gets:

$$p' = c_0^2 \rho' \quad \text{with} \quad c_0^2 = \left(\frac{\partial p'}{\partial \rho} \right)_{s=s_0} \quad (3.15)$$

Under these assumptions, the wave equation can be reduced to its homogeneous form:

$$\frac{\partial^2 p'}{\partial t^2} - c_0^2 \frac{\partial^2 p'}{\partial x^2} = 0 \quad (3.16)$$

This linear, one-dimensional, homogeneous partial differential equation with constant coefficients has a general solution, which consists of two separate parts. First part represents a progressive wave moving forward with a velocity c_0 and the second part describes a progressive wave moving in the opposite direction with a velocity c_0 .

In case of an inviscid moving medium with the velocity u_0 , the derived wave equations remain the same as for the stationary medium except that the local time derivative $\partial/\partial t$ that is replaced by the substantive derivative (material) D/Dt ($\partial/\partial t + \mathbf{u}\nabla$). In this case, it is said that the waves are convected downstream or upstream by mean flow. Introduction of this substantive derivative yields the convective one-dimensional wave equation:

$$\frac{D^2 p'}{Dt^2} - c_0^2 \frac{\partial^2 p'}{\partial x^2} = 0 \quad (3.17)$$

Similarly, to the original wave equation, the convective wave equation has a solution, which consists of two parts. First part represents the forward moving wave at an absolute velocity $u+c_0$ and the second part describes the backward moving wave at $u-c_0$. Further details with respect to the solution of one-dimensional waves will be provided in the following sections.

3.1.2 Validity of linearity assumptions in thermo-acoustics

The above derived wave equation is based on the linearized conservation equation, which requires that the fluctuations are small relative to the mean values, i.e., $p'/\rho_0 \ll 1$. Moreover, taking into account that $u' \sim p'/\rho_0 c_0$, and the isentropic relation $p' = c_0^2 \rho'$, it follows that [24]:

$$\frac{\rho'}{\rho_0} \sim \frac{p'}{\rho_0 c_0^2} \sim \frac{u'}{c_0} \quad (3.18)$$

Following up the considerations given in [24], for standard air conditions the limit of the validity of the linear acoustic theory is at a pressure fluctuation p' of about 200 Pa. Evaluating the term $\rho_0 c_0^2$ at STP⁹, one gets $\approx 10^5$ Pa, so that the relative pressure fluctuations with respect to $\rho_0 c_0^2$ are of the order $O(10^{-3})$. It seems to be consistent with Eq. (3.4). In gas turbine combustion systems the firing temperature are usually very high, and affect the entire system. Considering an ideal gas, the density is inversely proportional to the given temperature, while c_0^2 is proportional to the temperature. That leads to the net effect on the term $\rho_0 c_0^2$, which is small. It also indicates that the net effect on this term is independent on temperature. If a given gas turbine combustion system is firing at elevated pressures the relative pressure fluctuations with respect to $\rho_0 c_0^2$ can be even of the order $O(10^{-4})$. It proves that as long as the relative pressure fluctuations are of the order $O(10^{-3})$ the linear acoustic theory may be seen as the valid one.

⁹ STP - Standard Temperature and Pressure: T=293.15 K and P= 1 atm

3.1.3 Solution methods

Numerous different numerical techniques have been developed to solve thermo-acoustic problems described by the 2nd order wave equations introduced in 3.1.1. The most popular method, i.e., low order modeling, covers only one-dimensional wave propagation for low Mach numbers and low amplitude limits where linear acoustic assumptions still hold. Using this technique, frequencies at which the system becomes unstable, and mode shapes can be quickly predicted and the essential one-dimensional physics captured. Examples of modeling thermo-acoustic systems that can be entirely based on linear acoustics and can be represented by a network of simple acoustic elements are given in [8][9]. An alternative approach that is also valid in the linear range and for low amplitude oscillations, but extended to three-dimensional wave propagations is the Galerkin method [10]. Nonlinear solutions are mainly limited to special computational cases and are summarized in [11]. LES or even sometime in case of simple systems DNS can provide the most accurate description of mechanisms involved in thermo-acoustics, both in time and space [109][111][133]. The main drawback of these methods is that they are very computationally expensive. However, these techniques need special treatments for a flame and acoustic boundaries [110].

3.1.3.1 One-dimensional acoustic wave propagation

The sound field generated in a gas turbine combustor may be considered one-dimensional because of the typically large wavelengths associated with most longitudinal combustion oscillations. For example, the size of the reacting zone where the combustion process takes place is very small compared to the size of the acoustic wavelength in the combustor. For a frequency of 400 Hz, the acoustic wave length (defined by $\lambda=c/f$) in burnt gasses of 2000 K is of the order of 2.2 m, while the heat zone is approximately in the range of 0.1 m for a typical gas turbine combustion system. Acoustic wavelengths in a mixture of burnt gasses are shown below. The black rectangular represent the wavelength of 2.2m.

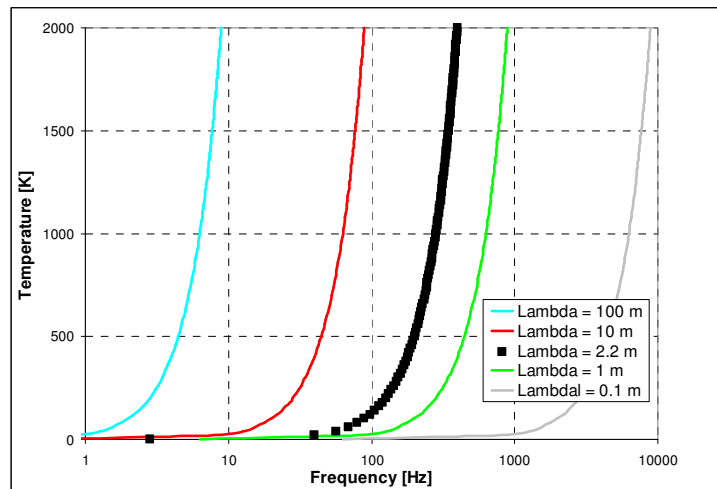


Fig. 3.1 Acoustic wavelength in a mixture of burnt gasses as a function of temperature and frequency

Fig. 3.1 clarifies that combustion oscillations have typical wavelengths of the order of several meters especially at lower frequencies. This condition, i.e. $L_{\text{flame}} \ll \lambda$, implies that all acoustic sources in the flame zone can be volume integrated and treated as one point acoustic source [24][112]. For this reason one-dimensional acoustic models [25][26][27][28] have been successfully applied to describe acoustics of a combustion system.

Consider a duct with a uniform-cross-section of area, a uniform temperature, and a density with no mean flow, i.e. $u_0=0$, in which the unsteady flow parameters are just a function of the axial space coordinate x and time t . Then, the linear, one dimensional, homogeneous wave equation (3.16) admits a general solution [29]:

$$p'(x,t) = p^+(x - c_0 t) + p^-(x + c_0 t) \quad (3.19)$$

where the function p^+ corresponds to the right traveling wave ($x=+\infty$) known as the forward traveling wave and the function p^- defines the left traveling wave ($x=-\infty$) known as the backward traveling wave, which is seen in Fig. 3.2.

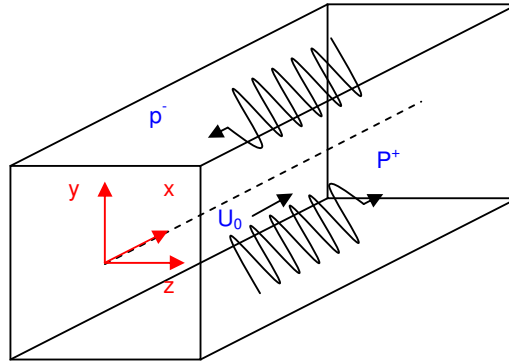


Fig. 3.2 Sound waves traveling in a tube

Using the one-dimensional form of the linearized momentum equation, the particle velocity in the x direction can be written as:

$$u'(x,t) = \frac{1}{\rho_0 c_0} (p^+(x - c_0 t) + p^-(x + c_0 t)) \quad (3.20)$$

In the most general case, the solution can represent the superposition of two progressive waves traveling in opposite direction. If the time dependence is assumed to have the exponential form $e^{i\omega t}$, the general solution becomes:

$$p'(x,t) = (p^+ e^{-ikx} + p^- e^{+ikx}) e^{i\omega t} \quad (3.21)$$

$$u'(x,t) = \frac{1}{\rho_0 c_0} (p^+ e^{-ikx} - p^- e^{+ikx}) e^{i\omega t} \quad (3.22)$$

where the wave number k can be replaced by the relation ω/c_0 with ω being the angular frequency. These amplitudes can be calculated considering the boundary conditions at both ends of the duct. When a mean flow is present in the duct, the wave number k^\pm accounts for the mean flow effect and modifies the effective speed of sound, and can be written as $\omega/c_0 \pm u_0$.

3.1.3.2 Acoustic damping

In Section 3.1.1 the wave equation is derived under the assumption that all losses associated with acoustic energy are neglected. However, in reality in many real situations dissipation can have a significant influence on acoustic wave propagation. This type of acoustic energy dissipation has been characterized by Kinsler et al. [33] as being composed of two acoustic losses. The first are the losses intrinsic to the medium. The second are the losses associated with the boundaries of the medium.

The effects of viscosity and thermal conductivity can result in an additional dissipation of acoustic energy. However, in combustion systems these thermo-viscous effects are often ignored because they are very small in comparison with other phenomena associated with the combustion process.

In the presence of a mean flow or at large acoustic amplitudes, additional sound damping can occur as a result of the generation of turbulence, either by large amplitude sound fields themselves or throughout the interaction of sound with the vortices in the flow [113]. Moreover, the mean flow effects at low Mach numbers provide an additional source of convective damping. The one-dimensional acoustic models derived using the convective wave equation account for these effects is given in [112].

Ingard et al. [34] has provided a simple theoretical model describing the damping mechanisms responsible for sound attenuation in hard-walled pipes carrying turbulent flow. The analysis of an oscillatory flow surrounded by a sound field is used to show a quasi-static modulation of the steady flow. A modulation of the pressure drop in the pipe can equivalently be expressed as turbulent friction acting on the oscillatory flow. Moreover, Munjal [29] has provided the solution for one-dimensional waves in a viscous medium. The solution provided by Munjal accounts for the additional aero-acoustic losses due to turbulent friction, and also the convective effects of the mean flow. Following the solution proposed by Ingard, one can obtain the propagation constants k^+ and k^- for the acoustic waves traveling in the downstream and upstream directions of the turbulent flow:

$$k^\pm = \frac{\omega/c_0}{1 \pm Ma_0} - i \left(\frac{\beta_t}{1 \pm Ma_0} + \frac{\beta_v}{1 \pm Ma_0} \right) \quad (3.23)$$

In the above written equation, β_v stands for the thermo-viscous damping coefficient, whereas β_t refers to the turbulent damping coefficient. The solution clearly shows that the total attenuation in a moving medium is the sum of the contributions of the visco-thermal and turbulence effects. The factor $1 \pm Ma_0$ represents only the Doppler effects due to the mean flow convection. Low Mach number flows are dominated by the damping caused by viscosity and heat conduction.

As the Reynolds number (main flow velocity) increases, this term decreases in contrast to the turbulence effects, which become the major contributor to the attenuation. The turbulent damping coefficient β_t can be written as follows:

$$\beta_t = \frac{Ma_0 F_f}{0.5D_h} \quad (3.24)$$

where D_h is the hydraulic diameter and F_f Froude's friction factor defined as the ratio of the pressure drop in an axial length equal to one diameter divided by the dynamic head $0.5\rho_0 u^2$. F_f is the empirically determined friction factor dependent on the Reynolds number and the wall roughness. For the typical flow velocities in exhaust muffles, F is given by Lee's formula:

$$F_f = 0.0072 + \frac{0.612}{Re^{0.35}} \quad \text{for } Re < 4 \cdot 10^5 \quad (3.25)$$

At zero flow and in the low-velocity flow regime, the attenuation caused by the thermo-viscous effects is approximated by

$$\beta_v = \frac{1}{0.5D_h c_0} \left(\frac{\omega \mu_c}{2\rho_0} \right)^{0.5} \quad (3.26)$$

with μ_c being defined as the coefficient of visco-thermal friction given by:

$$\mu_c = \mu \left[1 + \left(\kappa^{0.5} - \frac{1}{\kappa^{0.5}} \right) \left(\frac{K}{\mu c_p} \right)^{0.5} \right]^2 \quad (3.27)$$

It is also worth mentioning that experimental measurements of k by Ingard showed disagreement with theoretical values with discrepancies ranging from 15 to 50 %. However, almost all of these experiments confirm the functional dependence of k on $\omega^{0.5}$ and D_h .

It is interesting to compare the damping caused by the thermo-viscous effects to that caused by turbulence alone. For STP⁹ condition and for a circular pipe of diameter $D=0,1$ m, the comparison between two damping terms as a function of Mach number is depicted in Fig. 3.3. One can see that the turbulent term is dominant, and for higher Mach numbers the sound attenuation becomes independent of the thermo-viscous contribution.

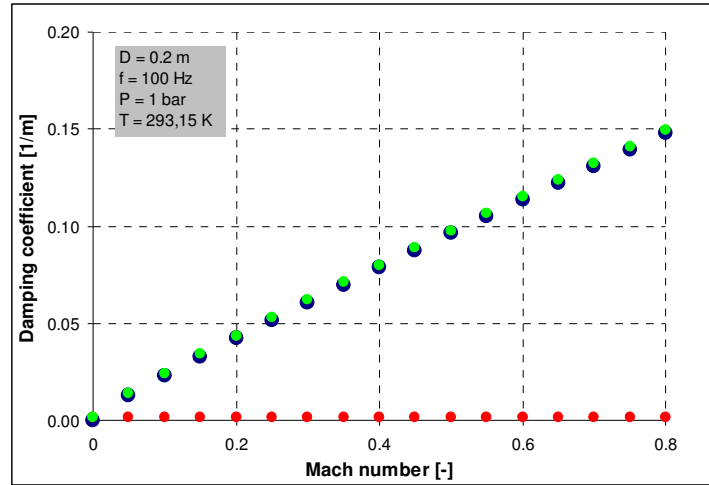


Fig. 3.3 Damping coefficient as a function of Mach number: red circles - thermo-viscous effects, dark blue circles - turbulence effects, green circle - sum of two effects

3.1.3.3 Acoustic Impedance

Impedance is the measure for the resistance of a fluid to incoming pressure waves. In the one-dimensional case, impedance at a certain location defines the acoustic behavior of the system beyond that location. Impedance is expressed as a complex number in the frequency domain. Considering a one-dimensional sound field, the specific acoustic impedance Z is defined as the complex quotient between the pressure perturbations and velocity perturbations:

$$Z = \frac{p'(x, \omega)}{u'(x, \omega)} \quad (3.28)$$

In general, the complex impedance value $z=a+ib$ is compound of a the real part, known as the *specific resistance*, and b the imaginary part known as the *specific acoustic reactance* of the medium for the particular wave being considered. For a freely propagating one-dimensional acoustic wave in a tube, the acoustic pressure in Eq. (3.21) and the acoustic velocity in Eq. (3.22) can be used to derive the characteristic impedance of a medium Z_0 defined by

$$Z_0 = \rho_0 c_0 \quad (3.29)$$

In acoustics, the characteristic impedance Z_0 is often utilized as a scaling factor between the pressure fluctuations and velocity fluctuations. The notation of impedance is also useful to characterize wave transmissions and reflections in ducts. Combining both the specific impedance and the characteristic impedance, one gets the dimensionless quantity called the reduced impedance:

$$Z_{red} = \frac{Z(x, \omega)}{Z_0} = \frac{1}{\rho_0 c_0} \frac{p'(x, \omega)}{u'(x, \omega)} \quad (3.30)$$

The absolute values of the reduced impedance can vary from 0 to $+\infty$. $|Z_{red}|=1$ corresponds to the situation when sound waves propagate freely and no sound is reflected back.

When the reduced impedance goes to infinity, it means that the sound wave is fully reflected on an acoustically hard wall. The impedance is also linked to the reflection coefficient R defined as the ratio of the reflected pressure waves to the incident wave in a given section $x=x_0$ in a duct:

$$R(x, \omega) = \frac{P^-}{P^+} e^{i(k^+ + k^-)x} \quad (3.31)$$

With the help of Eq. (3.30), (3.21) and (3.22) the reflection coefficient can be rewritten to

$$R(x, \omega) = \frac{Z_{red} - 1}{Z_{red} + 1} \quad (3.32)$$

The real part of the acoustic reflection coefficient R has values in the range of -1 to $+1$. The case when $R=1$ is known as a hard termination. Such a termination in the ideal case reflects the incident wave with the same magnitude and phase. When $R=-1$ the sound wave is reflected with a 180° phase change, and $R=0$ refers to a non-reflective termination.

3.2 One-dimensional acoustic network models

In this section, a short introduction into acoustic modeling using one-dimensional acoustic network models is given. With the help of these models, the acoustic field in a network of coupled elements can quickly be determined and analyzed in more detail. The individual elements in the network are represented by a transfer matrix, which describes the relationship between acoustic quantities at both ends of the acoustic element. The transfer matrix method (for more details see [28][29]) provides a powerful and efficient approach for the theoretical acoustic treatment of complex systems [114].

Most acoustic and thermo-acoustic systems can be modeled as a series of ducts with variable sections, which connect upstream and downstream. The acoustic wave can propagate through these ducts, and in the case of reacting flows may even interact with a heat source. Predicting wave propagation in these ducts is a crucial step in characterizing the entire system. For each one-dimensional acoustic element, the velocity perturbation u' and the pressure perturbation p' at the inlet and outlet to the element can be coupled by an acoustic transfer matrix.

The advantages of the network model are that the computational costs are very low as long as the analytical relation of the transfer matrix can be provided and incorporated into the model. This transfer matrix approach allows also for considering some additional effects accounting for temperature gradients, mean flows, viscous damping, non-linear flame models [78], and the occurrence of circumferential modes [77] to be included.

3.2.1 Transfer matrix method

In general, a low-order acoustic network model is compound of the individual acoustic elements of the system, each of them being represented by its respective transfer matrix. A representative model of the model of a premixed burner that can be utilized in stability analysis is shown in Fig. 3.4. The presented model consists of a plenum, burner, flame, combustion chamber and exit.

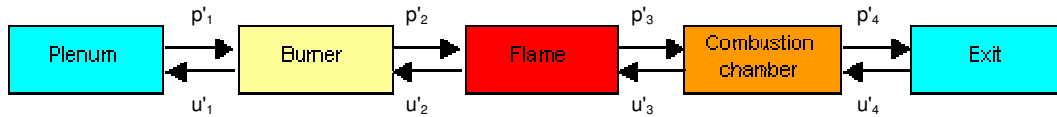


Fig. 3.4 An example of one-dimensional acoustic network model of a premixed burner

In the transfer matrix approach, the linearized form of acoustic transport equations for low Mach number flows is used. Within this approach, acoustic transfer matrices for simple geometric configurations such as ducts, diffusers, annular ducts, and area discontinuities are defined so that acoustic quantities at inlet and outlet are linked. The transfer matrix itself characterizes the acoustic properties of a given element, which transmits sound waves as a function of frequency. An example of a transfer matrix network expressed mathematically is [40]:

$$\begin{pmatrix} p'_K \\ u'_K \end{pmatrix} = G \begin{pmatrix} p'_1 \\ u'_1 \end{pmatrix} \text{ with } G = \prod_{k=1}^{K-1} T_k \quad (3.33)$$

where K corresponds to a series of acoustic elements defined by their transfer matrices having the following form [29]:

$$T_k = \begin{bmatrix} T_{11}^k & T_{12}^k \\ T_{21}^k & T_{22}^k \end{bmatrix} \quad (3.34)$$

The transfer matrix coefficients relate directly the acoustic variables before and after the element. The acoustic pressure and velocity p'_K and u'_K refer to the acoustic boundary upstream of the network of elements, and the variables p'_1 and u'_1 refer to the acoustic conditions downstream. To close the problem, it is required to specify boundary conditions at both ends of the network. An impedance boundary condition or a reflection factor is applied to account for an influence of the surroundings on the acoustic system under consideration. Either reflection factors or acoustic impedances can be specified as acoustic boundary conditions as follows [40]:

$$\frac{p'_K}{u'_K} = Z_j \text{ and } \frac{p'_1}{u'_1} = Z_1 \quad (3.35)$$

The transfer matrix coefficients for geometrically simple elements can be derived analytically, while for more complex acoustic elements CFD computations and experiments can be employed

From the modeling standpoint, the most demanding in term of complexity are the flame and burner including swirler vanes. A detailed one-dimensional analysis of thermoacoustic interaction mechanisms in a turbulent premixed flame is given in [115]. The four-pole theory [29] imposes a considerable simplification in the analysis of acoustic systems because the global transfer matrix of the entire system G is simply the product of the constituent transfer matrices. This means that the direct multiplication of the single elements, represented by the individual transfer matrix, leads to the transfer function of the system. The properties and geometry of the complete system is finally given by one matrix.

To better illustrate this approach, the entire acoustic network model of the premixed burner shown above can be described by a matrix equation G including the transfer matrix elements as follows:

$$\begin{pmatrix} p'_{plenumt} \\ p'_2 \\ u'_2 \\ \vdots \\ p'_{k+1} \\ u'_{k+1} \\ p'_{exit} \end{pmatrix} = \underbrace{\begin{pmatrix} Z_{inlet} & & & & & \\ & T_{11}^1 & T_{12}^1 & & & \\ & T_{21}^1 & T_{22}^1 & & & \\ & & & \ddots & & \\ & & & & T_{11}^K & T_{12}^K \\ & & & & T_{21}^K & T_{22}^K \\ & & & & & Z_{exit} \end{pmatrix}}_{G(f)} \begin{pmatrix} u'_{iplenum} \\ p'_1 \\ u'_1 \\ \vdots \\ p'_k \\ u'_k \\ u'_{exit} \end{pmatrix} \quad (3.36)$$

The boundary conditions provided and the global transfer matrix G constitute a linear system of equations. To determine the critical frequencies of a feedback system it is necessary to solve the eigenvalue problem. Solving this system with respect to frequency, i.e. $\text{Det}(G)=0$, provides the eigenfrequencies of the complete system. The resulting complex eigenvalues are the resonant frequencies ω_{res} of the system, $\omega_{res}=\omega'_{res} + i\omega''_{res}$. The real part determines the oscillatory frequency whereas the imaginary part represents either damping or amplification.

Corresponding to these eigenfrequencies, the amplitude and respectively phases of the acoustic pressure at each section in the network can be easily calculated using the forced response method [8].

3.2.1.1 Straight duct element

To illustrate the derivation of the transfer matrix T_k of a simple element, let us consider a duct with the length L_k and a constant cross-sectional area S_k , respectively. The symbolic conventions used in the derivation of the transfer matrix T_k are plotted in Fig. 3.5. The quantities at $x_k=0$ have the subscript 0, while the quantities located at $x_k=L$ have the subscript 1.

A description of deriving acoustic transfer matrices for simple acoustic elements including ducts is given in [24]. Following the approach proposed by Deuker et al. [28] and utilizing (3.21) and (3.22) the one-dimensional transport equations for sound propagation given in Section 3.1.3.1, one can derive the acoustic transfer matrix of a simple duct.

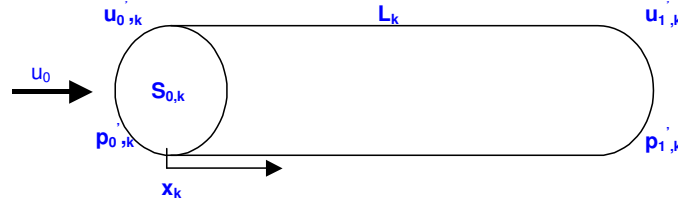


Fig. 3.5 Symbolic conventions for a straight duct element

In addition to this, by taking into account the effect of the mean flow represented by u_0 in the duct on wave propagations and imposing boundary conditions, i.e., the acoustic pressure and the acoustic velocity at position "0", one gets:

$$p'_{1,k} = p'_{0,k} \frac{e^{-k_{x1}L_k} + e^{k_{x2}L_k}}{2} + \rho_0 c_0 u'_{1,k} \frac{e^{-k_{x1}L_k} - e^{k_{x2}L_k}}{2} \quad (3.37)$$

$$u'_{1,k} = \frac{p'_{1,k}}{\rho_0 c_0} \frac{e^{-k_{x1}L_k} - e^{k_{x2}L_k}}{2} + u'_{1,k} \frac{e^{-k_{x1}L_k} + e^{k_{x2}L_k}}{2} \quad (3.38)$$

with the modified wave numbers k_{x1} and k_{x2} being defined by

$$k_{x1} = \frac{k}{1+Ma} \quad \text{and} \quad k_{x2} = \frac{k}{1-Ma} \quad (3.39)$$

It is convenient to present the obtained transfer matrix in matrix notation as:

$$T_k = \frac{1}{2} \begin{pmatrix} e^{-k_{x1}L_k} + e^{k_{x2}L_k} & \rho_0 c_0 (e^{-k_{x1}L_k} - e^{k_{x2}L_k}) \\ \frac{1}{\rho_0 c_0} (e^{-k_{x1}L_k} - e^{k_{x2}L_k}) & e^{-k_{x1}L_k} + e^{k_{x2}L_k} \end{pmatrix} \quad (3.40)$$

As shown, the great advantage of the transfer matrix is that the entire system of interest can be divided into simple geometrical elements such as ducts, diffusers, and area discontinuities of known acoustic behavior.

3.2.1.2 Area discontinuity element

Considering a series of connected ducts with cross-sectional areas ranging from S_k to S_{k+1} , whose length is $L_k = x_{k+1} - x_k$, it is possible to model discontinuities between two neighboring acoustic elements, an example of which is depicted in Fig. 3.6. For simplicity, let us assume that a mean flow, i.e. $u_0 \sim 0$, is not present in the acoustic flow field.

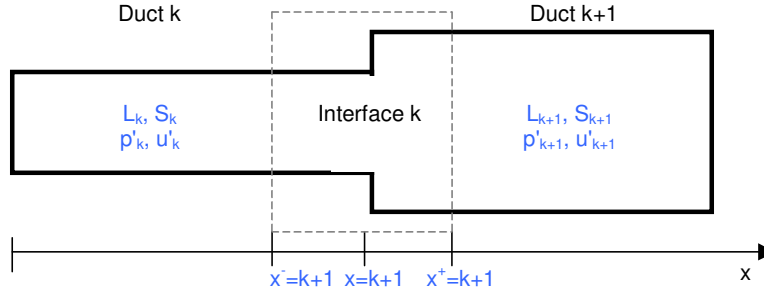


Fig. 3.6 The acoustic wave propagation in connected ducts

As a result of this assumption (no flow/acoustic and acoustic/turbulence interactions), the thermodynamical conditions may be treated as stable in all connected ducts. Moreover, fulfilling isentropic conditions, the linearized continuity and momentum equations, derived in Section 3.1.3.1, can be integrated between the sections x_k and x_{k+2} . Additionally, if the distance between x^-_{k+1} and x^+_{k+1} go to 0, it is possible to obtain the conditions at the discontinuity and to couple the acoustic properties upstream and downstream of it. The coupling of boundary conditions in terms of the acoustic pressure and the acoustic flow rate can be written as [40]:

$$p'(x^-_{k+1}, t) = p'(x^+_{k+1}, t) \quad (3.41)$$

$$S_k u'(x^-_{k+1}, t) = S_{k+1} u'(x^+_{k+1}, t) \quad (3.42)$$

The transfer matrix of the acoustic element connecting two ducts k and $k+1$, not including any mean flow effects, can be written as:

$$\begin{pmatrix} p'_{k+1} \\ u'_{k+1} \end{pmatrix} = \begin{pmatrix} 1 & 0 \\ 0 & \frac{S_k}{S_{k+1}} \end{pmatrix} \begin{pmatrix} p'_k \\ u'_k \end{pmatrix} \quad (3.43)$$

In reality, when the mean flow is non-zero in the acoustic element having different cross-sectional areas, an additional acoustic reflection or absorption at these discontinuities can be encountered. Due to the incident sound field, an unsteady vortex shedding occurs at the edge of expansion. The formulation proposed by Van Kampfen et al. [24] takes this mechanism partially into account.

3.2.1.3 Flame element

It has been already mentioned that due to the acoustic wavelength, which are much bigger than the length of combustion zone ($L_{\text{flame}} \ll \lambda$), the flame itself can be treated as acoustically compact. However, to be able to analyze the stability of thermo-acoustic systems using one-dimensional network models, the thermo-acoustic source term must be treated as a volume integrated quantity that is applied to a specific node of the network model.

Thermo-acoustic instabilities are caused by the fact that the acoustic sources represented by heat release fluctuations in the acoustic system are a function of perturbations occurring in the system itself. The heat release perturbation is, in general, a function of a given velocity perturbation u' or pressure p' at some earlier time $t-\tau$, in which τ , a commonly employed approximation [74], is the convective time that the perturbation needs to travel from the burner mouth to the flame front. Arriving at the flame front, the perturbation u' forces a heat release fluctuation Q' .

The $n-\tau$ formulation was originally developed for the study of high-frequency combustion instabilities in liquid-fueled systems [35]. This simple model provides a global description of the unsteady heat release rate associated with oscillating combustion systems and has been found to be useful in predicting the quantitative behavior of combustion oscillation in a variety of cases. Some other examples of using this approach can be found in [36]. Stow has extended the $n-\tau$ model to include some non-linear effects in [78].

A classical problem for combustion driven oscillations is the configuration of a thin flame stabilized in a double duct. It allows for a complete analytical solution of the stability problem under certain assumptions. Assuming that the size of combustion zone is much smaller compared to the wavelengths associated with most longitudinal combustion oscillations, the flame can be seen as a compact, i.e., infinitely thin.

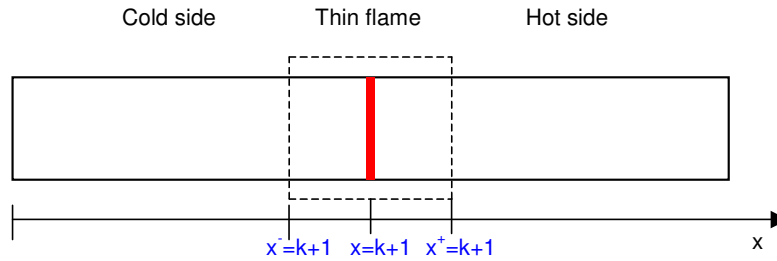


Fig. 3.7 Flame element: acoustic jump condition [40]:

Recalling the equations (3.41) and (3.42), and including the heat release source for the flame, one gets the relations accounting for the acoustic jump conditions for thin flames as follows [40]:

$$p'(x_{k+1}^-, t) = p'(x_{k+1}^+, t) \quad (3.44)$$

$$S_k u'(x_{k+1}^-, t) = S_{k+1} u'(x_{k+1}^+, t) + \frac{\gamma-1}{\rho_k c_k} Q'(t) \quad (3.45)$$

The following example helps to better understand the derivation of the $n-\tau$ model based heat release response. For simplicity let us assumed that the double duct configuration has a certain length of $2a$ as shown below, and the combustion oscillations are produced by perturbations of the velocity at the position where the thin flame is located at $u'(x=a, t)$ with a time-lag of τ .

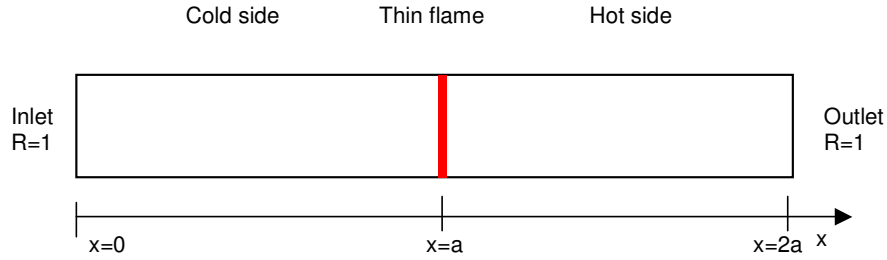


Fig. 3.8 Simple acoustic model with a flame [40]:

This time lag can be associated with a vortex that may be shed at the burner mouth and be convectively transported to the flame front where it burns out causing the heat release fluctuations Q' . One can write the following relation [40]:

$$Q'(t) = Snu'(x = a, t - \tau) \quad (3.46)$$

where the non-dimensional index n is called the interaction index and is associated with the intensity of the coupling between the velocity and the heat release oscillation. S indicates the cross-sectional area. The total unsteady heat release Q' produced by a flame is a volume integrated quantity. In general, it can be controlled by large-scale coherent structures, fluctuations of the equivalence ratio, fluctuations in the strain rate etc. If all variables oscillate with a harmonic function with time, one gets [40]:

$$\hat{Q} = Sn\hat{u}(x = a)e^{-i\omega\tau} \quad (3.47)$$

The ratio between the oscillating heat release and the unsteady heat release is known as the flame transfer function. The unsteady heat release term can be replaced by the flame transfer function derived above that allows for closing the set of one-dimensional acoustic equation. The equation can be introduced in the system matrix G . It results in a system matrix that has singularities for complex frequencies. The flame transfer function can also be expressed in terms of equivalence ratio perturbations or a superposition of the response to velocity and equivalence ratio perturbations, respectively [96].

3.2.1.4 Feedback mechanism in combustion systems

Thermo-acoustic instabilities can occur if the combustion source terms represented by heat release fluctuations overcome acoustic losses in relation to Rayleigh's criterion described in Section 2.1.1. Thus, in this context the stability analysis of combustion systems, accounting for the prediction of unstable acoustic modes, is an important issue when considering thermo-acoustic systems. Using this type of analysis one can obtain information about whether the combustor is stable or unstable.

An example of a perturbation, which is transported with the convection speed, is the equivalence ratio fluctuation. The fluctuation is produced in the burner at the position where fuel is mixed with air.

Incoming acoustic fluctuations cause at this position a perturbation in the amount of fuel and/or air that is supplied for mixing. As a result, the global equivalence fluctuation also oscillates. Next, this fluctuation is transported to the flame front and makes the flame front oscillate producing a heat release fluctuation. The flame response of a swirled non-premixed burner to fuel flow rate is investigated using LES in [111]. The other kind of perturbation is a velocity or total mass flow fluctuation at a reference location, that is, the burner exit. More detailed study of both types of perturbations and what influences on combustion dynamics they have can be found in [24]. A sketch of a generic partially premixed system with one fuel injector is shown in Fig. 3.9.

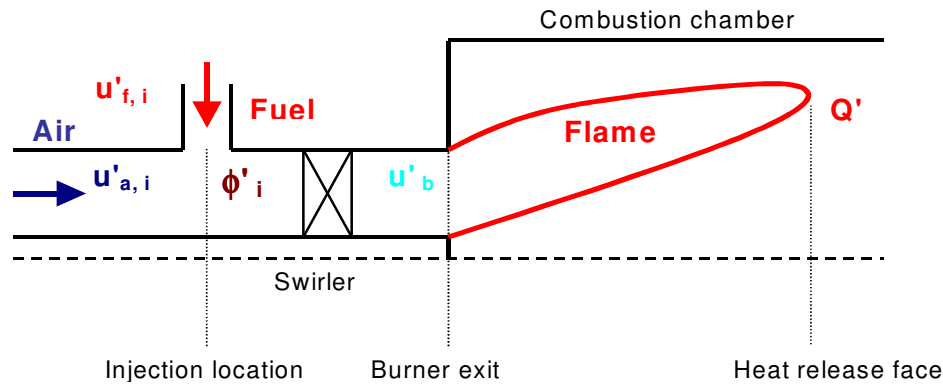


Fig. 3.9 A sketch of a generic partially premixed system

In general, the flame response induced by the equivalence ratio and velocity fluctuations can be derived starting from the instantaneous, volume intergraded heat release at the flame front by the combustion process written as [24]:

$$Q(t) = y_f \cdot \rho \cdot \dot{V} \cdot h_f \quad (3.48)$$

where y_f is the fuel mass fraction [-], ρ is the density [kg/m^3], V is the volume flow rate [m^3/s] and h_f denotes the specific reaction enthalpy [J/kg]. The typical value of the specific reaction rate for natural gas burnt in gas turbine combustion systems is $\sim 40.8 \text{ MJ}/\text{kg}$.

Linearising equation (3.48) around the mean value yields:

$$Q' = h_f \cdot \rho \cdot \dot{V} \cdot y'_f + h_f \cdot \rho \cdot y_f \cdot \dot{V}' + h_f \cdot \dot{V} \cdot y_f \cdot \rho' \quad (3.49)$$

Assuming incompressible flow and that the mass flow fraction is related the static pressure drop across the fuel line, the mass fraction fluctuation or the equivalence ratio fluctuations can be approximated at the flame front location by:

$$\frac{y'_f(t)}{y_f} = \frac{p'_i(t - \tau_i)}{2(p_{\text{fuelline}} - p_{\text{nozzel}})} - \frac{u'_i(t - \tau_i)}{u} - \frac{p'_i(t - \tau_i)}{c^2 \rho} \quad (3.50)$$

where τ_i is called the fuel injection time lag and is caused by the unsteady fuel injection that reaches the flame front location with some time delays.

Moreover, the fluctuation of the volume flow causes the heat release fluctuation at the flame front and is expressed as a lagged acoustic velocity oscillation [24][36]. This fluctuation having its origin at the burner exit is defined as:

$$\dot{V}'(t) = u'_{burnerexit}(t - \tau_b) A_{burnerexit} \quad (3.51)$$

where τ_b is the time due to the volume flow fluctuations. The last term from (3.49) can be neglected because it is very small and does not contribute much to the overall heat release fluctuation. Introducing an arbitrary harmonic function $\Phi'(t) = \hat{\Phi} e^{i\omega t}$ into (3.49) one gets:

$$\begin{aligned} \hat{Q} = & h_f \cdot \rho \cdot \dot{V}' \cdot y_f \cdot \underbrace{\left(\frac{\hat{p}_i \exp(-i\omega\tau_i)}{2(p_{fueline} - p_{nozzel})} - \frac{\hat{u}_i \exp(-i\omega\tau_i)}{u} - \frac{\hat{p}_i \exp(-i\omega\tau_i)}{c^2 \rho} \right)}_{\text{equivalence ratio fluctuation}} + \\ & + \underbrace{h_f \cdot \rho \cdot y_f \cdot \hat{u}_{burnerexit} \exp(-i\omega\tau_b) A_{burnerexit}}_{\text{volume flow fluctuation}} \end{aligned} \quad (3.52)$$

The reduction of equivalence ratio and volume flow fluctuations directly reduces the heat release fluctuation and minimizes the overall feedback mechanism.

3.2.1.5 Characterization of acoustic stability

As already mentioned, the entire combustion system can be subdivided into a network of simple acoustic elements. If a complete description of all elements is provided, the system of linear equations, represented by a global matrix, can be evaluated for complex frequencies. The eigenmodes of the system of linear equations correspond to oscillations of constant amplitude, as well as amplified or attenuated pulsations. Mathematically, this may occur when the determinant of the system matrix G is zero and has non-trivial solutions.

Some critical frequencies of the system feedback can be determined by solving the eigenvalue problem for a given system matrix G with the appropriate prescribed boundary conditions at both ends of the network model. If no time delays are present in the system, $\det(G)$ becomes zero for real eigenfrequencies of the system. In the case where a flame represented by a time lag model is present, $\det(G)$ becomes 0 for complex eigenfrequencies. Because the characteristic equation $\det(G)=0$ is usually highly non linear in the eigenfrequencies, iterative solution algorithms have to be employed for its solution, which entails a certain risk that not all eigenfrequencies are detected for complicated acoustic systems. There are several different numerical approaches for the solution of the characteristic equation. Van Kampfen et al. [24] used the Nelder-Mead simplex search method, which does not directly use numerical gradients and therefore requires only function evaluations.

Dowling et al. [78] proposed a very reliable although very expensive computational method to calculate the real and the imaginary part of $\det(R)$ throughout the complex plane. All eigenfrequencies ω_{res} for which $\text{Re}(\det(R))=0$ and $\text{Im}(\det(R))=0$ must be determined separately. In this manner, two groups of curves in the complex domain are found. The complex frequencies are localized at the intersection points in a third step. The resulting resonant frequencies ω_{res} of the system can be expressed as

$$\omega_{res} = \omega'_{res} + i\omega''_{res} \quad (3.53)$$

The real part represents the oscillatory frequency whereas the imaginary part corresponds to damping or amplification of this frequency. For $\omega''_{res} > 0$ the oscillation is damped while $\omega''_{res} < 0$ gives an amplified oscillation. Some other authors [39] utilize a growth rate GR to illustrate a quantitative measure for the amplification or the damping of the system. The growth rate can be defined as the ratio of the pulsation amplitude of two successive pulsation cycles:

$$GR = e^{-2\pi \frac{\text{Im}(\omega_{res})}{\text{Re}(\omega_{res})}} \quad (3.54)$$

$GR=1$ corresponds to the stability of a linear system or the limit of a non-linear system, respectively. When $GR > 0$ oscillations are amplified while for $GR < 0$ they vanish.

To obtain some insight into the feedback mechanism, let us consider a simple model for acoustically coupled instabilities. The complete analytical solution is derived by Poinso in [40]. The simple thermo-acoustic model represented by the Rijke tube is used in many numerical and experimental projects. Deuker et al. [28] successfully reproduced the experimental results of Heckel [21]. Van Kampen [24] shows that for constant time-lag the feedback mechanism strongly depends on the value of the interaction index. Following the proposed approach, consider the simplified model depicted in Fig. 3.8. At the position $x=a$, the thermo-acoustic source term is applied using the flame transfer function with the constant time lag of 0.010 s. Both ends are assumed to be treated as rigid walls. The velocity perturbation at the position $x=0$ affects the local heat release after a convective time delay τ and causes an additional velocity perturbation due to a local change in the heat source. For simplicity the temperature and diameters at the cold and hot side are equal. STP⁹ conditions are considered and the current fluid is represented by atmospheric air. The calculated complex eigenvalues are presented in Fig. 3.10.

As observed by van Kampfen, for the anechoic acoustic boundary condition ($\text{real}(R)=1$) the Imaginary part depends on the local heat release whereas the real does not. Considering the feedback loop mechanism, the lower amplification factor $n=0.5$ is not able to build up self-excited oscillations in the system. However, when the amplification factor n becomes larger than $n=1$, then the damping of the system decreases and the gain in the feedback loop adds energy to the loop and self-excited oscillations can build up.

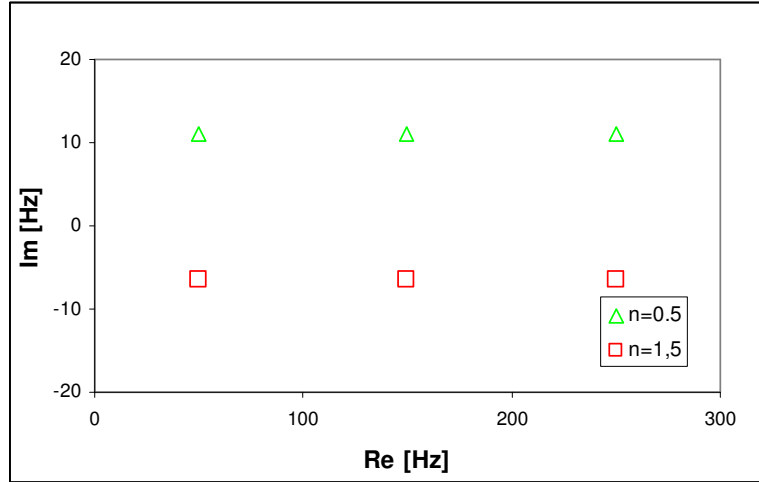


Fig. 3.10 The eigenfrequency of the simple model: green triangle - interaction index $n=0.5$, red rectangular- $n=1,5$

The real frequencies shown in Fig. 3.10 can be explained by considering the time that is needed to complete one feedback loop. The velocity perturbation at $x=a$ needs to travel τ_{sound} through the duct to reach the position at $x=0$. From that position, the sound perturbation travels back towards the flame. After a given convective time $\tau_{\text{convective}}$ that closes the feedback loop, it reaches the flame front again. When the total time of the feedback loop equals the time of half an acoustic period T , the induced heat release oscillations couple with the fluctuating heat release rate at the source location, and depending on the amplification self-excited oscillations can occur. It is valid to write the following expression [24]:

$$\tau_{\text{sound}} + \tau_{\text{convective}} = nT - \frac{T}{2} \text{ for } n = 1, 2, 3, \dots \quad (3.55)$$

The values of n correspond to the considered eigenvalues. However, It has to be pointed out that this expression is valid only for the anechoic conditions.

3.2.1.6 Limitation of the one-dimensional acoustic network codes

The validity of acoustic network codes are essentially limited for frequencies lower than the cut-off frequency. Above this frequency, transverse modes can occur in the tube. For a circular cross-section, the cut-off frequency is determined according to [29] by

$$f_{\text{cut_off}} = \frac{1.84c_0}{\pi d_h} \text{ where } d_h = \text{hydraulic diameter} \quad (3.56)$$

For example, let us consider a chamber geometry with a circular cross-section having $d_h=0.4$ m. In reality, this case can represent the combustion chamber geometry of an industrial gas turbine. The chamber is filled with burnt gas at 2000 K with $\kappa=1.25$. The speed of sound is approximately 840 m/s. The cut-off frequency is thus about 1230 Hz.

On the other hand, assuming only pure air at atmospheric conditions, i.e. at 293,15 K and 1 bar, one gets the cut-off frequency at approximately 500Hz. In the context of this thesis, the accuracy of test cases with combustion will not be considered for frequencies above 1000 Hz, and for non-reacting flows for frequencies above 500 Hz. For these temperature ranges, the assumption of one-dimensional wave propagation thus becomes reliable and can be applied.

4 Modeling of turbulent reactive and non-reactive flows using CFD

In the presented work steady and transient computational fluid dynamics simulations are used to analyze qualitatively the response of a fully and partially premixed flame to acoustic fluctuations at the burner tube exit.

In general, this chapter deals with the basic concept of the numerical methods utilized to model the turbulent reacting or non-reacting flow.

4.1 Theory and numerical modeling of turbulence

By nature, any turbulent flow exhibits a chaotic behavior both in space and in time. This irregular behavior is caused by fluctuations in all variables describing the flow field. The fluctuations in turbulent flows are caused by so-called turbulent eddies. These eddies strongly dominate the flow field and increase the transfer of mass, momentum and energy. The turbulence theory says that these eddies have not only one particular size but rather a broad range of large to small eddies exist simultaneously in a turbulent flow.

In general, the size of the largest eddies is determined by the geometrical diameter of the considered combustion system. The energy used to generate these eddies is extracted from the mean flow. In contrast to the generation of the largest eddies, the smallest eddies do not extract the energy directly from the mean flow but they are generated due to a continuous decay of large eddies, which break up into smaller ones until the energy cascade reaches the smallest scale of turbulent motion.

As mentioned above, the turbulent energy is transferred from the large to the small eddies in an inviscid process. The large eddies can be characterized by the length scale L_0 . In the case of gas turbine combustors, L_0 corresponds typically to the diameter of a burner in the combustor and u_0 is the characteristic velocity, which is the order of turbulence intensity u' . The quantity that determines the turbulent flow is the Reynolds number and is defined as [62]:

$$\text{Re} = \frac{u_0 L_0}{\nu} \quad (4.1)$$

with ν being the kinematic viscosity. For very intense turbulent energy transfer, the viscous effects do not play any significant role.

4.1.1 Numerical simulation of turbulence

The description of turbulent motion by means of Computational Fluid Dynamics (CFD) can be achieved using three numerical approaches with regards to complexity and computational requirements. The comparison of three different solution methods for an arbitrary variable as a function of time in a turbulent flow field is depicted in Fig. 4.1. By Direct Numerical Simulation (DNS), we imply that all relevant scales of the true motion of the fluid are adequately resolved in a computation. Only first principles (i.e. continuum mechanics) are used to derive the equations. For engineering computations this method is too computationally expensive. According to [60], the ratio between the Kolmogorov scale and the integral scale of the largest eddies is inversely proportional to the Reynolds number as follows:

$$\frac{\eta}{L_o} \sim \frac{1}{\text{Re}^{\frac{3}{4}}} \quad (4.2)$$

In a DNS simulation, one must resolve scales as small as η and as large as L . Thus, the grid spacing, Δx must be small like η and the extent of the domain large like L , so that in any coordinate:

$$N \sim \frac{L_T}{\eta} \sim \text{Re}^{\frac{3}{4}} \quad (4.3)$$

This implies that the total number of cells in a three-dimensional simulation is of $O(\text{Re}^{9/4})$ [24]. Obviously, with typical Reynolds number for gas turbine combustors in the order of 10^5 and much higher, DNS computations are not applicable to engineering problems. However, at relatively low Reynolds numbers DNS may be a very valuable tool to study the fundamentals of turbulent motion.

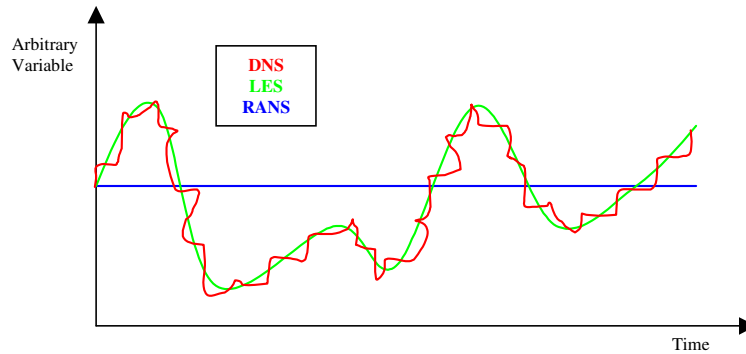


Fig. 4.1 Arbitrary variable in a turbulent flow solved by DNS, LES and RANS

In general, there are still two other computational approaches possible. By incorporating some additional assumptions related to the turbulence modeling, the computational effort to resolve the conservation equations can be decreased.

Large Eddy Simulations (LES) and Reynolds Averaged Navier Stokes (RANS) models can be employed to significantly reduce the computational cost of unsteady simulations. In LES computations, the turbulent large scale eddies are explicitly computed whereas the effects of smaller ones are modeled utilizing subgrid closure rules. On the other hand, RANS techniques are developed to solve for the mean values of all quantities. The balance equations for Reynolds and Favre averaged quantities are obtained by averaging the instantaneous balance equations. Since the small time scale of turbulent fluctuations do not need to be resolved, the RANS equations are relatively efficient to apply. As a result, solving the RANS equations requires much less computational resources than LES. The only price that must be paid for this speed up is the accuracy of results. The flow field resolved by the RANS model is often not as accurate as the solution obtained by LES because only mean quantities are taken into consideration.

4.1.2 RANS modeling

Balance equations for the mean quantities in RANS simulations are obtained by time averaging the instantaneous Navier-Stokes (NS) equations. However, the averaging procedure used introduces some unclosed quantities that have to be modeled by turbulence models. In section 3.1.1 the Reynolds decomposition rule was already presented to derive the acoustic wave equation. Recalling this procedure, the instantaneous variable $\Phi(x,t)$ can be decomposed into a mean and a fluctuating part as:

$$\Phi(x,t) = \overline{\Phi}(x) + \Phi'(x,t) \text{ with } \overline{\Phi'} = 0 \quad (4.4)$$

The time-averaged quantity is usually indicated with an over-line bar and the fluctuation part with a prime ('). Reynolds averaging rules are mostly used in constant density flows. For flows with a fluctuating density, like reacting flows where high density and temperature gradients are present, the Reynolds averaging can introduce some unclosed correlations, which are difficult to handle. To overcome these difficulties, the mass-weighted or density weighted averages known as the Favre average rule are introduced [40][63]. In the Favre decomposition, the time and density average part is designated by a tilde (~) and the fluctuating quantity by a double prime ("). The Favre average of a quantity $\Phi(x,t)$ can be then defined as [64]:

$$\tilde{\Phi} = \frac{\overline{\rho\Phi}}{\overline{\rho}} \quad (4.5)$$

where the Reynolds average of ρ is [80]:

$$\overline{\rho}(x,t) = \frac{1}{T} \int_{T/2}^{T/2} \rho(x,t+\tau) d\tau \quad (4.6)$$

with T being the time interval over which the averaging procedure is made and is much larger than the characteristic turbulence time scale. On this basis, the Favre averaged quantity Φ may be decomposed into:

$$\Phi(x,t) = \tilde{\Phi}(x) + \Phi''(x,t) \text{ with } \tilde{\rho}\tilde{\Phi}'' = 0 \quad (4.7)$$

Using the Favre decomposition rules introduced above, RANS equations for unsteady, compressible and reactive flows of mass, momentum, chemical species and total enthalpy can be rewritten as [63]

$$\frac{\partial \bar{\rho}}{\partial t} + \frac{\partial}{\partial x_i} (\bar{\rho} \tilde{u}_i) = 0 \quad (4.8)$$

$$\frac{\partial \bar{\rho} \tilde{u}_i}{\partial t} + \frac{\partial}{\partial x_j} (\bar{\rho} \tilde{u}_i \tilde{u}_j) + \frac{\partial \bar{p}}{\partial x_i} = \frac{\partial}{\partial x_j} \left(\bar{\tau}_{ij} - \bar{\rho} \tilde{u}_i'' \tilde{u}_j'' \right) \quad (4.9)$$

$$\frac{\partial \bar{\rho} \tilde{Y}_k}{\partial t} + \frac{\partial}{\partial x_i} (\bar{\rho} \tilde{u}_i \tilde{Y}_k) = \frac{\partial}{\partial x_i} \left(\left(\frac{\mu_t}{Sc_k} + \bar{\rho} \bar{D}_k \right) \frac{\partial \tilde{Y}_k}{\partial x_i} \right) + \bar{\omega}_k \text{ for } k=1, \dots, N \quad (4.10)$$

$$\frac{\partial \bar{\rho} \tilde{h}_{tot}}{\partial t} + \frac{\partial}{\partial x_i} (\bar{\rho} \tilde{u}_i \tilde{h}_{tot}) = \frac{\partial \bar{p}}{\partial t} + \frac{\partial}{\partial x_i} \left(\bar{\lambda} \nabla T - \bar{\rho} \tilde{u}_i'' \tilde{h}_{tot}'' \right) + \frac{\partial \overline{u_i \tau}}{\partial x_j} \quad (4.11)$$

The gravity and radiation effects are neglected. Furthermore, the term associated with the power production by volume forces f_k , is also disregarded. Sc_k stands for the turbulent Schmidt number for species k , μ_t is the turbulent viscosity calculated with help of turbulence modes and the thermal and molecular diffusivity are referred to λ and D , respectively. According to Stokes's law, the stress tensor τ_{ij} is defined [63]:

$$\tau_{ij} = \left(\mu' + \frac{2}{3} \mu \right) \frac{\partial u_i}{\partial x_j} \delta_{ij} + \mu \left(\frac{\partial u_i}{\partial x_j} + \frac{\partial u_j}{\partial x_i} \right) \quad (4.12)$$

where term μ' is sometimes called the bulk viscosity and for a monatomic gas mixture is zero. This term is usually negligible in combustion processes.

In addition to this, the equation for the mean total enthalpy h_{tot} and the equation of state for ideal gases can close the set of equations used to completely describe the reacting flow field. These equations are as follows:

$$\tilde{h}_{tot} = \int_{T_{ref}}^{\tilde{T}} c_p(\tilde{T}) d\tilde{T} + \frac{1}{2} \tilde{u}^2 + \tilde{k} + \sum_{i=1}^n \tilde{y}_i h_i^0 \quad (4.13)$$

The term h_i^0 defines the enthalpy of formation of species i at temperature T_{ref} .

$$\bar{p} = \bar{\rho} R \tilde{T} \quad (4.14)$$

where c_p is the specific heat at constant pressure and R is the gas constant.

The Favre decomposition and averaging lead to some unclosed terms in the set of equations (4.8)- (4.11) such as the Reynolds stress term. The main objective of turbulence modeling is to provide closures for the unknown quantities. All turbulence models contain some empirical constants, which are determined utilizing experiments and DNS computations.

4.1.2.1 Classical turbulence models for unclosed terms

The most popular turbulence models are the eddy-viscosity models, which assume an analogy between the turbulence and molecular viscosity diffusion. The eddy viscosity hypothesis of Boussinesq assumes that Reynolds stresses can be related to the mean velocity gradients and eddy viscosity by the gradient diffusion hypothesis, in a manner analogue to the relation between the stress and strain tensor in laminar Newtonian fluid. On this basis, the Reynolds stress term $\overline{\rho u_i'' u_j''}$ that appeared in eq. (4.9) can be generally described by viscous tensor τ_{ij} as [14][40]:

$$-\overline{\rho u_i'' u_j''} = -\overline{\rho u_i'' u_j''} = \mu_t \left(\frac{\partial \tilde{u}_i}{\partial x_j} + \frac{\partial \tilde{u}_j}{\partial x_i} - \frac{2}{3} \frac{\partial \tilde{u}_k}{\partial x_k} \delta_{ij} \right) - \frac{2}{3} \overline{\rho} k \delta_{ij} \quad (4.15)$$

where μ_t and k refer to the turbulent viscosity and turbulence kinetic energy. By analogy to the eddy viscosity hypothesis, the eddy diffusivity hypothesis states that the Reynolds fluxes of a scalar are linearly related to the mean scalar gradient. Utilizing this analogy, the turbulent total enthalpy flux

$\overline{\rho h_{tot}'' u_j''}$ may have the following form [14][40]:

$$-\overline{\rho h_{tot}'' u_i''} = \overline{\rho h_{tot}'' u_i''} = \Gamma_t \nabla h_{tot} \quad (4.16)$$

where the eddy diffusivity is defined as:

$$\Gamma_t = \frac{\mu_t}{Pr_t} \quad (4.17)$$

with Pr_t being the turbulent Prandtl number.

Over the last years, various turbulence models ranging from simple algebraic expressions that do not need any modeling to two equations models have been proposed to obtain the turbulent viscosity. For the purpose of this project only the k- ϵ and SAS turbulence model have been used.

k- ϵ Model

The most popular turbulence model in combustion applications, basically due to its numerical robustness is the well known k- ϵ model.

In this model, two additional transport equations accounting for the turbulence kinetic energy k and the turbulence eddy dissipation ε are solved. The turbulence viscosity is modeled as [40]:

$$\mu_t = C_\mu \bar{\rho} \frac{\tilde{k}^2}{\tilde{\varepsilon}} \quad (4.18)$$

where C_μ is an empirical constant. The transport equations used to obtain k and ε are as follows [40]:

$$\frac{\partial \bar{\rho} k}{\partial t} + \frac{\partial}{\partial x_i} (\bar{\rho} \tilde{u}_i k) = \frac{\partial}{\partial x_i} \left(\left(\mu + \frac{\mu_t}{\sigma_k} \right) \frac{\partial k}{\partial x_i} \right) + P_k - \bar{\rho} \varepsilon \quad (4.19)$$

$$\frac{\partial \bar{\rho} \varepsilon}{\partial t} + \frac{\partial}{\partial x_i} (\bar{\rho} \tilde{u}_i \varepsilon) = \frac{\partial}{\partial x_i} \left(\left(\mu + \frac{\mu_t}{\sigma_k} \right) \frac{\partial \varepsilon}{\partial x_i} \right) + C_{\varepsilon 1} \frac{\varepsilon}{k} P_k - C_{\varepsilon 2} \bar{\rho} \frac{\varepsilon^2}{k} \quad (4.20)$$

with P_k being the shear stress tensor acting as a source term given by

$$P_k = -\bar{\rho} \tilde{u}_i \tilde{u}_j \frac{\partial \tilde{u}_i}{\partial x_j} \quad (4.21)$$

The empirical constants employed in all calculations with the k - ε model can be found in Appendix 0 at the end of this thesis.

SST-SAS (Scale Adaptive Simulation) Model

The Scale-Adaptive Simulation (SAS) [67] can be seen as an improved URANS formulation, which allows the resolution of the turbulent spectrum in unstable flow conditions. The SAS model can operate in the standard RANS mode but has also the capabilities of partially resolving the turbulent spectrum in unsteady flow regions. SAS models adapt the length-scale automatically to the resolved scales of the flow field, which can result in a LES-like behavior in certain regions of the flow field. The distinguishing factor of the model is the use of the von Karman length-scale L_{vK} . The transport equations for k and $\Phi = k^{1/2} L$ of the SAS model reads [116]:

$$\frac{\partial(\rho k)}{\partial t} + \frac{\partial}{\partial x_i} (\rho u_i k) = P_k - c_\mu \frac{3}{4} \rho \frac{k^2}{\Phi} + \frac{\partial}{\partial y} \left[\frac{\mu_t}{\sigma_k} \frac{\partial k}{\partial y} \right] \quad (4.22)$$

$$\frac{\partial(\rho \Phi)}{\partial t} + \frac{\partial}{\partial x_i} (\rho u_i \Phi) = \xi_1 \frac{\Phi}{k} P_k - \xi_2 \mu_t S |U''| \frac{\Phi^2}{k^2} - \xi_3 \rho k + \frac{\partial}{\partial y} \left[\frac{\mu_t}{\sigma_\Phi} \frac{\partial \Phi}{\partial y} \right] \quad (4.23)$$

with μ_t being defined as:

$$\mu_t = c_\mu^{\frac{1}{4}} \Phi \quad (4.24)$$

The SAS relevant term in the transport equation for Φ is the term with the second derivative $|U''|$. As a result of this term, the length-scale L , predicted by the above model is proportional to the von Karman length-scale [67] as follows:

$$L_{vK} = \kappa \frac{|U'|}{|U''|} \text{ with } |U'| = S \text{ and } |U''| = \sqrt{\frac{\partial^2 u_i}{\partial x_j^2} \frac{\partial^2 u_i}{\partial x_k^2}} \quad (4.25)$$

In contrary to the standard URANS models, the SAS formulation is able to provide a turbulent length-scale, which is not proportional to the thickness of the turbulent shear layer but is proportional to the locally resolved flow structure. More details concerning the empirical constants from this model is given in Appendix 0.

4.1.3 Unsteady RANS modeling

The Unsteady Reynolds Averaged Navier–Stokes (URANS) equations can be employed to model turbulent motions in unsteady periodically changing flow fields. This feature will be utilized later on in this thesis to perform some unsteady computations forced with a periodically changing function. The averaged equations can be derived by decomposing the variable into a Favre mean value $\tilde{\Phi}$, a turbulent fluctuation, and a periodic fluctuation Φ^p as follows [24]:

$$\Phi = \tilde{\Phi} + \Phi'' + \Phi^p \quad (4.26)$$

In the proposed URANS approach, one assumes that the turbulent fluctuations occur at a much smaller time scale T_1 than the periodic fluctuations represented by T_2 (i.e. the characteristic frequency at which the turbulent fluctuations occur is much higher than the frequency of the periodic fluctuations). The illustration of two different time scales can be provided in Fig. 4.2

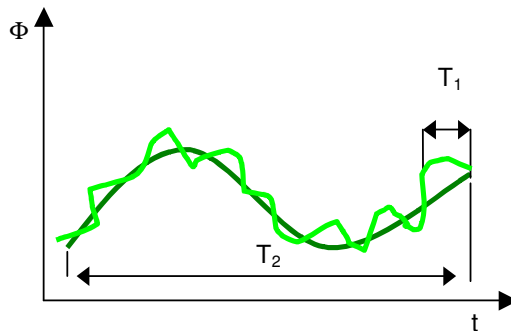


Fig. 4.2 Periodic oscillation with superimposed turbulent fluctuations [24]

T is a time scale, which is much larger than the characteristic time scale of the turbulent fluctuations T_1 but much shorter than the time scale of periodic fluctuations T_2 , so that it can be assumed that periodic fluctuations do not affect the turbulence fluctuations, i.e. $T_1 \ll T \ll T_2$.

Using this assumption, physical effects caused by two different scales can be easily separated from each other. It yields that the turbulence structures are unaffected by the unsteadiness and equation (4.26) can be rewritten as:

$$\Phi = \tilde{\Phi} + \Phi'' \quad (4.27)$$

where the Favre mean $\tilde{\Phi}$ is defined as the density-weighted quantity [24]:

$$\tilde{\Phi}(x, t) = \frac{1}{\bar{\rho}T} \int_{-T/2}^{T/2} \rho \Phi(x, t + \tau) d\tau \quad (4.28)$$

Using appropriate time scale T , one can use equation (4.28) to derive the RANS equation. It must be kept in mind that the time averages are determined at time scale T .

4.1.3.1 CFL requirement

In mathematics, the Courant-Friedrichs-Lewy (CFL) condition is a condition for convergence while solving certain partial differential equations numerically [117]. The CFL condition is defined as [24]:

$$CFL = (u_0 + c_0) \frac{\Delta t}{\Delta x} \quad (4.29)$$

where Δx is the grid spacing, Δt is the time step, u_0 the convective speed, and c_0 characterizes the speed of sound, respectively. This condition has a physical and numerical meaning. On the one hand, the CFL number is a measure, if a wave can cross a discrete grid distance Δx in the time interval, which is much smaller than a single time step Δt . On the other hand, it indicates whether the considered problem is numerical stable. Many numerical schemes (especially explicit schemes) used to solve computational fluid dynamics problems do not perform well when the CFL number is approaching one. However, the implicit time discretisation used in ANSYS CFX allows for using the CFX values well above one. It has been shown in [24] how to use this condition to estimate the time step size for a transient acoustic simulation. It has been concluded that for low Mach number flows, these disturbances, which are transported with the convective speed need less time steps to yield the same CFX condition. The other word in that case, the bigger time step can be utilized. In the context of this thesis, especially in the case of CFD-based flame transfer functions the CFL number will be bigger than one.

4.2 Combustion Modeling

The occurrence of a wide range of turbulent time scales in a turbulent combusting flow makes the mathematical description of turbulent flames very difficult. Furthermore, there is always a strong interaction between chemical reactions, heat releases and turbulence. High turbulence increases significantly turbulent mixing and therefore it intensifies the combustion process itself. The development of combustion models is partially restricted due to the complexity of combustion processes to be described. Most combustion models are based on drastic simplifications of the real physical processes. The complexity comes from three main points [40]:

- Combustion is an intrinsically unsteady process involving a large range of chemical time and length scales.
- Turbulence is characterized by various time and length scales.
- Strong two way coupling between turbulence and combustion.

In general, turbulent combustion may be classified in term of the level of the mixing between fuel and air in two groups: *premixed* or *non-premixed combustion*. The first group mentioned is more applicable to combustion in modern gas turbines, which operate mainly in premixed modes while the combustion in large furnaces and older gas turbines operate in non-premixed modes.

When fuel and an oxidizer, i.e. air, is mixed first and burns after, then the combustion process is termed *premixed*. As opposed to the first group, when combustion and mixing occur simultaneously, the combustion process is called *non-premixed*. In this case, the fuel and air are mixed in the flame itself by diffusion processes. Diffusion flames usually require a more complex mathematical description because of the fuel-to-air ratio ranging from zero in air to infinity in fuel. In addition to this, the flame zone is somewhat fixed at the position where the stoichiometric composition occurs.

From the one hand, the better mixing process in the premix burner helps to reduce the flame temperature peaks in the combustion chamber and therefore to decrease the NO_x formation. On the other hand, in the same time one has to face the problems of flashback, unstable combustions and flame dynamics. Additionally, it is also more difficult to stabilize a premixed flame compared to a non-premixed flame. In modern gas turbine combustion systems, it is common to first use a diffusion pilot flame to stabilize the main premixed flame.

A perfectly premixed combustion from a practical and technical point of view is needed but is very difficult to realize. First of all, it requires a long residence time for mixing processes and large volumes, which may be utilized to enhance diffusion processes. Unfortunately, in modern gas turbine combustion systems both time needed for mixing and volumes where the mixing process can take place are limited. These factors are more likely the key mechanisms that drive the designers to a compromise resulting in partially premixed flames, which allows for having small variations in the equivalence ratio.

From the point of view of this thesis, only turbulent premixed and partially premixed combustion processes in gas turbine combustion systems are considered in more detail.

4.2.1 Turbulent premixed flames

The Borghi diagram may be used to classify turbulent premixed combustion into the various combustion regimes (for more details see [40]). The diagram initially created by Borghi and later extended by Peters [68] classifies the flame regimes as a logarithmic function of two dimensionless parameters. The x-axis of the Borghi plot shown in Fig. 4.3 characterizes the size of the flame structures by means of the ratio between the characteristic length scales L_T to the laminar flame thickness δ_L . The characteristic size of the turbulent structure grows compared to the laminar flame thickness along the x-axis. The ratio of the turbulence intensity to the laminar flame speed is described by the y-axis.

In the classical Borghi plot, the interaction between the turbulent flow field and the flame front are described by means of three dimensionless numbers: the turbulent Reynolds number Re_t , the Damköhler number Da and Karlovitz number Ka defined as:

$$Re_t = \frac{\rho u'_t L_T}{\mu} \quad (4.30)$$

$$Da = \frac{\tau_m}{\tau_c} = \frac{L_T s_L}{u' \delta_L} \quad (4.31)$$

$$Ka = \frac{\tau_c}{\tau_k} = \left(\frac{L_T}{\delta_L} \right)^{\frac{1}{2}} \left(\frac{u'}{s_L} \right)^{\frac{3}{2}} \quad (4.32)$$

where the turbulent Reynolds number describes the ratio of the momentum forces (destabilizing effects) to the viscous forces (stabilizing effects). The Damköhler number denotes the ratio of the turbulent mixing time scale τ_m to the chemical time scale τ_c . The Karlovitz number refers to the ratio of the chemical time scale τ_c to the Kolmogorov time scale τ_k .

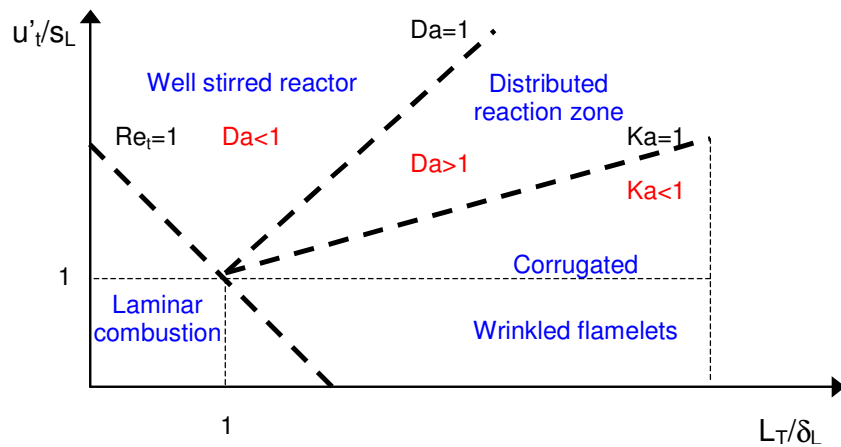


Fig. 4.3 Borghi turbulent combustion diagram [40]

Analyzing the Borghi diagram, the turbulent combustion regimes can be separated into three main zones. The separation lines are determined by $Ka=1$ and $Da=1$:

$Ka < 1$

The flame thickness is smaller than the Kolmogorov length scale and the system may be defined as a locally laminar premixed flame embedded into a turbulent flow. This region is called the “laminar flamelets region”. The flamelets can be wrinkled and stretched due to turbulence motions.

$Da < 1$

This combustion zone is called the ideally stirred reactor and is characterized by turbulent eddies embedded in the reaction zone. The time needed for the chemical reaction to occur is much larger than the time for turbulent mixing.

$Ka > 1$ and $Da > 1$

The turbulent integral time scale is still larger than the chemical time scale. This combustion region is referred to as the distributed reaction zone, where a portion of the turbulent eddies is embedded in the flame front. This leads to thickening of the flame front.

As postulated in [24][61] the majority of gas turbine flames are located in the distributed reaction zone. Further calculations made in [118] at based load operating conditions can prove this statement. However, some of the flames can also be placed either in the perfectly stirred reactor regions or in the flamelets regions. However, some of the considered flames depending on the operating conditions can also be placed either in the perfectly stirred reactor regions or in the flamelets regions.

4.2.2 Combustion models

The additional transport equation for species mass fraction involves the chemical source term ω . Considering turbulent flows and taking into account the non-linear character of this source term derived by the Arrhenius equation, the mean reaction rate cannot be calculated directly from averaged concentrations and temperatures due to the instantaneous temperature and mass fraction fluctuations, which might be large. The main goal of combustion modeling is to find a proper way of calculating the chemical source term. There is a large number of different turbulent combustion modeling concepts introduced in the technical literature in the last several years. The brief overview of combustion models currently used in CFD could be found in [40][68]. In the context of this thesis only two type of combustion model are of importance i.e. the EDM¹⁰ model and the EDM model combined with the FRCH.model

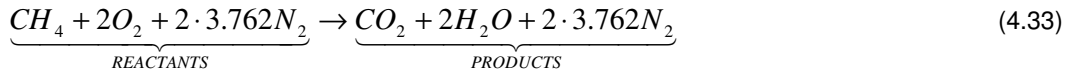
¹⁰ Eddy Dissipation Model

Eddy Dissipation Model (EDM)

The Eddy Dissipation Model is similar to the Eddy Break Up model already developed in 1970 by Spalding and is based on the concept that the chemical reaction is fast compared to the turbulent mixing process ($Re \gg 1$ and $Da \gg 1$). It assumes that the reactants, which are being mixed at the molecular level form the combustion products immediately. On this basis, the reaction rate may be seen to be fully controlled by the mixing time of reactants at the molecular level.

The Eddy Dissipation Model is also widely utilized by industry because in many industrial combustion processes the assumption is made that reaction rates are much smaller compared to mixing reactant rates.

The one-step global reaction mechanism for the complete stoichiometric combustion of methane in air defined as in [69]:



The average reaction rate of a global reaction ω by the EDM model can be expressed as the minimum of the reactants R and products P [14].

$$\omega_r = \min \left(A \frac{\varepsilon}{k} \min \left(\frac{[R]}{\nu'_{rR}} \right), A \cdot B \frac{\varepsilon}{k} \left(\frac{\sum_P [P]}{\sum_P \nu''_{rP}} \right) \right) \quad (4.34)$$

where A and B are model constants, $[R]$ and $[P]$ stand for the molar concentration of component P and R and ν refers to the stoichiometric coefficient. In turbulent flows, this mixing time is dominated by the eddy properties and, therefore, the rate is proportional to a mixing time defined by the turbulent kinetic energy, k , and dissipation ε . The turbulence time scale is estimated from the turbulence kinetic energy k and its dissipation rate ε according to [16]:

$$\tau_{EDM} = \frac{k}{\varepsilon} \quad (4.35)$$

which is an estimate of the characteristic mixing time scale.

Eddy Dissipation Model combined with the Finite Rate Chemistry Model (EDM/FRCH)

In contrary to the Eddy Dissipation Model, the combination of the Eddy Dissipation Model and the Finite Rate Chemistry Model can include effects of chemical kinetics. The EDM/FRCH concept allows one for considering the combustion of turbulent flows not only for reactive flows where the chemical time scale is very small but also to calculate turbulent flows dealing with finite rate chemistry.

The average reaction rate of an elementary reaction ω can be computed as the minimum of the EDM reaction rate and the chemical kinetics reaction rate [14].

$$\omega_r = \min(\omega_{r,EDM}, \omega_{r,FRCH}) \quad (4.36)$$

where for one global reversible elementary reaction the reaction rate $\omega_{r,FRCH}$ is defined as follows [16]:

$$\omega_{r,FRCH} = \left(F_r \prod_{I=A,B,\dots}^{N_c} [I]^{r'_I} - B_r \prod_{I=A,B,\dots}^{N_c} [I]^{r''_I} \right) \quad (4.37)$$

with $[I]$ being the molar concentration of the species A and B , and r' and r'' stand for the order of forward and backward reactions. Both the forward and backward rate constant are represented by the Arrhenius exponential temperature dependence as stated in [63]. The forward rate constant F_r can be written as:

$$F_r = A_r T^{\beta_r} \exp\left(-\frac{E_r}{RT}\right) \quad (4.38)$$

By analogy, a similar equation can be derived for the backward rate constant B_r . It is also seen that the reaction rate calculated by the Arrhenius law introduces a non-linear dependence on the temperature T . The parameters A_r , β_r and E_r are the pre-exponential factor, the non-dimensional temperature exponent and the activation energy, respectively.

EDM/FRCH with five step chemistry

One to three step global reaction schemes are useful in determining cooling-air flows and in the prediction of pattern factors, but are not able to predict emission [119]. Nicol et al. [71] introduced and validated the five-step global methane oxidation-NO formation mechanism for premixed methane-air combustion under atmospheric condition using GRI2.11 mechanism. The presented mechanism was then modified and adjusted to different pressure levels. The reaction mechanism takes into consideration not only the oxidation of methane but also the forward and backward reaction rate of carbon dioxide.

This reduced mechanism allows also for the prediction of the concentration of CO₂. In addition to this, gives an estimation of NO_x concentration referring to prompt NO and thermal NO. The global mechanism covers five separate chemical reactions with a total of seven species and reaction rates being estimated with different combustion models.

This reduced mechanism is tailored to a specific range of equivalence ratio, a particular pressure and possibly a particular range of inlet temperatures. As postulated by Nicol et al. [71], the elementary reactions and the combustion model adequate to the appropriate step can be listed as:

- **Step 1 - EDM/FRCH**



- **Step 2- EDM/FRCH**



- **Step 3- EDM/FRCH**



- **Step 4- FRCH – Prompt NO**



- **Step 5- FRCH –Thermal NO**



The presented five-step global mechanism can be used to model generic lean premixed gas turbine combustion systems at atmospheric condition because they allow for calculating the concentration of CO and NO. The reduced five-step global methane oxidation-NO formation mechanism introduced in this section is later utilized to model the combustion process in the generic premix atmospheric burner. The reaction coefficients, which are used to calculate Prompt and Thermal NO differ from each other. The reaction rate depends on pressure and must be adopted for different pressure levels.

5 Numerical System Identification of Thermo-acoustic Elements

Any combustor or other geometrical parts, belonging to gas turbine combustion systems can be treated as thermo-acoustic elements. By forcing such an element with controlled external acoustic signals and monitoring the response, a dynamical relationship may be derived between unsteady heat releases and acoustic variables p' or u' . The mentioned dynamical relation may have the form of a flame transfer function, coupling the excitation signal with the integrated heat release, or an acoustic transfer matrix relating the acoustic quantities upstream and downstream of a given element. The examples of the flame transfer function and acoustic transfer matrix have already provided in the previous sections.

The system identification method based on correlations between signals and responses known from control theory can be applied to reconstruct the dynamic flame behavior. The reconstruction procedure is a combination of an unsteady CFD computation and system identification [43]. The CFD/SI method is employed to determine flame transfer functions. Flame transfer functions based on CFD/SI are more precise as opposed to the conventional time lag model to characterize the dynamics between forcing and response. These frequency dependent relations either in the form of the flame transfer function or the acoustic transfer matrix can be incorporated into the acoustic network model. Doing so, it is possible to predict accurately the acoustically unstable modes of a whole system and the growth rate of instabilities [96].

CFD-based transfer function gives a more physical insight into flame/acoustic, flame/vortex interactions and of course into undergoing combustion processes. On the contrary, CFD-based acoustic transfer matrices are utilized to relate only upstream and downstream acoustics but cannot provide any physical details about what is happening inside the element.

The main objective of Chapter 5 is to provide a theoretical background to the numerical system identification known as the CFD/SI approach. This combined method is extensively used in this thesis. The CFD/SI approach was developed and first introduced by Polifke et al. [49]. The mathematical description of the reconstruction procedure of thermo-acoustic elements is given in detail. The optimal setting for the reconstruction is presented and different excitation techniques are reported.

5.1 Fundamentals of Numerical System Identification

The system identification deals with the problem of building mathematical models of dynamical systems based on observed data from the system. In loose terms, a system is an object in which variables of different kinds interact and produce observable signals.

The observable signals that are of interest are usually called outputs. External signals that can be manipulated by the observer are called inputs. Other are associated with disturbances. The distinction between inputs and disturbances is often less important for the modeling process. An example is depicted in Fig. 5.1.

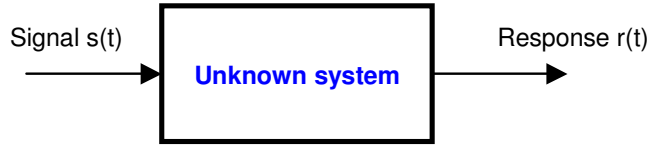


Fig. 5.1 Block representation of an arbitrary system [90]

5.1.1 Characterization of discrete time systems

Time series data taken from a transient CFD calculation with low-amplitude forcing of pressure and/or velocity at the boundaries of the computational domain can be regarded as acoustic discrete signals. These signals can be either received or emitted from the multi-port element [47][48].

The multi-port element can then be treated as a discrete time system, which operates on the discrete signals such that the input to the system, $s(t)$, is transformed into its response or output $r(t)$. The relationship between $s(t)$ and $r(t)$ is defined by the mathematical transformation operator χ such that [50]

$$r(t) = \chi\{s(t)\} \quad (5.1)$$

The internal structure of the system under consideration is not of interest to the user, therefore the system can be considered as a “back box”. Its input and output signals solely define the system. Moreover, the system can be considered *linear* if it satisfies the superposition principle [50].

$$\chi\{s_1(t) + s_2(t)\} = \chi\{s_1(t)\} + \chi\{s_2(t)\} = r_1(t) + r_2(t) \quad (5.2)$$

or

$$\chi\{a_1 s_1(t) + a_2 s_2(t)\} = a_1 \chi\{s_1(t)\} + a_2 \chi\{s_2(t)\} = a_1 r_1(t) + a_2 r_2(t) \quad (5.3)$$

for any arbitrary input sequence $s_1(t)$ and $s_2(t)$, and any arbitrary constant a_1 and a_2 .

In addition to this, the time discrete system can be considered as the *time invariant system* if and only if the eq(5.1) satisfies the following expression [50]:

$$r(t - t_0) = \chi\{s(t - t_0)\} \quad (5.4)$$

for all possible values of t_0 . The time shift for any arbitrary sequence $s(t)$ corresponds to the time shift in the output sequence $r(t)$.

If the output sequence $r(t)$ at time t is dependent on the inputs $(t-\tau)$ to t , where $\tau > 0$, the system is said to have memory of duration τ . If $\tau = \infty$, the system is said to have infinity memory. Further, a dynamic system is one that has finite memory where $0 < \tau < \infty$. In the case of $\tau = 0$ the system is termed static. The analyzed system is termed to be static if its output at any time depends only on its input at the same time. Such systems do not contain any delay elements and are memoryless. In the case when the system has finite memory, the causality of the system becomes very important. The system is said to be causal if its output at any time t depends on its present ($t=t_0$) and past ($t \leq t_0$) inputs, but not on future inputs. It satisfies the following relation [50]:

$$r(t_0) = f\{s(t_0, t_{0-1}, t_{0-2}, t_{0-3}, \dots)\} \quad (5.5)$$

with f being an arbitrary function.

The last important characteristic of a discrete system is the system stability. Mathematically, the system is said to be bounded input-bounded output (BIBO) stable if and only if every bounded input $s(t)$ produces a bounded output $r(t)$. For some positive and finite numbers A and B , the sequence $s(t)$ and $r(t)$ is bounded when [50]:

$$|s(t)| \leq A < \infty \text{ and } |r(t)| \leq B < \infty \quad (5.6)$$

The presented properties are very important with respect to thermo-acoustic systems excited with white noise. The stability of a system under consideration is a necessary condition to be able to apply the system identification procedure.

5.1.2 Linear Time Invariant (LTI) Systems

Discrete time systems mentioned above, which have additionally the properties of linearity and time invariance are termed Linear Time Invariant (LTI) Systems. LTI systems can be characterized both in time and frequency domains. Time invariant systems form the most important class of dynamical systems considered in practice and in the literature. This is due to the fact that they can be utilized to represent idealizations of the processes encountered in real life. The approximations involved are often justified by the design consideration based on linear theory.

Knowledge of responses to given outputs are required to properly describe discrete time systems. For LTI systems, the responses in time domain can be characterized by the response to a unit impulse sequence. Because of its linearity and time-invariance properties, the response of an LTI system to any arbitrary input sequence can be shown in terms of unity impulse responses of the system [49][50]. The unit impulse sequence for $t=0, \Delta t, 2\Delta t, 3\Delta t, \dots$ can be given as a sum of weighted impulses [53]:

$$s(t) = \sum_{k=-\infty}^{\infty} s(k)\delta(t-k) \text{ with } \delta = \begin{cases} 1 & t = k \\ 0 & t \neq k \end{cases} \quad (5.7)$$

where δ is the unit impulse and $k=1,2,3,\dots$. If the unit impulse response $h(t,k)$ indicates the response of the LTI system to the unit impulse sequence $\delta(t-k)$, the response of the system $r(t)$ can be rewritten as [53]:

$$r(t) = \mathcal{X}\{s(t)\} = \mathcal{X}\left\{\sum_{k=-\infty}^{\infty} s(k)\delta(t-k)\right\} \quad (5.8)$$

Making use of the superposition principle from (5.3), this expression is finally transformed into:

$$r(t) = \sum_{k=-\infty}^{\infty} s(k)\mathcal{X}\{\delta(t-k)\} = \sum_{k=-\infty}^{\infty} h(t-k)s(k) \quad (5.9)$$

Thus the sequence of the impulse response can completely characterize an LTI system.

5.1.3 Frequency response of LTI systems

It can be shown that eq. (5.9) is a convolution of $s(t)$ and $h(t)$. It can be also shown that according to the commutative law, which constitutes one of its properties [48] eq. (5.9) for $r(t)$ is rewritten as [53]:

$$r(t) = \sum_{k=-\infty}^{\infty} h(k)s(t-k) \quad (5.10)$$

Utilizing the input sequence represented by the complex exponential function $s(t)=\exp(i\omega t)$, the characteristic of any LTI systems can be shown in the frequency domain and one gets [53]:

$$r(t) = \sum_{k=-\infty}^{\infty} h(k)e^{i\omega(t-k)} = \left[\sum_{k=-\infty}^{\infty} h(k)e^{-i\omega k} \right] e^{i\omega t} \quad (5.11)$$

where the term in the bracket is defined as $H(\omega)$ and is known as the frequency response of the system. Thus we have obtained the following relation [53]:

$$H(\omega) = \sum_{k=-\infty}^{\infty} h(k)e^{-i\omega k} \quad (5.12)$$

Thus with a particular type of input signal, the response is equal to the signal up to a complex-valued multiplicative factor $H(\omega)$, which depends solely on ω .

5.1.3.1 z-Transformation

In contrast to the Laplace transform, the z-transform is used to study discrete time signals and systems. The z-transformation is a useful tool for considering discrete systems.

More details are given in [51]. Recalling eq. (5.12), one notices that the frequency response $H(\omega)$ of an LTI system is equal to z-transform of its impulse response h with argument $z=\exp(i\omega)$:

$$H(z) = \sum_{k=-\infty}^{\infty} h(k)z^{-k} \quad (5.13)$$

In general, an infinite number of coefficients $h(k)$ where $-\infty < k < \infty$ should be utilized to completely determine the frequency response. It is also known that it is not practically realizable while performing unsteady computations because only a finite number of time steps can be defined. A good estimate of the frequency response can be also obtained with smaller number of coefficients [49]. In this case the entire system can be characterized by some finite number of unit impulse responses L . Moreover, taking into account the causality of the system, the above equation transforms into [51]:

$$H(z) = \sum_{k=0}^L h(k)z^{-k} \quad \text{with } 0 < k < L \quad (5.14)$$

This form of the z-transform is stable as long as any term $|h(k)z^{-k}|$ has a finite value and when the sum $\sum h(k)z^{-k}$ converges for all $|z|>0$.

5.1.3.2 Inverse z-Transformation

Since the frequency response is periodic on $[-\pi, \pi]$, it can be viewed as an exponential Fourier series expansion where $h(k)$ represents the Fourier series coefficients. The inverse z-Transformation can be defined as follows [47]:

$$h(k) = Z^{-1}\{H(z)\} = \frac{1}{2\pi} \int_{-\pi}^{\pi} H(\omega)e^{-i\omega k} d\omega \quad (5.15)$$

Note that both the unit impulse response, h , and the frequency response, $H(\omega)$, characterizes a discrete time invariant system and can be freely converted into each other.

5.2 Models of LTI systems

System identification is the task of constructing or selecting models of dynamical systems to serve certain purposes [53]. Speaking strictly mathematically, system identification can be seen as the process whereby a mathematical model of a system is inferred from its input and output data. Systems can be classified under different model structures depending on their properties or characteristics [51]. To be able to identify an arbitrary system, a suitable mathematical model must be chosen. In general, the identification of this system is reduced to the determination of the model coefficients.

To describe the system represented by the black box model shown in Fig. 5.1, standard linear models may be employed without reference to the physical background as opposed to so-called "the Gray Box model" [50]. These models do not reflect any physical considerations of the system but rather are used only to adjust the fit to the data. To characterize causal LTI systems, one can use the equation [52][53]:

$$r(t) + \sum_{k=1}^{n_a} a_k r(t-k) = \sum_{k=0}^{n_b} b_k s(t-k) + \sum_{k=0}^{n_c} c_k e(t-k) \quad \text{with } n_a, n_b, n_c = 0, 1, 2, \dots \quad (5.16)$$

The above written equation is known as an ARX model [90]. AR refers to the auto-regression part of $r(t)$, that is, $\sum_{k=1}^{n_a} a_k r(t-k)$. X defines the extra input $\sum_{k=0}^{n_b} b_k s(t-k)$. The last term on the right hand side defines the disturbance term $e(t)$. This equation defines also a model structure. Any systems having such a structure can be characterized or identified if the coefficients a_k , b_k and c_k and their respectively polynomials order n_a , n_b and n_c , are known. Considering a special form of the ARX model where $n_a, n_c = 0$ for $k=0, 1, 2$, the equation reduces to the model structure known as the Finite Impulse Response (FIR) [54]:

$$r(t) = \sum_{k=0}^{n_c} h(k) s(t-k) \quad (5.17)$$

where one treats $r(t)$ as the output of the system due to the input $s(t)$. The coefficient b_k can be replaced by $h(k)$ referring to the unit impulse response vector.

5.3 Wiener-Hopf Equation

There are a number of mathematical techniques for performing the system identification procedure of an LTI system found in the literature [49][53][52]. If $s(t)$ is a scalar-valued random process that is the input to an LTI system and the $r(t)$ is also a random valued process that is the output of an LTI system. Then a specific formulation of the optimal linear least-mean-square estimator has the form of the Wiener-Hopf equation [53][50]. This equation provides the optimal unit impulse response and minimizes the estimation error and is written as [48]:

$$\Gamma h = c \quad (5.18)$$

Here Γ stands for the autocorrelation matrix, where c is the cross-correlation vector and h refers to the unit impulse response.

5.3.1 Auto-correlation matrix

For discrete and stationary processes the auto-correlation matrix Γ of the input sequence $s(t)$ defined as $s_i = s(i\Delta t)$, $i=0, \dots, N$ has the following form [49]:

$$\Gamma_{ij} = \frac{1}{N-L+1} \sum_{k=L-1}^{N-1} s(k-i)s(k-j) \quad (5.19)$$

or

$$\Gamma_{ij} = \frac{1}{N-L+1} \sum_{k=L-1}^{N-1} \begin{bmatrix} s(k)s(k) & \dots & s(k)s(k-L+1) \\ \vdots & \dots & \vdots \\ s(k-L+1)s(k) & \dots & s(k-L+1)s(k-L+1) \end{bmatrix} \quad (5.20)$$

where N is the length of $s(k)$ and L is the filter order or the number of samples needed to characterize effectively the system. The indexes i and j are in the sequence to $i, j=0, 1, 2, \dots, L-1$. The discrete signals $s(t)$ are auto-correlated, forming an auto-correlation matrix for one-port systems (SISO)¹¹.

The auto-correlation matrix for such a system has the dimension L -by- L . The physical interpretation of Γ can be seen directly from the definition of its elements. Each row in Γ shows how the correlation of $s(k)$ evolves with time over the system's time delay. The main diagonal for $i=j$ refers to the 0th lag correlation function of the input sequence $s(k)$ as it evolves with the time over the system's delay. That is, all elements located on the main diagonal represent how the stochastic properties of $s(k)$ evolve with time.

The definition of autocorrelation matrix can be extended to multi-port acoustic systems (MIMO)¹² with two input and two output signals [46][48]. For two input sequences s_1 and s_2 [49]

$$\Gamma_{ij}^{s_1 s_2} = \frac{1}{N-L+1} \sum_{k=L-1}^{N-1} s_1(k-i)s_2(k-j) \quad (5.21)$$

or in the matrix from:

$$\Gamma_{ij}^{s_1 s_2} = \begin{bmatrix} \Gamma(s_1, s_1) & \Gamma(s_1, s_2) \\ \Gamma(s_2, s_1) & \Gamma(s_2, s_2) \end{bmatrix} \quad (5.22)$$

The auto-correlation matrix for two port systems is characterized by four distinct quadrants Γ_{12} where the index 1 and 2 stands for the signals that are correlated. The global auto-correlation matrix Γ comprises of two auto-correlation sub-matrices (Γ_{11}, Γ_{22}) and two cross-correlation sub-matrices (Γ_{12}, Γ_{21}). The auto-correlation sub-matrices can be interpreted exactly as a one-port system. The form of Γ indicates the degree of correlation between the considered signals.

¹¹ SISO – Single Input –Single Output

¹² MIMO: Multi Input - Multi Output

If the signals are totally uncorrelated or weak correlated (Γ_{12} with $1 \neq 2$) then the form of Γ_{12} , and Γ_{21} is quite flat and should have a value approximately zero as shown in [48].

5.3.2 Cross-correlation vector

The cross-correlation vector illustrates the temporary change in the correlation of the response $r(t)$ with $s(t)$ as shown here [49]

$$c_{xy} = \frac{1}{N-L+1} \sum_{k=L-1}^{N-1} r(k)s(k-i) \text{ for } i=0,1,2,\dots,L-1 \quad (5.23)$$

The form of c indicates the degree of correlation of $x(t)$ and $y(t)$. For the one-port system the vector c reads:

$$c_i = \frac{1}{N-L+1} \sum_{k=L-1}^{N-1} \begin{pmatrix} r(k)s(k) \\ \vdots \\ r(k)s(k-L+1) \end{pmatrix} \quad (5.24)$$

where the first row refers to the sum of cross-correlations of signals and responses with zero time lag and consequently the last row defines the sum of cross-correlations of signals with maximum time lag. In general, it shows the time delay(s) between $r(k)$ and $s(k)$ if the input signal is not periodic. For periodic signals, the form of c depends on the periodicity of $s(k)$ and the relation between $s(k)$ and $r(k)$. This property was theoretically studied more in detail in [48].

5.4 Reconstruction of Thermo-acoustic Elements by Means of CFD/SI

It has been proposed recently by Gentemann and Polifke et al. [17][43] to employ advanced numerical tools from system identification to estimate acoustic transfer functions or matrices based on transient CFD data. With the help of CFD/SI, the power of computational fluid dynamics can be combined with the efficiency of network models using CFD-based thermo-acoustic elements. More specifically, time series of fluctuating flow variables at the system element under investigation are generated in transient CFD calculations with low-amplitude forcing at the boundary of the computational domain. The compressible Navier-Stokes equation is employed to resolve fluid motions and at the same time can be also used to resolve acoustic flow fields. As opposed to the Euler equation, the unsteady CFD computation has the extended capability of capturing mean flow/turbulent interactions, which may significantly affect damping.

An identification procedure or a reconstruction of thermo-acoustic elements with respect to one-port systems is discussed in the following section. Acoustic transfer matrices or transfer functions of a given thermo-acoustic element to be identified always belong to the system. domain, values of velocity and pressure are exported to files at every time step of the simulation.

In the identification procedure, the system of interest first has to reach the steady state condition or in other words; the converged steady state computation has to be performed first. Subsequently, the converged solution has to be excited or forced by input signals in order to produce a dynamical response of the system [59]. At defined planes upstream and downstream of the thermo-acoustic element located inside the computational

The considered system consists of the thermo-acoustic element itself and the reference plane. These are plotted in Fig. 5.2

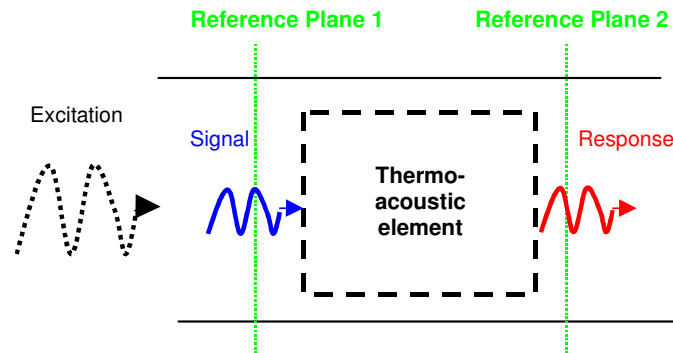


Fig. 5.2 The system of interest: a thermo-acoustic element and reference planes [50]

The following main steps have to be generally considered to reconstruct thermo-acoustic elements using the CFD/SI approach:

- acoustic boundary conditions
- choice of excitation signals,
- causality and proper choice of variables,
- placement of reference planes,
- optimal setting for solving the Wiener-Hopf equation

5.4.1 Acoustic boundary conditions

It is well known that the standard boundary conditions i.e. velocity and pressure boundary conditions available in CFD codes are reflective in nature. Moreover, Yuen et al. [120] has investigated the influence of boundary reflection coefficient on the system identification of acoustic two-ports elements. A real time system models based on the unit response filters implemented in Simulink has been used in that study. It has been found that the acoustic identification of two-ports element depends strongly on the boundary acoustic reflection coefficient. It has been shown that the numerical accuracy decreases with increasing values of $|R|$. After certain reflection coefficients $|R|_{\max}$ the identification of the system failed. In unsteady CFD calculations, the artificially generated pressure waves can reflect off of these boundaries and disturb the spectral analysis of signals and responses. For example, the coherence between the original signal and response might be distorted or the response might correlate with reflected signals, which would include unphysical long time-lags.

Externally applied forcing and the frequency response of the system can cause further resonant peaks and the model might be triggered at its eigenfrequencies, which could make the CFD/SI approach not reliable [55]. To avoid reflections of acoustic waves at boundaries, unsteady computations, i.e. URANS or LES have to be carried out if it is possible with non-reflecting boundary conditions [56]. In addition to this, to minimize the influence of reflective boundary conditions on the system identification procedure and to reduce the resonance effects in the computational domain, one can use an excitation signal based on white noise. Furthermore, white noise has the capability of exciting uniformly all frequencies from the frequency range of interest.

The CFD/SI approach depends on the statistical assessment of the root-cause effect between the excitation signal and the response in the system. In order to get an accurate assessment of this root-cause relationship, it is important to have:

- high coherence¹³ between the signal and response,
- direct path between the forcing signal and the flame response in the case of flame transfer functions or pressure and velocity fluctuations in the case of transfer matrices such that it excludes any additional acoustic reflections.

On the basis of these considerations, acoustically non-reflective boundary conditions should be used in unsteady CFD simulations. These boundary conditions have been implemented in ANSYS CFX10 and ANSYS CFX11 on the basis of the work of Widenhorn et al. [56]. The latest version of CFD ANSYS offers non-reflective boundary conditions for inlets and outlets. They are formulated in a way, which assumes local one-dimensionality of disturbance propagation (LODI = Local One-Dimensional Inviscid). With these boundary conditions, disturbances are separated into waves traveling into the domain and waves leaving the domain with different propagation speeds. The propagation speeds considered include the mean flow velocity u normal to the outlet plane responsible for convection of disturbances and the acoustic propagation velocities $u+c$ and $u-c$. Based on the LODI formulation [91], conservation equations are solved using the boundary condition. With the corrected primitive variables for the amplitudes of incoming waves the overall reflectivity is reduced. A more elaborated report of the implementation procedure is described by Zwart et al. [92] and by Widenhorn et al. [56].

The second non-reflecting boundary condition type used for LES-like computations in this work is based on a time domain impedance formulation. This formulation is slightly different from LODI but for SAS and LES is numerically more stable. The theory of this model and the implementation are presented in detail by Widenhorn et al. [93].

¹³ The coherence function is the function related to cross-correlation and is defined in terms of power spectral densities and the cross-spectral density by $c_{xy}(\omega) = \frac{|R_{xy}(\omega)|^2}{R_x(\omega)R_y(\omega)}$. A common use for the coherence function is in the validation of input/output data collected in an acoustics experiment for purposes of system identification. The coherence function is defined between 0 and 1. For ideally correlated signals the coherence is 1 and for not-correlated signals is 0.

5.4.2 Forcing signals

The term ‘forcing’ refers to the input time series that is used to force the system of interest in order to obtain its response. Of course, in the identification of a given thermo-acoustic system, the system’s frequency response is the most important parameter to be determined. It generally reflects how the input signal affects the system response at different frequencies.

Assigned amplitude bigger than 15% with respect to the main value may yield a problem with non-linearity of the system and cause the identification procedure to fail. Therefore, it is also important to keep the amplitude of excitation signals, A , at a certain level. Gentemann et al. [50] investigated the influence of various amplitude levels on the identification of transfer matrices and showed that the reconstructed transfer matrices can slightly differ from each other in terms of the reconstructed amplitude and phase. Moreover, the magnitude of the excitation amplitude must be so defined that it is sufficient to excite the system under investigation and simultaneously does not exceed the linearity of the analyzed system. Polifke and Gentemann et al. [54] have suggested the critical amplitude of excitation to be not larger than 15% of its mean value.

For identification purposes, the velocity at the inlets to the computational domain are excited by the addition of velocity fluctuations to the main values [17]:

$$u_{in}(t) = \bar{u}_{in} + u'_{in}(t) \quad (5.25)$$

Here u is the velocity where a bar notation stands for the mean velocity value and the notation with primes stands for the fluctuating part. For the reconstruction of transfer functions, it is sufficient to force the computational domain only at the inlets. In the case of the reconstruction of acoustic transfer matrices, it is obligatory to excite also the computational domain with two independent and uncorrelated excitation signals at the upstream and downstream boundaries. In this case, one looks for the relation between downstream and upstream side of the acoustic element. To be able to properly perform the identification experiment, one has to impose an additional pressure excitation signal at outlets such as [17]:

$$p_{out}(t) = \bar{p}_{out} + p'_{out}(t) \quad (5.26)$$

where the pressure with bar notation stands again for the mean static pressure and the quantity with the prime notation referring to the fluctuation part. In the work of Yuen et al. [48] the influence of different excitation signals on the identification procedure was given and several excitation techniques were investigated.

5.4.2.1 Harmonic function

Exciting the system with an excitation signal having a specific frequency can be achieved with harmonic signals.

These kinds of excitation signals are especially useful if the flame response at certain frequencies must be investigated in details. To better determine mechanisms responsible for dynamics of a flame, the sinusoidal forcing signals are imposed at inlets with the fluctuation part defined as:

$$u'_{in}(t) = A_{in} \bar{u}_{in} \sin(2\pi ft) \quad (5.27)$$

with t being time, f being the excitation frequency, and A_{in} standing for the amplitude. In this case, the frequency response can only be determined at particular frequency f . In this thesis, the validation of the CFD/SI approach is often performed by means of discrete forcing signals.

5.4.2.2 White noise

By definition, white noise can be characterized by a stochastic process whose elements are drawn from a random function and is equally distributed between 0 and 1. It has frequency component ranging from 0 Hz and ending up with the Nyquist frequency¹⁴ of the system. The white noise excitations for both boundaries are given by [17]

$$u'_{in}(t) = A_{in} \bar{u}_{in} X_{in}(t) \quad (5.28)$$

Considering outlet boundaries, one has to account for the overall total energy balance and therefore the pressure fluctuation term is defined as:

$$p'_{out}(t) = A_{out} \rho_{out} \bar{u}_{out}^2 X_{out}(t) \quad (5.29)$$

where $X_{out}(t)$ and $X_{in}(t)$ correspond to the randomly distributed functions changing from -0.5 and 0.5.

5.4.3 Causality and choice of variables

As stated by Polifke et al et al. [47], the choice of variables and causality of the filter used in the identification experiment are also crucial issues that should be kept in mind. The wrong choice of variable to represent acoustic phenomena may cause the system identification procedure to be unsuccessful.

The primitive acoustic variables p' and u' representing plane acoustic waves can be utilized to reconstruct acoustic transfer matrices. The primitive acoustic variable can be easily transformed to the equivalent form known as Riemann invariants f and g . The upstream and downstream traveling plane waves f and g are defined by the following relations [100][134]:

$$f = \frac{1}{2} \left(\frac{p'}{\rho c} + u' \right) \quad (5.30)$$

¹⁴ The Nyquist frequency, named after the Swedish-American engineer Harry Nyquist or the Nyquist–Shannon sampling theorem, is half the sampling frequency of a discrete signal processing system

$$g = \frac{1}{2} \left(\frac{p'}{\rho c} - u' \right) \quad (5.31)$$

The influence of the choice of variables to represent the underlying cause-and-effect relationships imposed by fluid dynamics and acoustics on the proper system identification is investigated by Polifke and Gentenmann et al. [47]. It is reported that not all primitive acoustic variables u' and p' provided by CFD computation can correctly represent the underlying physical laws, nor can they correctly indicate the “cause” and the “effect”. Let us consider the acoustic flow field in the tube shown in Fig. 5.3. The plane waves f and g propagate over the distance Δx between location u located upstream and d downstream of the black box.

The acoustic transfer matrix expressed by standard p - u notation for this element does not properly represent the cause-and-effect relationship. The acoustic variables p' and u' taken upstream (signal) and downstream (response) do not correctly describe the underlying cause-and-effect relationship imposed by physics.

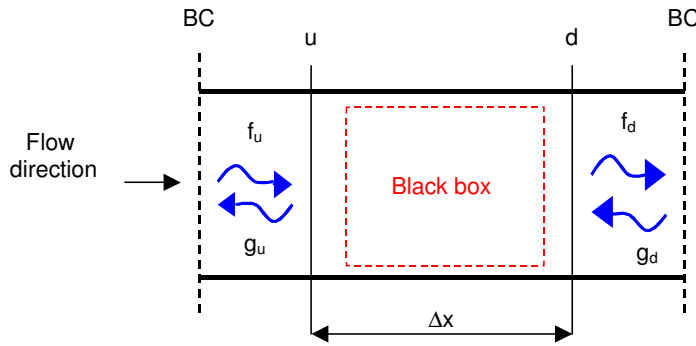


Fig. 5.3 Tube and wave propagation [46]

Considering this notation, it is not clear which variables should be used to characterize signals and which should be used for responses [134][100].

$$\begin{pmatrix} p' \\ \rho c \\ u' \end{pmatrix}_d = T_{pu} \begin{pmatrix} p' \\ \rho c \\ u' \end{pmatrix}_u \quad (5.32)$$

On the other hand, the cause-and-effect relationship can be correctly addressed by the scattering notation. A downstream traveling wave f_u at the upstream location should be considered as a signal, which leads to a response f_g at the downstream location after a time delay $\tau = \Delta x / c$. Similarly a wave g_d coming in from the downstream side has a response g_u . The acoustic transfer matrix of the simple tube is represented in the scattering notation as [50]

$$\begin{pmatrix} f_g \\ g_u \end{pmatrix} = T_{sr} \begin{pmatrix} f_u \\ g_d \end{pmatrix} \quad (5.33)$$

From the analysis made above, one can draw the conclusion that it does not make any differences which acoustic transfer matrix notation is utilized to characterize the black box. Eq.(5.32) and (5.33) are completely equivalent and can be freely transferred from one form into another. An elaborated description about the transformation of the variable notation is given in [94]. Nevertheless, it does make a difference whether a system identification procedure is formulated in the primitive acoustic variables or in the scattering notation. It is expected that the system identification formulated with variables as in Eq. (5.33) will work well with causal and non-causal filters due to the proper representation of the cause-and-effect relationship (i.e. $r(t)=f[s(t\pm\tau)]$). While, using the p - u notation good results can be obtained only if non-causal filters (i.e. $r(t)=f[s(t-\tau)]$) are employed.

5.4.4 Location of the reference planes

The reference planes, which are used to extract time series from CFD computations sometimes cannot be located directly at the position where a given acoustic element begins or ends. Therefore, the reconstructed acoustic transfer matrix need to be re-calculated taking into account additional elements accounting for the distance between the reference plane and the acoustic element to be reconstructed.

However, one necessary condition has to be fulfilled in the identification experiment, reference planes must enclose completely the acoustic element. In practice, it is also useful to define more than two reference planes distributing them over the axial distance up- and downstream of the acoustic element to verify and determine an influence from the location of reference planes on the reconstructed transfer matrix. To better understand the re-calculations procedure, let us consider the following 'black' box shown in Fig. 5.4, which is used to reconstruct the acoustic transfer matrix.

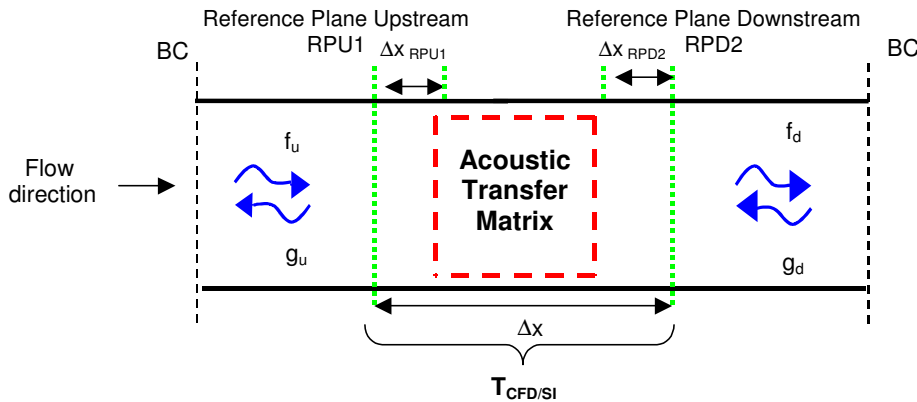


Fig. 5.4 Location of the reference planes and the boundary of the black box [50]

It is clearly shown that using the CFD/SI approach, one is able to reconstruct the acoustic element, but in this reconstruction additional parts represented here by T_{RPU1} and T_{RPD2} are also integrated. In reality, an additional part is a simple tube with the length Δx_{RPU1} and Δx_{RPD2} .

To estimate the acoustic element T of interest, one has to re-calculate T as [50]:

$$T = T_{RP1}^{-1} \cdot T_{CFD/SI} \cdot T_{RP2}^{-1} \quad (5.34)$$

In term of the reconstruction of flame transfer functions, the downstream reference plane can be approximately located at the position where no heat release is observed. Gentemann et al. [50] has found that it is sufficient to locate the downstream reference plane at the location equal to one diameter of a gas turbine burner. However, it is not applicable in all cases and it strongly depends on the considered configuration.

5.4.5 Extraction of time series

It should be avoided to locate reference planes to extract time series of pressure and velocity in the recirculation region and therefore it is highly recommended to place reference planes at the axial position where the flow field i.e. velocity and pressure profiles are uniform. This is more deeply investigated by Gentemann et al [50]. It was reported how a non-uniformity of the flow field due to incorrect positioning of reference planes resulted in a low quality of acoustic signals utilized in the identification experiment. It has been proposed to apply some averaging techniques to overcome this problem.

The time series of velocity and pressure exported from the reference planes located in the uniform flow represent the pure plane acoustic wave and can be directly used to perform the identification procedure. However, when any time series are taken at the location where the flow non-uniformities dominate, the averaging technique should be utilized [17]. An additional dispersion of acoustic signals due to the non-uniformity in the flow distribution in the propagation direction is then minimized by averaging. It was suggested to use the density-weighted averages with respect to the axial velocity u :

$$u(x,t)|_{RP} = \frac{\int u(x,t)\rho(x,y,z,t)dA}{\int \rho(x,y,z,t)dA} \quad (5.35)$$

where ρ stands for density and A refers to the cross-sectional area.

In most cases, the pressure is relatively uniformly distributed at both sides of the block box and is not as sensitive to the density change as to the velocity, and it may be only averaged over the cross-sectional area A . In the case of a large non-uniform pressure distribution, the density-weighted averages can be used:

$$p(t)|_{RP} = \frac{\int p(t)\rho(x,y,z,t)dA}{\int \rho(x,y,z,t)dA} \quad (5.36)$$

With regard to the reconstruction of flame transfer functions, velocity fluctuations characterize the signal and heat release fluctuations are treated as the flame response. The heat release rate from combustion chambers is integrated over the whole combustion chamber volume according to [95]:

$$Q(t)|_V = \iiint_V q(x, y, z) dV \quad (5.37)$$

where the heat release rate has $[W/m^3]$ units.

5.4.6 Acoustic variables p' and u' and normalization

To be able to use time series from CFD calculations in the identification experiment, the mean values of pressure and velocity must be subtracted from the exported time series to obtain fluctuation parts of p , u , and Q in the case of the reconstruction of flame transfer functions [50]. Using eq. (5.35), (5.36), and (5.37) one gets:

$$u'(t, x)|_{RP} = u(t, x)|_{RP} - \bar{u}|_{RP} \quad (5.38)$$

$$p'(t)|_{RP} = p(t)|_{RP} - \bar{p}|_{RP} \quad (5.39)$$

$$Q'(t)|_V = Q(t)|_V - \bar{Q}|_V \quad (5.40)$$

Here $u'|_{RP}$, $p'|_{RP}$, and $Q'|_V$ refer to the density weighted average velocity fluctuation u , the area averaged pressure fluctuation p , and the volume integrated heat release fluctuation, respectively. According to Gentemann et al. [50] the above written equations are completely reversible and a subtraction of the mean value does not cause any loss of acoustic information.

The primitive acoustic variables such as acoustic pressures p' may also be normalized to get a comparable order of the magnitude with the acoustic velocity u' . As a normalization factor, the acoustic impedance ρc can be utilized.

5.4.7 Optimal setting for numerical system identifications

The proper estimation of the length of the estimated unit impulse response L and the parameter m defining the time step for the identification process is obligatory in order to reconstruct thermo-acoustic or acoustic elements using the Wiener-Hopf equation. The accuracy of the system identification is significantly influenced by the order of the unit response filter used. In principle, an infinite number of coefficients is required to completely characterize an LTI system [47]. However, a finite number of coefficients can be handled, and a trade-off between numerical and statistical errors and errors due to inadequate resolution of the impulse response must be imposed.

Nevertheless, the main goal is to determine the optimal length of the unit impulse response, in the sense that it has the lowest possible order of L without incurring a significant loss of accuracy in the identification procedure.

5.4.7.1 Filter order L and jump factor m

The number of coefficients L of the impulse response vector, that is, the order of the response filter is an adjustable parameter in correlation analysis. Nevertheless, the large order of the response filter may lead to ill-conditioning of the auto-correlation matrix and cause the system identification procedure to fail.

As mentioned, it is not required that the increment dt of the time series used in the identification experiment is equal to the time step Δt of the CFD simulation. Therefore, the filter order L is referred to the number of coefficient of the unit impulse vector while m is used to account for the time step used in the identification process and is expressed by the relation [49]

$$dt = m \cdot \Delta t \quad (5.41)$$

The relation between L and dt value define the filter memory τ_{MEM} having the form [49]:

$$\tau_{mem} = (L-1)dt \quad (5.42)$$

Taking into account the so-called the jump factor m from (5.43) and the filter order can be used to reduce. The auto-correlation matrix and cross-correlation vector derived in Section 5.3 can be rewritten as follows [50]:

$$\Gamma_{ij} = \frac{1}{N - mL + 1} \sum_{k=mL-1}^{N-1} s(k - mi)s(k - mj) \text{ for } i,j=0,1,2,\dots,L-1 \quad (5.43)$$

$$c_i = \frac{1}{N - mL + 1} \sum_{k=mL-1}^{N-1} r(k)s(k - mi) \text{ for } i=0,1,2,\dots,L-1 \quad (5.44)$$

To study the importance of L parameter, let us consider Fig. 5.5 where the element T_{11} of the acoustic transfer matrix for a sudden change of dimensions is shown. This test-case will be analyzed in more detail in the subsequent chapter. The model is computed using CFD/SI with white noise excitation. The time step chosen for that simulation is $2.5 \cdot 10^{-5}$ s. For room temperature, speed of sound is of 340 m/s and the distance between the reference planes is defined to be 0.1m. The element is identified by the traveling acoustic waves with the characteristic time lag corresponding to the filter memory between reference planes which is about $3 \cdot 10^{-4}$ s.

For simplicity, it is assumed that the time step from CFD is equal the time step used in the identification procedure. Using eq. (5.42) and $L=10$ ($m=1$), the characteristic time delay is computed to be of $2.25 \cdot 10^{-4}$ s. The chosen L is not sufficiently large to properly perform the system identification. The L value being too small is clearly shown in the estimated absolute value. Whereas, for $L=20$ the necessary condition for the filter order is fulfilled and the reconstructed element matches reasonably well with the theoretical solution.

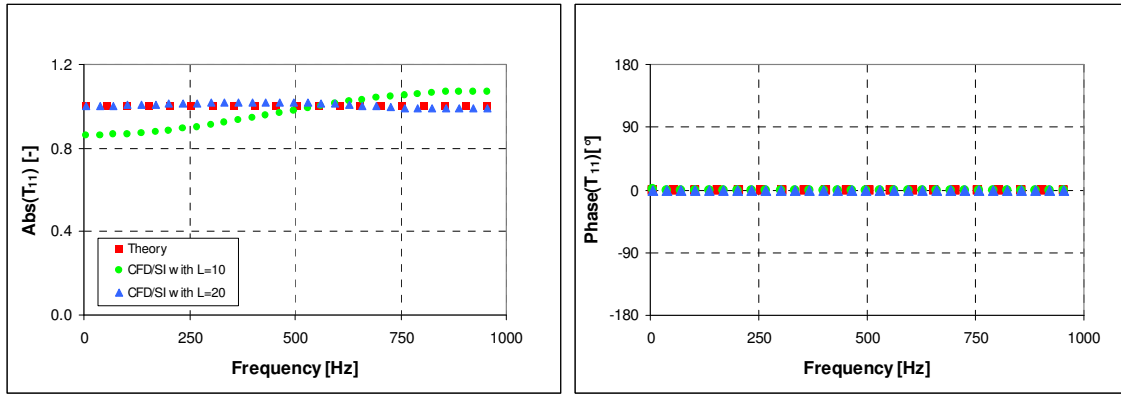


Fig. 5.5 Acoustic transfer matrix of a sudden change of dimensions for the transfer matrix element T_{11} : analytical solution (red rectangular) and CFD/SI for different length of L : $L=10$ (green circle) and $L=20$ (blue triangle)

The correlation between L , m and τ_{mem} for a representative time series is illustrated in Fig. 5.6. The time series starts at 0 and is characterized by the time step Δt from the CFD computation. Two different filters i.e. $L=6$ with $m=1$ and $L=3$ with $m=2$ are shown relative to the time axis. Employing eq. (5.42) one gets the maximum of the filter memory τ_{MEM}

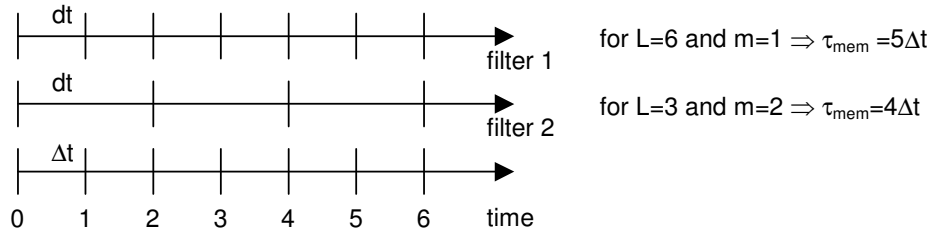


Fig. 5.6 Correlation between L , m and τ_{mem} for a given filter [50]

Three main conditions must be fulfilled for the identification procedure to be properly performed. These conditions can be summarized according to the study from [50] such as:

- The time step Δt of CFD computations must be smaller than the minimal time lag τ_{min} of the element.
- The filter memory τ_{mem} must be bigger than the maximum time lag of the element. However, in the case of $\tau_{mem} < \tau_{max}$, the time delay of the element cannot be correctly considered. The identification error for the unit impulse response increases drastically for the smaller values of τ_{mem} .
- On the other hand, the filter memory τ_{mem} cannot be much bigger than the maximum time lag τ_{max} of the element. In the case of $\tau_{mem} \gg \tau_{max}$ the identification error for the unit impulse response increases due to numerical inaccuracy (inversion of a large matrix). The parameter L needs to be set up to achieve a τ_{max} larger but still close to the time lag of the black box.

5.4.7.2 Sampling and frequency increment

Acoustic transfer matrices or flame transfer functions of a given thermo-acoustic element can be reconstructed by using the z-transformation of the unit impulse vector. The maximum frequency of interest is limited by eq. (5.41) and it follows that for a given sampling interval dt , the maximum frequency to be considered is defined by the well-known Nyquist criterion [51]:

$$f_{\max} = \frac{1}{2dt} \quad (5.45)$$

The condition for the maximum jump factor follows from the definition of the maximum frequency of interest and has the form [50]:

$$m_{\max} = \frac{1}{2f_{\max,chosen} \Delta t} \quad (5.46)$$

where $f_{\max,chosen}$ defines the maximum frequency of interest for the identification process. The sample length N , that is, the duration of the transient simulation determines in the combination with the sampling increment dt the sampling frequency or frequency resolution:

$$\Delta f = \frac{1}{Ndt} \quad (5.47)$$

The sampling frequency represents effectively a lower frequency limit $f_{\min} = \Delta f$ and the evaluation of the frequency response is limited to frequencies $f_{\min} < \Delta f$.

5.4.7.3 First approximation for a value of L

It was shown in the previous sections that the filter order L must be chosen such that the memory τ_{mem} of the filter is not smaller and not much bigger than any relevant time-lag of the “black box” that has to be identified. For plane wave propagation, the relevant time lag τ can be easily estimated by considering the time required for a sound wave to travel between the reference planes located downstream “d” and upstream “u” and can be approximated by:

$$\tau_{mem,opt} \approx \frac{\Delta x}{u} \quad (5.48)$$

where Δx refers to the axial distance between the reference planes and u is defined as the axial velocity. For acoustic elements in which the propagation speed is dominated by the speed of sound, the velocity u is equal to the speed of sound c .

On the other hand, in the case of the flame transfer function induced by equivalence ratio fluctuations the propagation velocity is mostly dominated by the convective speed u .

An expression for the estimate of L and m is obtained by making use of Eq.(5.42)

$$L \cdot m \approx \frac{\Delta x}{u \Delta t} \quad (5.49)$$

where m can differ between one and m_{max} according to eq. (5.46). Experience has shown that utilizing $m=1$ provides an acceptable approximation.

5.4.7.4 Optimal settings for L and m

In general, to carry out the reconstruction of transfer matrices or flame transfer functions correctly, the necessary conditions specified in Section 5.4.7.1 must be fulfilled first. Then, using eq. (5.49) and assuming $m=1$, one can provide a first guess $L_{opt,guess}$ to find the optimal value of L_{opt} . Subsequently, a range of values L_{guess} can be utilized to conduct a parameter variation of L according to [50]:

$$L_{guess,i} = 0.5L_{guess} \dots 2L_{guess} \text{ for } i = 1 \dots n \quad (5.50)$$

The performed parameter variation leads to the series of n -transfer functions calculated with respect to various values for L . To find the optimum value of L , the least square error between the transfer function based on the value of $L_{opt,guess}$ and the other transfer functions is estimated using [43]:

$$\bar{\Delta}(L_{guess,i}) = \sum_f \frac{(T(f, L_{guess,i}) - T(f)_{opt,guess})^2}{(T(f)_{opt,guess})^2} \quad (5.51)$$

It is found that too small values for L result in much higher numerical errors than for $L \gg L_{opt}$. This is expected and agrees with results by Ljung et al. [53]. For L being too small, the time lag of the systems exceeds the memory of the filter. Then, the filter becomes a poor representation of the black box. If L is too large, noise reduction of the filter becomes smaller and numerical errors become dominant because of the inversion of large autocorrelation matrices. This can be exploited if the functional behavior of the error is known. Fig. 5.7 shows the mean square variation between all chosen values of L and a guess value $L_{opt,guess}$. In this case, the identification procedure has been carried out to reconstruct the flame transfer function a prototype burner, which will be studied in the following sections.

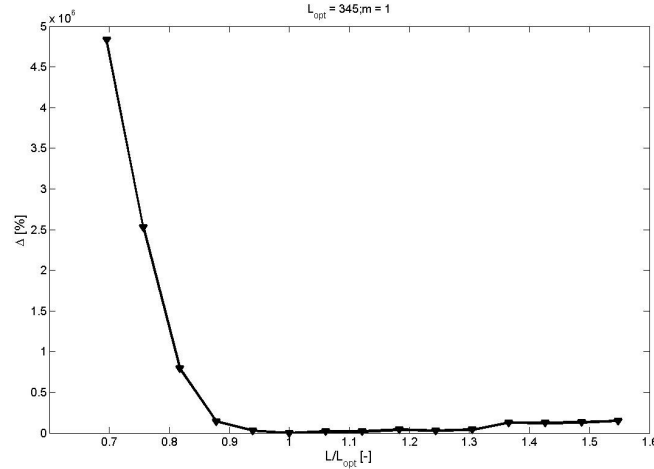


Fig. 5.7 The least square error as a function of L for a prototype burner

It should be noted that up to this point $m=1$ was utilized. To find the optimum value of the jump factor m_{opt} , the relative quadratic difference of the transfer function for the variation of m has to be estimated. By analogy to the definition of L interval, $m_{guess,i}$ can be formulated as [50]:

$$m_{guess,i} = 1 \dots \frac{1}{2 f_{max,chosen} \Delta t} \text{ for } i = 1 \dots n \quad (5.52)$$

where $f_{max,chosen}$ is the maximum frequency of interest. When the optimum value L_{opt} for $m=1$ is known, the relative quadratic difference for $m>1$ is rewritten to [50]:

$$\bar{\Delta}(m_{guess,i}) = \sum_f \frac{(T(f, L_{opt}, m_{guess,i}) - T(f, L_{opt}, m=1))^2}{(T(f, L_{opt}, m=1))^2} \quad (5.53)$$

To keep the memory of the filter τ_{mem} constant, the value of L_{opt} for $m>1$ must be fitted according to the jump factor m

$$L_{opt,m>1} \approx \frac{L_{opt,m=1}}{m} \quad (5.54)$$

The Relative quadratic difference of the element T_{11} from the acoustic transfer matrix of the truncated teardrop is depicted In Fig. 5.8. This test case is investigated in more detail in chapter 0. It is also noticeable that the shapes of relative errors are similar up to $m=6$. After this point, the curve shapes start strongly deviating from each other. In this case the optimum length of L was determined to be 65 and the optimum jump factor is found for $m=6$.

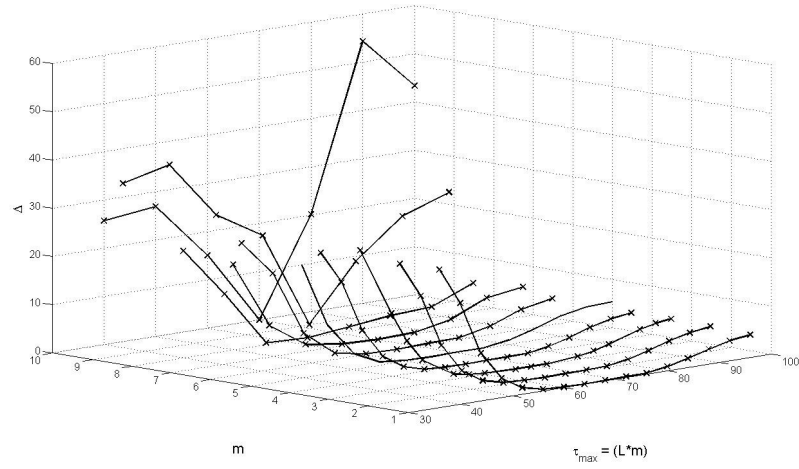


Fig. 5.8 Relative quadratic difference of the transfer matrix element T_{11} of the truncated teardrop for a variation of m values

6 Duct with a sudden change of dimensions

Knowledge of acoustic properties of particular elements, which are used in 1D codes, is very important when analyzing acoustic systems especially in terms of their stability. Description of these elements is often simplified to a modeling of complex geometries as a network of acoustic elements. As mentioned before, their transfer matrices, which describe the transmission of acoustic variables as a function of frequency.

Ducts with a sudden change of dimensions are commonly used in thermo-acoustic designs, e.g. in combustion chambers, burners or exhaust pipes. To properly model acoustic systems involving such elements, it is necessary to know the transfer matrix of this element.

Fig. 6.1 shows the sketch of the considered geometry and a distribution of acoustic waves propagating within the geometry. It is easy to notice that the shape of the propagating plane wave is changed due to the sudden area contraction.

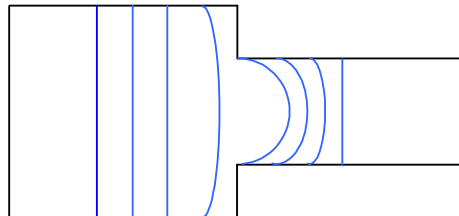


Fig. 6.1 Geometry of a sudden change of dimensions [50]

The sudden change of cross sectional area is utilized as a test case for the CFD-based estimation method. The CFD/SI approach to reconstruct acoustic transfer matrices is then compared with experimental data, finite element calculations and an analytical model. Additionally, the sensitivity study on time, spatial resolution and time scheme is performed and interpreted in more detail.

6.1 Analytical model for a sudden change of dimension

The mass conservation and momentum equations must be used to derive an analytical description for this acoustic element. If an acoustic wavelength is larger than the length of this element L , it can be written that $kL = L\omega/c < 1$ and this element can be treated as an acoustically compact element. It should be kept in mind that a transfer matrix is being determined for low Mach number flows.

As shown by Gentemann et al. [17] using some mathematical simplifications and doing same algebraic transformations the equations describing the compact acoustic element can be written:

$$\left[A \left(\frac{p'}{\rho c} M + u' \right) \right]_u^d + i \frac{\omega}{c} l_{red} A_d \frac{p'_u}{\rho c} = 0 \quad (6.1)$$

$$\left[\left(\frac{p'}{\rho c} + M u' \right) \right]_u^d + i \frac{\omega}{c} l_{eff} u'_u + \zeta M_u u'_u = 0 \quad (6.2)$$

The above written equations can easily be transformed into the transfer matrix form. Neglecting all 2nd order quantities for low Mach numbers, one gets the following acoustic transfer matrix:

$$\mathbf{T} = \begin{pmatrix} 1 & \left[1 - \zeta - \left(\frac{A_u}{A_d} \right)^2 \right]_u^d M_u - i \frac{\omega}{c} l_{eff} \\ -i \frac{\omega}{c} l_{red} - M_d & \frac{A_u}{A_d} \end{pmatrix} \quad (6.3)$$

where l_{red} denotes the capacitance effect, l_{eff} stands for the effective length and the acoustic losses over the element are represented by ζ .

6.2 CFD coupled with System Identification (CFD/SI)

As it is already described in Section 5.4, the reconstruction of acoustic transfer matrices is based on the combination of CFD and an acoustic postprocessor. The unsteady forced CFD calculation is employed to provide the time series of velocity and pressure, which are then statistically correlated in the acoustic postprocessor [17]. The setup for a CFD calculation in the generalized form is shown in Fig. 6.2. BC stands for the boundary conditions in the computational domain. As depicted below, the main flow enters the model on the left hand side and leaves the computational domain after a sudden acceleration due to the area contraction on the right hand side.

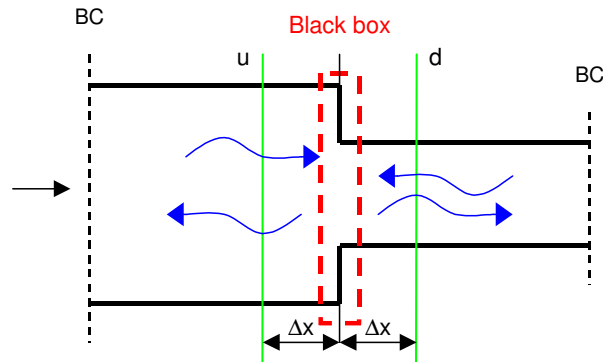


Fig. 6.2 Acoustic element represented by the generalized CFD setup

The steady flow field needs to be obtained first. Next, the steady state computation is acoustically forced on both CFD boundaries by addition of the fluctuating component of velocity and pressure. It results in acoustic waves traveling through the “black box” represented here by the acoustic transfer matrix to be reconstructed. Once the waves reach the boundaries, they are partially reflected and transmitted. Due to a very low Mach numbers, all unsteady computations in this study have been performed with standard CFD boundary conditions. At the location indicated by u (upstream) and d (downstream) of the acoustic element, time series of velocity and pressure are exported to extract the acoustic waves. The axial distance between the reference planes is defined as Δx . The external acoustic postprocessor developed by Polifke et al. [47] is then utilized to perform the correlation analysis and to reconstruct the acoustic transfer matrix of the duct with a sudden change of dimension.

6.2.1 Boundary conditions and CFD model

The CFD model is assumed to be a 2D case and is axisymmetric. The grid consists of 12000 hexahedral elements, which is sufficient to resolve a relatively simple flow. The inlet circular diameter D_1 is contracted from 0.2 m to D_2 , which is equal to 0.104 m at the outlet of the model and the total length of the geometry is 0.8 m. The considered CFD domain is sketched in Fig. 6.3.

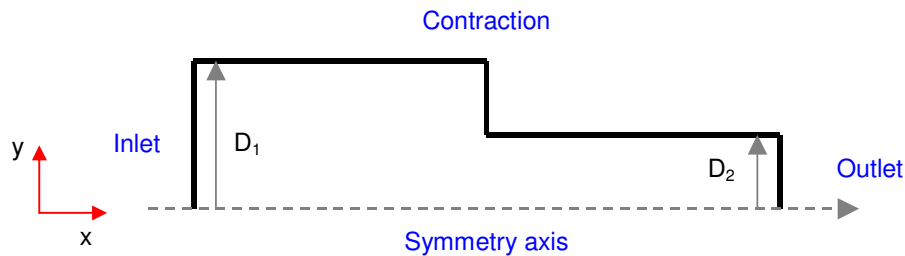


Fig. 6.3 Simplified CFD model of a sudden change of dimensions

At the inlet the normal velocity of 0.7 m/s and the static temperature of 293 K are applied. The outlet is set to simulate the average pressure of 1 atm. Both the steady and the transient flow fields are calculated with commercial package ANSYS CFX 10.0 [13].

Fluid Model	Ideal Gas Law
Turbulence Model	k- ϵ
Advection Scheme	High Resolution
Heat Transfer Model	Total Energy
Transient Scheme	Second order Euler
Time step	2.5e-5 s
Number of Time steps	10000

Tab. 6.1 Numerical models – duct with a sudden change of dimensions

The unsteady computation is calculated using standard CFD boundary conditions. Numerical models, which are used for steady and transient calculations are summarized in Tab. 6.1

The perturbation magnitudes at the inlet and the outlet are equal to 10 % of the mean axial velocity and static pressure. Due to lack of acoustically properly defined acoustic boundary conditions, the standard CFD boundary conditions are used. These types of boundary conditions in terms of acoustic waves behave as an acoustically reflective boundary. The velocity can represent an acoustically rigid wall and static pressure and an acoustically open boundary condition. To force the entire system the white noise excitation is applied. This kind of excitation signal has a great benefit compared to the other excitation (forcing) techniques. This technique is capable of distributing uniformly excitations in time domain and can give a good quality of analyzed signals.

Following up Gentemann and Polifke et al. [17], the time step size of 25 microseconds and maximum number of time steps of 10000 have been chosen for the transient computation. The interesting frequency range $[f_{\min}, f_{\max}]$, which is utilized in correlation analysis are determined by the sampling frequency f_s and the sample length $N\Delta t$. According to Eq. (5.45) and (5.47) the frequency range is bounded between 4 Hz and 20000 Hz.

6.2.2 Steady state solution

Fig. 6.4a shows the contour plot of axial velocity taken at the central plane ($z = 0$ m). It is easy to notice that the flow gradually accelerates and achieves the maximum local axial velocity at the position where the contractions of the duct takes place, i.e. at 0.4 m. Due to the strong acceleration, a small region with negative axial velocity has occurred and a recirculation zone has been formed. It is also well seen that the axial velocity is not uniformly distributed along the y -axis what is mainly caused by the contraction. In this case, it is necessary to use some averaging techniques introduced before to consider the axial velocity fluctuations at this position. Doing so, the extracted and area averaged axial velocity fluctuations can be directly used to reconstruct the acoustic transfer matrix of this element.

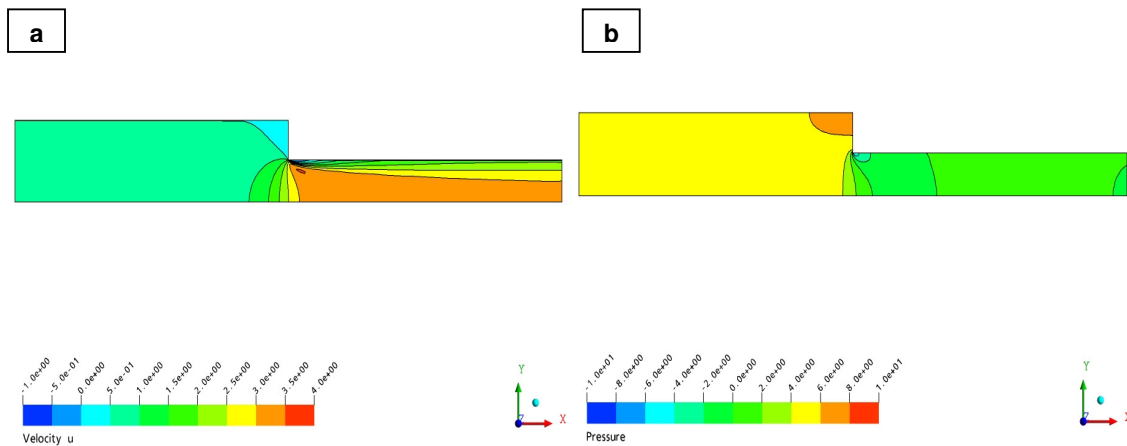


Fig. 6.4 Local axial velocity and pressure distributions

The averaged axial velocity at 0.4 m is approximated equal to the cross-sectional area ratio between two considered parts of the CFD model. It is the well-known behavior of the velocity and can be explained using the continuity equation for steady state flows in ducts. The location of the maximum velocity can then be checked looking at the pressure distribution at the same plane. It is expected to get the minimum static pressure at the location of the maximum local axial velocity. On the other hand, the static pressure at the central plane $z=0$ m is shown in Fig. 6.4b. The position of the minimum static pressure well corresponds to the position where the maximum velocity is found.

6.3 Validation of CFD/SI with Measurements, FEM and Analytical Model

The System Identification (SI) introduced in Section 5.4 is used to estimate the acoustic transfer matrix for the pipe with a sudden change of area at relatively low Mach number. After performing the steady state computation, the white noise excitation has been applied to force the entire system at both boundaries. During the transient run the time series of pressure and velocity are reordered and exported to be used in correlation analysis. As suggested in [17] the non-causal filter is chosen and the notation for primitive acoustic variables p' and u' is utilized. The influence of the axial distance between the reference planes, at which transient data are taken, on the CFD/SI approach is investigated by Gentemann et al. [50]. Following the numerical findings, the distance of 0.1 m is found to be the optimum value and should be taken. In addition to this, Gentemann has investigated the number of time steps for reconstructing acoustic transfer matrices with some care. It has been found that the number of time steps lower than 3000 affected the acoustic transfer quality with respect to the amplitude and phase. In the current investigation, the number of time steps of 10000 is chosen and therefore no negative influence from this factor is expected to occur. Moreover, for the current configuration the Identification experiment is done for the L parameter of 12 and $m=1$ and the first estimation of L is based on the relation (5.49). The estimated transfer matrix is compared with the analytical model, measurements and FEM calculations, which can be found in [17].

By definition, using the two-microphone method, it is possible to calculate acoustic pressure and velocity at a reference position. Moreover, using setups consisting of two microphones located up- and downstream, one is capable of evaluating any acoustic transfer matrix. However, some experiments show that this method is very sensitive to errors introduced by mean flows and the fact that these microphones may be located very close to the pressure node [121]. For this reason, the acoustic measurement can be based on the extended multi-microphones method proposed by Paschereit et al. [72]. By increasing the number of microphones, the stability of the proposed method and its accuracy can be improved.

The second approach used to validate the CFD/SI method is FEM. The finite element method is utilized to resolve the pressure field in the computational domain. The FEM computation can be seen as the computational equivalent of the multi-microphone method in the frequency domain [73]. By solving the Helmholtz equation, any consideration of mean flow and turbulence effects is excluded.

It could be neglected because of the low Mach number flow. By analogy to the multi-microphones measurement approach, the pressure signal is recorded at two locations upstream and downstream of the acoustic element of interest and the transfer matrix of a connection element is known. Knowing the acoustic pressure, the acoustic velocity can be simple calculated. Fig. 6.5 and Fig. 6.6 show the normalized amplitude and phase for all four acoustic transfers matrix elements in the primitive acoustic variable p' and u' notation. Moreover, the magnitude of the reconstructed elements is normalized by the characteristic impedance. The reconstructed transfer matrix is compared to the theoretical model, FEM calculations and measurements. The considered frequency interval is from about 5 to 1000 Hz.

The coefficient T_{11} defines the ratio between the acoustic pressure upstream and downstream of the reconstructed element. It is noticeable that all amplitudes excluding some small deviation at ~ 100 Hz and ~ 900 Hz correspond well to the acoustic theory, FEM results and measurements. The same tendency can be observed in terms of the reconstructed acoustic phase. The phase agrees well with all data series over the considered frequency range. There are small deviations ~ 150 Hz found what could be directly associated with the measurement uncertainties. In this frequency range, the siren is not able to provide the constant excitation amplitude and does not operate properly.

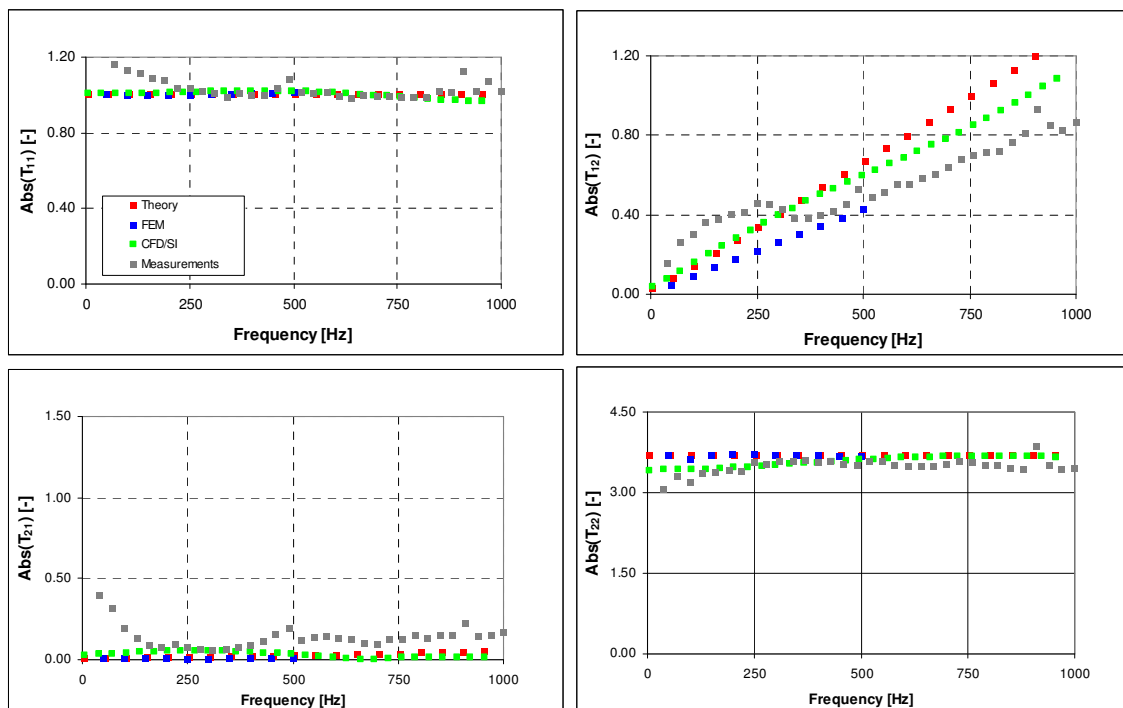


Fig. 6.5 Acoustic Transfer Matrix: Normalized Amplitude: red rectangular – analytical model, blue rectangular – FEM, grey rectangular – measurements, green rectangular – CFD/SI

The coefficient T_{12} represents the relation between the acoustic pressure after the analyzed area expansion to the acoustic velocity before the considered element. The CFD/SI based values are in a good agreement with the analytical model up to 250 Hz. The FEM solution and with the experimental data above ~ 250 Hz show the smaller phase gradient and the largest deviations are observed above ~ 500 Hz where some simplifications of the analytical model used do not hold anymore.

Furthermore, some mismatch regarding the experiments is found at lower frequencies. The CFD/SI method shows a good fit to the analytical model in the whole frequency range. All computational methods predict the correct trend but do not fit the results completely. Examining the reconstructed phase, one sees almost perfect agreement in the entire frequency range for all methods applied. The phase below the frequency value of 250 Hz is slightly over-predicted by the measurement data.

The element T_{21} of the estimated acoustic transfer matrix connects the velocity upstream of the acoustic element with the pressure downstream. It is well seen that in the case of the calculated absolute values all computational approaches agree well except for the experimental results, which strongly deviate below 100 Hz. A possible explanation could be the power of excitation signals provided during the experiment. It looks like that in the frequency range the siren used is not able to force the system with the same excitation amplitude. On the other hand, the largest disagreement between the CFD/SI and the other approaches is seen for the calculated phase. The phase angles of the transfer matrix slightly differ from each other for all four results. The phase calculated based on the analytical model changes from π to $\pi/2$. The FEM solution locates between $-\pi/2$ and $\pi/2$, whereas the CFD/SI result increasing from $-\pi/2$ to a value $\pi/2$ after a large frequency range. The phase jump can be caused by the absolute value approaching zero in this frequency range. Moreover, for frequencies bigger that 250 Hz the measurements and analytical model and FEM solution agree.

Using the acoustic transfer matrix coefficient T_{22} the relation between the velocity downstream and upstream of the element with a sudden change of dimension is characterized. The amplitude value is defined by the contraction ratio and apart from small deviation below 250 Hz are reasonable captured. The phases of four data series without any exceptions show the perfect agreement.

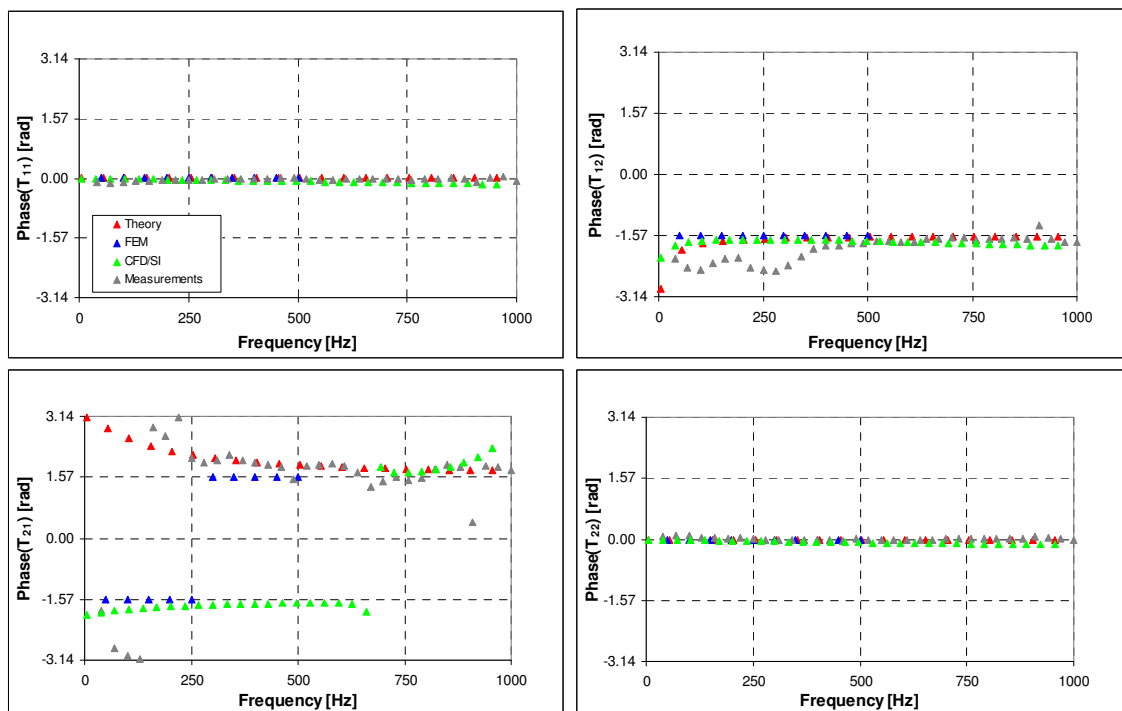


Fig. 6.6 Acoustic Transfer Matrix: Phase: red triangle – theory, blue triangle – FEM, grey triangle measurements, green triangle – CFD/SI

6.4 Optimal values of L and m for CFD/SI

To optimize the length of the impulse response L and m used in the Wiener Hopf equation, it was necessary to run the optimization module from the acoustic postprocessor. Using the relative quadratic difference of the element T_{11} from Section 5.4.7 enabled to find the optimum value of L and m . The relation (5.42) is reliable and can be utilized to compute a first guess of L corresponding to the filter memory. As a first guess, the value $L=12$ is and $m=1$ were employed, giving already satisfactory results. Having this in mind, it was found that the value of $L=17$ is the current optimum. Nevertheless, the difference between the guessed and optimum value are very small. As shown in Fig. 6.7, the values of m bigger one result in the small deviation in the relative quadratic difference and can be used in the system identification.

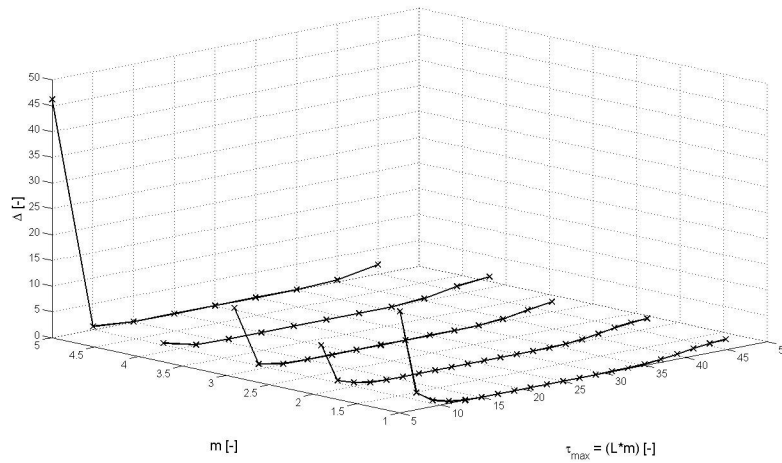


Fig. 6.7 The Relative quadratic difference of the element T_{11} as a function of L and m

In general, the value of m ranging from 1 to 4 can be employed in the system identification method and are capable of giving reasonable results. The largest relative error is found for $m > 4$.

6.5 Sensitivity study

The main purpose of this sensitivity study is to show whether the CFD/SI approach is sensitive to any changes in space and time discretisation or time scheme. Theoretically, any changes in these parameters may affect an application of the unsteady CFD computation combined with system identification and cause a wrong interpretation of the numerical results.

6.5.1 Spatial discretization dx

There is no study in the literature showing the influence of the computational grid on acoustics calculated by means of URANS. Therefore, different mesh densities are used to check whether

the space discretization dx could considerably affect the propagation of acoustic waves and the reconstruction of acoustic transfer matrices. Three different computational meshes consisted of 11000, 23000, and 41000 nodes are utilized to carry out all unsteady RANS computations. 11000 is used in the baseline. Using these meshes it is possible to mimic an abrupt change of the number of grid points per one wavelength. Moreover, the CFL condition could be varied and the influence on CFD/SI could be studied.

To separate the influence from other numerically significant parameters when performing URANS, the time step size of $2.5e-5$ s and the other numerical models including boundary condition are not varied. It might be felt intuitively that not sufficient number of grid points in the computational domain might affect the acoustic wave propagation. By definition, using a very coarse grid (less than 20 points per wavelength), one is not able to correctly resolve the entire flow field including pressure and velocity distributions (the CFL criterion cannot be correctly fulfilled). In this case, the higher numerical wave dissipation and dispersion may directly affect the propagation of acoustic waves. In addition to this, the pressure amplitude and axial wave distribution may be strongly deteriorated. Therefore, a very weak correlation between acoustical signals downstream and upstream of a given element can be expected.

However, this is rather not the case here. Using the coarsest mesh and defining the highest frequency of interest to be 1000 Hz, one gets about 105 supporting points per one wavelength. This number of grid points seems not to be adequate to change the acoustic wave propagation. It is clearly proved analyzing the reconstructed acoustic transfer matrix elements.

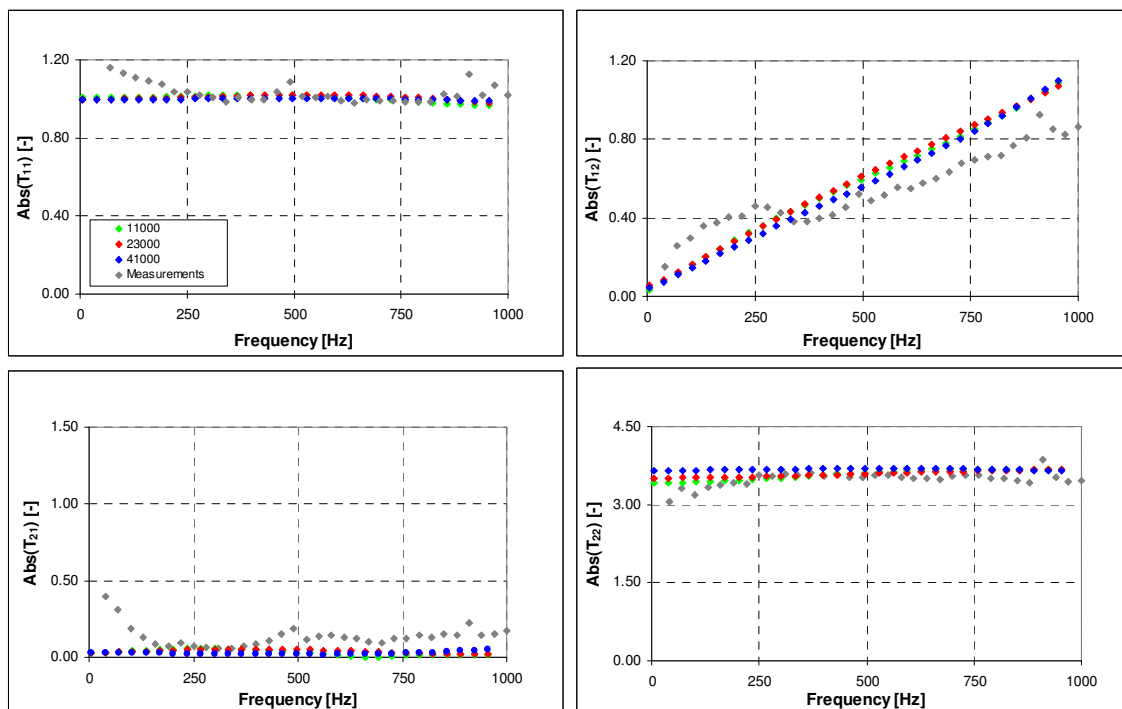


Fig. 6.8 Spatial discretization dx variations: Normalized amplitude: green diamond – 11000 nodes, red diamond – 23000 nodes, yellow diamond 41000, grey diamond – measurements

Fig. 6.8 shows the reconstructed acoustic transfer matrix of a sudden change of dimension for the different mesh sizes with comparison to the experimental data. Evaluating the amplitude, almost perfect agreement between the different meshes is found. There are small discrepancies shown. Especially in the element T_{12} and T_{22} the amplitudes differ slightly from each other. In general, one can draw the conclusion that the space resolution dx in this test case has hardly any influence on the reconstruction of the acoustic amplitude and the coarsest mesh seems already to be adequate for the reconstruction of this transfer matrix.

Analyzing the phases in Fig. 6.9, one can draw a very similar conclusion as in the case of the predicted amplitude. There are some small inconsistencies in the predicted phase of T_{21} . The magnitude of this element is located very close to zero. This very small value could be responsible for this jump about 2π in the calculated phase. In general, it looks like that there are almost no deviations between all different mesh densities over the whole frequency range. All reconstructed phases are nicely overlapped by each other.

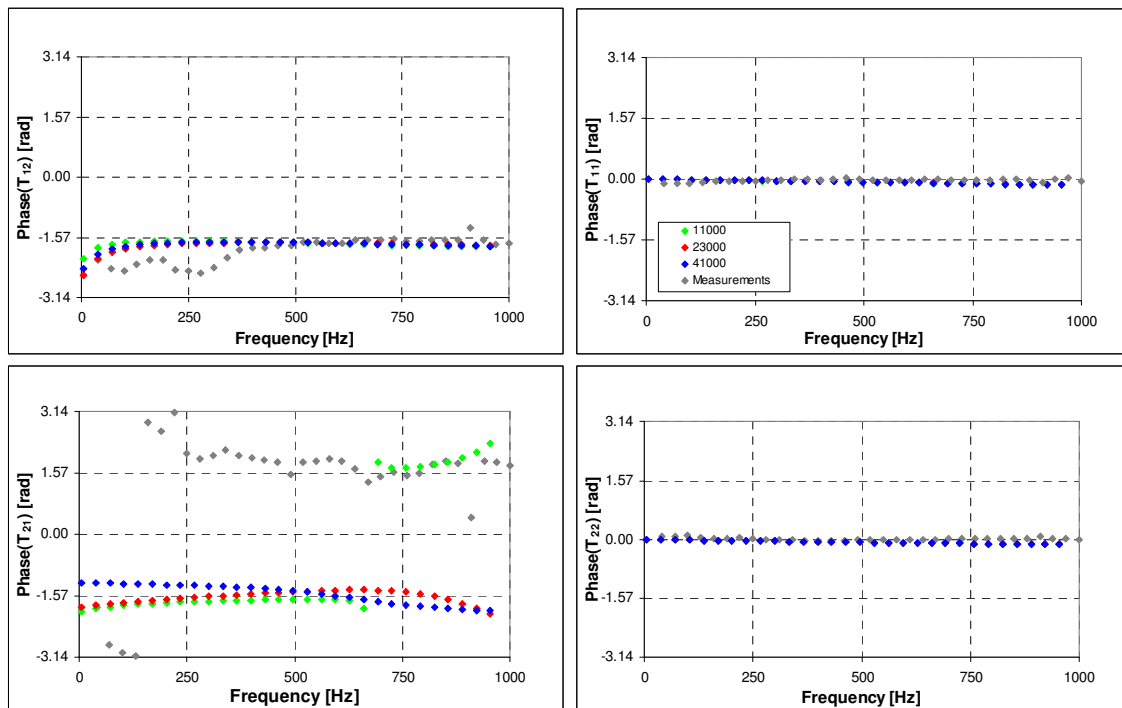


Fig. 6.9 Spatial discretization dx variations: Phase: green diamond – 11000 nodes, red diamond – 23000 nodes, yellow diamond 41000, grey diamond – measurements

6.5.2 Time discretization dt

Time discretization becomes a very important issue while utilizing the CFD/SI approach based on unsteady computations. To better understand the importance of time resolution dt in the system identification, let us consider the case with a sudden change of dimensions with two different time steps. The reference acoustic transfer matrix is estimated using the time step $2.5e-5$ s and is compared to the acoustic transfer matrix reconstructed with $dt = 5e-5$ s. The other numerical parameters and the mesh size in these runs are kept unchanged.

It is known that there are some differences between the exact solution of the considered differential equations, and the fully converged solution of their discrete representations. These differences are referred to discretization errors. Generally speaking, the discretization error is caused by some truncation errors introduced by using the Taylor series expansion. These truncation errors indicate how well the discrete representation of a given differential equation can be represented in the time domain. Large truncation errors can introduce a very high numerical dispersion and damping. The influence of the number of time steps on the relative truncation error has been deeply investigated by Van Kampen et al. [24]. It has been found that utilizing an explicit second order time discretisation over 40 time steps per one period must be used get the relative error of 1% in the time derivative. It has been suggested to keep the number of time steps N about 40 to represent the variations in time space. According to the error analysis made by Van Kampen, the relative error in the time derivative and absolute value for a given number of time steps has the distribution shown in Fig. 6.10

If one assumes that the maximum frequency of interest in both test cases is 1000 Hz. Thus, in the first test case (keeping in mind the relative error in the time derivative of 1%) using the time steps size of 2.5×10^{-5} s yields to the number of time step of 40. Since, the second time step size is $dt=5 \times 10^{-5}$ s, one gets only $N=20$. Referring to the distribution of the relative error, it can be found that for the second test case, the relative error is in the order of 5% when looking at the frequency about 1000 Hz.

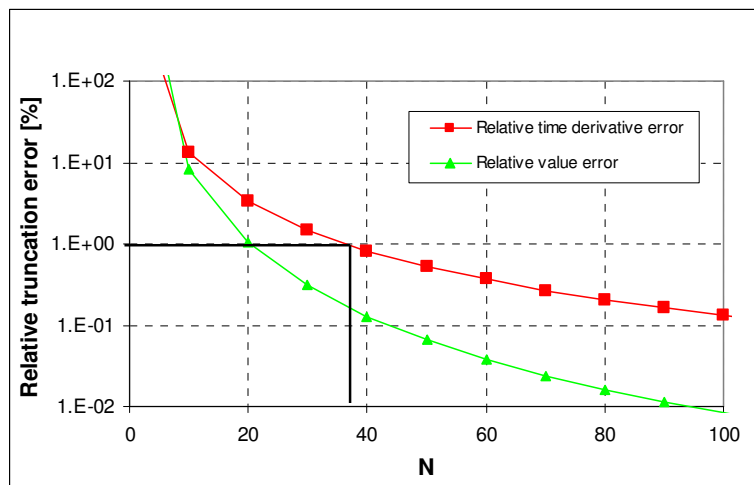


Fig. 6.10 Relative truncation errors as a function of number of time steps N [24]: red rectangular – relative time derivative error, green triangle – relative absolute error

Referring to the error analysis one should expect to find out some deviations between the reconstructed amplitudes at higher frequencies located close to the maximum frequency of interest. The calculated amplitudes of the acoustic transfer matrices are shown in Fig. 6.5. Indeed, there are some very small differences found close to 1000 Hz especially for T_{22} . In reality, these kinds of inconsistencies can be neglected. The reason for this kind of unexpected results is that the maximum frequency of interest is only 1000 Hz. At this frequency, the relative truncation error in the order of 5% is expected.

Extending to higher frequencies may show the relevance of this analysis and clearly illustrate the influence on the system identification. For example, at 1500 Hz and employing the time step $dt=5e-5s$ one gets only $N=13$ and the relative truncation error in the order of 13%.

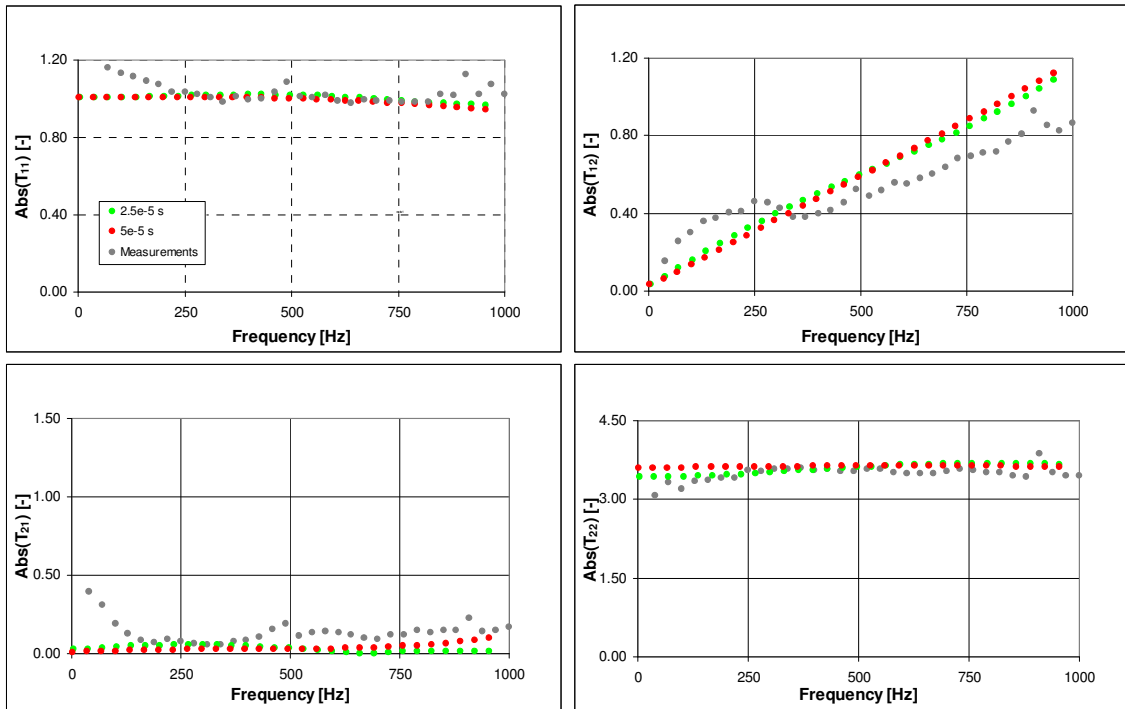


Fig. 6.11 Time discretization dt variations: Normalized Amplitude: green circle – $dt=2.5e-5s$, red circle $dt=5e-5s$, grey circle – measurements

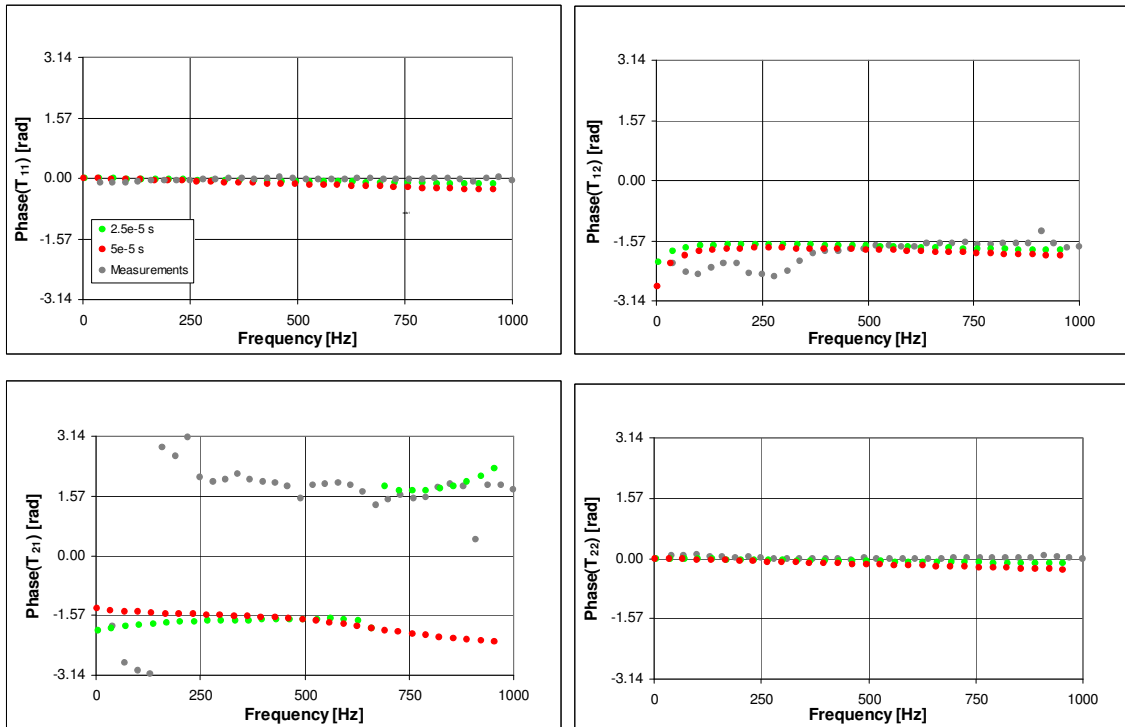


Fig. 6.12 Time discretization dt variations: Phase: green diamond – $dt=2.5e-5s$, red diamond $dt=5e-5s$, grey triangle – measurements

Fig. 6.12 depicts the reconstructed phases. The detailed investigation of four transfer matrix coefficients provides a clear picture that the time step may affect the results based on the CFD/SI approach. As mentioned earlier, at frequency higher than 1000 Hz these differences may be even more pronounced. As expected, in the case of phase, the deviations are more distinct between the different time step sizes. This is visible at higher frequencies. The larger discrepancies from the results obtained with $dt=5e-5$ s are in the phase distribution in the element T_{21} . The strong deviation starting at frequency ~ 600 Hz is observed

6.5.3 Time scheme variations

As already shown, using larger time step size may further lead to some inaccuracies in the identification of acoustic transfer matrices. Therefore, in transient simulations, the implicit second order Euler time discretization scheme is often used. With the first order backward Euler scheme, the start and end of time step values are respectively approximated using the values of the old and current time level solution. It is robust, fully implicit, bounded, conservative in time, and does not have a timestep size limitation. Similar to the first order backward Euler scheme, the implicit second order Euler time discretization scheme is also robust, implicit, conservative in time, and does not have a time step size limitation. However, it is second-order accurate in time, but is not bounded and may create some nonphysical solution oscillations. More details in terms of the time discretisation schemes used in these simulations are given in Appendix 0.

Now, let us employ the first order backward Euler scheme to derive the acoustic transfer matrix and compare to the reference test case reconstructed with the second order Euler. The reconstruction of the acoustic transfer matrices of a sudden change of dimensions are performed with $dt=0.25e-5$ s. The computational mesh is the same in both cases.

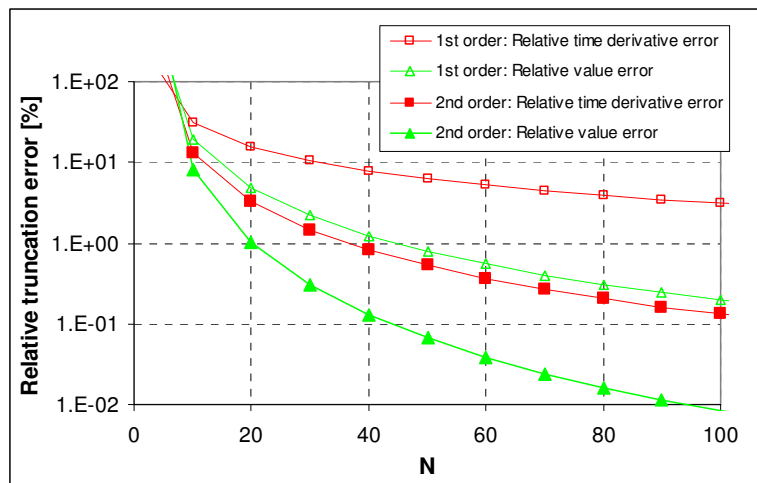


Fig. 6.13 First and second order truncation errors order as a function of number of time steps N: not filled red rectangular – 1st order, filled red rectangular – 2nd order

The influence from the relative truncation error on the identification of the acoustic transfer matrices, which has been studied in pervious section, is now extended to the first order Euler scheme.

Following the derivation made in [24] it is possible to extend the truncation error analysis to the first order Euler scheme. Fig. 6.13 shows the relative truncation errors as a function of the number of time steps for the first and second order schemes. Referring to the previous section, it is assumed that for $N=40$ one can expect that the relative truncation error in the time derivative drops down to about 1%. In the case of the first order Euler scheme to be able to go down to the same error order one needs to use about 150 time steps per one period.

Unfortunately, this relative time derivative error is only inversely proportional to the number of time steps and has an extremely flat distribution compared to the relative time derivative from the second order scheme. In the case of the first order Euler scheme, keeping the same number of time steps $N=40$ one should expect a strong numerical dissipation due to not sufficient number of points in the time dome. As the consequence of this investigation, the first order Euler scheme can be used to do some preliminary studies. However, final computations should be performed based on the second order scheme.

As could be expected, the amplitudes of the derived acoustic transfer matrices strongly deviate for higher frequencies. The amplitudes for both time schemes are depicted in Fig. 6.14. The larger discrepancies compared to the reference test case and measurements are found in the matrix element T_{21} . The differences between the reference amplitude and the amplitude estimated based on the first order at ~ 500 Hz start strong diverging from each other. Beside of this, there are also small variations observed for the remaining elements especially for the element T_{12} .

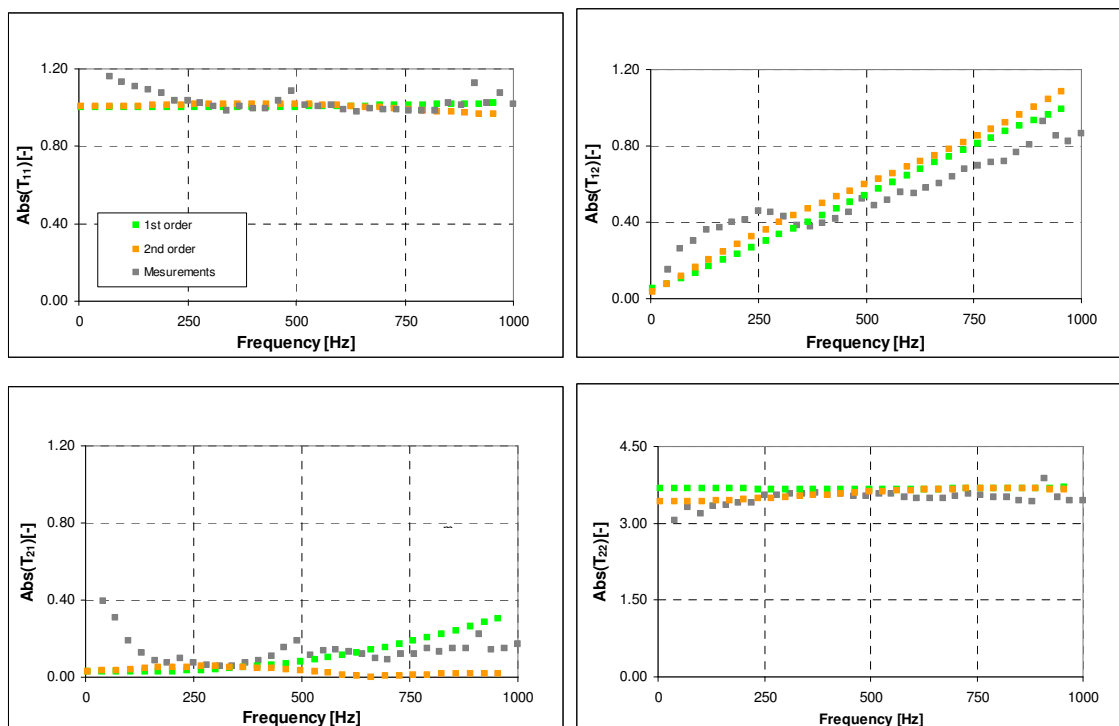


Fig. 6.14 Time scheme variations: Normalized Absolute value: green rectangular – 1st order, orange rectangular – 2nd order, grey rectangular – measurements

The phases of the reconstructed transfer matrices are presented in Fig. 6.15. Similar to the amplitude distribution, the phases for the matrix coefficient T_{12} and T_{21} diverge from the reference case very much. For the elements T_{11} and T_{22} there are no changes noticeable. Overall, it looks like that the amplitudes themselves are considerably modified and damped as opposed the reconstructed phases.

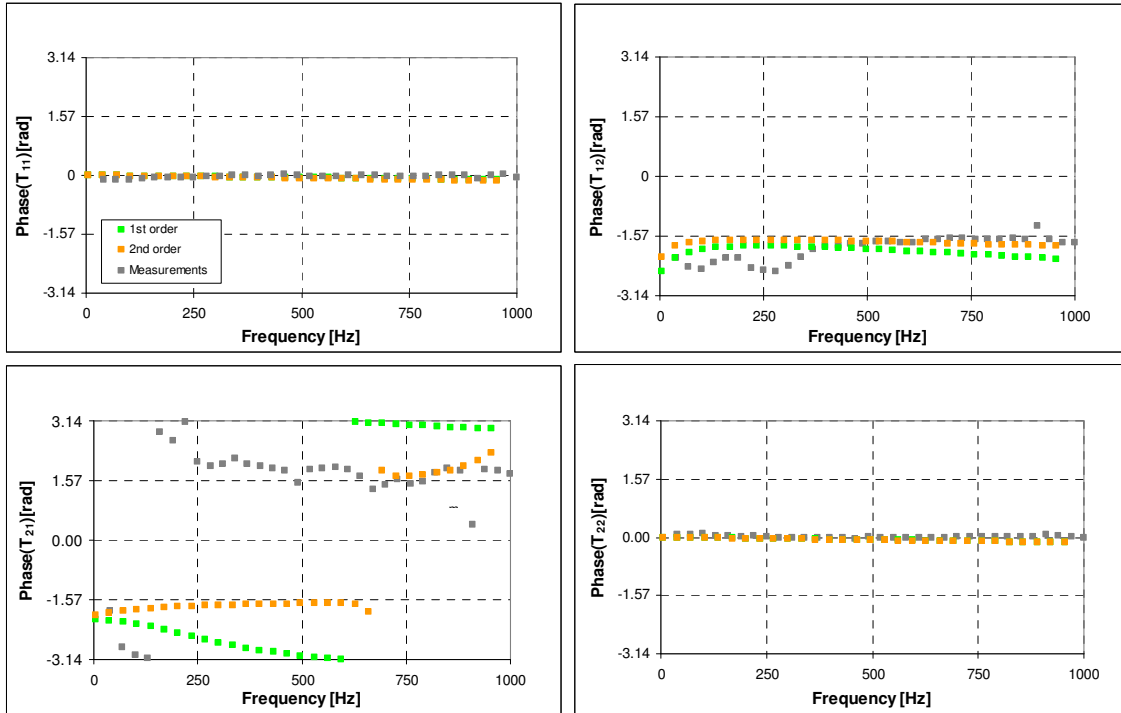


Fig. 6.15 Time scheme variations: Phase: green rectangular – 1st order, orange rectangular – 2nd order, grey rectangular – measurements

7 Truncated teardrop specimen

Acoustic properties of simple 1D acoustic elements, which can be used to represent a given gas combustion system are very important. The 1D acoustic characteristic is key to be able to perform the overall stability prediction. However, knowing only acoustic transfer matrices, which characterize the acoustic element with respect to the sound transmission, is not sufficient to model an acoustic system. In addition to acoustic transfer matrices, information referring to acoustic boundary conditions is also required. These acoustic boundary conditions can be prescribed either by reflection coefficient or by acoustic impedance. To model a generic gas turbine combustion system, the knowledge about the downstream and upstream acoustic boundary is crucial. In this study the downstream acoustic boundary condition is to be modeled using CFD/SI. It is well known that the acoustic boundary conditions applied while modeling a gas-turbine combustion system may directly affect combustion stability by influencing the mode shapes and natural frequencies. Depending on what these acoustic boundary conditions represent, these boundary conditions can act as a source of additional acoustic damping in the entire system.

A special facility has been assembled at the Science & Technology Center in Pittsburgh in 2003 for cold-flow measurements of impedance on the truncated teardrop section. This section is used to mimic outlet acoustic boundary conditions from a gas turbine test rig. The data from these measurements are utilized to support directly the validation of the CFD/SI procedure. The experimental setup consists of a straight channel with the truncated teardrop specimen closed by an acoustic absorber and is shown in Fig. 7.1.

In this Chapter, the reconstruction of acoustic transfer matrices using the CFD/SI approach for a truncated teardrop specimen mounted within a straight channel is performed and investigated in detail. Subsequently, because of the lack of experimental results, the obtained transfer matrices are verified by means of the one-dimensional acoustic network model.

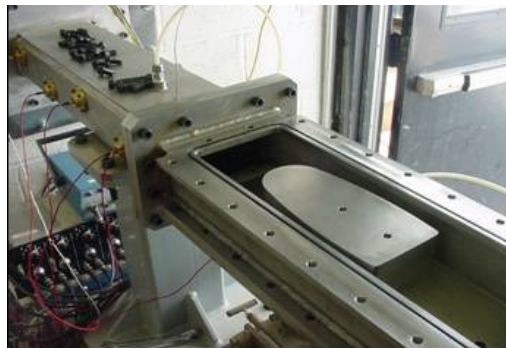


Fig. 7.1 Truncated teardrop specimen in position for impedance measurements

Moreover, the reconstructed transfer matrices are implemented into the one dimensional acoustic network code to predict impedances in the front of the truncated teardrop section and the results are directly compared to the experimental data. Finally, the sensitivity study on: mean flow velocity ($Ma=0.07$ and $Ma=0.4$) and acoustic boundary conditions used are carried out. From this thesis standpoint, a more relevant case seems to be the case $Ma=0.4$ and therefore all computational results are presented only for this Mach number.

7.1 CFD/SI approach to reconstruct acoustic transfer matrices

As already discussed in the previous chapters, an unsteady forced CFD calculation must be performed in order to provide the time series of velocity and pressure. Having the time series the correlation analysis in the acoustic postprocessor [17] can be performed and a given acoustic transfer matrix can be estimated. The setup for a CFD model of the truncated teardrop specimen in the generalized form is given in Fig. 7.2. The abbreviation BC stands for the computational boundary conditions. The mean flow enters the considered section on the left hand side and leaves the section after a sudden acceleration due to the area contraction. After passing the section with a smallest cross-section, the axial velocity gets reduced again because the cross-sectional downstream diameter is similar to the upstream diameter. As in the case of the sudden change of dimension a steady flow field is calculated first and then excited on both boundaries by an addition of the fluctuating velocity and pressure. Forcing signals generate the acoustic waves, which travel towards the “black box” represented here by the acoustic transfer matrix of the truncated teardrop specimen.

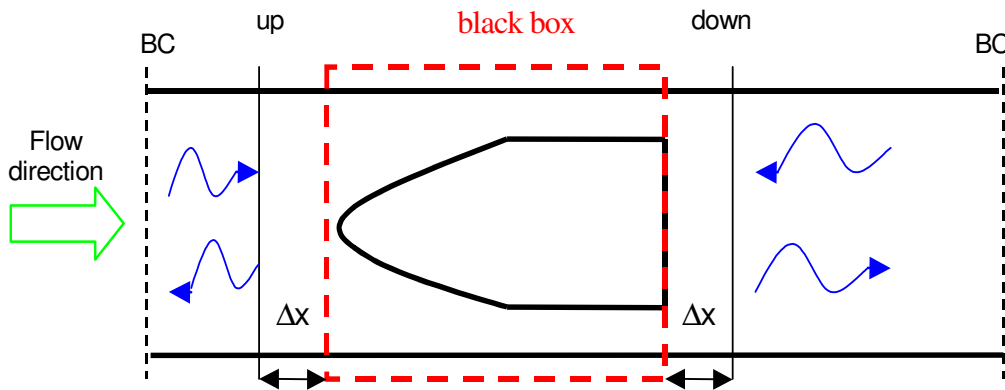


Fig. 7.2 The truncated teardrop element represented by the generalized CFD setup

7.1.1 CFD model and Boundary Condition

The CFD model represents a full 3D geometry of a given section. The hexahedral grid is generated using ICEM CFX and has about 340.000 hexahedral elements. It seems to be reasonable to resolve a relatively simple flow field. However, it must be also mentioned that no grid dependents study has been performed to check whether the computational mesh is fine enough to capture any changes in the flow field.

The CFD geometry has rectangular cross-section over the whole geometry. For the simplicity, the diameter D_{in} is transferred to the equivalent hydraulic diameter $D_{h,in}$ and D_{out} to $D_{h,out}$. From now on, all diameters considered in this test case refer to the hydraulic diameter. Following the changes of cross-sectional area, the larger diameter is located at the inlet and is subsequently contracted to the minimum value. After this contraction of the cross-sectional area, the downstream diameter $D_{h,out}$ is expanded to $D_{h,in}$. The total length of the model is $\sim 1.7\text{m}$. The CFD computational domain with specified BC is shown in Fig. 7.3.

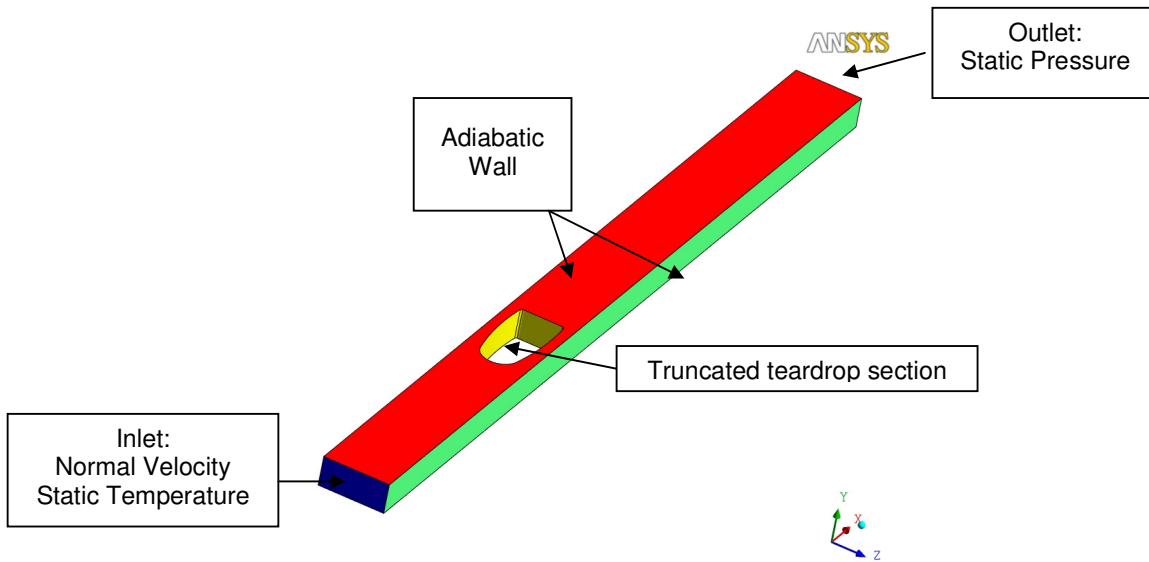


Fig. 7.3 BC and CFD model of truncated teardrop specimen

At the inlet a normal velocity of average Mach number of $M=0.4$ is imposed at the minimum cross-section. For the outlet boundary condition, the atmospheric static averaged pressure is assumed. Moreover, the temperature of 293 K is applied. Since the acoustic wave propagation is considered, the flow compressibility is taken into account in the total energy equation. Both the steady and the transient flow fields are calculated with the commercial package ANSYS CFX 5.8. in Tab. 7.1.

Fluid Model	Ideal Gas Law
Turbulence Model	k- ϵ
Advection Scheme	High Resolution
Heat Transfer Model	Total Energy
Transient Scheme	Second order Euler
Time step	2.5e-5 s
Number of time steps	10000

Tab. 7.1 Numerical models- truncated teardrop specimen

Simultaneously, making use of two independent and random functions at the inlet and the outlet the excitation signal equal to 10 % of the mean axial velocity and the average pressure are imposed. Due to lack of properly defined acoustic boundary conditions, the full reflective boundary conditions given by ANSYS CFX 5.8 are utilized. To minimize the interaction between the excited and reflected acoustic waves, the white noise excitation is utilized. Following up the recommendations from Gentemann and Polifke et al. [17] and the results from the sensitivity study from previous sections, the time step of 25 microseconds and maximum number of time steps of 10000 have been chosen for the transient computation. According to (5.45) and (5.47) the frequency range is limited from 4 to 20000 Hz. Furthermore, if the maximum frequency of interest is 1000 Hz the number of points in the time domains is estimated to be 40. It should guarantee a good time resolution for acoustics.

7.1.2 Steady state flow field

Fig. 7.4a gives the contour plots of the normalized pressure distribution at $y=0$ m. As expected, the highest local pressure is found in the front of the truncated teardrop section. It results from the stagnation point located is at this position where the kinetic energy of the flow is transferred into the pressure energy. It is also well seen that at the position where the minimum cross-section is defined, the minimum of pressure is shown.

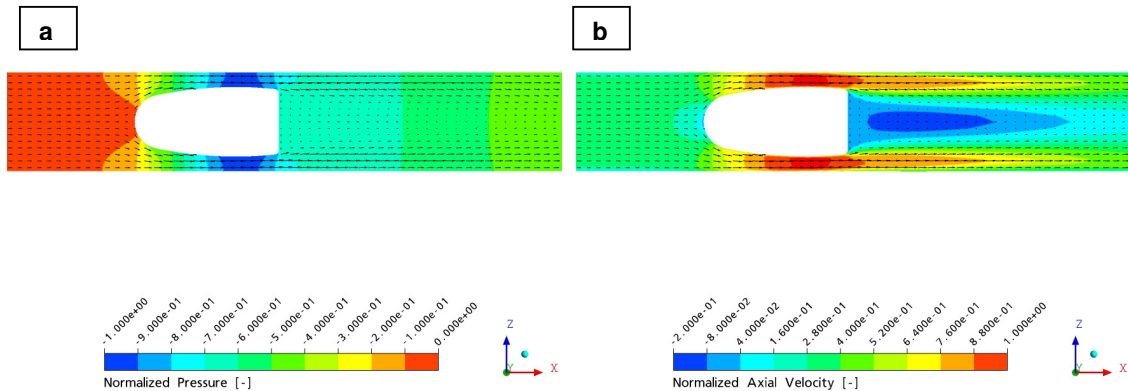


Fig. 7.4 Truncated teardrop specimen: normalized pressure and axial velocity distribution at $y=0$ m

The normalized axial velocity distribution is depicted in Fig. 7.4b. Analyzing the axial velocity, it is noticeable that the flow accelerates gradually and achieves the maximum local axial velocity at the position where the maximum contraction of the cross-section takes place achieving the averaged Mach number of 0.4. Due to this geometry structure, the flow detaches from the truncated teardrop walls and forms the central recirculation zone with the negative axial velocity. Unfortunately, using URANS it is not possible to examine this mechanism more in detail. Of course, some vortices formed at this edge can interact strongly with acoustic and affect acoustic wave propagations.

7.2 Acoustic transfer matrix by means of CFD/SI and one-dimensional acoustic modeling

The one-dimensional acoustic code is utilized to model the truncated teardrop specimen. A chain of connected diffusers with variable cross-sections is utilized to approximate the investigated section. The acoustic properties for each acoustic element used here are well known and validated. Munja et al. [29] has provided the theoretical description of acoustic wave transmissions through diffusers, ducts and area discontinuities. The chain of the simple acoustic element representing the investigated truncated teardrop specimen is presented in

Fig. 7.5. As already mentioned, the one-dimensional model consists of junctions (J), area discontinuities (AD) and diffusers (DIFF). Using this model, the acoustic transfer matrix can be derived and compared to the CFD/SI approach.

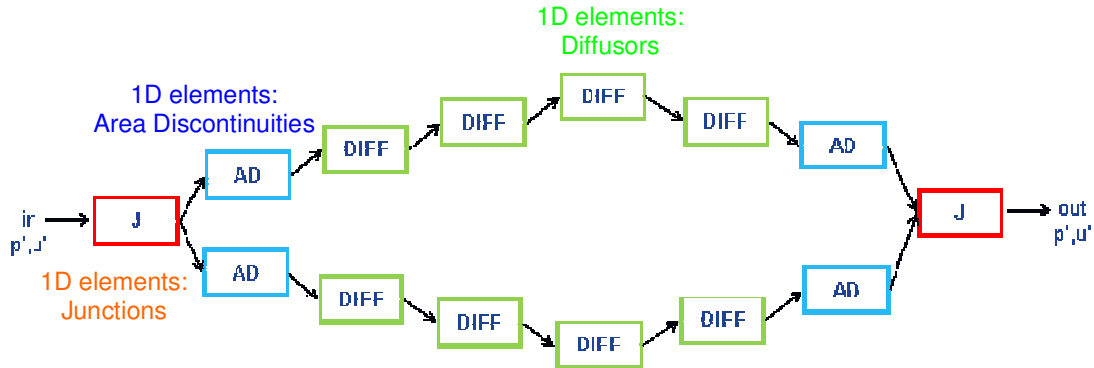


Fig. 7.5 One-dimensional acoustic representation of a truncated teardrop

The absolute values of the acoustic transfer matrix of the truncated teardrop are shown in Fig. 7.6. The magnitude is normalized by the characteristic impedance of air at the inlet section to this testcase. Moreover, the frequency axis has the dimensionless form represented by the Strouhal number St . In general, a frequency range up to $St=2$ is considered. At this frequency, an occurrence of transverse modes may be expected and therefore for this frequency the validity limit for the one-dimensional acoustic wave representation is defined. The comparison between the transfer matrices reconstructed by means of one-dimensional acoustic network code and CFD/SI is shown. Up to $St=1.0$, the overall agreement is almost perfect. Above $St=1.0$ some discrepancies in the amplitude distribution are noticeable.

The acoustic transfer matrix element T_{12} does not match the acoustic network code prediction with reasonable accuracy. The reason for this behavior may be due to the acoustic damping effects caused by flow-turbulence interactions, which are not well represented by the one-dimensional approach. On the other hand, it may happen that CFD has a problem at higher frequencies to calculate properly acoustics. Unfortunately, there is no experimental data, which can prove the first or the second statement.

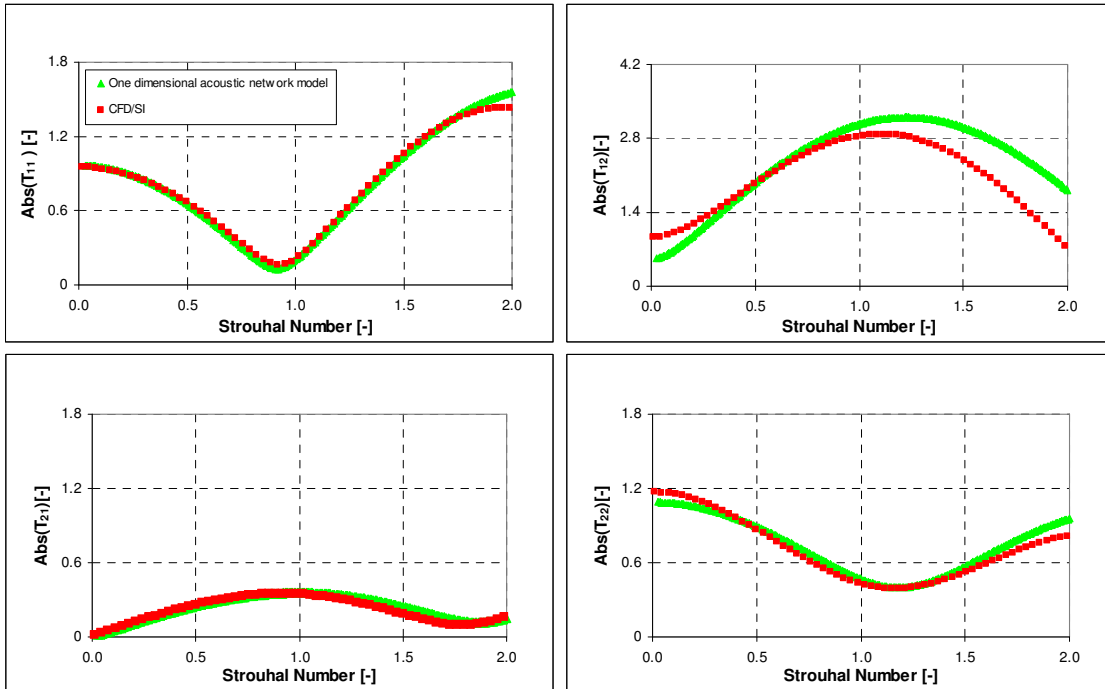


Fig. 7.6 Acoustic transfer matrices of the truncated teardrop specimen: normalized absolute value: red triangle – CFD/SI, green rectangular – one dimensional acoustic network model

Evaluating the phases given in Fig. 7.7, satisfactory results are obtained. The phase reconstructed using the CFD/SI method matches well the prediction of the one-dimensional acoustic network. However, in the case of the acoustic matrix element T_{21} the larger differences are seen.

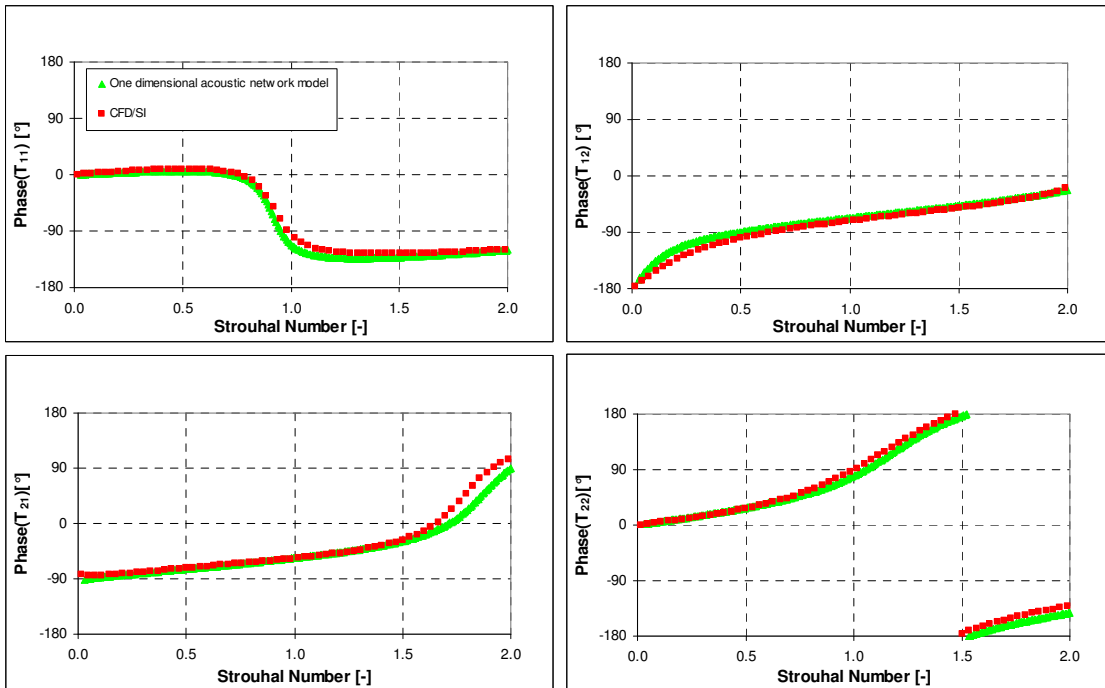


Fig. 7.7 Acoustic transfer matrices of the truncated teardrop specimen: phase red triangle – CFD/SI, green rectangular – one dimensional acoustic network model

It should be also noted that the accuracy of the one-dimensional approach results shown at higher frequencies can be limited due to the one-dimensional assumption that may not hold completely at these frequencies.

7.3 Optimal values of L and m

The location where the time series of pressure and velocity are taken is defined to be 0.05 m. This distance is rather arbitrary and is based on some previous experiences with CFD/SI. However, this issue has been investigated in [50]. The first outcome of this study was that these reference planes should be far enough to avoid some 3D acoustic effects (not uniform pressure and velocity distribution). The second outcome was that the distance Δx does not have practically any influence on the CFD/SI approach. The estimated acoustic transfer matrix is recalculated with regard to the distance Δx based on eq. (5.34).

Employing the equation for the relative quadratic difference (5.53) allows for finding an optimum of the filter memory characterized by L . Making use of the simple relation (5.49) and assuming $m=1$, a first estimation of L can be made. In this case L is found to be 40. However, based on equation (5.51), the optimum of L being 65 is determined. The relative quadratic difference of the first element T_{11} of the derived acoustic transfer matrix is shown in Fig. 7.8. The difference between the guessed and optimum value is relatively high and may result from the relatively complex flow pattern within the truncated teardrop specimen. It should be mentioned that at the edge of the truncated teardrop maybe some vortices are formed and are partially captured by URANS. On the other hand, maybe some reflected acoustic waves interacted with each other changing the coherence function between signals and responses. As shown, for values of m bigger than one the relative quadratic error slightly increases when going for higher m values. The point at $m=8$ is chosen to be the optimum. Some deviations above the optimum of m are observed.

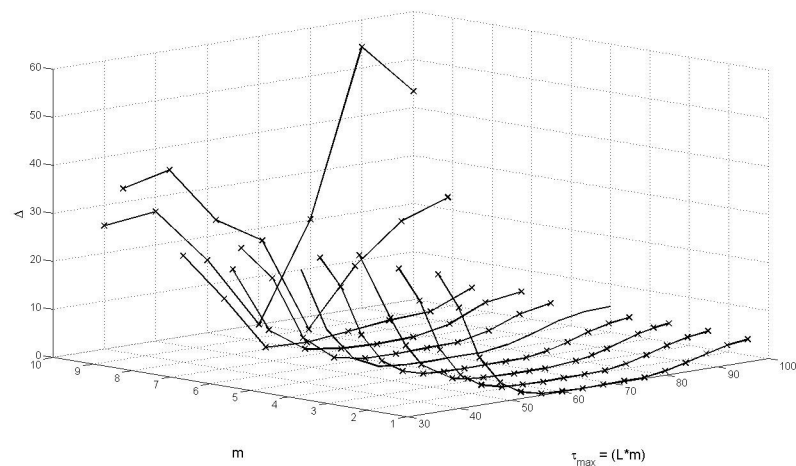


Fig. 7.8 The relative quadratic difference of the element T_{11} of the truncated teardrop specimen

In general, the value of m ranging from 1 to 8 can be employed in the acoustic postprocessor and can give the reasonable results.

7.4 Acoustic reflectivity at boundaries

Acoustic reflectivity at computational boundaries is a very important issue while reconstructing acoustic transfer matrixes. It is reported in the literature [55] that externally applied forcing signals in a given system can generate additional, undesired reflected acoustic signals due to the CFD boundaries. At these physical boundaries, an artificial reflection of acoustic pressure is created and travels back into the CFD domain. Furthermore, these artificially generated acoustic waves can start interacting with the forcing signal and cause the system identification to fail. One way to avoid the undesired interactions between reflected pressure waves or to reduce a negative influence on the CFD/SI method is to employ white noise excitations [17]. Other possibility to diminish this negative influence is to define acoustic proper boundary conditions with respect to acoustics. Widenhorn et al. [56] proposed and implemented non-reflective boundary conditions into the commercial CFD code ANSYS CFX 10.0. It has been demonstrated that these boundary conditions affect significantly acoustic wave propagation and do not cause any reflection at boundaries. The acoustic waves can freely leave the computational domain and are not reflected back.

In this section, the reconstructed acoustic transfer matrix with different acoustical BCs is shown. As a reference, the test case with standard reflective BCs is utilized. The results are evaluated with respect to the acoustic transfer matrix obtained using the one-dimensional acoustic network model. To be consistent, all computations have been performed in CFX11 with the same numerical setups except the acoustic boundary conditions.

In Fig. 7. the absolute values of the derived acoustic transfer matrices are given. Some deviations caused by acoustic reflectivity at the computational boundaries in terms of the absolute values are found. In the element T_{11} , the strongest deviation at $St > 1$ between the case with RBCs at the inlet and NRBCs at the outlet, the network model, and the case with NRBCs at the inlet and outlet is seen. Since this coefficient is determined by the ratio that relates downstream pressure to upstream pressure, it seems that in this case of NRBCs at the inlet and outlet the downstream pressure is much smaller than in the other cases. In general, one can conclude that the differences in the absolute values can be caused by a superposition between viscous damping effects and amplifications of acoustic waves due to the reflective boundary condition. It is well known that the results from one-dimensional acoustic network codes may be slightly over-predicted because the linearized Euler equation does not account directly for non-linear effects and mean flow/turbulence interactions. There are some additional correction factors, which can be used in 1D models. By using these factors one can mimic acoustic damping due to the turbulence effect [28][94]. However, these corrections cannot replace any CFD simulations.

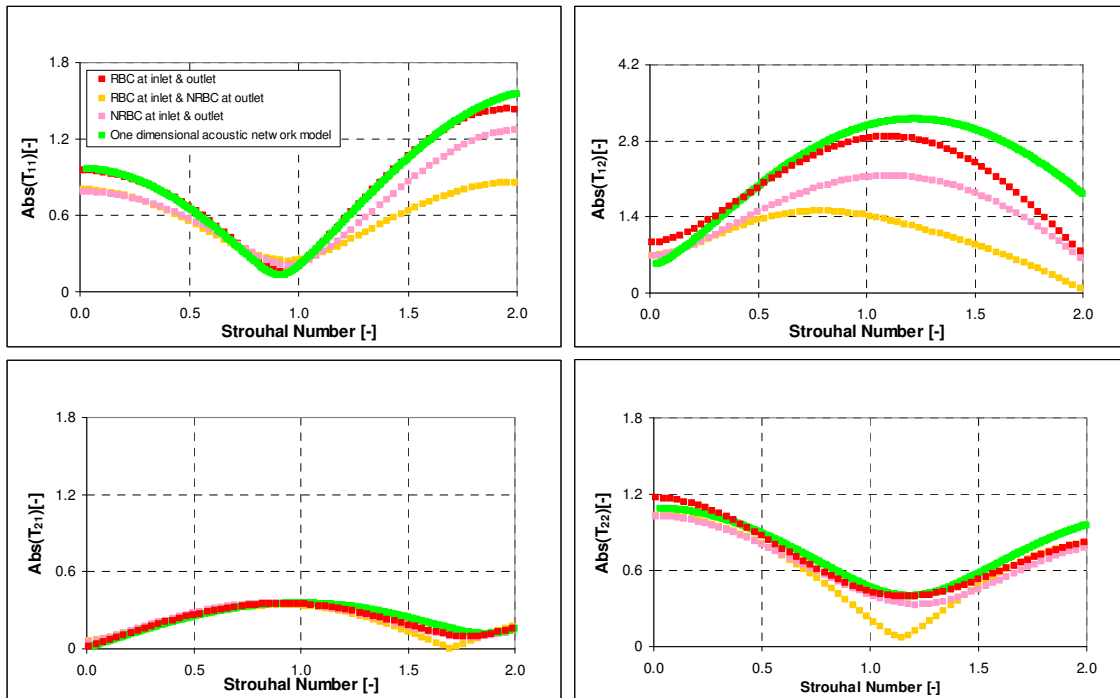


Fig. 7.9 Acoustic reflectivity vs. acoustic transfer matrices of the truncated teardrop specimen: normalized absolute value: CFD/SI with RBCs - red rectangular, CFD/SI with NRBCs at inlet and outlet-purple rectangular, NRBCs at outlet and RBCs at the inlet- yellow rectangular, TMA modeling - green rectangular

On the other hand, the acoustic transfer matrix reconstructed utilizing acoustic reflective boundary conditions tends also to be over-predicted compared to the cases where no acoustic reflection is observed. Similar tendency in the amplitude distribution to the element T_{11} is shown in element T_{12} where the same phenomenon with a high pressure drop is addressed. The absolute values for all cases differ from each other. The lowest is referred to the model with the hard acoustic boundary condition at the inlet and the soft acoustic boundary condition at the outlet. In contrary, the highest values are in the case of the analytical prediction. The predicted values in all models cannot follow the analytical model. For the remaining coefficient T_{21} and T_{22} the obtained values are in good agreement with the one-dimensional approach.

In Fig. 7. the derived phases for the different CFD setups are presented. As seen, all considered cases are in good agreement with the TMA model. There are some variations found for the case marked with yellow colors. This case is associated with the soft boundary conditions at the outlet and the full reflective at the inlet. It must be added that these different acoustic boundary conditions applied at the inlet and outlet can affect slightly all acoustic modes of the entire system including the truncated teardrop section. In other words, these slightly different acoustic mode distributions can be also responsible for these not matching results. Furthermore, the calculated phase can also prove that the acoustic pressure distribution is different by using different acoustic boundary conditions.

One has to remember that the measurement campaign is performed in the test rig, which does not use perfectly non-reflective boundary conditions.

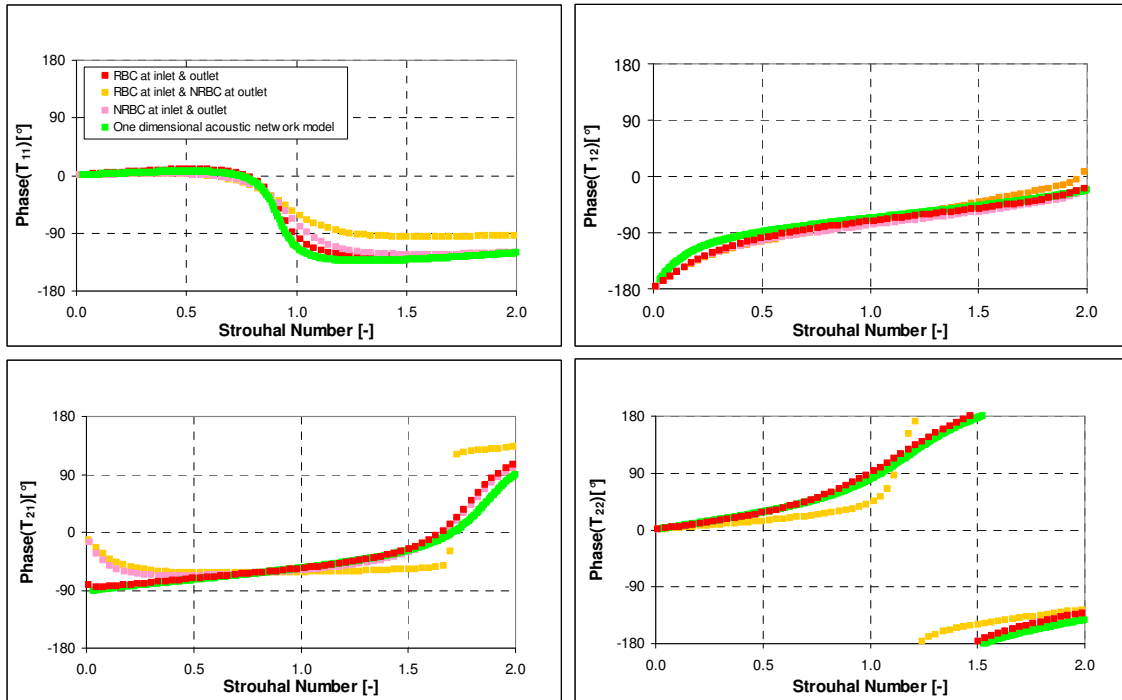


Fig. 7.10 Acoustic reflectivity vs. acoustic transfer matrices of the truncated teardrop specimen: phase: CFD/SI with RBCs - red rectangular, CFD/SI with NRBCs at inlet and outlet-purple rectangular, NRBCs at outlet and RBCs at the inlet- yellow rectangular, TMA modeling - green rectangular

Summarizing, quantitatively all the methods have given the same answer but since no measurements are available is hard to judge, which of them give the most reasonable values. However, it may be assumed that CFD with NRBCs has some potential to provide the most accurate prediction. Since it is known that by using NRBCs theoretically no additional reflections can occur in the system and therefore the coherence function between signals and responses should have the maximum value. Having this in mind, the identifications procedure based on CFD/SI and this kind of boundary condition should give the most accurate acoustic transfer matrix.

7.5 Impedance calculation

In this section the indirect comparison between the CFD/SI method and the one-dimensional approach represented by the TMA model with the experimental data is given. As it is shown in Fig. 7.11, the truncated teardrop specimen is placed in a straight channel. Further downstream of this section, a sound absorber is mounted in order to dissipate acoustic waves. The main goal of the conducted experimental work was to measure the impedance at the leading edge of this specimen.

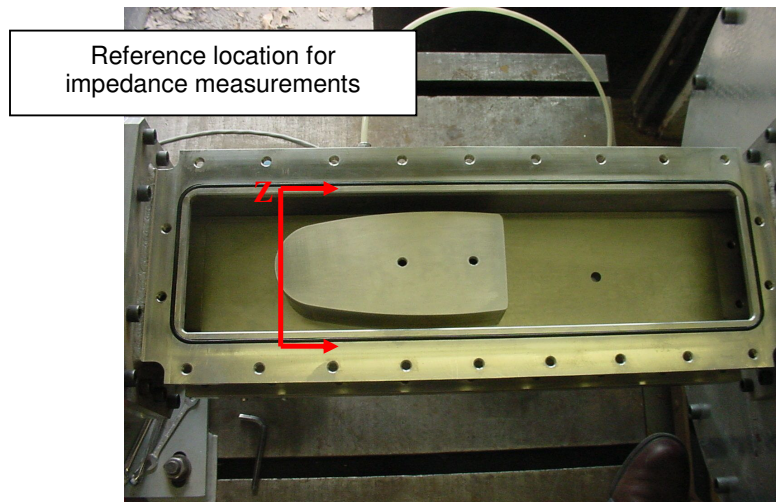


Fig. 7.11 Reference location for Impedance measurements of the truncated teardrop specimen

Unfortunately, it is not possible to calculate directly the impedance of this section using CFD. Despite of the fact that acoustic non-reflective boundary conditions are available, the acoustic impedance characterizing the entire downstream section cannot be directly reconstructed using CFD. CFD is not capable of using impedance boundary conditions yet. There is some ongoing work on this topic. Widenhorn et al.[93] has already demonstrated that using these boundary conditions an arbitrary acoustic reflection accounting for a phase shift can be applied. However, this impedance boundary condition has not been implemented into commercial CFD solvers yet. At the moment, CFD can be employed to derive the acoustic transfer matrix of a given section. On this basis, the one dimensional acoustic network code must be used to compute the acoustic impedance in the front of the truncated teardrop specimen at the reference location marked by red in Fig. 7.11. Therefore, the CFD/SI method is going to be employed to derive the acoustic transfer matrix of this specimen and then the TMA model with the element represented by the CFD-based acoustic transfer matrix is utilized to predict the acoustic impedance. Taking into account the results from the study on acoustic reflectivity at boundaries, the unsteady CFD calculation to derive the acoustic transfer matrix has been carried out with the NRBC concept. All details with regard to the numerical set up are already given in section 7.1.1. Furthermore, the TMA model with originally implemented simple elements representing the truncated teardrop specimen is set up and used to write out the impedance at the same positions for the comparison purpose.

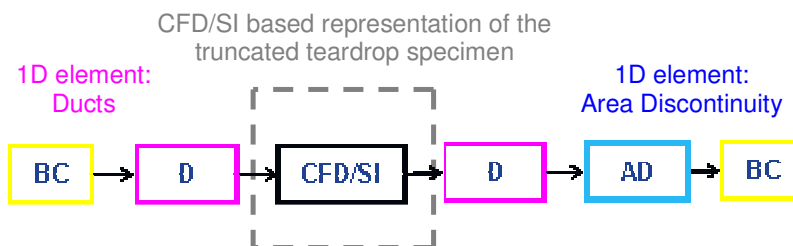


Fig. 7.12 TMA model with the truncated teardrop specimen represented by the CFD/SI approach

The simplified TMA model with an element based on the CFD/SI prediction, which represents the truncated teardrop specimen, is shown in Fig. 7.12. In addition to the considered element, the other elements describing acoustic wave propagation in the upstream and downstream section are also presented. It is seen that the overall complexity of the model has drastically been minimized.

In contrast to the simplified TMA model, the section of interest is also modeled with TMA elements such as diffusers with variable cross-sectional areas. The model itself is much more complex, consists of several additional elements, and requires some experience to be set up. As shown, the truncated teardrop specimen is compound of several connected ducts (D), diffusers (DIFF), junctions (J), and area discontinuities (AD). Fig. 7.13 shows the one-dimensional acoustic representation of the original experimental truncated teardrop specimen.

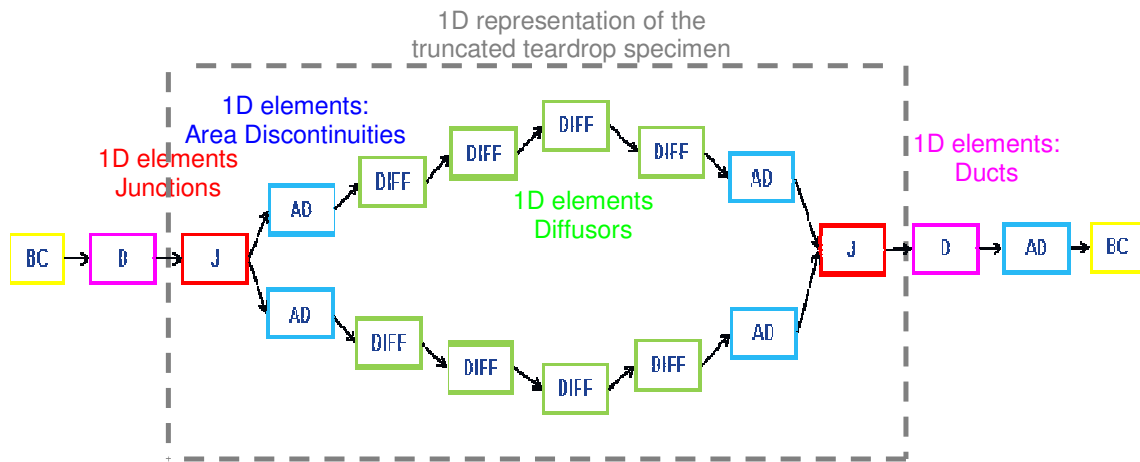


Fig. 7.13 TMA model of the truncated teardrop specimen

The downstream boundary conditions are adjusted to match reasonable the acoustic experimental data. Using an acoustic absorber, it can be expected that acoustic waves are fully absorbed and no acoustic reflection is present. However, in reality the acoustic absorber does not entire absorb the acoustic energy and some portion of acoustic waves are reflected back into the truncated teardrop specimen. The downstream reflection coefficient has been varied to get the best fit with respect to the acoustic measurements. As a result, the reflection coefficient of minus 0.8 is set at the exhaust passage.

The impedance at the leading edge of the considered section has been predicted and directly compared to the experimental data. The impedance is normalized by a characteristic impedance of air at STP⁹ taken at the inlet section and is plotted in Fig. 7.14. The vertical axis is plotted in the logarithmic scale and the frequency range is represented by the Strouhal number. A reasonable match between the experiments, TMA and TMA with an element using the transfer matrix from the CFD/SI for frequencies lower than the Strouhal number of 1.5 has been found

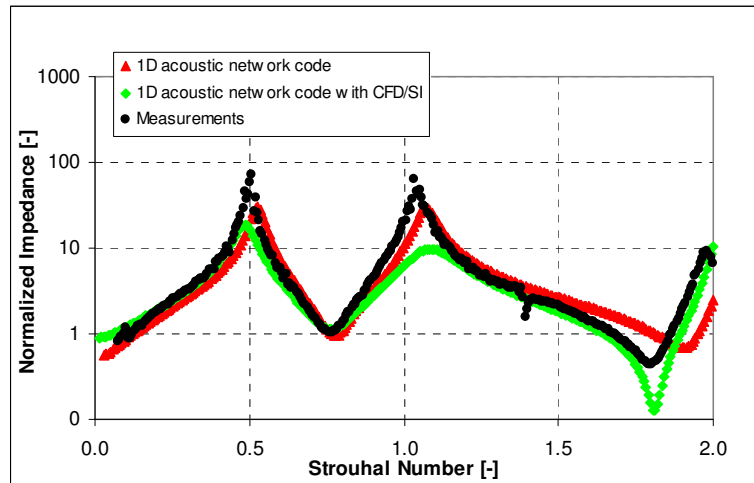


Fig. 7.14 Normalized Impedance of the truncated teardrop specimen: Amplitude, black circle measurements, red triangle –TMA model, green diamond – TMA model with the truncated teardrop specimen represented by the CFD/SI approach

At higher frequencies, neither in the case with the original TMA model or the TMA model combined with the CFD/SI element the impedance magnitude cannot fit the experimental results well. The trends are correct but the amplitudes are somewhat mismatched. The main reason for this is acoustic damping, which is not correctly represented in both cases. CFD seems to underpredict the amplitude due to turbulence, which affects the propagation of acoustic waves. The CFD-based magnitude can be theoretically improved if a more suitable turbulence model is used. In this case, the $k-\epsilon$ seems to be overpredicting significantly the turbulence production in the considered section. On the other hand, despite of the fact that the TMA tool does not account for flow/turbulence interactions is still capable of predicting the impedance values. Furthermore, two characteristic peaks referring to the resonance found in the test rig have been captured but in the experimental data these values are much more pronounced. It is evident that in this case, acoustic damping is much smaller compared to the 1D acoustic network model and the 1D acoustic network model with the truncated teardrop specimen represented by CFD/SI.

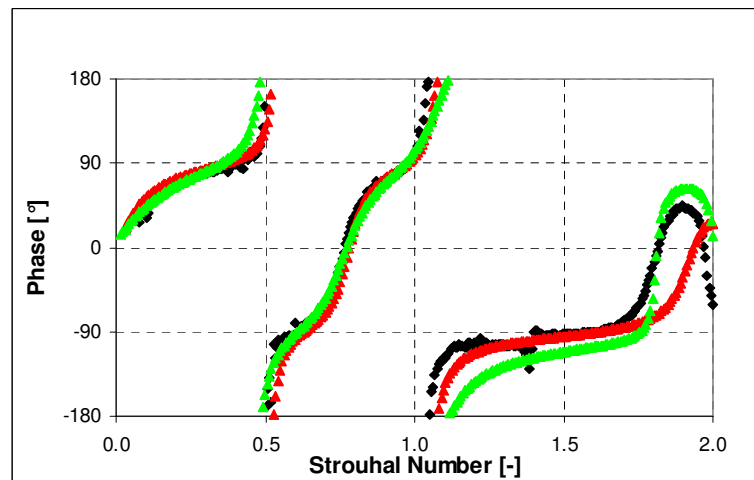


Fig. 7.15 Normalized Impedance of the truncated teardrop specimen: Phase, black circle-measurements, red triangle –TMA model, green diamond – TMA model with the truncated teardrop specimen represented by the CFD/SI approach

The predicted phases of the truncated teardrop section are plotted in Fig. 7.15. The phases from the TMA model are compared to the experiments and a satisfactory agreement is obtained. As expected, there are some deviations seen for St larger than 1.0. For higher frequencies, the viscous damping effect seems to be over-predicted and this cause the additional phase shift compared to the experimental results.

8 Atmospheric test rig with a generic burner

An atmospheric test rig has been built and tested at the University of Karlsruhe in order to investigate the flame transfer function of a generic gas turbine burner featuring a premixed swirling flow. This experimental setup has been selected to show the capabilities of URANS calculations combined with SI in the estimation of flame transfer functions. Additionally, the CFD/SI approach is validated with the URANS simulation forced at several discrete frequencies. Moreover, the reconstructed phase is compared with experiments and with the time lag model to investigate whether the flame response can generally be characterized by a time lag behavior.

A sensitivity study on time resolution, combustion model, and acoustic boundary conditions is presented in detail.

8.1 Test rig description

Fig. 8.1 gives an overview of the investigated experimental setup. The main parts of the test rig are: the pulsating unit, the 16 air supply tubes entering the burner housing, the prototype burner and the quartz glass tube forming the combustion chamber, and the exhaust gas pipe. Information that is more detailed is provided by [74].

The prototype of a gas turbine burner used for the investigation is sketched in Fig. 8.2. The prototype burner comprises two concentrically arranged swirler passages. Through the outer passage i.e. 'main passage', about 90% of the flow is discharged with an equivalence ratio of 0.5. Diagonally inclined vanes are utilized to generate the swirling motion in the combustor. The premixed fuel/air mixture entering the central passage is swirled by an axial swirler mounted at the exit of the passage.

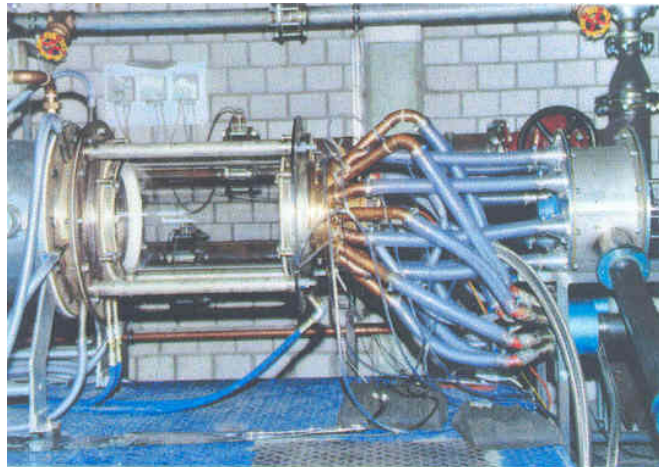


Fig. 8.1 Picture of the investigated experimental test rig [74]

The fuel mixture has a high equivalence ratio of 0.8. By using an additional pilot flame, the flame excitation during pulsation of the 'main flame' can be prevented. The pilot flame makes the combustion process of the main flame more stable.

In the measurements of the flame transfer function, hotwire probes are used to measure the burner exit velocity fluctuations, and a photomultiplier is used to detect heat release fluctuations of the flame by the signature of the chemiluminescence of the OH molecule. The data obtained is utilized in order to determine the phase and amplitude relation between the input signals.

The pulsating unit modulates an adjustable part of the mass flow at various frequencies of pulsation. Constant Temperature Anemometry (CTA) is employed to control the strength of excitation. The hot-wire probes are located 60 mm upstream of the burner exit, in the channel between two swirl vanes of the outer swirl generator.

The photomultiplier detects the integral UV radiation intensity of the flame at two different measuring positions. The first position is located at the end of the combustion chamber to observe the outlet cross-section of the burner through a quartz glass window. Secondly, the entire flame is viewed from the side through the quartz glass tube. In addition, the ICCD-camera is utilized for the phase-correlated OH-imaging of periodical structures.

The simultaneously measured hot-wires and photomultiplier signals were analyzed with a two-channel frequency analyzer utilizing a high sampling rate of 102.4 kHz.

The measured flame transfer function is normalized with its reference value taken at 10 Hz. At the reference frequency, the flame behaves as a quasi-steady flame [74]. The measurements are made at different pulsating levels and for two different thermal loads. Furthermore, fully premixed and technically premixed modes are investigated. For the formation of the time-independent and spatial homogeneous mixture the different fuel gas/air mixture mass flows are mixed in independent mixing units located upstream of the pulsating unit. In the case of the technical mixture formation, the fuel gas is injected steadily through arrays of orifices in the swirl vanes into the pulsating air flow 70 mm upstream the burner exit, avoiding safety risks caused by flashback of the flame into the burner housing.

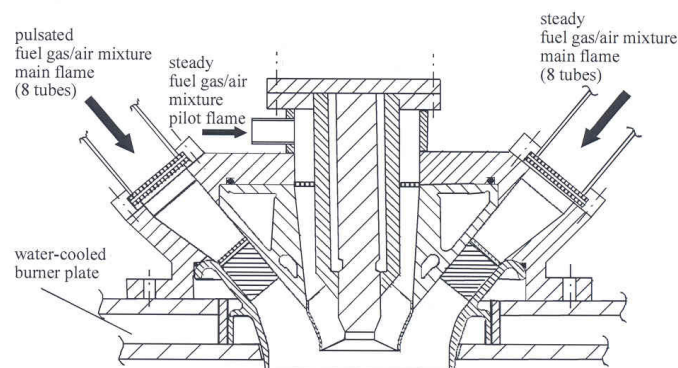


Fig. 8.2 Sketch of a prototype burner [74]

In the case of the fully premixed mode, only the air volume flow rate is pulsated, whereas in the technically premixed mode both the air and fuel volume flow rates are forced simultaneously. The results based on different forcing levels i.e. 16% and 24% (mean volume flow rate) for the fully premixed case, do reveal some small differences in the frequency response in terms of magnitude and phase angle. During the experiment, the sinusoidal modulation of mass flow is carried out for the frequencies from 10 up to 120 Hz.

For the purpose of this work, only computational results related to the fully premixed case are presented. The pulsation amplitude equal to 16% of the mean volume flow rate with thermal load of 277 kW is validated against computations. In addition to this, various sensitivity studies have been carried out.

8.2 URANS modeling

In order to properly represent all flow effects in the analyzed test rig, a 3D computational mesh should be built. However, for the current case, URANS calculations are performed only in a 10-degree segment with periodic boundary conditions. This simplification is much less computationally expensive than the analysis of a full 3D case. To assure the consistency of the results from the 10 degree sector model, the velocity, temperature and CH₄ flow fields at $z=0$ m are additionally compared to the 360 degree model described in [74] with no significant differences found. The geometry of the 10-degree sector, which is used to mesh the computational domain, is shown in Fig. 8.3.

The combustor has a diameter of 300 mm and a length of 500 mm. The exhaust passage is about 50 mm smaller in diameter and is about 600 mm long. The computational domain comprises 120,000 hexahedral elements.

1D velocity profile boundary conditions are applied at the axial and diagonal inlet. The velocity profiles are taken from a calculation of the whole burner, including the swirler vanes, and are circumferentially averaged. The investigated case is assumed to be the fully premixed, that is, the fuel and oxygen concentration is represented by the averaged CH₄ and O₂ mass fractions, respectively. The air/fuel mixtures at the inlets are slightly preheated to a temperature slightly above 300 K. The liner wall is treated as an adiabatic wall and the exhaust passage is kept at a constant temperature.

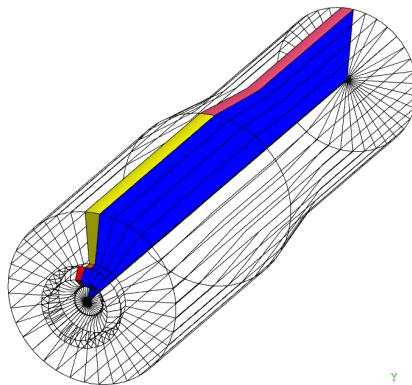


Fig. 8.3 Ten degree segment of URANS model

The outlet pressure is set to 1 atm. A more transparent characterization of the used boundary conditions and the CFD model is provided in Fig. 8.4.

Since the flame response on acoustic perturbations is considered, all calculations are carried out taking into account the compressibility of the flow. Doing so, it is possible to capture not only all perturbations traveling with a convective speed but also acoustic perturbations traveling with speed of sound. The 2nd order Euler backward discretization in time and the high resolution scheme for spatial discretization are used [15]. The calculations are performed with CFX10 with non-reflective acoustic boundary conditions at the outlet. The heat release is modeled by employing the Eddy Dissipation concept combined with one-step kinetics. The numerical models used are summarized in Tab. 8.1 shown below.

Advection Scheme	High resolution
Time discretization	2 nd order Euler backward
Fluid Model	Compressible Gas
Turbulence Model	k- ϵ
Combustion Model	EDM with one-step kinetics
Heat Transfer	Total Energy
Time Step	1E-4 s
Time Steps	5000

Tab. 8.1 Numerical models - Atmospheric Test Rig

It is already demonstrated in some previous URANS studies [75] that the time step of 0.1 ms is sufficient to capture the dynamical response of the flame to the inlet velocity forcing.

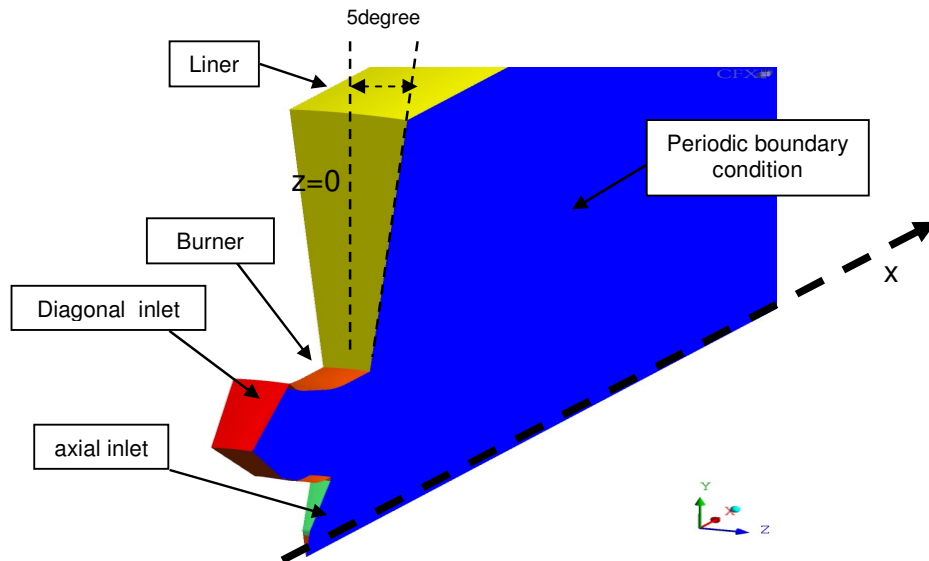


Fig. 8.4 Boundary conditions and CFD model of an atmospheric test rig

The physical justification for choosing such a small time step is associated with the fact that velocity perturbations are mainly transported through the system with a convective speed. By using such a small time step, acoustic pressure waves can only be partially captured at higher frequencies.

However, it is not a problem in this case because a convective speed is dominant and the frequency range from 10 to 250Hz is to be considered. A total number of time steps used in this validation is 5000. Using a given value of N and corresponding dt result in bounding frequencies between $f_{min}=2$ Hz and $f_{max}=5000$ Hz according to the Nyquist theorem described in section 5.4.7.2. Moreover, taking into account the maximum frequency of interest at 250Hz and the current sampling frequency, one gets 50 points in the time discretisation per one period of pulsation. Recalling some studies from the previous chapters, this seems to be the sufficient frequency resolution to capture all variations in the flame transfer function. Moreover, the influence from the chosen time is also the subject of this investigation.

It is well known that the standard boundary conditions available in CFD codes maintain high acoustic reflection coefficients at computational boundaries. It can be well seen when performing unsteady runs. For the purpose of this study, to minimize partially the influence from reflected acoustic waves non-reflective boundary conditions at the outlet are employed.

8.3 RANS Solutions

In the first part of the study, the RANS reacting flow calculation using the EDM model with one-step chemistry is performed. The resulting flow field is a starting point to do a forced URANS computation. The normalized axial velocity distribution is depicted in Fig. 8.5a. Because of the swirling motion imposed by the swirler vanes, an inner recirculation zone is established. The recirculation zone is indicated by the black iso-lines $u=0$ m/s. Furthermore, the outer recirculation zone marked by black iso-lines is visible. The system is operated in a low velocity range not exceeding 25 m/s. Based on the burner outlet diameter, the Reynolds number is about 50.000. Due to the recirculation of hot combustion products in the shear zone, the flame can be stabilized.

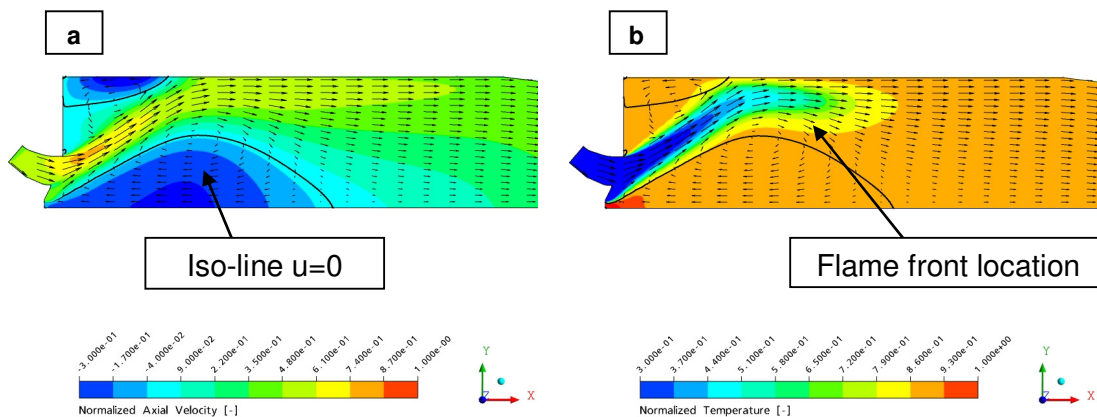


Fig. 8.5 Atmospheric test rig: a - normalized axial velocity distribution, b - normalized static temperature

The second important variable in reacting flow studies is the temperature distribution, which may indicate the flame front location. Fig. 8.5b provides a picture of the normalized temperature

distribution showing the highest temperature near the outlet of the central swirler. Such a high temperature is caused by the comparatively high equivalence ratio and helps to stabilize the combustion process with respect to the blow off limit.

8.4 Validation of the flame transfer function calculation

Using the CFD/SI method, the flame transfer function (FTF) in the considered generic test rig is reconstructed. The L parameter, which is to be used in the identification process, is estimated and optimized. The optimization process is performed by means of the theory described in the previous section. The L parameter has a value of 278.

Fig. 8.6 shows the normalized amplitude of the flame transfer function as a function of frequency. To be more consistent with the experimental data, the amplitude is also plotted in the logarithmic scale. Similar to the experiment, the computed amplitudes are normalized by the amplitude value at 10 Hz. As explained in [74] at this frequency the flame behaves as a quasi-steady flame and does not respond to any flow perturbations. The amplitude of FTF is shown up to 250 Hz because for higher frequencies no response in the flame can be noticed. It is seen that there are some discrepancies in predicting the absolute values. For frequencies lower than ~ 55 Hz indicated in Fig. 8.6 as a critical frequency, CFD/SI is not able to follow the trend of the experimental curve, and the calculated magnitude does not match the measurements. The decrease of amplitude in the experiment in the frequency range between 20 Hz and 40 Hz is explained by occurrence of self-excited oscillations [74]. These oscillations originated from an acoustical coupling between the combustion chamber connected to the burner geometry. The acoustic coupling at a given frequency affects the modulation of the mass flow rate out of the burner. This behavior leads to undesirable forcing amplitudes of the mass flow rate and could in extreme cases blow-off or flashback of the flame. From the FTF standpoint, it is hard to interpret finally the results from CFD/SI in this frequency range.

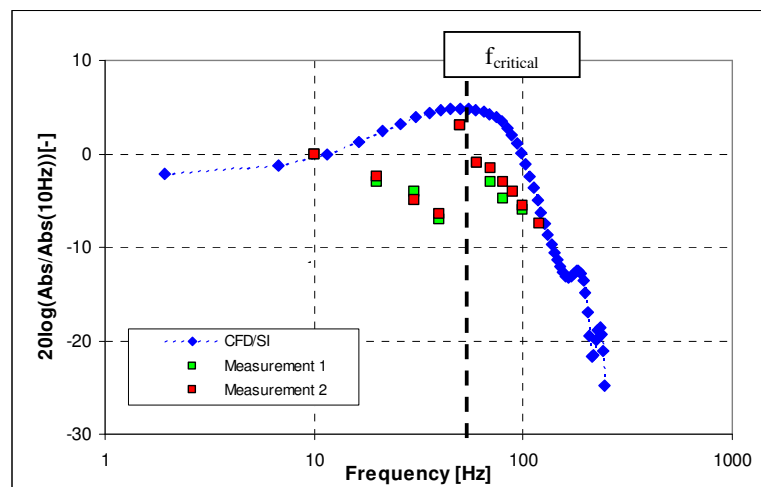


Fig. 8.6 Flame transfer function: normalized amplitude. green and red rectangular – measurements with $P_u=16\%$, blue diamonds – CFD/SI

Moreover, it is found that the absolute values agree qualitatively at ~ 55 Hz and the peak in the amplitude is evident. Both experiment and CFD/SI can capture the sudden increase in the amplitude exceeding unity. The Interpretation of the experimental results by Klsheimer and Bchner et al. [74] is that the increase of the absolute value at about 55 Hz can be explained by the formation and combustion of coherent ring vortex structures. During the formation of the large-scale vortices downstream of the burner exit, unburned fuel/air mixture and exhausted gases are enclosed in the created vortices. The subsequent decrease in the amplitude for frequencies higher than 55 Hz is caused by combustion under more oxygen-diluted conditions due to the additional entrainment of exhaust gases. The dynamical behaviour of the flame cannot be entirely resolved by the k - ϵ turbulent model but the overall trend is reproduced. It looks like CFD is only able to capture the increase of the flame surface (volume enclosed by the flame) caused by the forcing signal but is not able to resolve the flame surface itself accurately. In the LES context, more reliable information related to the formation of the large-scale vortices can be obtained.

In Fig. 8.7, the comparison between measurements and the calculated phase are displayed. The phase decreases continuously with an increase in frequency according to the well-know behavior of the time lag law. The calculated phase shows a relatively good agreement with experimental data. For lower frequencies up to ~ 30 Hz, the phase is predicted reasonably well. However, the CFD-based phase shows a bit smaller timelag values. Using the experimental data the mean timelag can be estimated to be about 16 ms while CFD/SI gives the value of 14 ms. Between the frequencies of 40Hz and 50 Hz, a kind of mismatch with respect to the experimental data and CFD/SI is observed. Trendwise, the phase of the flame transfer function for frequencies higher than 55 Hz is computed correctly and follows the experimental values. On the other hand, the LES results of Selle et al. [76] disagree slightly with the concept of flame dynamics being totally controlled by a global time lag

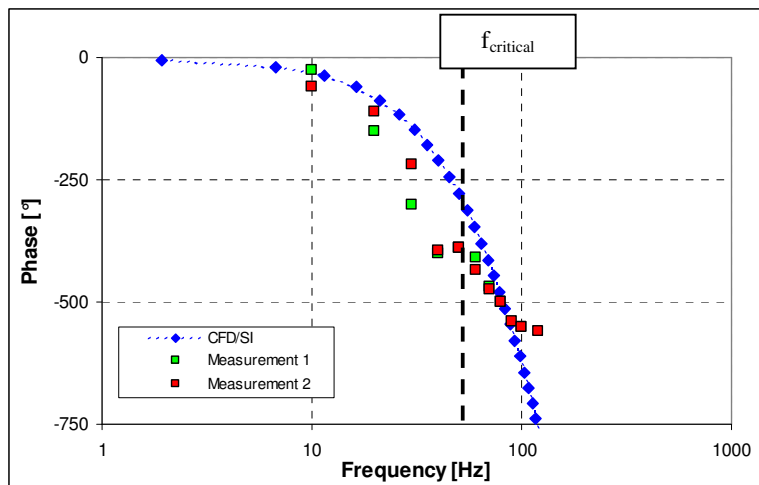


Fig. 8.7 Flame transfer function: phase, green and red rectangular – measurements with $Pu=16\%$, blue diamonds CFD/SI

The LES study has shown that the vortex formation and combustion can be the real mechanism controlling the delay. The outcome of this study is that the correct amplitude and phase distribution

can only be captured when the reacting turbulent flow field accounting for different vortex formation mechanisms is numerically well resolved.

8.5 CFD/SI vs. time lag approach

In this chapter, the phase distribution obtained by means of the CFD/SI method is compared to the conventional time lag approach. The time lag approach has been used successfully in the past to describe flame dynamics [36][85]. The Time lag distribution for the current test case is determined by the Lagrangian Particle Tracking module and solving an additional transport equation for a scalar in the RANS computation. The Lagrangian Particle Tracking module is utilizing the fully developed and converged RANS flow field. An representative fully converged reacting flow used in the time lag calculation is shown in Section 8.3. This method has been implemented into a commercial CFD code and further improved at Siemens. CFX10 has been utilized to perform the so-called particle tracking calculation to provide the CH₄ mass fraction and particle traveling time distributions. The time lag τ is determined by the average value of PDF (Probability Density Function) of the particle time lags. Krebs et al. [36] has presented the formulation of the analytical flame transfer function using a mean time lag value.

Following the computational approach in [36], the mean time lag τ is derived from the RANS computation. The Probability Density Function and Distribution Function (DF) suitable for this case are plotted in Fig. 8.8. Having the probability density function of the particle time lags the distribution function can be estimated. The distribution function can vary from 0 and 1. The mean time lag value is determined based on DF at the position where the DF value is approximately 0.5. In this case, the normalized time lag is 0.5. The estimated mean time lag τ can be then utilized in the analytical n - τ model.

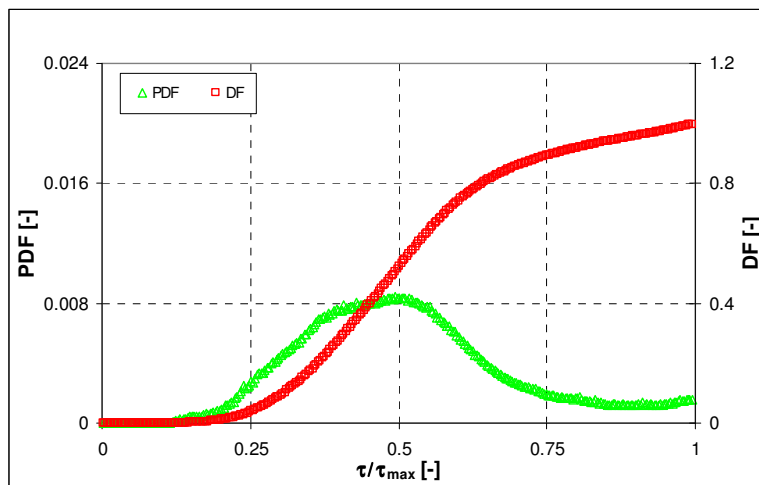


Fig. 8.8 PDF and DF distributions of the atmospheric test rig: green rectangular – PDF (probability density function), red rectangular – DF (distribution function)

More details with regard to the analytical $n\text{-}\tau$ model are given Appendix 0. Fig. 8.9 summarizes the reconstruction of the phase angle based on experimental data, CFD/SI, and time lag. It is shown that the phases at lower frequencies can be calculated accurately by means of steady state computations and the numerical results between different approaches are in good agreement.

It should be pointed out that the time lag approach has already quantified for this configuration by Krebs et al. [36]. The phase of the flame transfer function by means of the time lag approach has successfully compared with the experimental data. In the context of this thesis, a reasonable match especially considering the shape of the calculated phase for both computational approaches has been achieved. It must be added that in the case of the analytical $n\text{-}\tau$ model one sees the uniform phase distribution represented by a mean time lag value. As opposed to the standard time lag model, the CFD/SI approach is capable of providing the frequency dependent phase distribution represented by a time lag distribution.

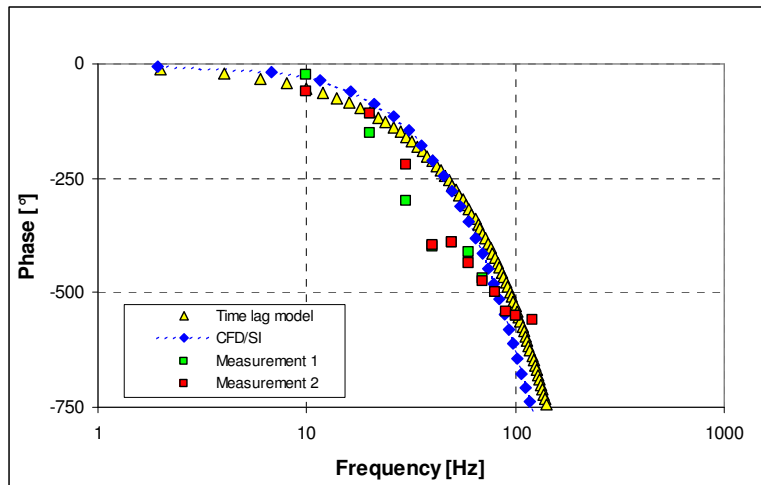


Fig. 8.9 Flame transfer function: phase: green and red rectangles – measurements with $P_u=16\%$, blue diamonds – CFD/SI, yellow triangles – time lag model with $\tau=14.8$ ms based on a RANS simulation

The differences between the measured time lag and the computed time lag may be explained by some inaccuracies in capturing the flame front location. Unfortunately, there is no additional experimental data addressing this issue, which could be used to validate the current combustion model. It is also observed that for frequencies lower than ~ 30 Hz the time lag model slightly differs from the CFD/SI method. For the frequency range between 30 Hz and 70 Hz, the calculated phases are identical. Nevertheless, the overall agreement between both computational methods is good. Some variations of the predicted phases can be observed at higher frequencies where the assumption of a constant time lag does not hold anymore.

8.6 CFD/SI vs. Harmonic forcing

To confirm the shape of the amplitude and phase of the reconstructed flame transfer function, additional unsteady computations with forcing at discrete frequencies have been performed.

In Fig. 8.10, the amplitudes in the logarithmic scale for single excitations are compared to the CFD/SI method. For excitations at single frequencies, the flame transfer function can be calculated using the Fourier transformation of forced signals and responses. This comparison demonstrates the capabilities of the CFD/SI approach with white noise excitation. At about 170 Hz and 200 Hz there are two dip frequencies shown. In general, it means that at these frequencies the magnitude of FTF tries to approach zero. Of course, this behavior cannot be entirely mimicked by using a harmonic forcing function defined only at particular frequencies. Despite small variances in terms of absolute values for higher frequencies, the overall agreement is found to be satisfactory.

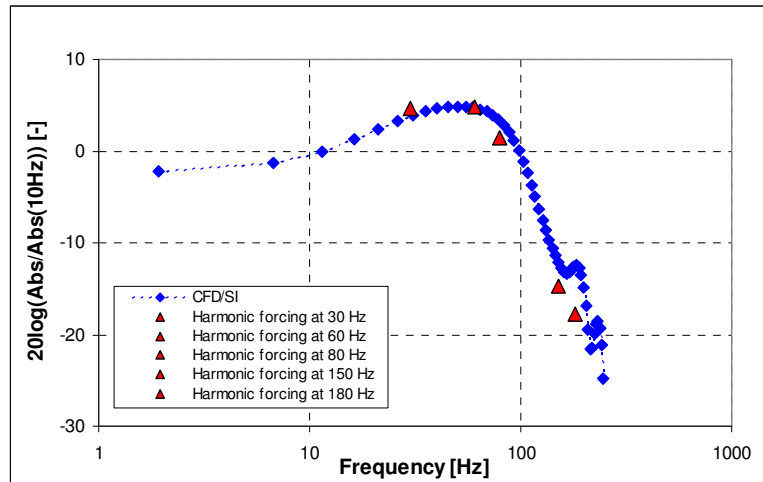


Fig. 8.10 Flame transfer function- Normalized amplitude: red triangles – URANS with single sinusoidal excitations, blue diamonds – CFD/SI

The phase shows a perfect match with the CFD/SI approach. Thus, in terms of computational time required, it is favorable to perform one URANS simulation with a broadband excitation instead of several single runs excited at one discrete frequency

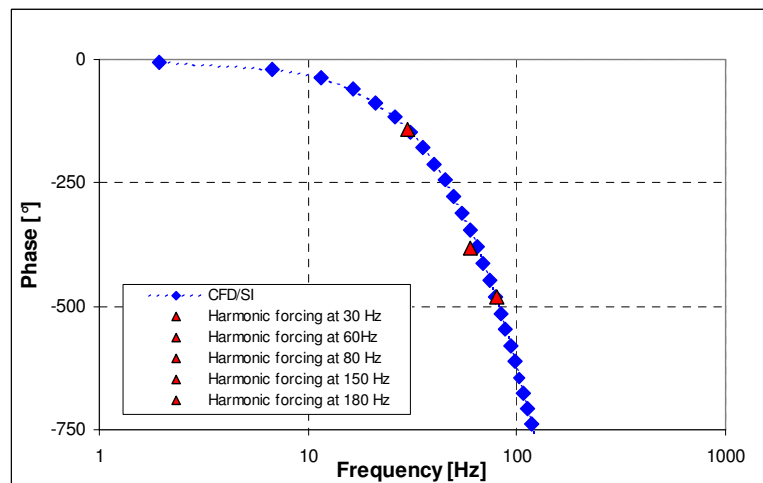


Fig. 8.11 Flame transfer function - phase: red triangles – URANS with single sinusoidal excitations, blue diamonds – CFD/SI

Moreover, the CFD/SI approach is capable of proving the frequency dependent phase distribution compared to the time lag model using a mean time lag value. Sattelmayer et al. [102] has investigated the influence from equivalence ratio fluctuations on combustion dynamics. As a result of this study, it has been proposed to extend the n - τ model to incorporate a time lag distribution instead of using only a mean time lag value.

8.7 Sensitivity study

A sensitivity study has been performed in order to determine some physical parameters or models having an influence on the reconstruction of flame transfer functions by means of the CFD/SI approach. It is found in the literature that combustion modeling could affect flame dynamics by changing flame front locations, which directly affect time lag distributions and the overall heat release. Secondly, turbulence modeling and the way in which the turbulent flow field is resolved may also change the global heat release by varying the molar reaction rate depending on some turbulent quantities. Moreover, the time resolution may also have some influence on the dynamical behavior of combustion systems by an incorrect representation of propagation of acoustic perturbations. If the time step is too large, a given time discretization may be unable to support the propagation of acoustic disturbances and dynamics could be numerically damped. Finally, as stated in previous sections, the CFD/SI method requires proper acoustical treatments of boundary conditions, which may significantly modify flame responses.

8.7.1 Combustion modeling

Three different combustion models are investigated in order to determine their influence on predictions of reconstructed flame transfer functions. These models are the Eddy Dissipation model, the Eddy Dissipation combined with one-step chemistry, and the Eddy Dissipation combined with five-step chemistry.

As a reference case, the reconstructed flame transfer function calculated with the EDM/FRCH concept with one-step chemistry has been utilized. The results obtained with this particular model best matched the experimental data. This reconstructed flame response is already investigated in more detail and the results have been reported in [59]. All unsteady computations have been carried out with a time step of 0.0001 s, with non-reflective boundary conditions at the outlet, and with white noise excitation at the diagonal inlet. The total number of time steps performed is more than 5000.

In Fig. 8.12, the normalized reaction rates taken at the central plane ($z=0$) are shown. The back iso-lines divide the computation domain into three regions. Lack of wall heat losses (adiabatic walls) leading to the flame that is directly located and stabilized between the upper and central shear zone. The flame attaches the combustor walls. However, if heat transfer at walls is considered the nominal flame shape and length can be significantly affected. In fact, by influencing the flame shape and length one has to expect that the flame response is going to be changed. The impact from heat losses on the flame shapes has been investigated in more detail in [122]. It is shown that heat losses significantly

modify the flame shape and length. It is also clear seen that there are some differences in the reaction rate distributions. As known, the EDM-based combustion process can be only controlled by the turbulent quantities (for instance turbulent mixing). Therefore, in this case the calculated reaction rate cannot be modified and is the highest. The largest burning rate causes a rearward shift in the flame location to the burner mouth. It results in the highest combustion rate occurring exactly at the burner exit. As a consequence of this movement, the combustion zone is much shortened compared to the other models, which directly influences the time lag distribution and the phase relation between heat release and pressure fluctuations. Evaluating the EDM/FRCH model with one- and five-step kinetics combustion models (depicted in Fig. 8.12 b and c), one sees from one side the longer combustion zones indicating that the burning rate is reduced comparing to the EDM combustion model and from the other hand the differences in the flame length. Generally speaking, the combined combustion models provide the larger flame lengths due to the lower burning rates. The EDM/FRCH combustion models calculate the reaction rate taking the minimum value from the reaction rate based on the EDM and FRCH combustion model

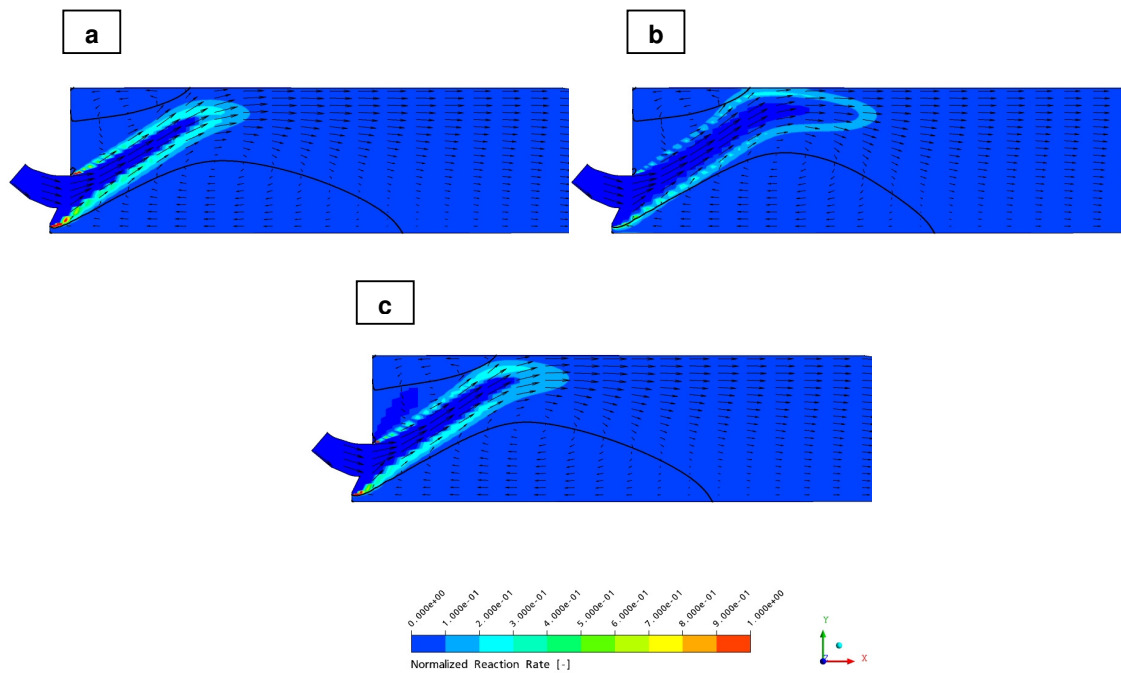


Fig. 8.12 Normalized molar reaction rate: a) EDM, b) model EDM/FRCH, c) model EDM/FRCH model with five step kinetics

The combination of two combustion models based on the EDM and FRCH concept, which uses the global one step mechanism, predicts the size of the combustion zone to be much bigger and more distributed than in other cases. It results in a longer flame, wider time lag distribution, and bigger mean time lag value. Similar to the combustion model with one step chemistry and the model using five step mechanism predict the combustion zone that is bigger than in case of the EDM combustion model fully controlled by turbulent time scale. However, the five-step model gives the combustion zone

significantly shorter than the one- step EDM/FRCH model. The main reason for this is the reaction mechanism used. In this case, CH₄ is initially converted into CO and H₂O and the second reaction finally gives CO₂. Nevertheless, in this analysis only the molar reaction rate involving the conversion of methane species CH₄ into CO is taken into account. The second reaction is fully excluded. This exclusion reduces the volume integrated heat release and makes the heat release distribution much shorter. The entire five step mechanism used in this study is presented in Section 4.2.2.

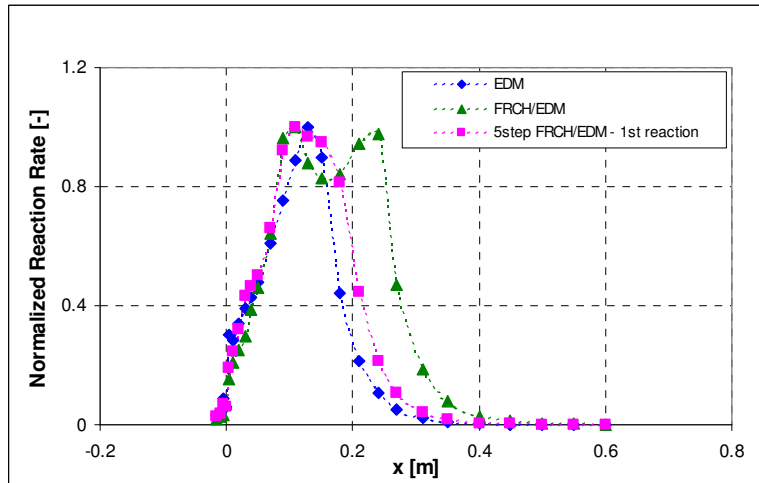


Fig. 8.13 Normalized reaction rate distribution: blue diamonds - EDM, red rectangular - EDM/FRCH with 5 steps chemistry and green triangle – EDM/FRCH with one-step

To be consistent with the time lag calculation using the Lagrangian Particle Tracking module, which is used to track CH₄, all heat release distributions are based on the reaction rates involving only CH₄ conversion. Considering the normalized reaction distribution over the x-axis presented in Fig. 8.13, similar conclusions on the flame length can be drawn. As already discussed, the EDM combustion model indicated by blue diamonds provides the highest reaction rate and therefore the shortest flame what is well indicated here. It is also seen that all maxima are located very close to each other. However, the way in which the time lag values are distributed plays the most important role and has the biggest influence on the flame response.

As opposed to the one-step EDM, the one-step EDM/FRCH model slows down the reaction rate by taking the minimum value calculated based on the EDM and FRCH reaction rate. The slowest reaction rate leads to the brightest axial heat release distribution. Furthermore, as a result of the formulation of this model, one can see two maximum.

As expected, the various flame lengths have a direct influence on the flame transfer reconstruction using the CFD/SI. Fig. 8.14 and Fig. 8.15 show the normalized amplitude and phase of the flame transfer functions in comparison to the experimental data. Indeed, there are some differences noticeable. All magnitude values are shown in the logarithmic scale, and as in the experiment, have been normalized by an amplitude value at 10 Hz where a quasi-steady flame during the experiment is observed. The amplitude of FTF is shown up to 250 Hz because for higher frequencies no response of the flame is noticed. In all cases, two characteristic peaks are shown. The amplitude of the flame

transfer function behaves as a low pass filter. After some initial peaks, it gets reduced with respect to the amplitude at higher frequencies. However, despite small variances in terms of absolute values at higher frequencies, the overall agreement is found to be satisfactory. These differences are mainly caused by the variation in the flame length. The nodal point at which the magnitude of FTF tends to reach minimum is caused by the cancellation of the calculated heat release fluctuations. By definition, if the length of a given acoustic/convective wave is equal to the flame length at a given oscillation frequency the heat release fluctuations cancel out each other and the magnitude is supposed to go to zero. In the current study if one is looking at the axial heat release distributions the following conclusions can be drawn $\tau_{EDM/FRCH} > \tau_{EDM/FRCH\text{with5steps}} > \tau_{EDM}$. Moreover, taking into account the average axial velocity at the diagonal inlet equal to 45 m/s and that the first nodal point for the EDM/FRCH with one step chemistry is located at about 120 Hz, one calculates the length of the convective wave equal to about 0.28 m. The length of the convective wave corresponds well with the flame length representing the flame front location and it proves that the first nodal points can be located at about 120 Hz.

It is pronounced that the flame dynamics of the EDM/FRCH model with one-step chemistry is much weaker than the EDM or EDM/FRCH with five steps chemistry. In all cases, the magnitude of FTF goes down at 120 Hz. Moreover, the dynamics of the EDM/FRCH with one-step chemistry decreases much quicker at higher frequencies.

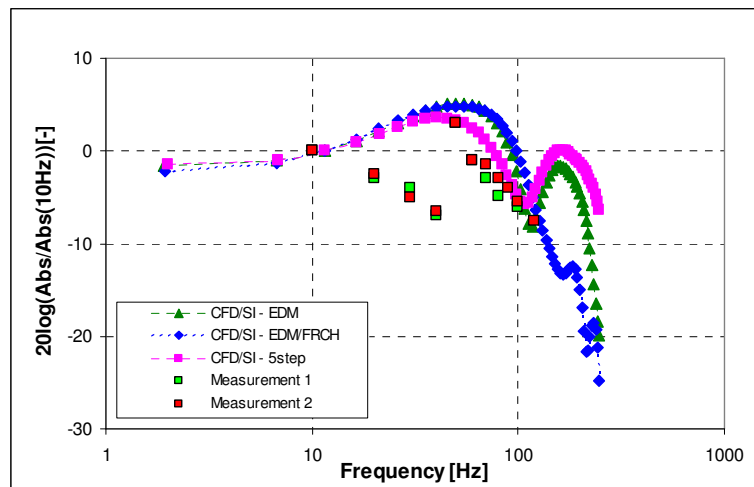


Fig. 8.14 Flame transfer function - normalized amplitude: blue diamonds – EDM/FRCH with one step chemistry, crimson rectangular EDM/FRCH with five steps kinetics, green triangle – EDM, green and red rectangles – measurements with $Pu=16\%$

Nevertheless, these findings are in contradiction with the statement given by Van Kampen in [24]. Van Kampen claims that the amplitude of the flame transfer function can be modeled with a standard time lag model accounting for a time lag spread $\Delta\tau$. The time lag spread correction modifies the magnitude of flame transfer functions and causes a low pass filter-like behavior. The larger time lag spread the lowest frequency where the flame response tends to zero. The results obtained are only partially consistent with the proposed approximation and some discrepancies have been found.

It must also be added here that this type of behavior is characteristic for partially premixed systems. However, there are some similarities with the current fully premixed system especially with regard to the magnitude of FTF found.

The differences in the flame lengths are even more pronounced by the predicted phase in Fig. 8.15. The phase slope of the EDM/FRCH model can follow the experimental results except in the frequency range between 30-50Hz where self-excited oscillations take place. This phase is characterized by the largest time lag of 14 ms while the other characteristic time lag ranging from 10 to 12 ms. These values can be seen as the direct consequence of the heat release distribution. In practice, a time lag value describes the traveling time, which is required for a disturbance to reach the flame front position. These results are in good agreement with the time lag approach and for the longest flame, the largest time lag value is expected which is obviously the case here.

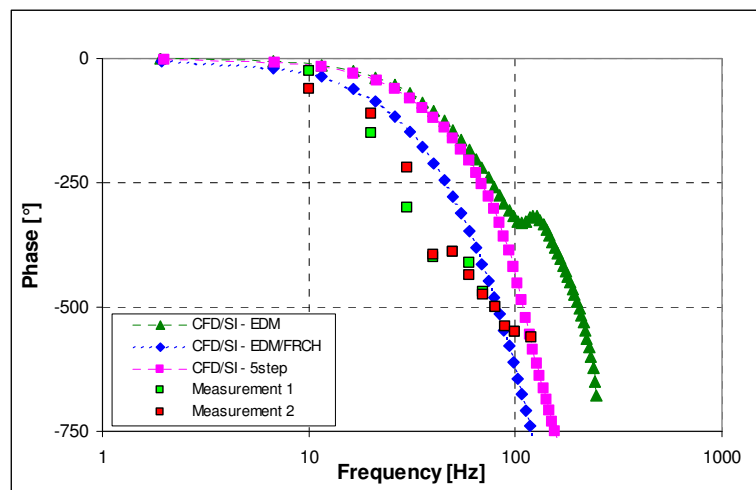


Fig. 8.15 Flame Transfer Function. Phase. blue diamonds – EDM/FRCH with one step chemistry, crimson rectangular EDM/FRCH with five steps kinetics, green triangle – EDM, green and red rectangles – measurements with $Pu=16\%$

8.7.2 Boundary conditions

As pointed out in Chapter 5.4 the proper acoustical representation of the URANS boundary conditions is an important point that should be taken into account when analyzing flame dynamics using the CFD/SI approach. There are many examples in the literature [56][123][124] showing the importance of this aspect on the context of thermoacoustic modeling. Improper acoustic boundary conditions may have an influence on the dynamics of the thermoacoustic system and can lead to the incorrect interpretation of CFD-based results. Additional acoustic reflections occurring on computational boundaries lead to some acoustic waves traveling back into the computational domain, which can start interaction with some eigen modes present in the system and cause unexpected resonance peaks. These aspects may make the CFD/SI approach unreliable for interpreting the dynamics of flames represented by FTF.

The purpose of this section is to show how the numerical results obtained using CFD/SI may be affected by different kinds of acoustic BCs. In general, three different types of BCs are considered, i.e., fully reflective at inlets and outlets. These BCs are usually available as standard BCs in all commercial codes. Then reflective BCs at inlets and non-reflective BCs at outlets and finally non-reflective BCs both at inlets and at outlets can be tested out. These non-reflective BCs do require some special treatment with regards to numerics. A more elaborated report of the implementation procedure is described by Zwart et al. [92] and by Widenhorn et al. [56].

Unsteady computations have been carried out using ANSYS CFX Version 11.0. The latest release of this commercial package enables the choice of different acoustic BCs at outlets and inlets. As a reference test case, the flame response derived using the EDM/FRCH concept with one-step kinetics and the non-reflective boundary condition at the outlet has been chosen. The time step chosen is 0.0001 s and the total number of time steps is about 5000.

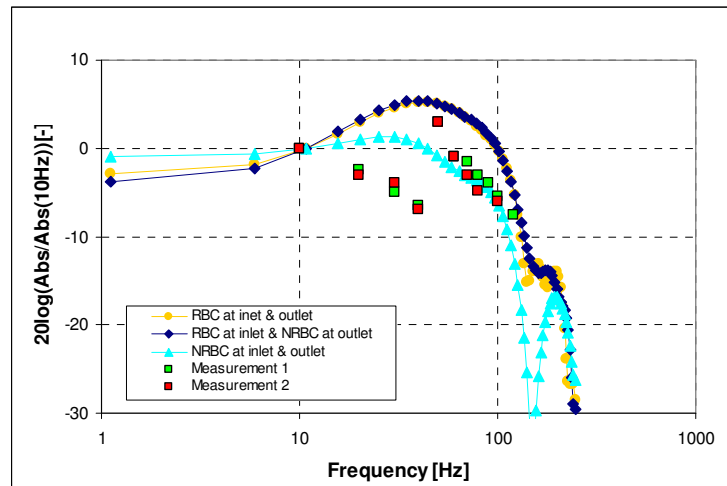


Fig. 8.16 Flame transfer function. normalized amplitude: yellow circle – reflective inlet & outlet, dark blue diamonds reflective inlet & non-reflective outlet, blue triangle – non-reflective inlet & outlet

Fig. 8.16 depicts the reconstructed amplitudes for various sets of acoustic BCs. Similar to the previous plots, the amplitudes have been normalized by a value at 10 Hz and are shown in the logarithmic scale. It is evident that the amplitudes for standard BCs for both the inlet and outlet, and non-reflective BCs at the outlet are almost identical. The peaks of amplitudes at about 50 Hz are also established. At higher frequencies, the flame dynamics tends to decrease again. Contrary to these results, the amplitude for the flame response calculated with both non-reflective BCs does not increase suddenly but increases almost constantly following the measurements. There is no strong peak observed at the frequency of about 50 Hz. It looks like that the reflected acoustic wave can change the reconstructed magnitude of FTF. In addition to this, the amplitude shape better fits to the experimental data and increases a bit faster giving the maximum value at about 35 Hz. Considering the measurements, an increase of the amplitude is evident. According to an interpretation of Lohrmann et al. [74], an occurrence of ring vortex structures leads to an overshoot in the measured

amplitude. Indeed, it is proven by Giauque et al. [37], that the ring vortex structure is responsible for the observed increase. Nevertheless, one knows that to reproduce well some coherent structures more sophisticated turbulence modes are required.

Comparing the magnitude of FTF from the experimental test rig with the URANS computations with the reflective BCs and with only non-reflective outlet, it looks like the CFD runs can replicate the resonance within the combustion chamber that most likely triggers the flame response. As a consequence, it causes an over-prediction in the FTF amplitude. Further, the amplitude distribution can be to some extent explained by interpreting the results obtained with non-reflective BCs. In case of NRBCs, the resonance effect has not been observed and the flame response has not exceeded unity significantly. The second maximum arises but it is not modified by any resonance effects.

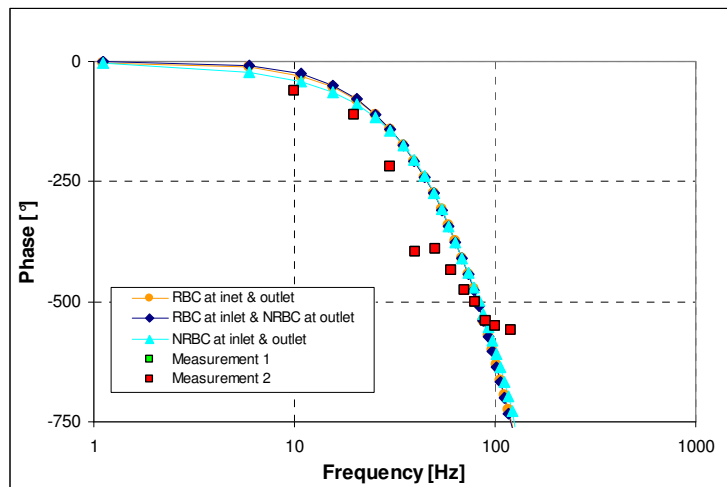


Fig. 8.17 Flame transfer function - phase: yellow circle – reflective inlet & outlet, dark blue diamonds reflective inlet & non-reflective outlet, blue triangle – non-reflective inlet & outlet

Moreover, it is worth mentioning the overall shape based on the experimental data and CFD are very similar to each other. However, the shape of the CFD-based magnitude is shifted a bit to higher frequencies. It is directly related with the characteristic time lag distribution.

In Fig. 8.17 the reconstructed phases are given. They do not differ much from each other, with only some negligible differences at lower frequencies. For these phase predictions, it seems that this type of BC's does not play a role. In general, it looks like an additional reflected acoustic wave can affect the flame response significantly but cannot modify the reconstructed phase.

8.7.2.1 Harmonic excitation at 60 Hz

To examine the mechanism causing the amplitude overshoots, the harmonic excitation at 60 Hz has been applied and the influence of the different acoustic boundary conditions is investigated. To evaluate the results described above, only two cases i.e. the reflective and non-reflective boundary conditions at the inlet and the outlet are taken into account.

Time evaluation of the normalized heat release response is plotted in Fig. 8.18. The heat release has been normalized with respect to its average value

As expected, there are some noticeable differences between these two kinds of BCs. First of all, the calculated flame responses, represented here by the volume integrated heat release fluctuations, exhibit the shape of a harmonic function. However, it is seen that the calculated shape of this function does not reproduce a perfect sinusoidal function. There are some non-linear effects, which have been captured by CFD and which tend to modify slightly the original shape imposed by forcing. On the other hand, it is also shown that the absolute values oscillate between $\pm 21\%$ of the mean HR. It must be added that the largest heat release response is observed in the case of RBC. The reason for these observations can be explained with the help of the reflected pressure waves occurring in the computational domain. Of course, it can be speculated about different roots of these differences. If one comes back to RANS equations, which can be used to solve a reacting flow. The first possibility is that the reflected waves due to the compressibility of the fluid affect local velocity distributions. To keep mass flow rate through the combustor constant the local density must change. Consequently, the calculated turbulent viscosity, turbulent kinetic energy and turbulence dissipation rate change. Finally, these mainly local variations have an effect on the molar reaction rate that is well reproduced by the time evaluation of the heat release. Analyzing this behavior from the flame response point of view, the other possibility is that even though the combustor is only forced at one frequency the flame has to respond to the forcing function at 60Hz and to the reflected pressure wave. The flame starts also interacting with the reflected acoustic wave and modifies the calculated molar reaction rate. This can be seen in the volume integrated heat release fluctuations.

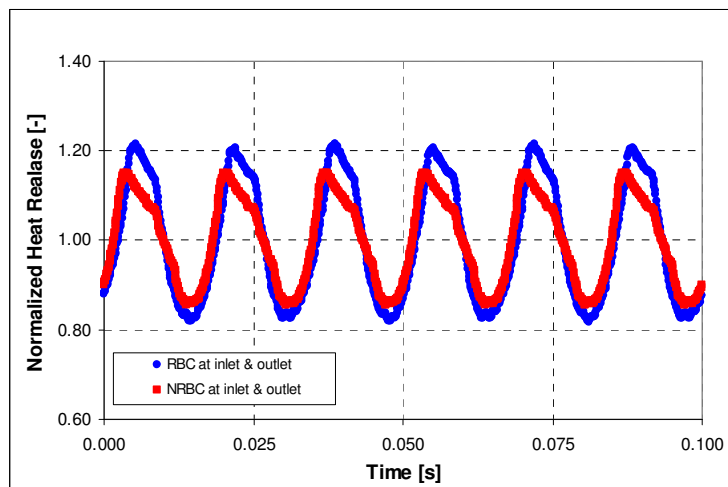


Fig. 8.18 Normalized heat release time evaluation at 60 Hz: blue circle – reflective inlet & outlet, red rectangular non-reflective inlet & outlet

Fig. 8.19 depicts the pressure time evaluation of the same monitor points for the investigated cases. Analyzing the pressure signals in the case of the flame response calculated with non-reflective BCs, a simple characteristic forcing frequency at 60 Hz can be found.

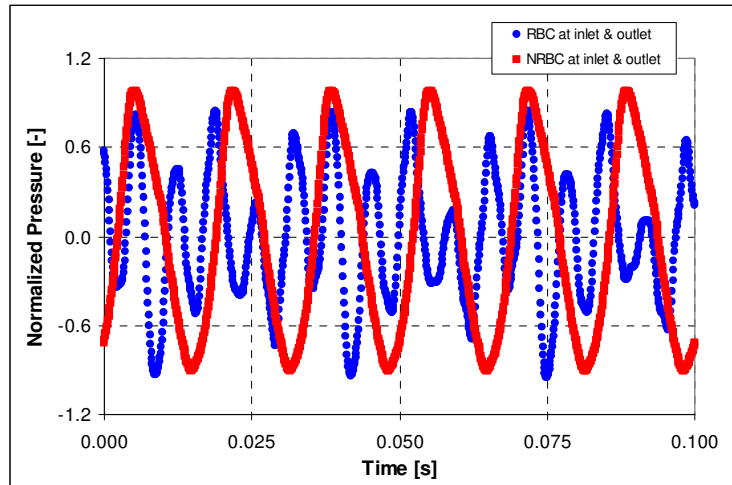


Fig. 8.19 Normalized pressure time evaluation at 60 Hz: blue circle – reflective inlet & outlet, red rectangular – non-reflective inlet & outlet

Moreover, looking at the pressure evaluation in time for the flame response using standard BCs, it is seen that the pressure fluctuations are much stronger and the applied harmonic forcing is comprised not only of a single frequency but also of other components - most likely of higher order harmonics. It is granted that in this case the pressure signal results from a superposition of some different frequency components. The main component originates from the applied harmonic forcing at 60 Hz and the remaining components probably originate from a reflection on the boundary of the CFD domain.

These different frequency components can be determined using the Fourier transformation. The frequency spectrums for two pressure time series are provided in Fig. 8.20

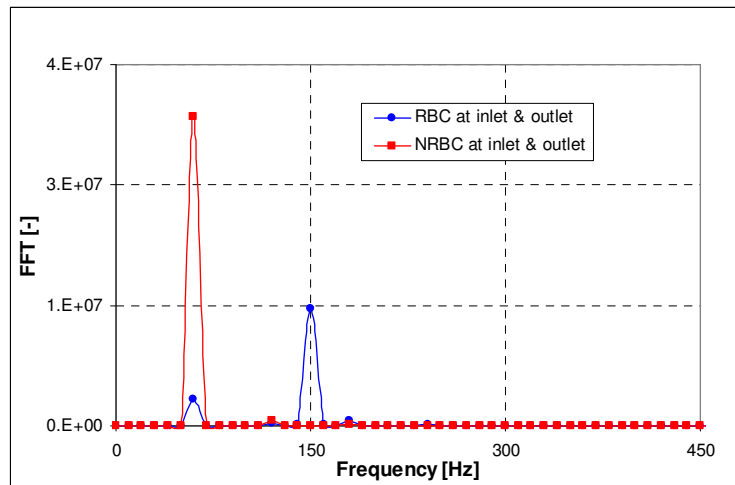


Fig. 8.20 Fast Fourier transform of pressure at the same monitor point: blue circle – reflective inlet & outlet, red circle – non-reflective inlet & outlet

. In case of NRBC, the frequency at 60 Hz and some very weak higher order harmonic are shown. On the other hand, in the case with RBC two characteristic peaks at 60 Hz and 150 Hz are pronounced. Fourier transformed pressure signal is clearly showing the second frequency component.

However, the origin of this peak at 150Hz cannot be simply identified. The frequency of the second peak is somewhat unexpected. To make sure that these numerical findings are correct the RANS calculation with forcing at 60 Hz and the FFT transformation must be repeated. One hypothesis is that the second peak originates directly from a reflection.

8.7.3 Time resolution

It is also important to study the influence from time resolution represented here by the time step Δt in URANS computations on the CFD/SI method since time resolution may strongly modify the propagation of acoustic disturbances. To avoid the influence from the applied acoustic BCs, all cases have been calculated with NRBCs and the FRCH/EDM model with one-step chemistry is utilized. Similar to the previous analysis, the number of time steps is defined to be about 5000.

In Fig. 8.21 the normalized amplitudes for different time step sizes are shown. The calculated amplitudes do not match the experimental data with respect to the maximum amplitude. However, using NRBCs is helping minimize the numerical reflection at the boundary. By minimizing the acoustic reflection at the inlet and outlet, the risk of showing up some resonances in the system is considerably reduced. It is well known that additional reflected pressure waves can have the direct influence on the absolute value at a given resonance frequency. It can cause the magnitude of FTF to exceed unity. It is also seen that the calculated magnitude has a bit different shape. By reducing the interaction between forcing and resonance, one makes the maximum magnitude more flat. On the other hand, the magnitude distribution has an additional peak at about 70 Hz.

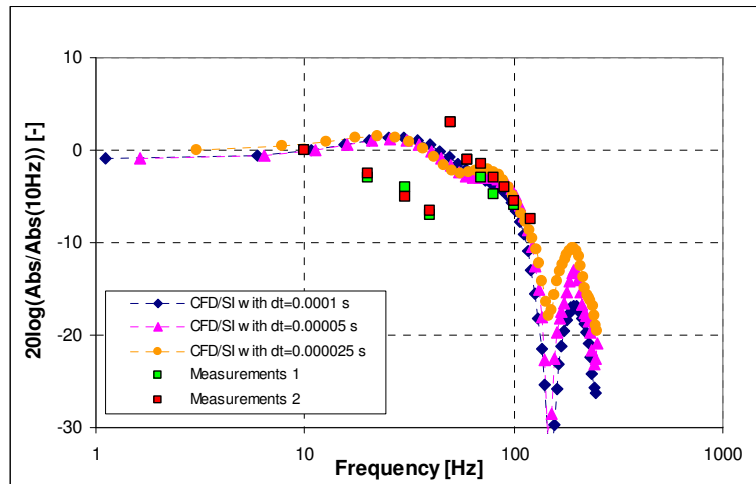


Fig. 8.21 Flame transfer function: normalized amplitude: orange circle – $\Delta t = 0.000025$ s, pink triangle – $\Delta t = 0.00005$ s, blue diamonds – $\Delta t = 0.0001$ s

The overall agreement between different time steps is found to be satisfactory. Up to the frequency of about 35 Hz, the time step used seems not to play any role. The small differences at higher frequencies are observed at which the number of intermediate time points come into play. At about 130Hz, the third peak in the calculated magnitude of FTF is captured. These three time steps are able to reproduce the third amplification in the flame response reasonable. In the case of the time step equal 0.0001 s, the third peak is captured but the absolute value of this peak is smaller compared to the other cases.

In general, the reconstructed flame response amplitudes show agreement with the numerical results obtained with time step sizes ranging from 0.000025 to 0.0001 s.

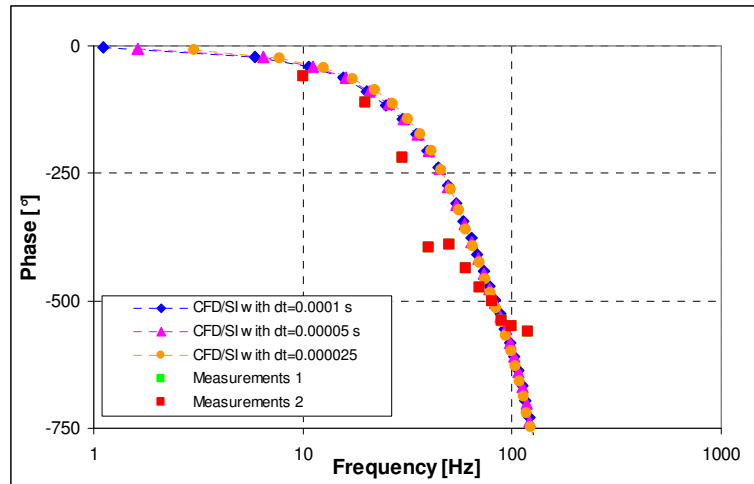


Fig. 8.22 Flame transfer function: phase: orange circle – $\Delta t = 0.000025$ s, green triangle – $\Delta t = 0.00005$ s, blue diamonds – $\Delta t = 0.0001$ s

As plotted in Fig. 8.22, the utilized time steps do not have any influence on the phase angle based on the results from CFD/SI. It is possible to draw a conclusion that using even bigger time steps in the order of 0.0001 s, one can reconstruct the phase with reasonable accuracy.

9 Industrial test rig with a generic burner at elevated pressure

An industrial test rig with a generic burner has been built by Siemens to test a prototype combustion system operating at elevated pressure with respect to combustion dynamics. The experimental test rig is selected to apply the CFD/SI method to estimate the flame response to velocity (volume flow) fluctuations at the main burner exit. The other reason is to find out whether the prediction of thermoacoustic stability characteristic to this prototype combustion system can be improved using the CFD/SI-based flame transfer functions.

In addition to this, the reconstructed phase of the flame transfer function is compared to the conventional time lag approach. Moreover, the flame responses based on different computational approaches are used in the TMA model and a thermoacoustic stability analysis to determine unstable frequencies is performed. Finally, some pressure spectrums coming from the measurement campaign are utilized to validate numerical results from the TMA model (one-dimensional acoustic network code).

The simplified test facility setup with a prototype combustion system shown in Fig. 9.1 consists of a support housing, fuel system, combustor basket and transition part. The prototype combustion system utilizes four fuel stages: A, B, C and D.

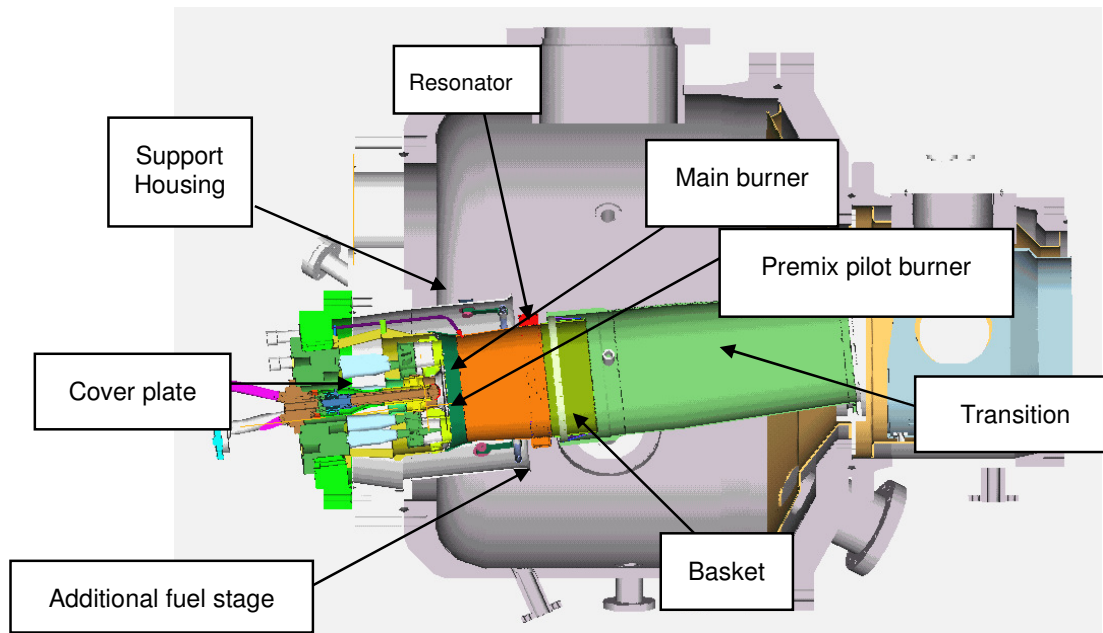


Fig. 9.1 An industry test rig with a prototype combustion system

Having this kind of fuel distribution gives more flexibility in operating such a system. The C stage is located upstream of the main burner and is used to improve the mixing process in the fuel line and per definition is supposed to help in tuning the dynamic characteristic of this prototype gas turbine combustion system.

In addition to this, to be more precise, the combustor basket is compound of a forward section, base plate assembly, and liner. The upstream end of the combustor basket is connected with a cover plate. On the other combustor side, the downstream end of the combustor basket has an interface with the cooled transition. In order to control and to damp thermoacoustically-induced oscillations at higher frequencies there are some resonators mounted on the basket sidewall.

9.1 URANS Modeling

The analysis model is an $1/8^{\text{th}}$ sector of the combustion system consisting of the burner outlet, basket and extended liner. The CFD model with a transition piece and the numerical boundary conditions are given in Fig. 9.2. The computational domain for this test case starts downstream of the main and pilot swirl vanes and ends at the transition exit mouth. A hexahedral mesh consisting of about 2,000,000 nodes having determents above 0.35 and angles larger than 18 degrees is utilized.

Similar to the atmospheric test configuration, the mixing calculations to extract the inlet profiles are made separately and prior to the reacting flow study. This assumption allows significantly reduced computational costs of unsteady simulations. By making this simplification, it is assumed that the extracted profiles can fully reproduce the flow field at a given cross section. The other assumption is that there are no interactions between the swirler vanes, upstream plenum, and nozzle exit, which may lead on the one hand to some hydraulic instability [125] and on the other hand to thermo-acoustic instabilities [100].

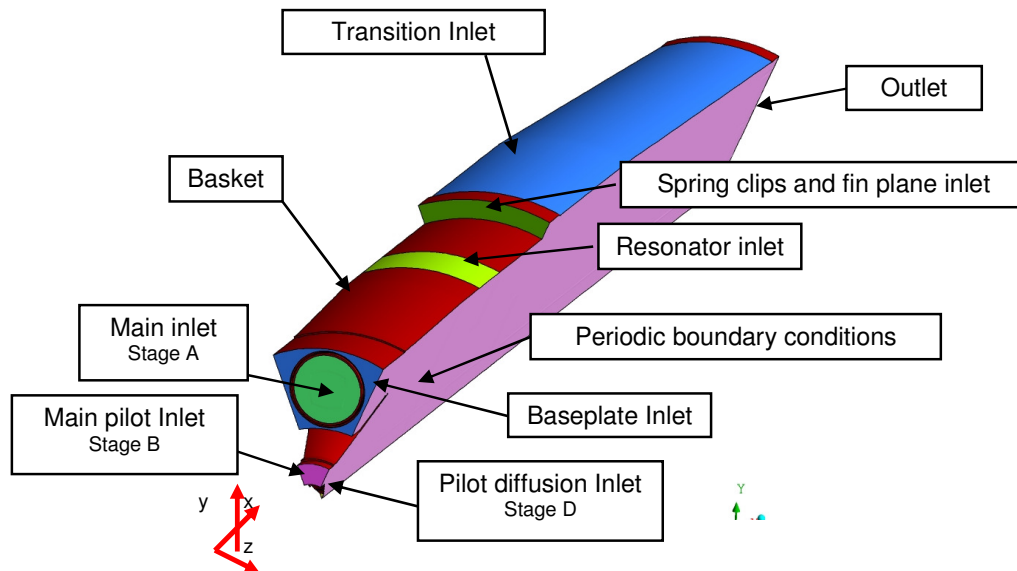


Fig. 9.2 CFD boundary conditions for a $1/8^{\text{th}}$ sector model

However, it seems to be a valid action because in the current forced response analysis, one only has to take into account the flame response to a forcing signal induced by mass flow rate fluctuations. No additional coupling mechanism between self-excited combustion dynamics and flame is considered.

Thermodynamic conditions are specified according to the full load test conditions. The test rig operated at elevated pressure and with preheated air. The total amount of fuel is split over the main fuel stages in the following percentage: ~73,5% for the main inlet and ~10% for the pilot main inlet. The remaining fuel mass flow is utilized in the fuel stage C located further upstream to enhance the mixing process and in the diffusion pilot. Secondly, the cooling mass flows especially those going throughout the resonator, spring clips and fin plane, and transition sections are considered.

As mentioned above, the mixing passages are not implicitly resolved in the considered model. There are separate mixing calculations for the main A and B swirl vanes have made in order to provide two-dimensional profiles of velocity, fuel concentration, temperature, and turbulence prior to the reacting flow computation. Sample normalized axial velocity and CH₄ Mass Fraction distributions for the main section are given in Fig. 9.3 a and b.

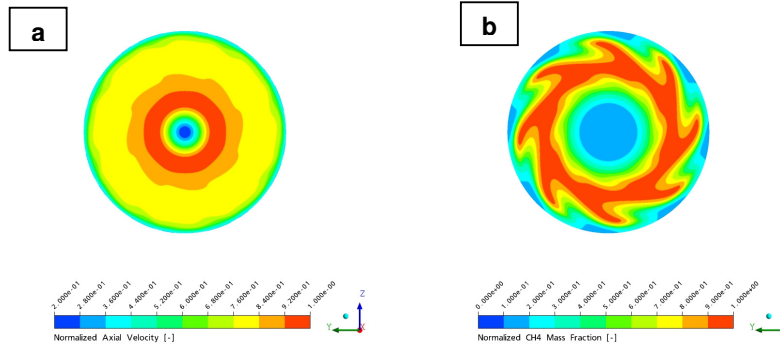


Fig. 9.3 Normalized velocity and CH₄ mass fraction for the main inlet A

Since the flame response on acoustic perturbations is considered, all calculations are performed taking into account the compressibility of the flow. The 2nd order Euler backward discretization in time and the high resolution scheme for spatial discretization are used [15].

Spatial discretization	High resolution
Time discretization	2 nd order Euler backward
Fluid Model	Compressible Gas
Turbulence Model	k - ε
Combustion Model	EDM/FRCH with one step chemistry
Heat Transfer	Total Energy
Time Step	1.e-4 s
Time Steps	5000

Tab. 9.1 Numerical models - Industrial Test Rig at elevated pressure

Since it is only needed to reproduce a volume integrated heat release within the combustion chamber, the Eddy Dissipation concept combined with one-step kinetics is employed to model the combustion process [16]. The numerical models used are given in Tab. 9.1

The URANS simulation is performed with the time step of 0.0001 s thus enabling the frequency resolution up to 5000 Hz. Moreover, the non-reflecting boundary condition implemented in CFX10 at the outlet of the transition is applied. To analyze only an influence of the volume flow fluctuations on the overall heat release, the total mass flow at the main inlet A is perturbed with the white noise excitation, while the equivalence ratio is kept constant. The excitation amplitude is equal to 10% of the averaged axial velocity. As shown by Gentenmann et al. [43] forcing only axial components can lead to the swirling velocity fluctuation, which can affect the flame response. To avoid additional dynamics caused by a change in the swirl number [126], all three-velocity components are simultaneously perturbed with the same forcing signals.

9.1.1 Steady State Solution

Fig. 9.4a provides the normalized axial velocity distribution at the monitor plane located at $z=0$ m. It is apparent that the flame is stabilized between the central recirculation zone and the outer basket wall. The main burner has a relatively high swirl number compared to the pilot burner swirl number. The flow is expanding through the main burner section obtaining the highest velocity at the main pilot burner cone due to a change in the cross-sectional area. In addition to this, some small regions with negative axial velocities are found. These zones are mainly located at the spring clips and plate fin inlet and result from an additional cooling mass flow injection.

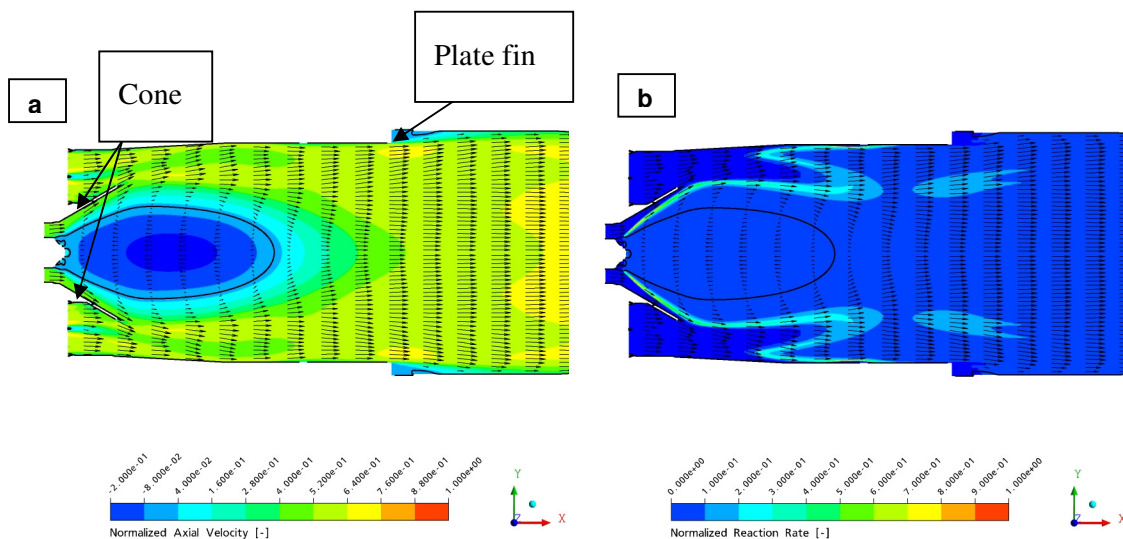


Fig. 9.4 Normalized axial velocity distribution and normalized molar reaction rate distribution at $z=0$ m.

The normalized reaction rate distribution is depicted in Fig. 9.4b. The reaction starts at the diffusion holes going further over the pilot cone and reaches the maximum rate at the basket wall close to the

resonator inlets. The flame front location can be easily determined. Using the different swirl numbers for the main and main pilot inlet allows for splitting the main molar reaction rate into two separate regions. The larger amount of fuel seems to be burnt out above the central recirculation zone and still far away from the outer basket wall. The larger flame is moved towards the central line in the combustor. The second part of the flame is attached to the outer wall. There is also some reaction going on located further downstream in the basket. However, it looks like this is not dominant and most likely does not affect the over flame response much.

9.2 Reconstruction of flame transfer function

The CFD/SI approach is utilized to reconstruct the flame transfer function induced by velocity fluctuations. The calculated flame response is supposed to reproduce the interaction between the axial velocity fluctuations originating at the main inlet (fuel stage A) and the integrated heat release fluctuations. Because of the fact that the estimated dynamical flame response is applied in stability analysis, a broad frequency range (white noise) is considered. The highest frequency at which an occurrence of first transverse modes is expected is covered.

In addition to this, the CFD/SI application is validated with a harmonic forcing function. By using this kind of forcing, one is able to force the entire system at discrete frequencies and to obtain the flame response. The flame transfer function, which is obtained at discrete frequencies, is then utilized to compare with CFD/SI. In this case, as is shown below the satisfactory results are obtained. After evaluating the least square error of L for CFD/SI, the L parameter is estimated to be 230 and is then used in the identification procedure. The reconstructed flame transfer function is given in Fig. 9.5. The amplitude is normalized by the amplitude close to 0 Hz. The frequency is represented by the Strouhal Number up to a value of 1.0.

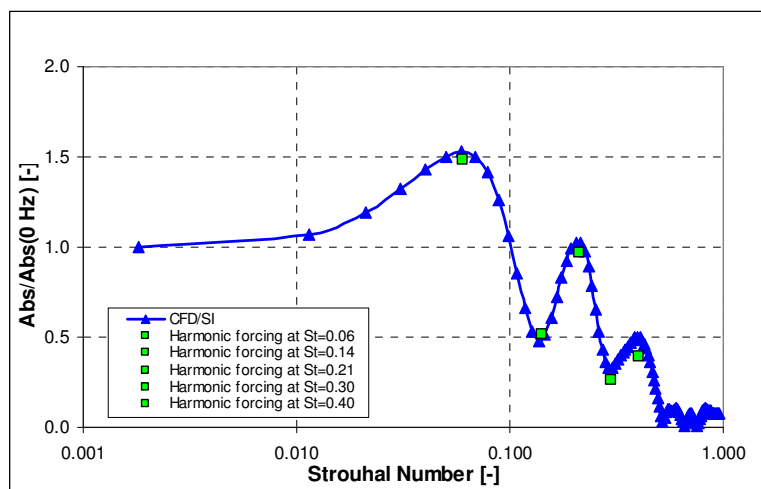


Fig. 9.5 Flame transfer function: normalized amplitude, blue triangle – CFD/SI, green rectangular – harmonic excitation

The highest dynamics at about $St=0.080$ is observed. As expected, the flame behaves as a kind of low-pass filter and at higher frequencies the amplitude decays asymptotically indicating that the thermoacoustic system cannot respond anymore on the applied perturbations.

The first dip frequency refers to the characteristic frequency at which the flame length is approximately equal to the length of acoustic wave. It means that the heat release oscillations cancel each other out within one oscillation period. On the other hand, it can be concluded that the response itself is too small and cannot change the overall dynamical characteristics of the entire system. The reproduced maximum values can be an indication of some additional thermoacoustical or hydraulic mechanisms, which are partially captured by URANS and which can play a role in the stability of this prototype combustion system.

The reconstructed phase of the flame transfer function is shown in Fig. 9.6. Overall, it looks like that the flame dynamics is represented by the time lag. A slope of the phase angle indicates that the global time lag value corresponds to the time needed for a disturbance to reach the flame front location and to cause the flame response.

In general, one can conclude that as opposed to the standard time lag model, the CFD/SI-based phase angle is characterized here by the time lag values, which are not constant over the frequency range and changes dynamically. The other words it means that the time lag value is changing for each frequency. Of course, this behavior strongly depends on gas turbine combustion systems of interest.

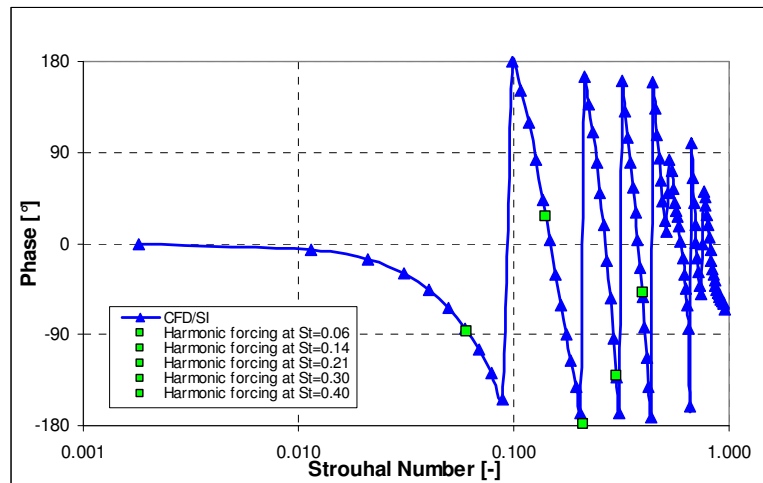


Fig. 9.6 Flame transfer function: phase angle, blue triangle – CFD/SI, green rectangular – harmonic excitation

9.3 Experimental pressure spectrum measurements vs. stability prediction based on a one-dimensional acoustic network code

The main purpose of this chapter is to compare the experimental pressure spectrum measurement made in the basket of the prototype combustion system with a stability prediction based on the one-dimensional acoustic network code. This acoustic network code is already introduced in the previous chapters.

It is already demonstrated many times in the literature [5][28][44][96] that in general one-dimensional acoustic network codes are able to capture dynamics of a system at lower frequencies. On this basis, the acoustic matrix approach (TMA) assessing one-dimensional acoustic wave propagation is used to acoustically model the prototype experimental test rig at elevated pressure.

The TMA model of the considered combustion system starts at the air inlet duct. This model does not include the compressor section. The inlet boundary cross-section is assumed to be anechoic meaning that acoustic wave traveling into the air inlet duct is entirely absorbed. Moreover, all fuel stages, the flow sleeve inlet and the plenum itself and the exhaust pipe are also considered in the stability prediction.

Since an assumption with regard to the thin flame model is utilized, the location of maximum heat release is represented by a single location and is found to be close to the resonators. The location on the flame element is determined based on the CFD computation provided.

9.3.1 CFD/SI vs. time lag approach

In the TMA model, two different computational approaches representing dynamic flame responses are utilized in order to predict unstable frequencies. As in the case of the atmospheric test rig with a prototype burner, the first approach utilized is the standard time lag model based on steady state computations to characterize the flame behavior.

The normalized time lag distribution showing PDF (Probability Density Function) and DF (Distribution Function) is given in Fig. 9.7. The time lag value is calculated based on DF, which is 0.5. It is found that the normalized time lag value of about 0.14 corresponds to DF=0.5. As expected, it differs from the value estimated based on CFD/SI. In contrast to the standard time lag model, CFD/SI is able to provide the time lags, which are a function of frequency and accounts for the changes in flame dynamics. The comparison between the phase distributions estimated on the standard time lag approach and CFD/SI is depicted in Fig. 9.8.

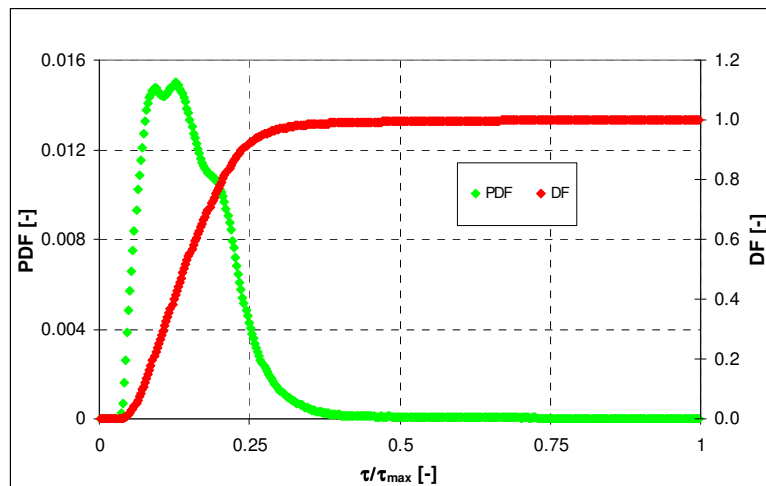


Fig. 9.7 PDF and DF distributions: green rectangular – PDF (probability density function), red rectangular – DF (distribution function)

It is seen that especially the phase calculated with CFD/SI changes significantly at lower frequencies compared to the time lag based on RANS. These variations in the phase between the CFD/SI approach and the standard time lag model are very noticeable and may cause some changes in the stability of the system. The phase based on CFD/SI shows a very weak or almost no flame response at higher frequencies, as should be the case here. As opposed to the CFD/SI approach, the standard model shows that there is still a relationship between heat release and velocity fluctuations.

With regard to the amplitude, it can be shown that in the time lag model the amplitude is kept constant over frequencies. The time lag model in details is presented in Appendix 0. The correction term introduced in the time lag approach proposed first by Sattelmayer et al. [102] can partially mimic the real flame behavior and cause a decrease of amplitude values at higher frequencies. However, it must be pointed out that the proposed time lag model is meant to be use to model FTF induced by phi fluctuations.

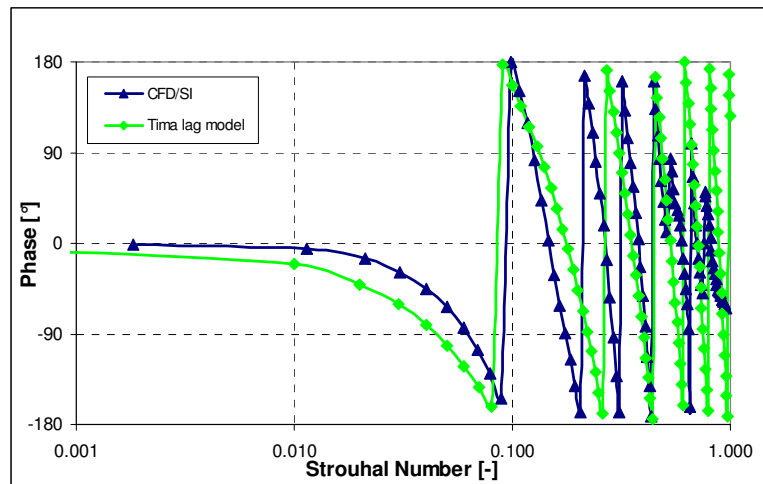


Fig. 9.8 Flame transfer function: phase: green triangles – time lag model, dark blue triangles – CFD/SI

9.3.2 Stability prediction based on CFD-based transfer functions

Comparing these both computational approaches to model FTF, it may be expected that utilizing CFD/SI one can improve the prediction of thermoacoustic stability. It has already been shown that the amplitude and phase of the reconstructed flame transfer function in contrast to the standard time lag mode is also a function of frequency and does not have a constant value over frequencies of interest.

Fig. 9.9 gives the simplified original sketch of the one-dimensional acoustic network model (TMA). It shows the complexity of the gas turbine combustion system. The model consists of several simple acoustic elements such as ducts, diffusers and area discontinuities used to model one-dimensional wave propagation in the experimental test rig. The acoustic element responsible for the correlation between heat release fluctuation induced by equivalence ratio fluctuation and total mass flow fluctuation is the flame element. These two mechanisms are taken into account by this multi-port flame element. The flame element acoustically connects all fuel stages by means of flame transfer functions. The flame element is located exactly at the axial position where a flame in the combustion chamber is found.

To gain some confidence regarding the TMA stability prediction, a simple sensitivity analysis is performed. It is necessary to use TMA and to see whether TMA can respond to a small change in the mean time lag value. It is also needed to clarify if these small changes in FTFs can be reflected in the stability map. Of course, to be able to isolate all interactions between different flame transfer functions, FTF induced by Φ is not changed and only FTF induced by u' is being varied. In this case, the standard time lag model is utilized to represent both types of flame responses. Performing the TMA sensitivity analysis with FTF induced by u' allows for capturing some changes in the overall system characteristics. As written above, it is assumed that only the mean time-lag value representing the phase of the flame transfer function induced by u' is being changed. This phase defines the relation between heat release and acoustic velocity fluctuations. Indeed, some small variations change significantly TMA-based stability map. The damping values can be widely changed, which is directly reflected in the thermo-acoustical stability of the entire system. The reference mean time lag is scaled up and down from -15% to +15% of its mean value and the calculated stability map by means of the TMA damping values are plotted below in Fig. 9.10. The negative damping value means that the considered system becomes unstable whereas the positive ones define the stable system. From the gas turbine operation point of view, this state should be avoided at any time during the operation of gas turbine combustion systems. As opposed to the experimental data (two distinct pressure peaks) the TMA analysis has provided more eigen modes of the systems. However, from the numerical standpoint one should only look at these modes located close to these strong pressure peaks from the measurements. It is seen that scaling down and up can slightly change the calculated damping coefficients much. Overall, it appears that at all calculated frequencies the change in the main time lag value does affect the TMA stability analysis

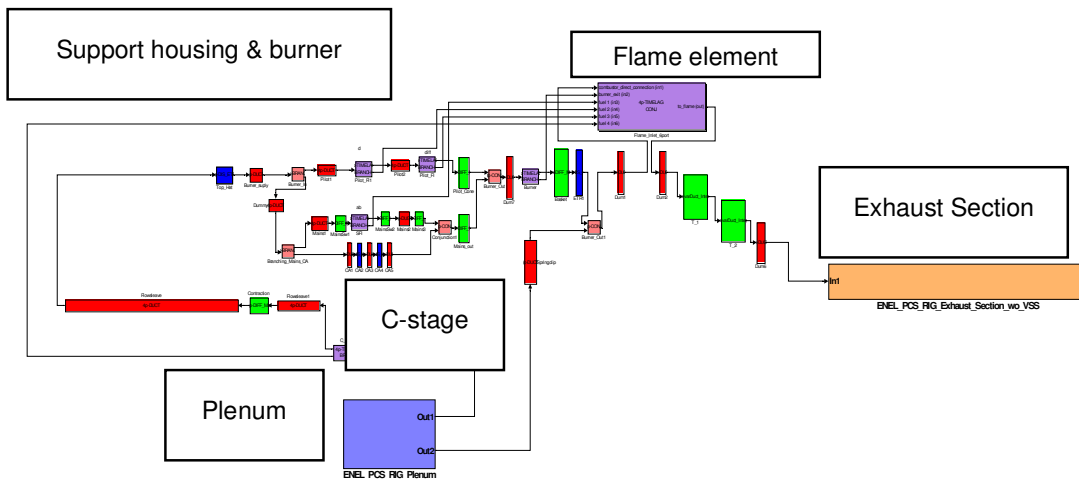


Fig. 9.9 TMA model of industrial experimental test rig at elevated pressures

It is also shown that the increase of the main time lag value moves slightly the damping coefficient to the region with more negative values. Within this region, the prototype gas turbine combustion system is forced to become unstable and the most pronounced influence can be found at about Strouhal Number (St) equal 0.19.

In the case of the second pressure peak, the scaled up time lag forces the entire system to be more unstable and much closer to the experimental results. This kind of analysis assures that TMA is capable of capturing small changes in FTFs. Therefore, TMA can be used to compare CFD/SI and standard time lag – based FTFs with respect to the gas turbine combustion system stability.

It must be added that there is scatter in the pressure data that can make this kind of analysis very difficult to interpret. For the purpose of this thesis, only single pressure spectrum from the steady operating point has been taken and used as a reference point.

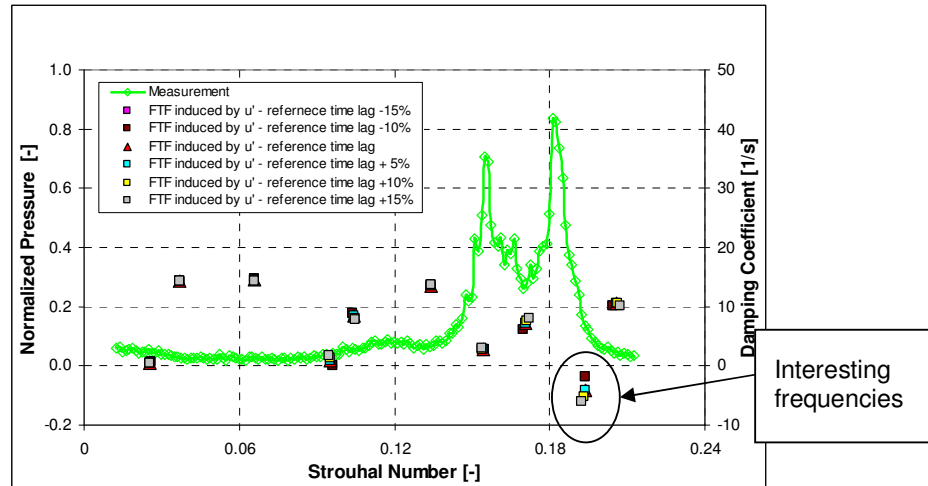


Fig. 9.10 TMA sensitivity to a small change in the mean time lag value: rectangular - TMA with FTF induced by u' (based on the time lag approach) with different mean time lag values, green diamonds - measurements

In order to compare the stability map calculated based on the CFD/SI and time lag approach, two test cases have been calculated. The first case uses the n - τ model for both mass flow (velocity) and equivalence ratio fluctuations. This model has already been introduced in the previous chapters and even more details can be found in Appendix 0. In the second case, the CFD/SI method is employed to model the flame response due to total mass flow fluctuations and the n - τ model to characterize all equivalence ratio fluctuations. In addition to this, the reconstructed flame transfer function has been scaled down to match the initial flame response magnitude at lower frequencies, which is used in the first case. In this stability prediction, the k constant from the n - τ model representing the flame response to velocity fluctuations is assumed 0.5.

The prediction of the unstable frequencies using TMA is compared with the experimental measurements. During the experiments there are only two strong unstable frequencies at about $St=0.15$ and about $St=0.18$ detected. On the left hand side of Fig. 9.11 the normalized pressure spectrum recorded during the experimental run is shown. On the right hand side of this figure the damping coefficient representing the stability of the system from the TMA prediction is given. When the damping value goes below zero at a given frequency it means that the considered system becomes unstable at this particular frequency. On the other hand, when the damping value of a given system goes up and significantly exceeds zero the system becomes stable.

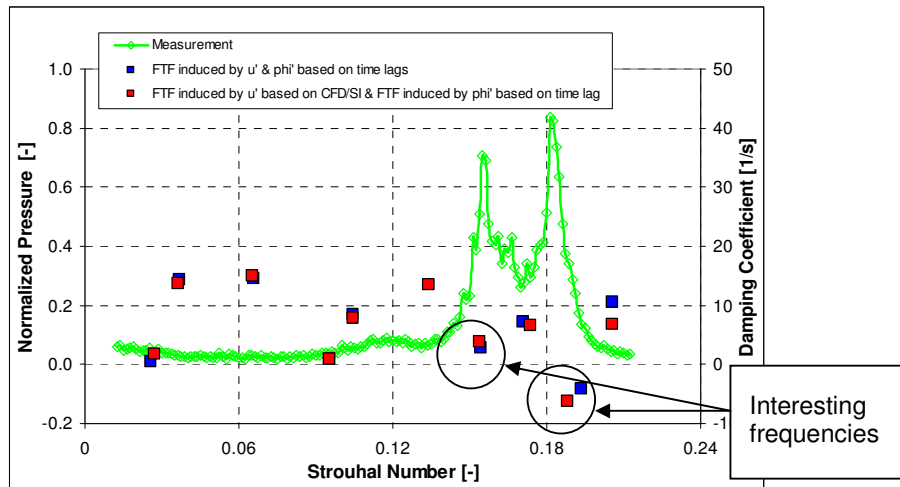


Fig. 9.11 Predictions and measurements of the stability margin for the considered system: red rectangular - TMA model with FTF induced by u' based on the CFD/SI, blue rectangular - TMA model with FTFs based on the time lag approach, green diamonds - measurements

Analyzing the numerical results, it can be concluded that both computational methods agree favorably with each other except at higher frequencies. However, the TMA prediction provides more eigenfrequencies than the experimental data. From the stability prediction standpoint, only eigenfrequencies located close to the pressure peaks found during the experimental test are of interest. Black circles indicate these frequencies. There are some significant variations at higher frequencies. It is seen that especially at the second interesting frequency the damping coefficient is much lower in the case of CFD/SI than in the case of the prediction based on the standard time lag model. The reason for this behavior can be explained by the differences in the flame responses. There is no flame response at higher frequencies for CFD/SI, whereas the time lag model uses the constant amplitude that is not frequency dependent. It looks like this larger magnitude makes the system more stable whereas the system tends to be more unstable at this frequency. Trendwise, one can say that the predicted frequencies in both considered cases at about $St=0.15$ and $St=0.19$ are in good agreement with the experimental data.

However, it should be noted that the small differences between different computational approaches are caused by the choice of the investigated acoustic feedback mechanism representing the system dynamics. It seems that the total flow (velocity) fluctuations do not have a significant influence on the overall system characteristics. Most likely larger change in the stability prediction should be seen if the flame transfer function induced by equivalence ratio fluctuations is studied.

10 SAS based forced response of an atmospheric test rig with a generic burner

The proper resolution of the dynamical behavior of systems under investigation requires time and space dependent evaluation of 3D aerodynamic design features and the impact of these features on the combustion system. The System Identification coupled with URANS computations known as CFD/SI can be used to determine dynamics represented by flame transfer functions but it cannot show the evaluation of time and space resolved coherent structures, which may directly influence flame responses. Alternative methods to analyze the combustion dynamics of gas turbine combustion systems thus are LES-like computations: for instance Scale Adaptive Simulation (SAS) or Detached Eddy Simulations (DES).

10.1 SAS modeling

The full 3D computational model of the atmospheric test rig with a generic burner is employed to perform a LES-like computation. The SAS model allows for the resolution of the part of the turbulent spectrum in unstable flows. From the acoustic standpoint, SAS is supposed to better capture the acoustic wave propagation because the turbulent spectrum is not modeled but partially resolved. The acoustic system modeled using SAS should be able to mimic a real acoustic system. On this basis, one can expect to get a more accurate magnitude and phase of flame transfer functions. The most significant difference of SAS compared to URANS is that the SAS model adapts the length-scale automatically to the resolved scales of the flow field, which results in a LES-like behavior in unsteady regions of the flow field. The SAS model is characterized by the use of the von Karman length-scale L_{VK} . The detailed numerical model is given in 0. Depending on how fine the turbulence spectrum is going to be resolved, the proper resolution of flows featuring unstable behavior requires computational grid with a LES quality.

The mesh and time steps are an inherent part of the model. LES models make use of the grid scale for filtering out the turbulence. There are some guidelines found in the literature [127]. The grid resolution requirement in the attached boundary layers is the same as that of a regular RANS solution (10-15 nodes in the boundary layer). In the detached region, the grid has to be designed in all three-space dimensions to allow at least the resolution of the largest turbulent structures. In the absence of advance knowledge about turbulence structures, the grid should be isentropic in all three directions. The currently used mesh consists of about 2.100.000 nodes and is especially refined in the region where the flame position is expected to occur.

As in the case of a segment model from Section 0, the combustor has also a diameter of 300 mm and a length of 500 mm. The exhaust passage is about 50 mm smaller in the diameter and is about 600 mm long.

Due to very high computational costs the swirler vanes are not explicitly resolved in the LES-like computation and 1D velocity profile boundary conditions are imposed at the axial and diagonal inlet. The velocity profiles are taken from a calculation of the whole burner geometry including the swirler vanes and are circumferentially averaged. Of course, when doing so it is explicitly assumed that there is no direct interaction between the swirler vanes and the upstream section with respect to any kind of instabilities [125]. Furthermore, analyzing some publications [31][37] the following conclusion can be drawn: it is a common practice not to simulate the swirler section in order to reduce significantly the computational time of LES simulations. The investigated case is assumed to be the fully premixed i.e. the fuel and oxygen concentration is represented by CH₄ and O₂ mass fractions, respectively. The air/fuel mixtures at the inlets are slightly preheated to temperature above 337 K. The liner is treated as an adiabatic wall and the exhaust passage wall is kept at a constant temperature. The outlet pressure is set to one bar. The three dimensional geometry with boundary condition specification is shown in Fig. 10.1

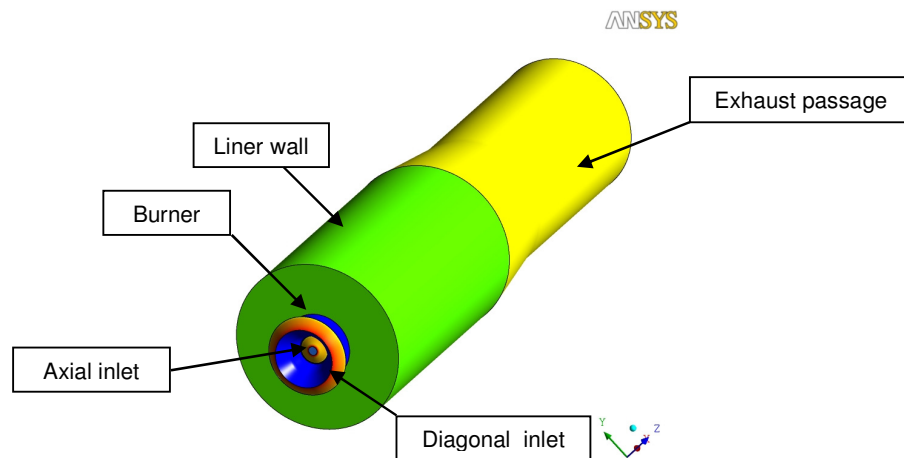


Fig. 10.1 SAS geometry and boundary conditions

The SAS calculations have been conducted using the total energy equation accounting for the compressibility of the flow. The 2nd order Euler backward discretization in time and the high-resolution scheme for spatial discretization are used [15]. Moreover, the Eddy Dissipation concept combined with one-step kinetics is utilized to model the combustion process. A summary of all models used are given in Tab. 10.1.

The time steps in the order of 1.25E-5 s are sufficient to resolve and capture dynamics of a flame up to 500 Hz. With respect to the time resolution, one gets more than 160 points per one wavelength, which is reasonable value.

It is known that artificial acoustic reflections due to compressibility occurring at the CFD boundaries may theoretically modify and even affect the unsteady flow features or in the worst case excite the system. For this reason, NRBC at the inlet and outlet have been used. At the outlet, the second non-reflecting boundary condition type has been used. In this case, NRBC are based on an impedance formulation in the time domain. The theory of this model and the implementation are presented in detail by Widenhorn et al. [93]

Spatial discretization	High resolution
Time discretization	2 nd order Euler backward
Fluid Model	Compressible Gas
Turbulence Model	SAS
Combustion Model	EDM with one-step kinetics
Acoustic BCs	Inlet and outlet non-reflective BCs
Heat Transfer	Total Energy
Time Step	1.25e-5 s
Total number of Time Steps	18000
Start up	7000
Statistical Averaging	11000

Tab. 10.1 Numerical models- SAS of an atmospheric test rig

10.2 SAS based space and time-resolved flow field

There are two important parameters, mesh density and CFL number, which should be taken into consideration while resolving flows using a SAS formulation. As mentioned, to be able to obtain results similar to LES, a very fine computational mesh especially in detached regions is required.

The grid is plotted in Fig. 10.2a. Indeed, it can be seen that the mesh is very fine in the region close to the burner mouth and in the region where the occurrence of a chemical reaction is expected. In addition to this, the grid quality is checked by means of the so-called blending factor offered by the CFX11 postprocessor. A value of one corresponds to the RANS quality and zero to the LES region. From the right figure is clearly seen that the region of importance is fully covered by the LES quality. In the LES context, not considering any heat transfer at the outer wall allows for reducing the size of the computational mesh significantly.

Since an implicit coupled solver is used, the CFL number is not restricted to unity and this number can be exceeded without losing any numerical stability of the CFD code. However, it is recommended [67] to keep its value close to unity. In this case, the CFL number is less than one in the entire region of interest.

As may be expected, there are some differences between the RANS and SAS - based flow field. These variations can be directly caused by the turbulence model. The instantaneous normalized velocity, averaged and RANS distribution are plotted in Fig. 10.3. In all figures, the same velocity scale is utilized. Both in the RANS and in the SAS solution a inner and outer recirculation zones are formed.

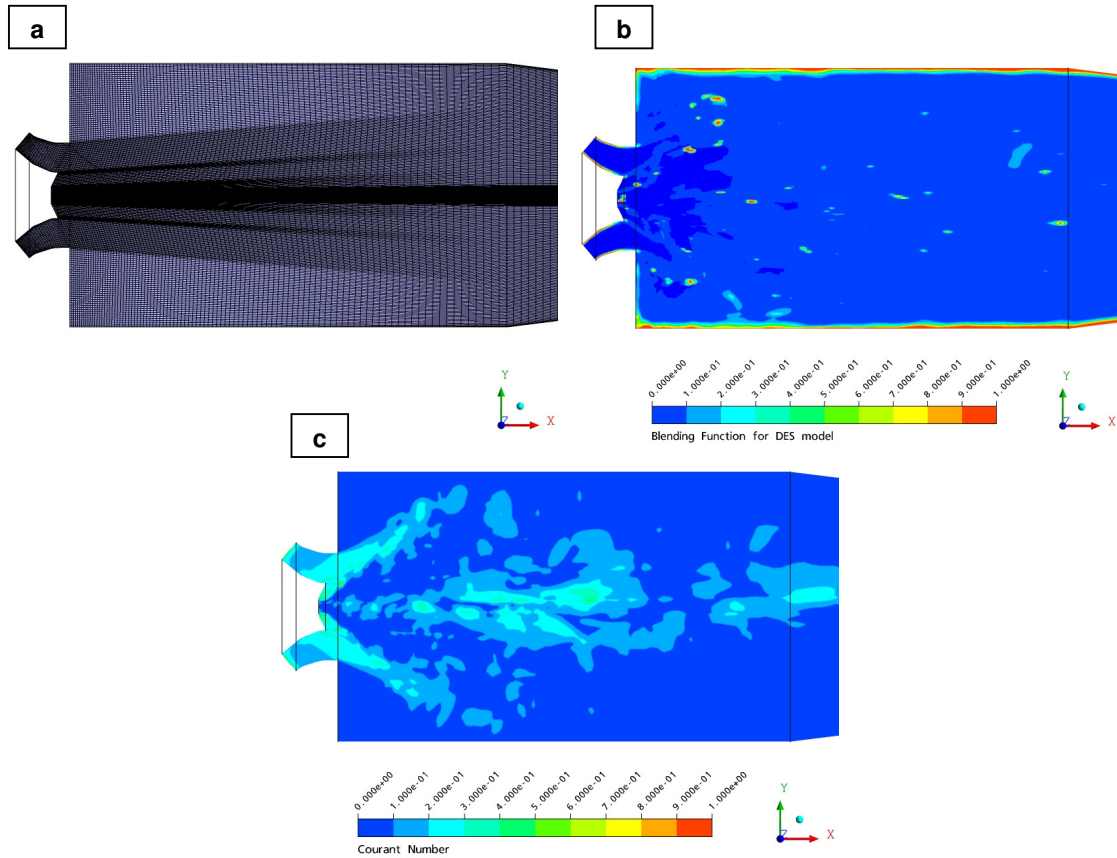


Fig. 10.2 Grid resolution (a), blending factor (b), and CFL number of SAS model (c)

The recirculation zones are indicated by the black iso-lines $u=0$ m/s. It is clearly shown that the flame is stabilized between the inner and outer shear zone. Additionally, comparing the averaged velocity flow field, it is seen that the inner recirculation region is a bit shorter and weaker in the case of SAS than in RANS. The region with the lowest axial velocity is shifted further downstream in the case of the SAS-based solution. Moreover, looking at the velocity distribution more closely it is seen that the averaged velocity is not also symmetrically distributed. All these variations may have three different roots. First, the better-resolved turbulence directly affects the reaction rate and the flame burns faster and becomes much shorter. The shorter flame length is stabilized closer to the burner exit. The second possibility is that the flow field is by nature unstable and is not symmetrically distributed with respect to the x-axis. In this case, the non-symmetrical flow field can be caused by vortex shedding at the burner mouth. It can be a proof that the URANS approach is useful but sometimes is not adequate to study some unsteady flow features. Using URANS, some information may be lost or wrong interpreted. Therefore, it is worth running some LES/SAS to check at least flow distributions and compare with RANS or URANS.

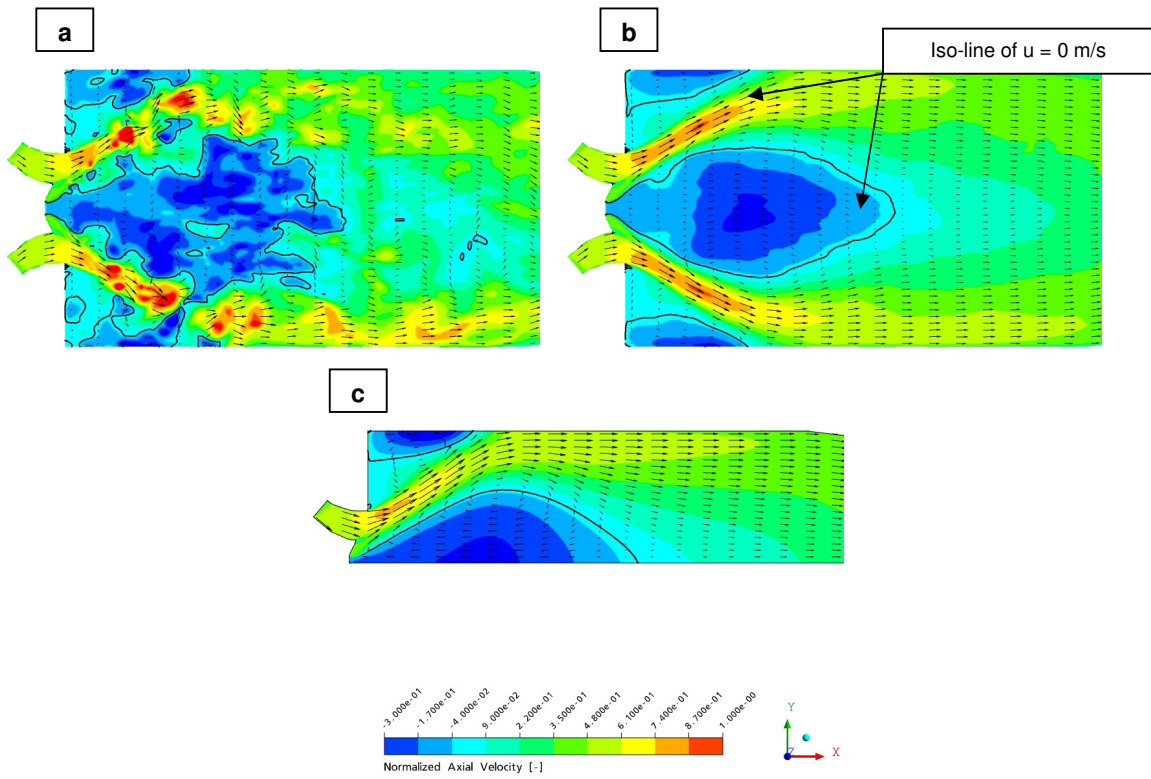


Fig. 10.3 The axial velocity distribution: instantaneous SAS (a), averaged SAS (b), and RANS solution (c)

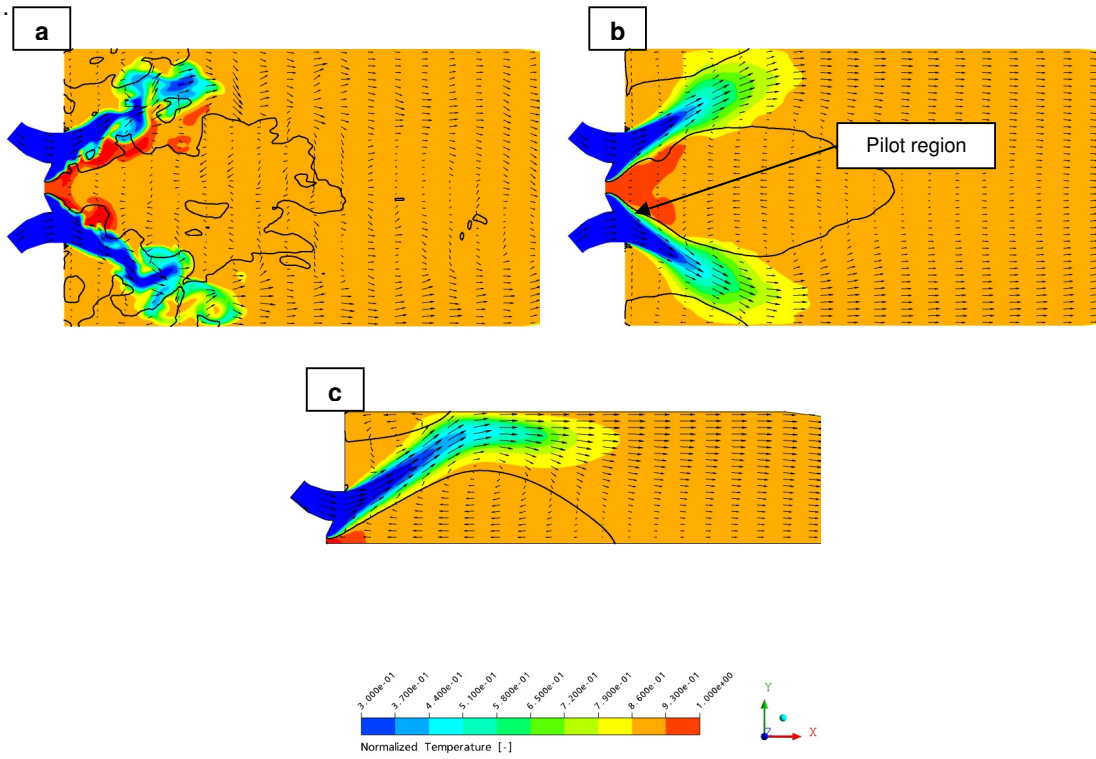


Fig. 10.4 The normalized temperature distribution: instantaneous SAS (a), averaged SAS (b), and RANS solution (c)

The other reason may be the statistical averaging itself. In this case, only 11000 time steps are taken into account to average the instantaneous flow field. This time corresponds to about two residence times for a particle traveling with an average convective velocity through the computational domain. Unfortunately, there is no experimental data, which can be utilized to validate the instantaneous and averaged velocity flow field. However, there are many examples in the literature showing capabilities of SAS in resolving unsteady turbulent flows [67][125]. On this basis, it can be assumed that SAS can better resolve the unsteady flow compared to RANS.

The comparison between the normalized temperature distribution based on RANS and SAS is given in Fig. 10.4. The temperature scale is the same in all cases. The instantaneous temperature flow field is averaged over 11000 time steps. It is again shown that there are some differences in the temperature field. These differences can be caused by the calculation of the molar reaction rate, which is based on the SAS input. The statistically instantaneous averaged temperature gives more distributed and much longer pilot region. As in the case of the axial velocity distribution, the temperature field is not symmetrical along the x-axis. In addition to this, the SAS model predicts the flame length being shorter than in case of the RANS solution. In all cases, the hottest region appears near the burner exit.

Unstable flame contours are shown by the iso-surface of $Y_{\text{CH}_4} = 0.003$ coloured by the normalized axial velocity. The mass fraction of Y_{CH_4} can be used to indicate the flame location in the investigated reacting flow field. A vortex-like shape characterizes the flame surface. The highest velocity is seen at the edge of this surface. It is also well shown that the flame surface is not uniform and is strongly wrinkled by turbulence.

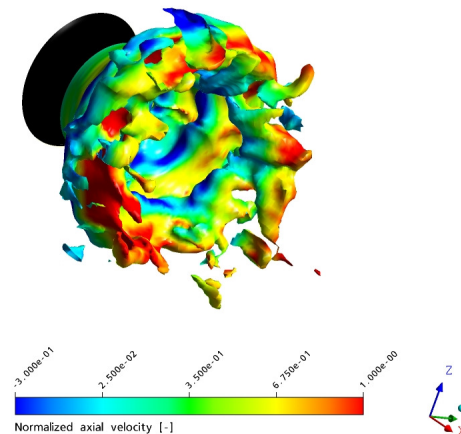


Fig. 10.5 $Y_{\text{CH}_4} = 0.003$ iso-surface colored by the normalized axial velocity

10.3 SAS with a harmonic forcing

To analyze and understand flame dynamics of this prototype burner in more detail, the developed turbulent structures captured by the SAS computation have been additionally forced at 90 Hz. The visualizations of coherent structures are subsequently compared to the previous LES calculation and measurements.

As stated by Lohrmann et al. [74], the increase of the absolute value at about 55 Hz that has been also shown and analyzed in previous chapter of this thesis can be explained by the formation and combustion of coherent ring vortex structures that are responsible for driving the overall flame dynamics. During the formation of the large-scale vortices downstream of the burner exit, unburned fuel/air mixture and exhausted gases are enclosed in a flame volume and burnt. Subsequently, at higher frequencies the decrease in the amplitude of the flame transfer functions is caused by combustion under more oxygen-diluted conditions caused by an enlargement of the flame volume.

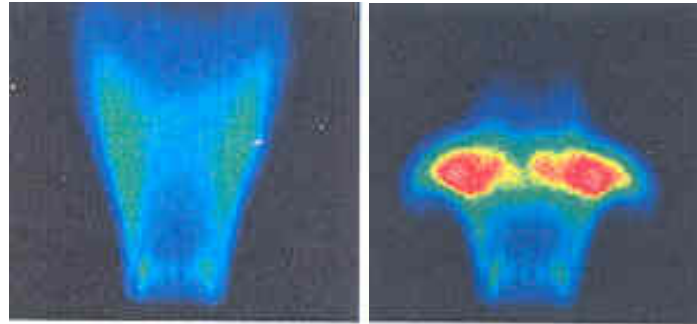


Fig. 10.6 Flame visualization from [74]: left: quasi-steady flame at about 10 Hz, right: ring vortex structure at about 55 Hz

The physical background of the behavior of the flame transfer function at about 55 Hz is also visualized in [74], and the reference to the experimental findings is provided by Fig. 10.6. These figures show the visualization of the flame under and above the critical frequencies. Above the critical frequency of about 55 Hz ring vortices are formed, which first leads to an increase in the amplitude of the flame transfer function. The creation of these vortex structures causes that the flame cone angle to become much bigger and the flame volume is somehow reduced. At even higher frequencies, the enclosed flame volume is significantly increased. However, these ring vortex structures are still formed but the combustion process that takes place at leaner conditions resulting in lower amplitude.

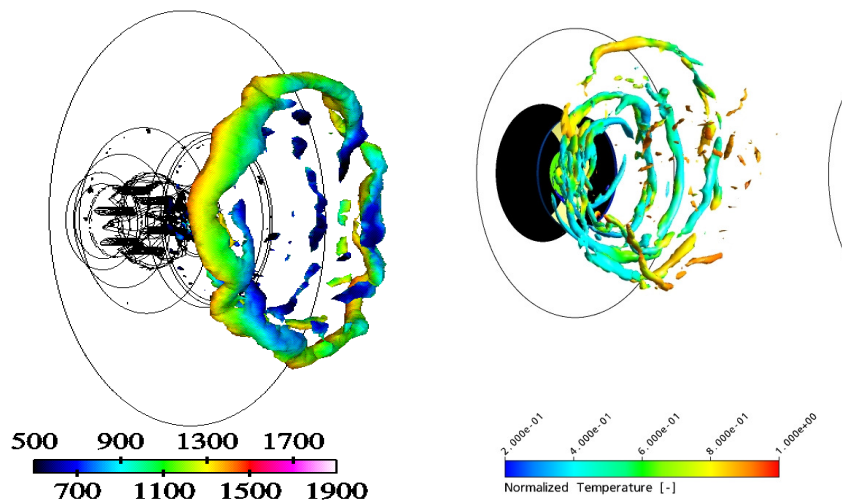


Fig. 10.7 Visualization of ring structures induced by the inlet forcing: Left - LES from [76] at 120 Hz, Right - SAS at 90 Hz

The results of LES studies made by Selle et al. [76] for this atmospheric generic burner can also confirm the experimental findings. The LES calculation is forced at 120 Hz (amplitude of 24% of the mean mass flow rate) utilizing the sinusoidal signal and it is found that the first effect of forcing is the creation of a large toroidal ring vortex. This vortex started at the lips of the burner and grew when propagating downstream. Selle visualizes the vortex structure in Fig. 10.7 left. Using the vortex criterion, which is based on the second invariant of the velocity tensor it is possible to detect the creation of vortex structures [135].

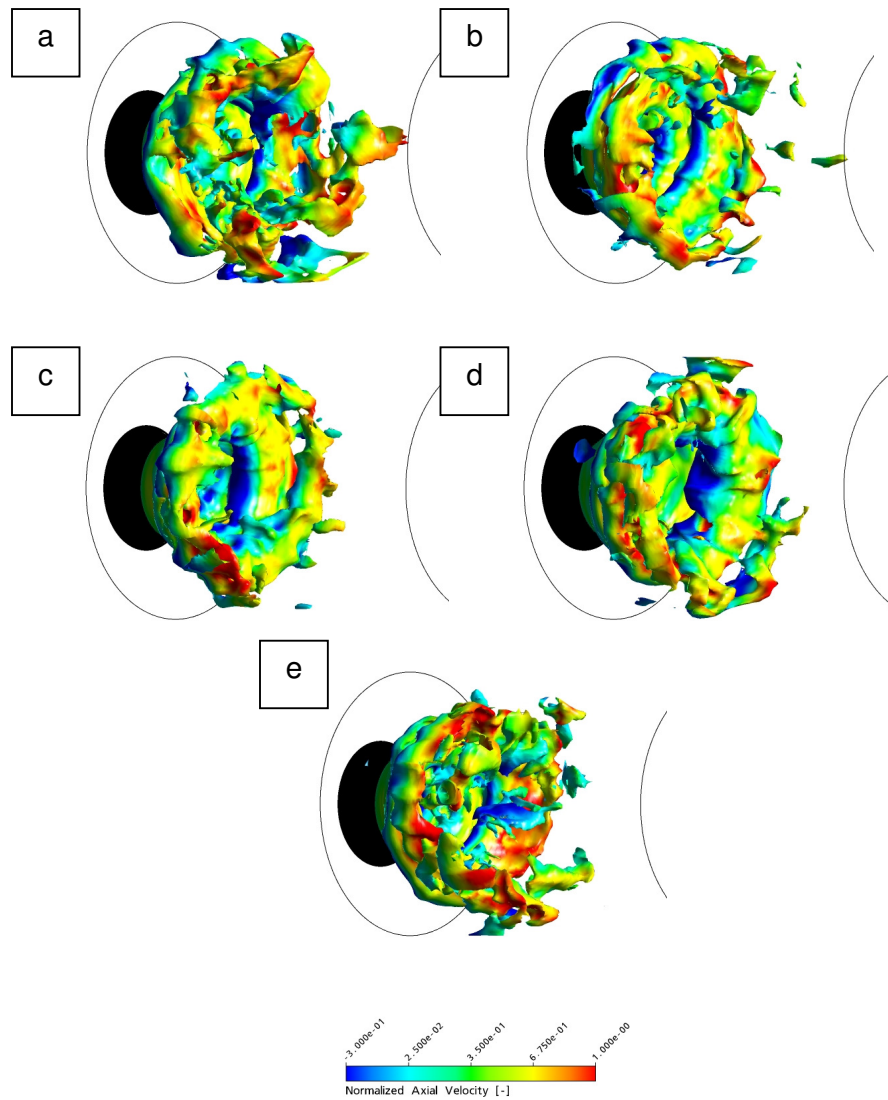


Fig. 10.8 CH₄ iso-surfaces for five phases of a forced cycle at 90 Hz

When the value of this creation is positive, the rotation rate is greater than the deformation rate, which implies the presence of a coherent structure¹⁵

¹⁵ The Q-criterion locates regions where rotation dominates strain in the flow. Letting \mathbf{S} and $\mathbf{\Omega}$ denote the symmetric and antisymmetric part of $\nabla\mathbf{u}$, one defines \mathbf{Q} as the second invariant of $\nabla\mathbf{u}$, given for incompressible flow by $Q=0.5(|\mathbf{\Omega}|^2 - |\mathbf{S}|^2)$

Utilizing the Q-criterion the coherent structures have been identified in the SAS simulation. Despite of the fact that the current reacting flow is forced at 90 Hz, very similar results compared to [76] have been obtained. The SAS-based ring vortex structure colored by the normalized temperature is plotted in Fig. 10.7 left. It is seen that the ring vortex structure consists of several smaller coherent structures. However, these structures are more spread in the radial direction. It can be to a greater degree caused by the system response at this particular forcing frequency. It has also been demonstrated in the previous chapters that at approx. 55 Hz the maximum of the flame response amplitude is detected. At this frequency, the flame volume is significantly reduced in the axial direction but it expands in the radial direction accordingly. By looking at Fig. 10.7 it can be proved that the flame is mainly expanding its volume in the radial direction. Further, it may be expected that the strong increase in the flame surface area at 90 Hz causes a much stronger flame response compared to 120 Hz.

Fig. 10.8 displays flame surfaces at five different phases of the forcing cycle. The flame surface perturbations are shaped by the ring vortex. The vortex ring is formed at the burner exit. The flame surface itself varies through the forcing cycles and exhibits various complex structures. The minimum flame surface is reached at 3 *rad* and this surface is also associated with the lowest heat release. In contrary, the maximum of the heat release is found at 5 *rad*.

In Fig. 10.9 one can find the time evaluation of the area averaged axial velocity recorded at the diagonal inlet and the volume integrated heat release. There are five different reference positions specified, which correspond to the different phase of the forcing cycle. At the beginning of the analyzed period the flame at point *a* is relatively long and exhibits the maximum heat release fluctuations. While the velocity fluctuations oscillate between -1.1 and 1.1 times its mean value, the total heat release varies from -1.25 to 1.25 its mean value out of phase to the inlet velocity.

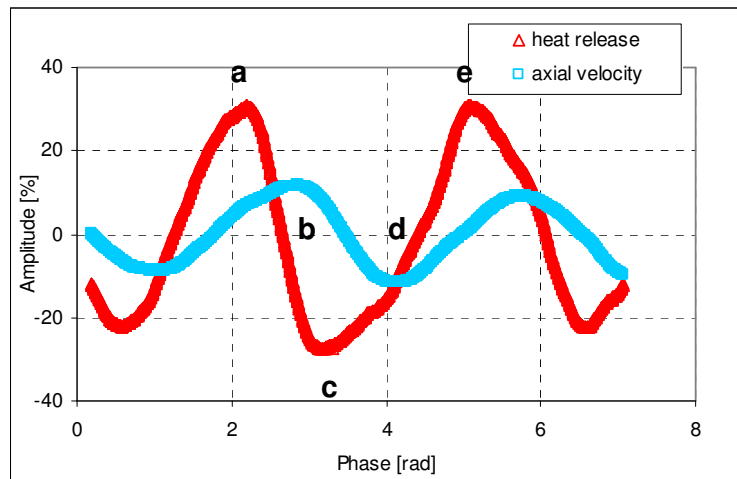


Fig. 10.9 Time evaluation of the averaged velocity at the diagonal inlet (red triangles) and the volume integrated heat release (blue triangles)

The pictures in Fig. 10.8 can be associated with the time evaluation when the ring vortex structure is being rolled-up i.e. the flame is being moved backward and suddenly shrunken. These points are characterized by decreasing of the global heat release. At the positions *e* the flame is again being moved forward and the cycle starts again.

To get a full picture of SAS ability to resolve the acoustically forced system, the SAS-based phase of flame transfer function compared with the experimental measurements is given in Fig. 10.10. In general, it is to be expected that the SAS-based flame response should be captured more accurately than the URANS-based flame response. Unfortunately, looking at the SAS-based phase at 90 Hz it is hard to draw this conclusion. It is clearly seen that the SAS phase prediction compared to the measured phase is off about 100 degrees. It appears that the calculated flame length is much shorter and therefore the real time lag cannot be well reproduced. The time and space resolved flow field shown in Fig. 10.4 can prove it. On the other hand, it has been shown by Selle et al. [76] that the key driving mechanism is directly related to the creation of large coherent structures and is not directly influenced by the time lag. A more deep study to clarify these discrepancies must be performed.

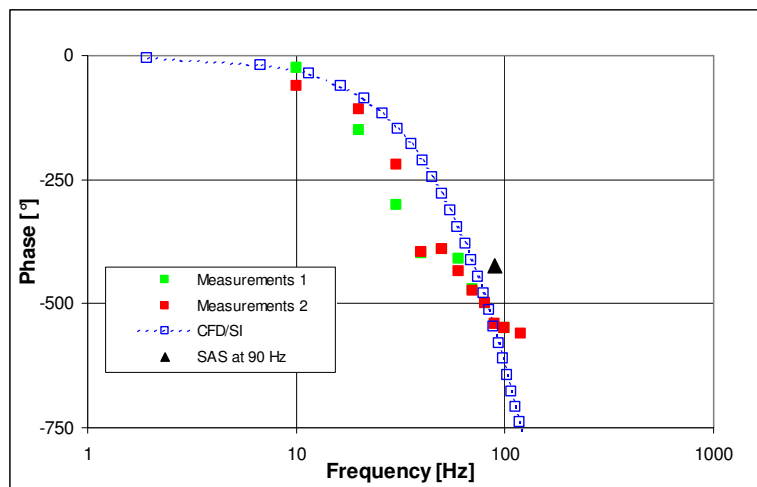


Fig. 10.10 Prediction and measurement of the phase of flame transfer function: SAS-based phase (dark triangle), CFD/SI (blue rectangular), and measurements (red and green rectangular)

The one possible source of this mismatch, which may considerably affect the calculated phase, is the current resolution of the frequency. It must be added that relatively few forcing cycles have been used to calculate the Fourier transformed flame response. In this case, the area averaged axial velocity is very low and it is very time consuming to consider enough cycles to get the meaningful statistically averaged values out of this simulation. The total computational time is then reduced by decreasing the total number of the calculated forcing cycles. It may happen that this action has decreased the numerical relevance and accuracy of the calculated phase.

11 SAS of Industrial Test Rig at elevated pressure

The full 3D computational model is utilized to perform a SAS computation of the investigated prototype industrial gas turbine combustion system. As already shown, it is important to analyze some unsteady flow features using LES-like computations in order to be able to determine some potential mechanisms that may drive thermo-acoustically induced oscillations. For that reason, SAS is supposed to resolve the turbulent reacting flow and acoustics of a given system more accurately than URANS.

11.1 SAS modeling

To be able to properly capture flow dynamics, a very fine computational mesh especially in the burner exit region is required. The currently used mesh consists of ~ 9.000.000 elements and is especially refined in the region where the reaction is expected to occur.

Similar to the segment model from Section 9.1, the 3D CFD model consists of the full basket and transition piece, which leads to an exhaust section. Due to very high computational costs especially in the case of SAS computations, the swirler vanes are not explicitly resolved in the present SAS computation. Instead 2D inlet profile boundary conditions are imposed at the main and pilot inlet. The inlet profiles are taken from a RANS calculation of the whole burner including the swirler vanes.

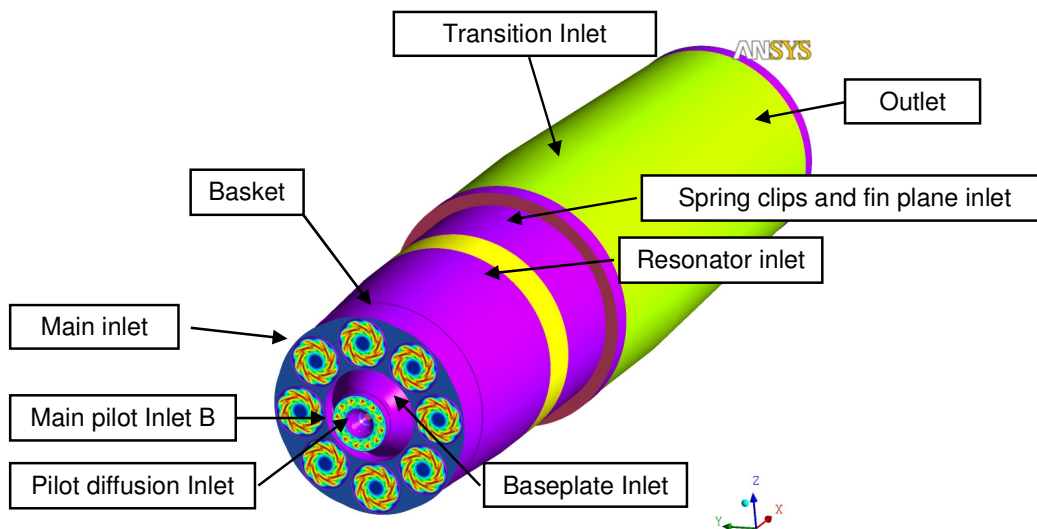


Fig. 11.1 SAS boundary specification for the full 360-degree model

Thermodynamic conditions are specified according to the full load condition. The test rig is operated at elevated pressure and with preheated air. The total amount of fuel is split over four fuel stages in the following percentage: ~73,5% for the main inlet, and ~10% for the main pilot inlet. The rest of the total amount of fuel belongs to the C stage and diffusion pilot.

Similar to the computation made with a segment model, the remaining fuel mass flows are utilized in the fuel stage C located further upstream to enhance the mixing process and in the diffusion pilot. Secondly, the cooling mass flows especially those going throughout the resonator, spring clips and fin plane, and transition sections are considered.

The total energy equation has been set up to take into account the compressibility of the reacting flow. The 2nd order Euler backward discretization in time and the high-resolution scheme for spatial discretization are used [15]. To describe the combustion process, the Eddy Dissipation concept combined with one-step kinetics is utilized. All numerical model used are listed in Tab. 11.1

Spatial discretization	High resolution
Time discretization	2 nd order Euler backward
Fluid Model	Compressible Gas
Turbulence Model	SAS
Combustion Model	EDM with one-step kinetics
Acoustic BCs	Inlet and outlet non-reflective BCs
Heat Transfer	Total Energy
Time Step	1.25E-5 s
Total number of Time Steps	6500
Start up	4000
Statistical Averaging	2500

Tab. 11.1 Numerical models- SAS of Industrial Test Rig at elevated pressure

As in the case of SAS for an atmospheric prototype gas turbine burner the time step of 1.25E-5 s has been picked up to resolve and capture dynamics of a flame. With regard to statistics, the statistical averaging is made after a time corresponding to two convective times through the combustor calculated based on the average axial main inlet velocity.

The so-called NRBC at the inlet and outlet have been used. However, in the case of the outlet acoustic conditions, the second type of non-reflecting boundary conditions has been used. NRBC uses an impedance formulation in the time domain, which is much more numerically stable. For more details, readers are referred to [93].

11.2 SAS space and time-resolved flow field

The computational mesh, CFL number and blending factor can be used to determine whether the present computational mesh and time step are appropriate for the LES-like computation. These three parameters are visualized and given in Fig. 11.2. To save some CPU time the mesh has been mainly refined in the combustor. It is seen that the mesh has been significantly refined compared to the RANS grid in the region further downstream after the pilot cone location where the combustion process takes place. However, the blue region shown for the blending factor indicates that this area is fully covered by the computational mesh having the LES mesh quality. Since an implicit coupled solver is used, the CFL number is not restricted to unity. In this case, the CFL number smaller than unity dominates most of the computational domain. As expected, there are still some regions where this number is bigger than unity. Fortunately, in these areas no steep temperature, velocity and mass fraction concentration gradients are expected.

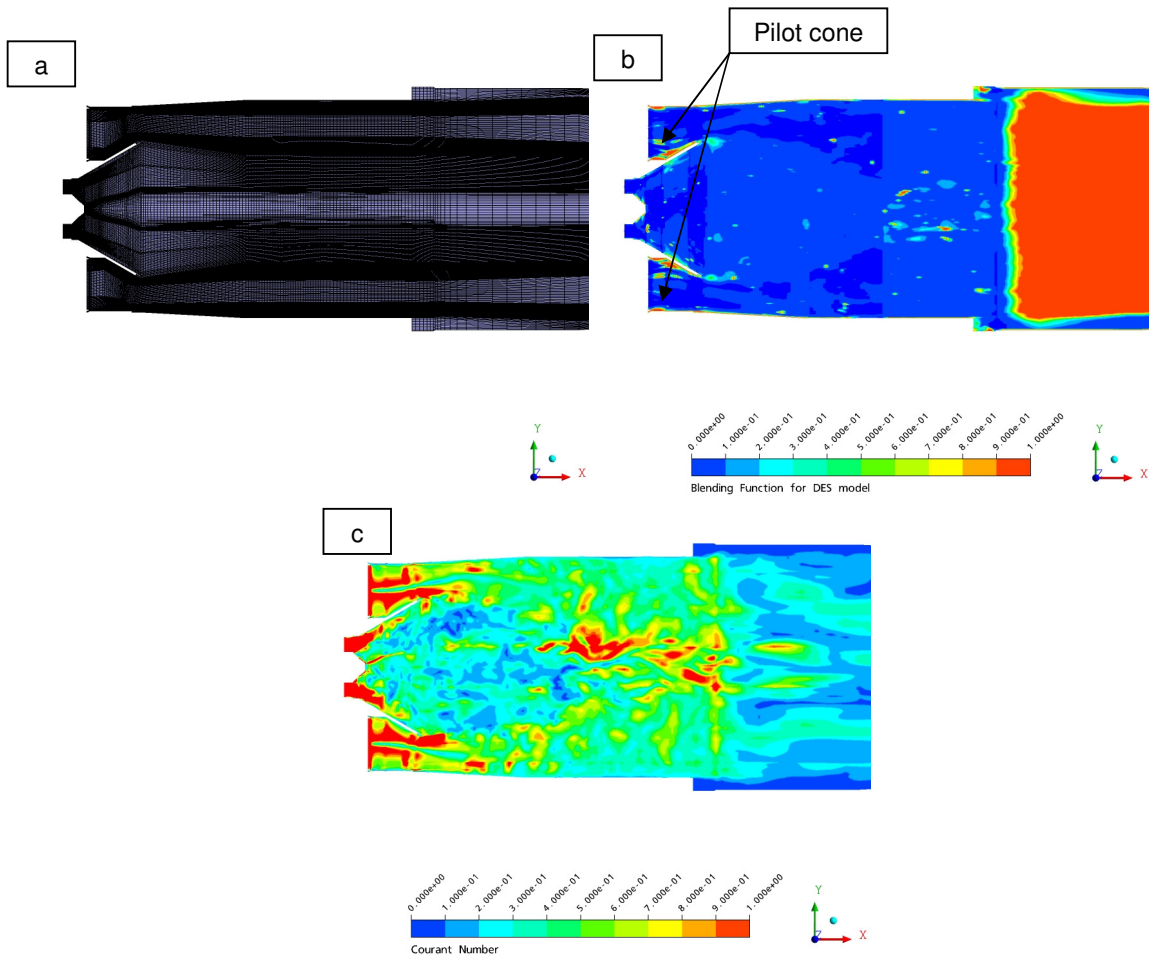


Fig. 11.2 Grid resolution (a), blending factor (b) and CFL number of the SAS model (c)

The instantaneous normalized axial velocity distribution calculated with the SAS model is shown in Fig. 11.3. The scale is the same in all figures.

It is clearly seen that both in the RANS and SAS solution all inner recirculation zones due to the large differences in the swirl numbers between the main and pilot inlet are formed. The recirculation zone is indicated by the black iso-lines $u=0$ m/s. The flame is stabilized directly between the inner shear zone having very high swirl number and the motion originated at the main inlet characterized by the small swirl number. It may be expected that the size of this recirculation zone can be to some extent responsible for the system dynamics and play an important role in the stability of this prototype combustion system. The size of the inner zone seems to be identical in both different models.

Additionally, comparing the averaged flow fields, it is clearly found that the axial velocity in the transition piece is much higher in SAS than in the case of the RANS model. A relatively coarse mesh in the case of the SAS computation is more likely responsible for this over-predicted axial velocity. It looks like that using this coarse mesh the turbulence spectrum and instantaneous flow field cannot be correctly resolved. However, in the case of flame/acoustic interactions this region is not of interest and it can be assumed that from the thermoacoustics point of view, by refining this region one does not get any valuable information. Nevertheless, if there is a need to improve these results with regard to the axial velocity prediction the mesh refinement in this region should be made. Secondly, considering the normalized velocity vectors, the normalized axial velocity is a bit smaller in the case of RANS. It can be directly related to the SAS model and the turbulent flow field is modeled. It is well known that the $k-\epsilon$ tends to overpredict turbulence.

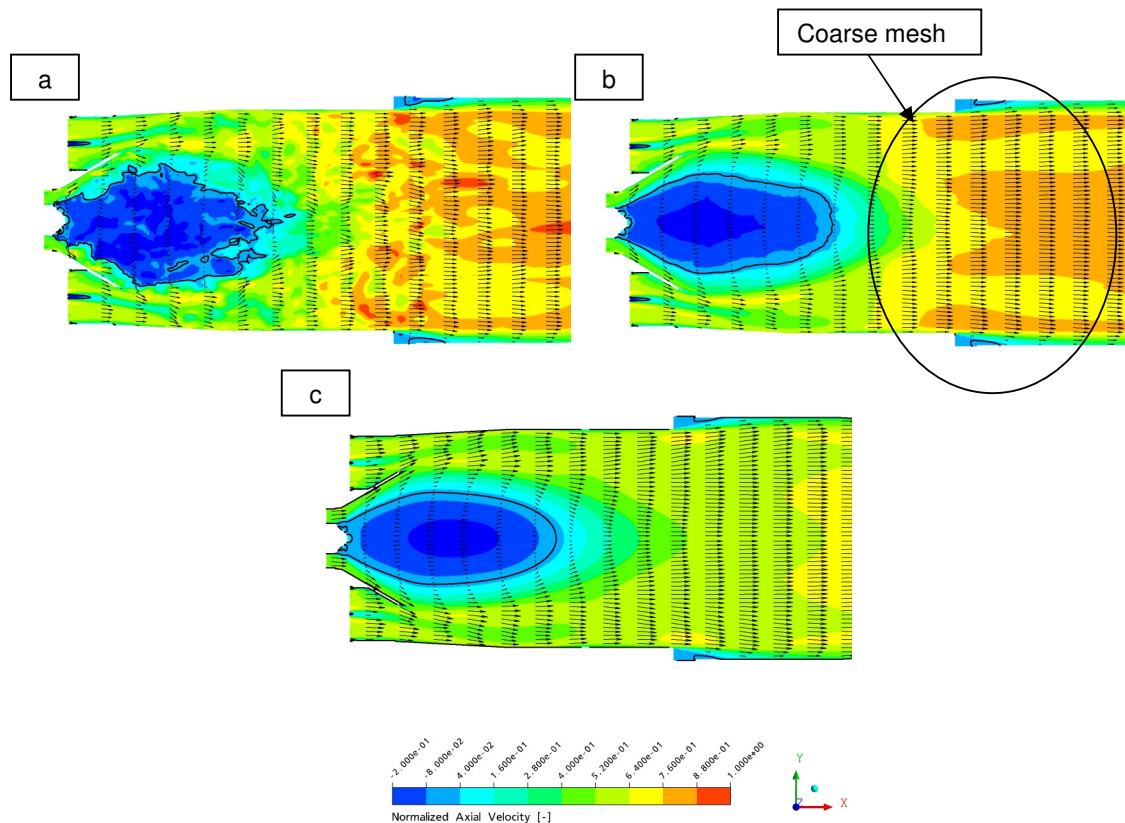


Fig. 11.3 The normalized axial velocity distribution: instantaneous SAS (a), statistically averaged SAS (b), and bottom RANS solution (c)

The comparison between the temperature distribution based on RANS and SAS is given in Fig. 11.4. The temperature is normalized and dimensionless values are plotted. First of all, in all considered cases, the hottest region appears near the pilot cone. The SAS model predicts the flame length being comparable to the length of the RANS-based solution. The second colder region further downstream, which appears in RANS due to the differences in the swirl number, is not revealed in the case of SAS. It seems that SAS predicts higher temperatures at this position. The main reason for these differences can come from the fact that there is the different number of grid points in these regions in both cases. It has already been mentioned that to minimize the computational cost of the SAS computation in the transition piece a coarse mesh is utilized. The temperature differences are significant. In addition to this, in the case of SAS lack of axis-symmetrical flow behavior has been found. There are two possible scenarios, which can be utilized to explain this no axis-symmetrical flow behavior. The first possibility can be referred to the statistics of the calculated flow field. The other scenario is that the flow field due to some unstable features is not axis-symmetrical by nature.

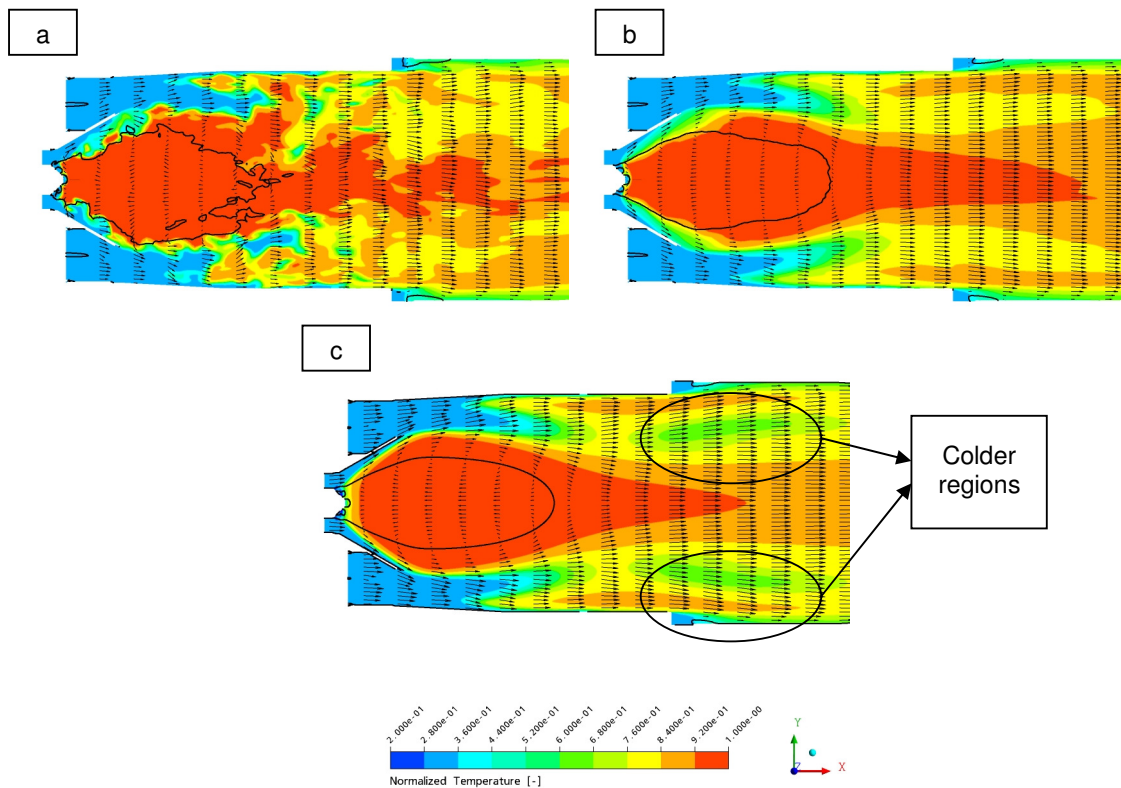


Fig. 11.4 The normalized temperature distribution: upper left corner – instantaneous SAS, upper right corner averaged SAS and bottom RANS solution

As opposed to RANS, using LES-like computations allow for analyzing and monitoring some unsteady flow features under the full load condition. Utilizing the vortex criterion¹⁵, which is explained in [14], it is possible to visualize and detect vortex shedding in the basket. In this case, the generation of coherent structures has been well captured by SAS and is depicted in Fig. 11.5.

The structures are coloured by the normalized temperature. As expected, the highest indicated temperature is located near the pilot and all diffusion holes. At the main inlet, the coherent structures driven by the weak swirl are shown. In addition to this, five very strong unsteady structures have been developed at the exit of the diffusion holes and have been driven by the high swirling flow further downstream. Using the same value of the iso-surfaces of the strain rate invariant¹⁵ it can be seen that the unsteady structures originated from the diffusion holes are larger and much more distinct compared to these ones from the main inlets. It might be seen as one of the possible mechanism affecting an overall combustion dynamics.

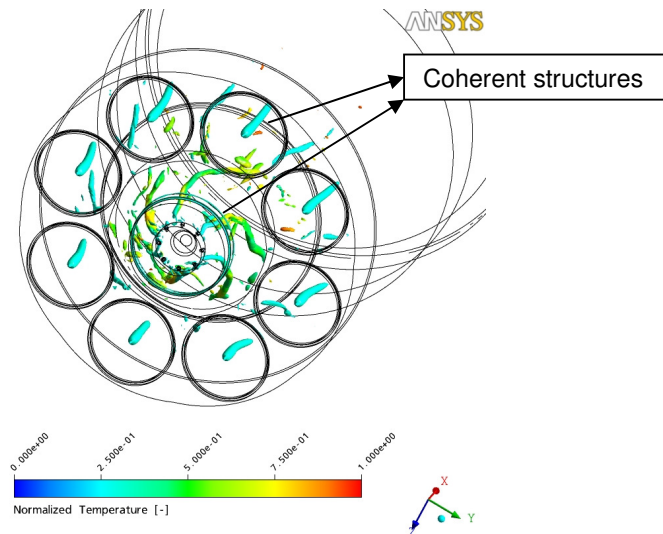


Fig. 11.5 Visualization of coherent structures by strain rate invariants colored by the normalized temperature

These findings can be partially proven by the results obtained from the TMA stability analysis from 9.3.2. It has been shown that there are very small differences in the overall stability based on the time lag approach and CFD/SI with regard to the flame transfer function induced by velocity fluctuations. Analyzing the calculated coherent structures, one could expect that the calculated flame response to velocity or volume flow perturbations at the main cannot be the dominant ones in the analyzed combustion system. There are some other key mechanisms, which can play a role. It appears that these unstable vortex structures driven by the very high swirl number can to some extent control the unsteady flame behavior and therefore the dynamics of this system.

In the light of the current SAS-based results, there may be two possible explanations of the numerical results from the previous TMA stability analysis:

- The flame response to equivalence ratio fluctuations originating at the injection point in the pilot and main inlet are the stronger ones and driving the system and of course can significantly affect the stability prediction

-
- Very large coherent structures developed in the pilot cone region are the most dominant ones and are responsible for driving the system. Very high swirl number is modifying the inner recirculation zone and therefore changing the time lag distributions for both FTF induced by u' and ϕ' in this region. As a consequence, URANS is not capable of reproducing entirely this unstable mechanism and LES-like simulations are required to calculate FTFs.

Nevertheless, some further investigations and a deeper understanding of the CFD/SI flame response to equivalence ratio fluctuations of the main and pilot inlet are required to determine all possible mechanisms affecting the flame response. In addition to this, it can also be expected that the SAS-based flame response to velocity and equivalence ratio fluctuations can change even more the stability characteristics of this system. On this basis, the SAS-based flame transfer functions have to be used in a new TAM stability analysis.

12 Simulation of self-excited oscillations

The computation of self-excited oscillations is the more demanding in terms of computational costs and set up than the forced response method. The main reasons for this are small time steps [80] (which can prevent numerical damping), appropriate combustion models [129][130], and of course well-reproduced acoustic boundary conditions [88] for a given gas turbine combustion system. In general, to properly reproduce the thermoacoustic feedback loop in combustion systems, the entire combustor geometry should be taken into account up to a position where acoustic boundary conditions are well defined. By definition, this geometry should include all inlets and outlets located upstream and downstream at positions where well-defined acoustic boundary conditions can be found.

Furthermore, using recently developed CFD-based non-reflective or even impedance boundary conditions has an advantage compared to standard CFD reflective boundary conditions. First of all, in the case of the non-reflective boundary conditions, only acoustic reflection coefficients at the CFD boundary can be adjusted to properly represent real and physical acoustic boundary conditions [128] [132]. Unfortunately, only the real part of the CFD-based reflection coefficient can be fitted. It is known that the proper established longitudinal acoustic mode can only affect combustion instabilities by forcing pressure fluctuations at physical frequencies corresponding to natural acoustic modes. These physical frequencies can affect the Rayleigh criterion and enhance the coupling mechanism between heat release and pressure fluctuations. If they are in phase with the heat release is adding additional acoustic energy, while if they are out of phase they can suppress instability.

In practice, such computational domains including all mixing passages and injection points are almost computationally prohibitive. To keep computational time low these geometrically complex systems must be strongly simplified. This is a penalty that must be paid to reduce overall computational costs. The CFD domains are usually cut off downstream of the swirl-vane trailing edges and at the combustion chamber exits. At these locations, acoustic and URANS boundary conditions can be approximated by means of constant values or one- or two-dimensional profiles. Generally speaking, there are two different ways to perform the computation of self-excited oscillations in such simplified computational domains. This computation effort can be realized by:

- applying acoustically well-defined boundary conditions i.e. acoustic reflection coefficients or impedance enabling a proper representation of the relation between fluctuating variables, which is currently very difficult to perform due to the lack of impedance BC implemented in commercial codes, or

- an alternative approach is to fit standard (reflective BC) boundary conditions to reproduce a feedback mechanism between acoustic waves and heat release fluctuations. In other words, it means that one has to locate a static pressure boundary condition at locations at which pressure nodes are expected, and a velocity at the position where velocity nodes may be assumed. For example, at the exit of a combustor a very high Mach number, which can choke the flow, may be present. It may be assumed that at this position mass flow or velocity boundary conditions can be utilized. With respect to acoustics, it can be shown that using these kinds of boundary conditions, acoustic velocity nodes ($u' = 0$) are given. If an exhaust gas goes directly to the exhaust pipe connected to the surrounding atmosphere it can be assumed that at this position acoustic opening boundary conditions ($p' = 0$) are given. If this is not the case, it is demonstrated in [129] that total pressure boundary conditions at the inlet and the fully reflective standard BCs at the outlet in the form of a pressure node ($P_{st}=0$) can be set. Doing so, one may allow velocity and pressure to fluctuate and to develop self-excited oscillations based on total mass fluctuations if any significant pressure fluctuations exist.

It should also be mentioned that the time step used in the computation of self-excited oscillations must be relatively small otherwise pressure and velocity fluctuations can be directly damped by numerics. The major damping effect may also occur due to turbulent viscosity, which may not allow pressure oscillations to grow in time.

12.1 URANS calculation of self-excited oscillations

The second approach has been applied to the atmospheric test rig with a generic burner to demonstrate that there are possibilities to perform a calculation of self-excited oscillations using commercial codes. However, it should be noted that in this case there are no experimental data available, which can be used to show any development of self-sustained oscillations during the test rig operation. Thus, this investigation has been made only for demonstration purposes.

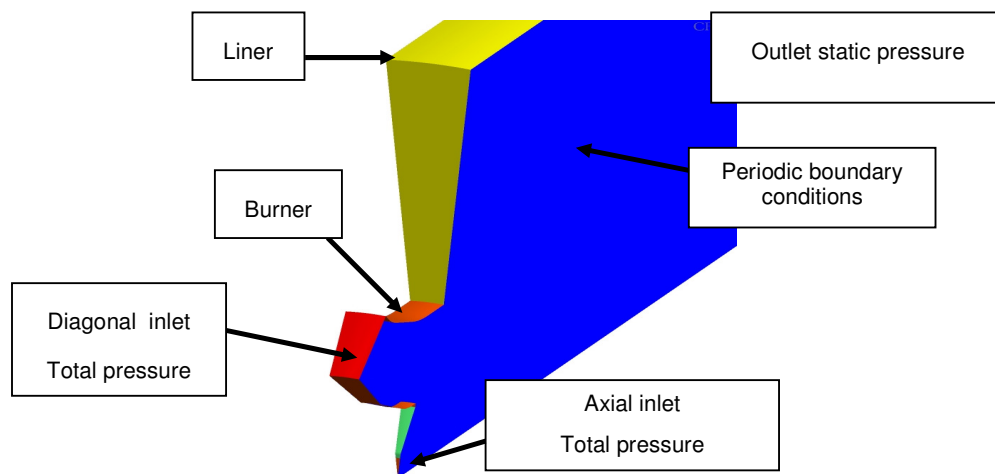


Fig. 12.1 URANS Boundary conditions for a calculation of self-excited oscillations

A segment model has been employed to reduce the entire computational cost. The boundary conditions shown and described in section 8.2 have been slightly modified to enable velocity and pressure fluctuations to be changed during the unsteady run. First, the velocity profiles at the diagonal inlet are re-calculated into the total pressure boundary conditions

In addition to this, only velocity vectors indicating flow directions have been utilized. This modification allows for not fixing the velocity and pressure at the axial and diagonal inlet and keeping a constant total mass flow through this section.

Secondly, the static pressure boundary condition at the outlet is utilized to sustain a high acoustic reflection coefficient at the outlet boundary. In reality, the exhaust gasses go directly to the exhaust pipe opened to the atmosphere. Doing so, one enables the acoustic pressure waves to interact with the flame, which theoretically should close the investigated feedback loop. The time step dt used is 0.00005 [s] and the other settings are already listed in section 8.2. A more detailed specification of boundary conditions is given in Fig. 12.1.

After 1000 time steps some self-excited oscillations have been encountered in the computational domain. About 10000 time steps are needed to fully develop the self-excited oscillations. It is observed that in this phase the pressure amplitude is significantly increased. As the simulation is running, the static pressure stayed at the same level. Fig. 12.2 depicts the time evaluations of pressure for a monitor point located in the computational domain very close to the diagonal inlet. As expected, the boundary conditions applied let the self-excited pressure oscillations develop. As stated by Poinso et al. [40] the time evaluation of pressure can be spread over three characteristic phases i.e. growth, overshoot, and limit cycles.

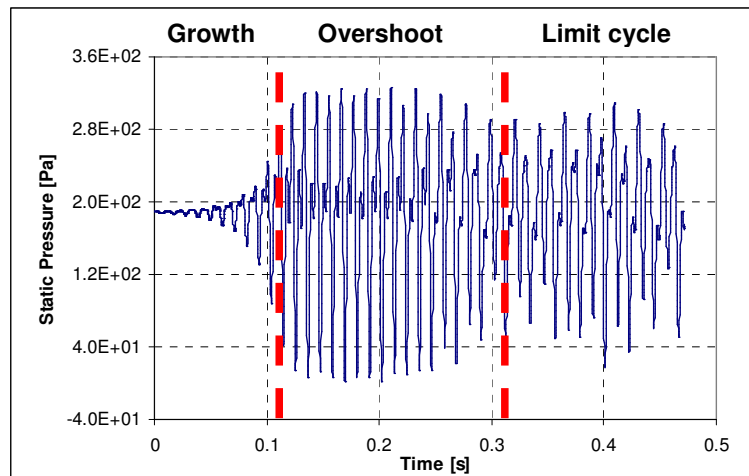


Fig. 12.2 Pressure time evaluation of a monitor point for $dt=0.00005$ s and characteristic phases

The growth phase is responsible for an initial growth of combustion instabilities and is reasonably captured in the current computation. It is well seen that the pressure fluctuations started growing after some initial iterations and reached the values exceeding the limit cycle. The overshoot phase is characteristic of self-excited computations and is captured between 0.1 and 0.25 [s]. Starting at ~ 0.3 s the limit cycle and the constant pressure amplitude have been reached.

The constant pressure amplitudes are characteristic for this phase and stop growing with time. The calculations of self-excited oscillations have a great advantage compared to the forced response method. These calculations can replicate system dynamics in the manner similar to the real experimental set up where any self-excited oscillations are accounted for. By definition, these simulations should be able to capture any modes in the computational domain as soon as it is amplified. However, it must be added that it is very difficult to perform these computations using real gas turbine combustion systems because of limits in the given computational domain and time step.

In the case presented here, only the total mass flow fluctuations are considered while in gas turbine combustion systems both mass flow and equivalence ratio fluctuations play very important roles. Unfortunately, the coupling mechanism can be only analyzed when resolving the whole fuel passage with impedance boundary conditions prescribed at fuel injections positions. However, using the proposed computational approach, it is possible to only determine the feedback mechanism with respect to the mass flow fluctuations at the diagonal and axial inlet.

12.2 Validation of CFD-based acoustic modes by means of a one-dimensional acoustic code

Because of the lack of any experimental data of the dominant frequencies (self-excited mode) in the investigated test rig, the simplified one-dimensional acoustic network (TMA) model has been created to calculate and compare the frequencies, which have been found by the unsteady RANS computation.

The TMA model of the considered combustion system begins at the diagonal and axial inlets and is cut off at the computational outlet. At the outlet, standard static pressure is prescribed. Doing so, one is able to impose an acoustically open boundary condition at the outlet. On the other hand, it is hard to mimic total pressure boundary conditions. In this case, neither velocity nor pressure is fixed at this position. However, if it is assumed that at both inlets density are small and remains constant, a total pressure based-impedance boundary condition can be derived. Both inlets are modeled using the impedance boundary conditions. An estimate of inlet acoustic impedance has been calculated based on equation E.3

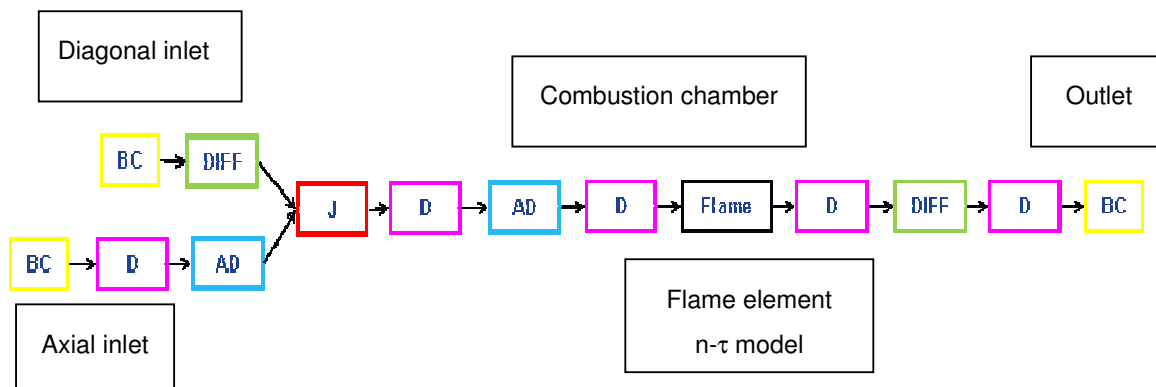


Fig. 12.3 TMA model of a generic burner

These impedance boundary conditions neither are measured nor modeled using the entire fuel and airside geometries. To match the mode frequencies, which are found by the URANS calculation, these impedance values have been iteratively changed.

Since a thin flame model is utilized, the axial location of maximum heat release is utilized to impose the thin flame jump conditions. As in all previous cases, the axial location of the flame front is estimated based upon the CFD-based data, due to the fact that the fully premixed system is used. The flame response due to velocity fluctuations is only considered and represented by the standard time lag model with the time lag value of 14.5 [ms]. The one dimensional acoustic network model is shown in Fig. 12.3. It has been calculated that the impedance values of 13 and 10 correspond to the diagonal and axial impedance respectively. Tab. 12.1 summarizes all acoustic boundary conditions, which have been used to match the CFD-based results.

	Axial Swirler Acoustic BC	Diagonal Swirler Acoustic BC	Outlet Acoustic BC
Case	Impedance (Real Part)	Impedance (Real Part)	Reflection Coefficient (Real Part)
1	9.00e-001	-1.25e+001	-1
2	9.00e-001	-1.30e+001	-1
3	9.00e-001	1.30e+001	-1
4	1.00e+000	1.30e+001	-1
5	9.00e-001	1.40e+001	-1

Tab. 12.1 TMA acoustic boundary conditions for a generic burner

The prediction of the unstable frequencies for five different sets of boundary conditions using TMA is compared with the URANS computation and is plotted in Fig. 12.4. It is easy to notice that there are two distinct peaks at about 90 Hz and 180 Hz. It can be seen that the second peak is strongly reduced. This is most likely caused by acoustic damping, which is much more pronounced at higher frequencies. Furthermore, the second peak most likely represents the second harmonic. In addition to this, there are two other much weaker peaks.

Generally speaking, the TMA-based prediction agrees well with all the unstable modes, which are calculated by the URANS computation. Of course, there are some mismatches in the calculated frequencies, which might be caused by the geometrical approximations made in TMA. It appears that that the 4th and 5th case give the best match from the stability prediction point of view. Using these boundary conditions TMA is able to find four frequencies: two stable and two unstable located very close to the URANS solution. However, it should be pointed out that the TMA model itself and the flame model are simplified. On this basis, the TMA estimations are not fully relevant and can only provide a general overview about the dominant feedback mechanism between pressure and heat release

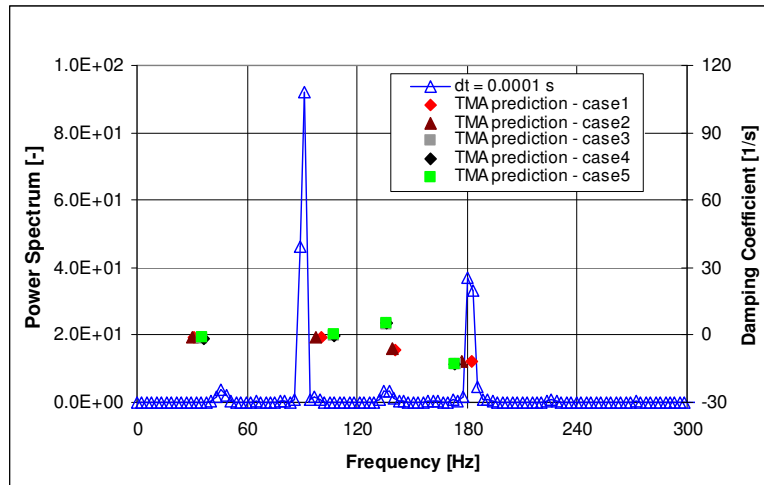


Fig. 12.4 TMA prediction vs. URANS computation: red rectangular – TMA prediction, blue triangle – URANS computation

13 Conclusions and recommendations

The study presented in this thesis has been initiated to efficiently reduce and better control the creation of large amplitude pressure oscillations caused by the thermo-acoustic feedback mechanism in gas turbine combustors. The main objective of the presented work is to provide a numerical test rig based on time and space resolved CFD computations. Using advanced computational methods such as URANS, SAS, SI and TMA in the investigation of combustion dynamics and flame/vortex interactions allows for a relatively low cost numerical means for verifying various design concepts in terms of the detection and the reduction of combustion instabilities.

The main objective of this thesis is to investigate and validate the application of advanced CFD-based computational tools for the simulation of thermo-acoustic systems. The novel contribution of this study is the use of unsteady CFD computations coupled with the System Identification method to reconstruct flame transfer functions and acoustic transfer matrices under realistic operating conditions. By employing these unsteady CFD-based flame responses, it is possible to improve the stability prediction of one-dimensional acoustic network models. The transfer matrix approach has been further developed with regard to one-dimensional acoustic elements such as flame and straight duct elements. The prediction of the flame transfer function is also improved by utilizing acoustic non-reflective boundary conditions. This results in a more accurate acoustic representation of these elements and increases the overall capability of the one-dimensional acoustic tools to capture unstable acoustic models.

The reconstructions of acoustic transfer matrices and flame transfer functions have been mainly conducted using the CFD/SI method. This method is the combination of unsteady CFD computation forced with an external signal and an acoustic postprocessor based on the Wiener-Hopf formulation.

The first test case under non-reacting flow conditions used to validate CFD/SI is the duct with a sudden change of dimension. In this case, reflective acoustic boundary conditions have been applied. For low Mach number flows using these boundary conditions, a correlation analysis and the reconstruction of the acoustic transfer matrix of this acoustic element have been successfully performed. The CFD-based results are compared to an analytical model, measurements and FEM and no significant discrepancy has been found. Additionally, the sensitivity analysis including time discretization and space discretization, time discretization schemes, and the influence on the CFD/SI approach has been performed. It is seen that the variation in the space discretization has not affected the calculated absolute and phase values. Contrary to this, the time discretization and the time scheme have the largest impact on the derived transfer matrices especially at higher frequencies where acoustic damping due to the turbulent viscous effects is much stronger.

In the second test case, a truncated teardrop acoustic element has been examined. Using CFD/SI the acoustic transfer matrix of this element is determined. It is worth noting that in this test case the Mach number at the minimum cross-section was 0.4. To quantify the results, an additional one-dimensional acoustic network model of this acoustic element has been built. Employing this one-dimensional acoustic code the acoustic transfer matrix is calculated. The reconstructed acoustic transfer matrices have been compared to each other and no significant differences have been found.

It is demonstrated that acoustic reflectivity has some impact on both the absolute and phase values. Employing the reconstructed acoustic transfer matrix in TMA, the impedance has been calculated at the reference plane where the measurements are made. Some discrepancies especially at higher frequencies are clearly seen that may result from acoustic damping, which is much better captured by CFD than TMA. However, reasonable agreement between the measured and estimated values has been found.

For a test case with reacting flow, an atmospheric generic test rig has been chosen. In this case, the flame transfer function of a generic burner is reconstructed using system identification combined with unsteady CFD computations. The flame transfer function estimated using the CFD model with the reflective boundary condition at the diagonal inlet and the non-reflective boundary condition at outlet are used as a reference test case. It is shown that CFD/SI is able to provide the amplitude and phase, which are dependent on frequency, whereas using the conventional time lag approach based on steady state computation only the phase can be frequency dependent. An increase above unity of the amplitude of the flame transfer function, which is related to the current flame dynamics, is also captured by unsteady CFD. In addition to this, the benchmark between the CFD/SI and the flame transfer function estimated at discrete frequency has been made and the results are satisfactory. A sensitivity study reveals some additional dependences of the CFD/SI approach on combustion modeling, acoustic treatment of boundary conditions and the time step size. It has discovered that the various combustion model concepts can lead to various flame responses.

Nevertheless, the most important parameter is the acoustic treatment of boundary conditions. The dynamics of the system determined while performing unsteady computations with reflective boundary conditions or with only one non-reflective boundary condition have been considerably over-predicted. It is shown that the real amplitude is much smaller and indeed, it indicates a much weaker flame response. Furthermore, it has demonstrated that in this case, the time discretization does not strongly affect the accuracy of the identification procedure and therefore the reconstruction of the flame transfer function does not depend greatly on the time step size used.

The industrial test rig at elevated pressure featuring a prototype combustion system has been used to demonstrate the ability of CFD/SI to estimate flame transfer functions of a real installation. The segment model is utilized to perform the unsteady computation and is forced with white noise. The time series of velocity and heat release has been correlated resulting in the flame response to the total mass flow rate at the main inlet. The estimated flame transfer function is then employed in a one dimensional acoustic network code and the stability margin has been calculated. The flame is modeled using two different computational approaches.

For the first the flame model, the standard n - τ model has been employed using a time lag value from steady CFD. For the second, the flame response has been computed by CFD/SI.

Both models have been applied to describe the correlation between the total mass flow rate and the heat release fluctuations. As in the experimental data, after performing the stability analysis two distinct peaks indicating unstable modes are found. For the first acoustic unstable modes the differences with respect to the damping values and the frequency, at which these modes have occurred, are rather negligible. The second unstable frequency has been more accurately predicted with regard to the peak from the pressure measurement using the derived flame transfer function based on CFD/SI.

Using the SAS model allows for the resolution of the turbulent spectrum in unstable flow conditions. Because of the automatic adaptation of the length-scale to the different scales in the flow field, the SAS model has a LES-like behavior in unsteady regions. This model has been utilized to simulate the mechanisms responsible for flow instability. In the case of the atmospheric generic test rig it is seen that the flame length from URANS is over-predicted compared to the SAS computation. It is apparent that the reacting flow is totally dominated in the burner exit by the development of coherent turbulence structures. Additionally, the SAS computation has been forced at 90 Hz to visualize the coherent structures, which in this case are mainly responsible for the flame dynamics. The ring vortex structures are well captured by SAS, which have also been seen in the measurements and the previous LES computations of Sell et al. [31].

The SAS model has also been used to analyze the flow field of the generic test rig operating at elevated pressure. The coherent structures originated in the pilot region where the inner recirculation zone is located are found to be possible driving mechanism of the flow instabilities.

The computation of self-excited oscillations using fully reflective boundary conditions and total pressure boundary conditions at the diagonal inlet of the generic burner have been successfully performed for the atmospheric test rig. After a sufficiently long period of time the development of self-excited oscillations have been captured. Two dominant frequencies in the pressure spectrum for the CFD model have been detected and compared with the results from the TMA calculation. As opposed to the CFD model, TMA predicted four unstable eigenfrequencies but two of them are identical to those from the CFD computation. It is very likely that these remaining two frequencies have been smoothed out due to viscosity effects.

As shown, the CFD/SI approach is a valuable tool in reconstructing acoustic elements. However, a more realistic evaluation of CFD/SI would be more helpful to show the capability of this tool. It is recommended that CFD/SI should be applied to the calculation of acoustic transfer matrices and flame transfer functions of more geometrically complex acoustic elements involving cooling flows and other flame types. Pressure losses, heat losses and of course acoustics/turbulent interactions should be by definition better represented by CFD/SI. On the other hand, flame responses derived by CFD/SI are more accurate and better describe the flame dynamics. Amplitude and phase of flame transfer functions are always a function of frequency and show a low-pass filter behavior. The standard time lag approaches have some difficulties in reproducing real FTF induced by velocity or equivalence ratio fluctuations.

Similarly new and more advance combustion models, and more sophisticated turbulence models, i.e. SAS or LES, should be employed to investigate whether the predictability of the flame front location and combustion/vortex and combustion/turbulence interactions can be further improved.

Finally, impedance boundary conditions employed in realistic computations of self-sustained oscillations should significantly reduce the number of test runs and help to find any unstable modes as long as it gets amplified.

Combining these two design philosophies, i.e. the forced response approach based on CFD/SI and calculations of self-sustained oscillations, may significantly reduce the effort and cost invested during the design phase of a gas turbine combustion system and help to build more efficient, powerful and most of all cleaner gas turbine combustion systems.

Appendix

A Turbulence models

k-ε model

The typical value associated with the coefficients used in the k-ε model [40] in CFX ANSYS are given in table shown below.

$C_{\epsilon 1}$	$C_{\epsilon 2}$	C_{μ}	σ_k	σ_{ϵ}	Pr_t	Sc_t
1.44	1.92	0.09	1.0	1.3	0.9	0.9

Tab. A.1 Coefficients for k-ε models

SAS model

In table shown below, the typical values associated with the coefficients used in the SST-SAS model [14] are given.

C_{μ}	κ	ζ_1	ζ_2	ζ_3	σ_k	σ_{ϕ}
0.09	0.41	0.8	0.0326	3.51	2/3	2/3

Tab. A.2 Coefficients for SST-SAS model

B Time discretization

CFX uses a fully implicit time discretisation scheme. Here, the second order time discretisation scheme is utilized. However, in some cases, for the sake of comparison the first order time discretisation scheme is also used. This time discretisation scheme approximates the start and the end of time step values using the old and current time level solution values. Both the first and the second order time discretisation schemes are listed as follows:

First Order Backward Euler Scheme:

$$\frac{\partial \psi^n}{\partial t} = \frac{\psi^n - \psi^{n-1}}{\Delta t} \quad (\text{B.1})$$

Second Order Backward Euler Scheme:

$$\frac{\partial \psi^n}{\partial t} = \frac{\frac{3}{2}\psi^n - 2\psi^{n-1} + \frac{1}{2}\psi^{n-2}}{\Delta t} \quad (\text{B.2})$$

C Analytical time lag models

The formulation of the analytical flame transfer function using the time lag approach can be simplified as follows [36]:

The n - τ model

$$F(\omega) = ne^{-i\omega\tau} \quad (\text{C.1})$$

where n is the amplification factor and τ stands for the time lag

This simple time lag model was modified and further extended to account for time lag spread in equivalence ratio fluctuations by Sattalmayer et al. [102]

The modified n - τ model

$$F(\omega) = n \frac{\sin \omega \Delta \tau}{\omega \Delta \tau} e^{-i\omega\tau} \quad (\text{C.2})$$

where n is the amplification factor, $\Delta\tau$ is the time lag spread and τ is the time lag, respectively.

The amplitude of an exemplary flame transfer function accounting for different time lag spreads is given in Fig C.1. It is shown that for $\Delta\tau=0$ [s], the modified time lag model reduced to the standard time lag formulation. For larger time lag spreads the amplitude much quicker reduced. The amplitude is being reduced and shows a low-pass filter like behavior

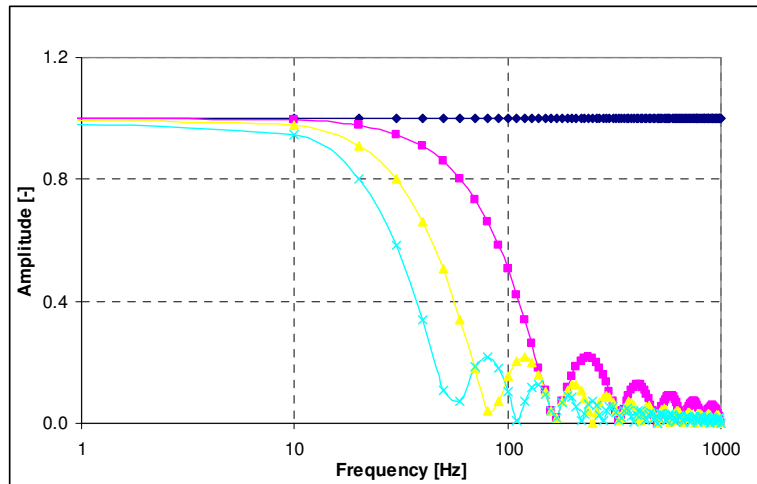


Fig. C.1 Amplitude of an exemplary flame transfer function: dark blue rectangular ($\Delta\tau=0$ s), purple rectangular ($\Delta\tau=0.002$ s), yellow rectangular ($\Delta\tau=0.006$ s), and light blue rectangular ($\Delta\tau=0.009$ s)

The time lag spread has no effect on the phase distribution provided in Fig C.2. The curves are overlapped by one other.

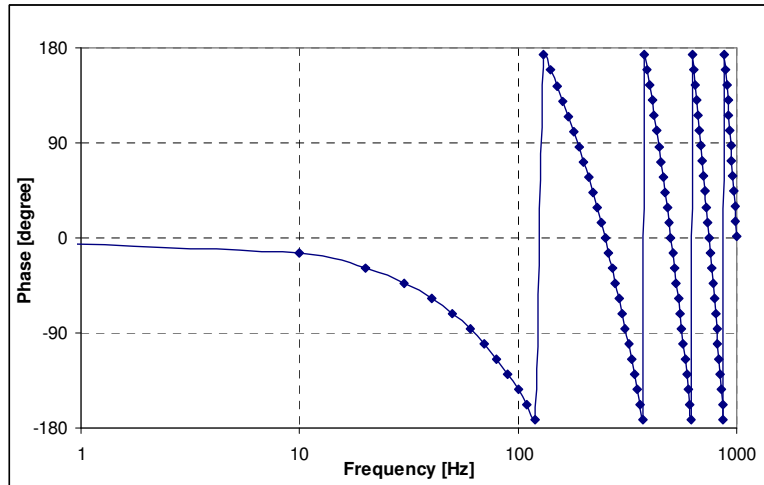


Fig. C.2 Phase of an exemplary flame transfer function: dark blue rectangular ($\Delta\tau=0$ s), purple rectangular ($\Delta\tau=0.002$ s), yellow rectangular ($\Delta\tau=0.006$ s), and light blue rectangular ($\Delta\tau=0.009$ s)

D Solution error analysis

In the transient runs, an implicit second order Euler time discretization scheme is used to march through time (See appendix B). Errors due to a discrete approximation result mainly from truncation errors in the time distretization. In practice, these approximations produce in direct-time integration amplitude and phase errors, as illustrated in Fig D.1. Van Kampfen et al. [24] has already analyzed these kinds of error. However, for the purpose of this thesis the study has been extended to the analysis of the first order time discretisation scheme.

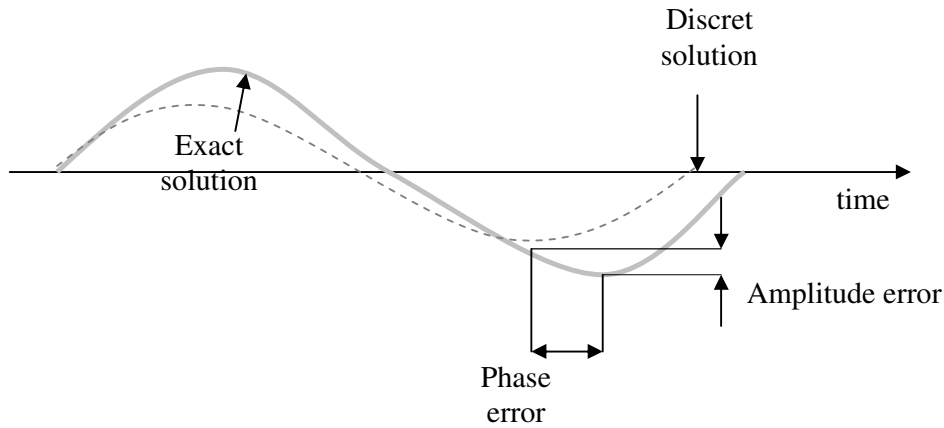


Fig. D.1 Possible amplitude and phase errors due to the discrete approximation [24]

The truncation error is derived as a function of the number of time steps per period. This derivation can be employed later on to determine the time step size and by the inverse analysis to estimate the sufficient number of time steps in unsteady runs.

The truncation error of the implicit first order discretisation scheme (see Appendix 0) can be expanded using the Taylor series for the discrete approximation. The Taylor series of a variable φ has the largest approximation error $O(\Delta t)$, which can be written as:

$$\varepsilon = \frac{\Delta t}{2} \frac{\partial^2 \varphi}{\partial t^2} \quad (\text{D.1})$$

As proposed by van Kampfen [24], the estimated truncation errors of the first order Euler are referred to the exact time derivative. Assuming a sinusoidal fluctuation, the maximum truncation error can be written as:

$$\varepsilon_{1storder} = \frac{2\Pi^2 f}{N} \quad (\text{D.2})$$

and referring this error to the exact derivative, one gets the relative maximum truncation error defined as:

$$\mathcal{E}_{1storder,derivative} = \frac{\mathcal{E}_{1storder}}{2\pi f} \frac{\pi}{N} \quad (D.3)$$

The absolute relative error in the instantaneous value ψ can be estimated by multiplying the second order term with Δt . Doing so, the error in the time derivative is converted into the absolute error in the instantaneous value:

$$\mathcal{E}_{1storder,value} = \frac{2\pi^2}{N^2} \quad (D.4)$$

E Approximation of impedance boundary conditions

Assuming that total pressure for a given section is constant, one can derive an estimate for acoustic impedance for TMA. Let us consider a constant total pressure at the diagonal inlet for the generic burner shown in chapter 0, one gets:

$$p_{\text{tot, diagonal inlet}} = p + \frac{1}{2}\rho u^2 = \text{const.} \quad (\text{E.1})$$

Furthermore, if ρ is only a function of static pressure and remains not significantly changed during the occurrence of self-excited oscillations it is possible to linearize this equation around mean values.

$$p' + \rho \bar{u} u' = 0 \quad (\text{E.2})$$

The approximated impedance at the diagonal inlet can be expressed by

$$Z_{\text{diagonal inlet}} = \frac{p'}{-u'} = \rho \bar{u} \quad (\text{E.3})$$

Similar derivation can be also provided for the axial inlet.

HPC - computational resources

Since the project is of an interdisciplinary nature, its success is dependent on advanced, state-of-the-art combustion CFD methods and unsteady CFD. Because the main focus of the current work is related to unsteady CFD, special emphasis needs to be put on the availability of computing resources. The entire computational work has been performed utilizing an AMD 64-bit Opteron Cluster with a total amount of 240 processors.

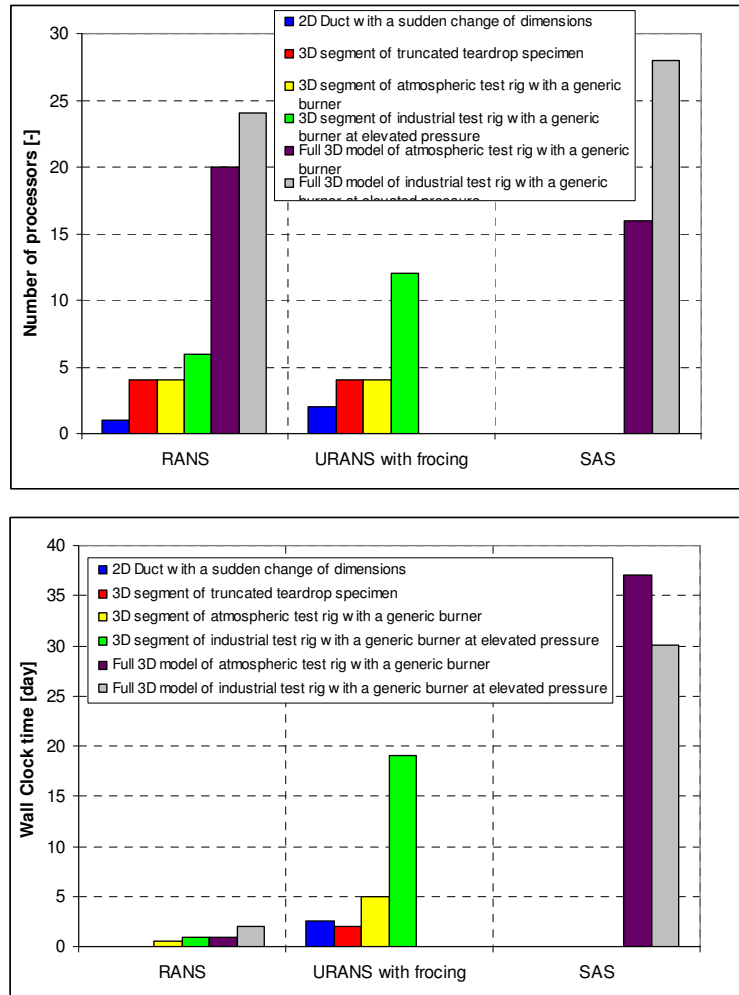


Fig. F.1 Comparison of wall clock time and number of processors for different configurations

Mainly URANS and SAS computations have been carried out to compute acoustic transfer matrices and flame transfer functions. It is also well known that there are mainly three factors influencing total physical run time of unsteady computations: time resolution (time step), spatial resolution (number of grid points), and number of time steps to be performed.

It is important that every computation is optimized in terms of number of processors assigned versus increase in computational speed, given that there is an upper CPU limit where no further increase can be achieved

A direct comparison between some test cases described in detail at later stage of this thesis is given in Fig F.1. It is shown that by increasing model complexity from a 2D to a full 3D case, and by including an additional transport equation for species with more sophisticated turbulence modeling, results in dramatically increasing computational time. For URANS with forcing, wall clock time varied from 2 to 19 days in the case of the 3D segment model of the industrial test rig at elevated pressure. Besides, one has to wait more than one month for SAS computations using 28 processors.

In case of the fully 3D model of the industrial test rig at elevated pressure an optimum number of processors has been investigated more in details. All the Information has been collected on several preliminary unsteady runs. All the computations have performed with the same setup and the same number of iterations is made. The final computation has been performed on the Linux Cluster with more than 7 nodes. Each node is a compound of four AMD 64 Opteron Processors. One time step including time needed for writing out intermediate results takes approximately 450 wall clock seconds. The complete SAS computation takes about 30 days. An exemplary speed up represented by the wall clock time as a function of number of processors is plotted in Fig F.2. Analyzing this plot, 24 processors can be chosen as the optimum number. For more processors, no significant 'computer speed up' is expected.

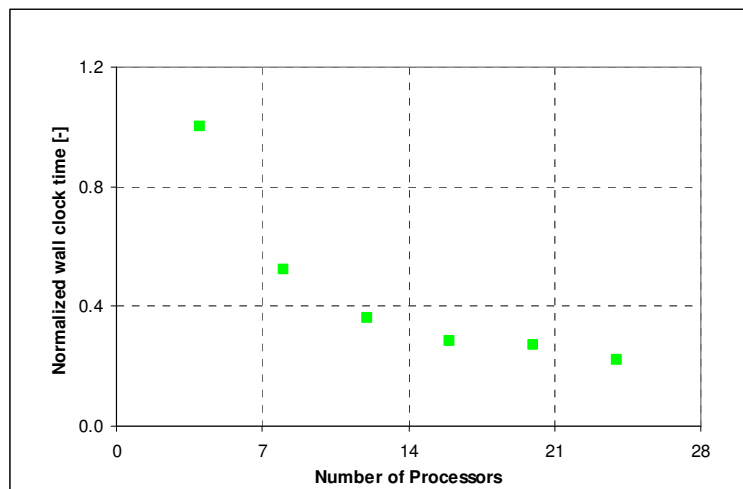


Fig. F.2 Computer speed up - SAS of industrial test rig with a prototype combustion system at elevated pressure

Literature

- [1] European Environmental Agency, World Health Organization, Air and Health, 1999 http://reports.eea.europa.eu/2599XXX/en/index_html
- [2] Moore, M.J., NO_x emission control in gas turbines for combined cycles gas turbine plant, Proceedings of Institution of Mechanical Engineers, Vol. 211 Part A
- [3] Candel, S.M., Poinsot, T.J., Interaction between acoustics and combustion. Proceedings of The Institute of Acoustic, 10(2):103-153, 1988
- [4] Vigor, Y., Lieuwen, T., Combustion Instabilities in Gas Turbine Engines: Operational Experience, Fundamental Mechanisms, and Modeling, Progress in Astronautics and Aeronautics, 2005
- [5] Lieuwen, T., Investigation of combustion instability mechanisms in premixed gas turbines, PhD Thesis, Georgia Institute of Technology, 1999
- [6] Dowling, A.P., Stow, R.S., Acoustic Analysis of Gas Turbine Combustors, J. of Propulsion and Power, Vol.19, No.5, 2003
- [7] Kunze, K., Untersuchung des thermoakustischen Flammenübertragungsverhaltens in einer Ringbrennkammer, Dissertation, TU München, 2003
- [8] Bohn, D., Deutsch, G., Krüger, U., Numerical prediction of the dynamic behavior of turbulent diffusion flames, ASME TURBO EXPO 1996, 96-GT-133, 1996
- [9] Schuermans, B.B.H., Polifke, W., Modeling transfer matrices of premix flames and comparison with experimental results, ASME TURBO EXPO 1999, 99-GT-132, 1999
- [10] Culick, F.E.C., Combustion instabilities in propulsion systems published in Unsteady Combustion, p.173-243, Kluwer Academic Publisher, 1996
- [11] Dowling, A.P., Nonlinear self-excited oscillations of a duct flame, J. Fluid Mechanics, 346, pp.271-290
- [12] Menon, S., Jou, W., Large eddy Simulations of combustion instabilities in an axisymmetric ramjet, Combustion Science and Technology, 75, pp.53-72
- [13] ANSYS, Inc., Canonsburg, USA, ANSYS CFX 10 - Manual for Users
- [14] ANSYS, Inc., Canonsburg, USA, ANSYS CFX 11 - Turbulence and Wall Function Theory Guide
- [15] ANSYS, Inc., Canonsburg, USA, ANSYS CFX 11- Discretization and Solution Theory
- [16] ANSYS, Inc., Canonsburg, USA, ANSYS CFX 11 -Combustion Theory
- [17] Gentemann, A., Fischer, A., Evesque, S., Polifke, W., Acoustic Transfer Matrix Reconstruction and Analysis for Ducts with a sudden change of area, 9th AIIAA/CEAS Aeroacoustics Conference and Exhibit, 12-14, Hilton Head, South Carolina, 2001
- [18] Berenbrink, P., Hoffmann, S., Suppression of Dynamic Combustion Instabilities by Passive and Active Means, ASME-Paper 2000-GT-0079, 2000.
- [19] Scarinci, T., Halpin, T., J.L., Industrial Trend Combustor – Combustion Noise Characteristics Transactions of the ASME, J.Eng. Gas Turbines and Power, 2000
- [20] McManus, K.R., Poinsot, T., Candel, S.M., A review of active control of combustion instabilities, J. of Propulsion and Power, 19, pp.765-781, 1993

-
- [21] Heckl, M.A., Active control of the noise from a Rijke tube, *J. of Sound and Vibration*, Vol. 124, 1988, pp.117-133
- [22] Hermann, J., Orthmann, A., Hoffmann, S., Application of Active Instability Control to a Heavy Duty Gas Turbine, XIV ISABE, 5-10 Sept., Florence, Italy, A99-34186, 1999
- [23] Bird, R.B., Stewart, W.E., Lightfoot, E.N., *Transport phenomena*, John Wiley & Sons, 1960
- [24] Van Kampen, J., Acoustic pressure oscillations induced by confined turbulent premixed natural gas flame, PhD Thesis, University of Twente, 2006
- [25] Dowling, A., Hubbard, S., Acoustic Resonance of an Industrial Gas Turbine Combustion System, ASME TURBO EXPO 2000, 2000-GT-0094, 2000.
- [26] Krueger, U., Hueren, J., Hoffmann, S., Krebs, W., Flohr, F., Bohn, D., Prediction and Measurements of Thermoacoustic Improvements in Gas Turbines with Annular Combustion Systems, ASME TURBO EXPO 2000, 2000-GT-0095, 2000.
- [27] Konstantin Matveev, Theoretical Instabilities in the Rijke Tube: Experiments and Modeling, PhD Thesis, California Institute of Technology, 2003
- [28] Eberhard Deuker, Ein Beitrag zur Vorausberechnung des akustischen Stabilitätsverhaltens von Gasturbinen-Brennkammern mittels theoretischer und experimenteller Analyse von Brennkammerschwingungen, Dissertation, RWTH Aachen, 1995
- [29] Munjal, M.L., *Acoustic of ducts and mufflers with application to exhaust and ventilation systems design*, John Wiley & Sons, Inc., 1945
- [30] Rayleigh, J.W.S. The explanation of certain acoustical phenomena. *Nature*, pp. 319-321, 1878
- [31] Selle, L., Lartigue, G., Poinso, T., Koch, R., Schildmacher, K., Krebs, W., Prade, B., Kaufmann, P., Veynante, D., Compressible Large-Eddy Simulation of turbulent combustion in complex geometry on unstructured meshes. *Combust. Flame* 137, 489-505, 2004
- [32] Kailasanath, K., and Gutmark, E.J., *Propulsion Combustion: Fuels to Emissions*. Taylor and Francis. 1997
- [33] Kinsler, L.E., Frey, A.R., Coppens, A.B, Sanders, J.V., *Fundamentals of acoustics*, John Wiley & Sons, Inc, 1999
- [34] Ingard, U., Singhal, V.K., Sound attenuation in turbulent pipe flow, *J. Acoust. Soc. Am.*, Vol.55, No. 3, March 1974
- [35] Crocco, L., Cheng, S.L., *Theory of combustion instability in liquid propellant rocket motors*, Agardograph No.8, Butterworths Science Publication, 1956
- [36] Krebs, W., Hoffmann, S., Prade, Lohrmann, B., Büchner, H., Thermoacoustic flame response of swirl flames, ASME TURBO EXPO 2002, June 3-6, Amsterdam, NL, GT- 2002-30065, 2002
- [37] Giauque, A., Selle, L., Poinso, T., Buechner, H., System identification of a large scale swirled partially premixed combustor using LES and measurements. *Journal of Turbulence*, 6(21) 1 – 20
- [38] Truffin, K., Poinso, T., Comparison and extension of methods for acoustic identification of burners, *Combustion and Flame*, 142, pages 388-400, 2005
- [39] Sattelmayer, T., Polifke, W., Assessment of Methods for the Computation of the Linear Stability of Combustors, CTS 2003
- [40] Poinso, T., Veynante, D., *Theoretical and Numerical Combustion*. Second Edition, Edwards, 2005
- [41] Nicoud, F., Poinso, T., Fluctuating energies and stability criteria for thermo-acoustic instabilities: is the Rayleigh criterion right?, Elsevier Science, 2004
- [42] Polifke, W., Paschereit, C.O., Determination of thermo-acoustic transfer matrices by experimental and computational fluid dynamics, ERCOFTAC Bulletin 38, September 1998
- [43] Gentemann, A., Hirsch, C., Kunze, K., Kiesewetter, F., Polifke, W., Sattelmayer, T., Validation of flame transfer function reconstruction for perfectly premixed swirl flames, ASME TURBO EXPO 2004, June 14-17, Vienna, Austria, GT2004-53776, 2004

-
- [44] Bohn, D., Deuker, E., An acoustical model to predict combustion driven oscillations, Paper G 20, 20th Int. Congress on Combustion Engines (CIMAC), London, 1993
- [45] Krueger, U., Hoffmann, S., Krebs, W., Judith, H., Bohn, D., Matouschek, G., Influence of turbulence on the dynamic behavior of premix flames, ASME TURBO EXPO 1998, Stockholm, Sweden, ASME 98-GT-323, 1998
- [46] Polifke, W., Poncet, A., Paschereit, C.O., Döbbeling, K., Reconstruction of acoustic transfer matrices by instationary computational fluid dynamics, *Journal of Sound and Vibration* (2001) 245(3), 483-510
- [47] Polifke, W., Gentenmann, A., Order and realizability of impulse response filter for accurate identification of acoustic multi-ports from transient CFD, Tenth International Congress on Sound and Vibration, Stockholm, Sweden, 7-10 July 2003,
- [48] Yuen, S.W., Theoretical Studies to the Identification of Thermo-acoustic Systems, Diplomarbeit, TU München, 2003
- [49] Polifke, W., Numerical Techniques for identification of Acoustic Multi-Ports, VKI Lecture Series, March, 2004
- [50] Gentemann, A., Identifikation von akustischen Transfermatrizen und Flammenfrequenzgängen mittels Strömungssimulation, Dissertation, TU München, 2006
- [51] Proakis, J.G., Manolakis, D.G., Digital Signal Processing: Principles, Algorithms and Applications. Prentice Hall, 3rd edition, 1996
- [52] Oppenheim, A.V., Schafer, R.W., Discrete-Time Signal Processing. Prentice Hall, 2nd edition, 1999
- [53] Ljung, L., System Identification-Theory for the user. Prentice Hall PTR, 1999
- [54] Gentmann, A., Polifke, W., Estimation of Flame Transfer Functions and Implementation into Acoustic Network Codes, TU München, Internal Report, 6. August 2003
- [55] Polifke, W., Wall, C., Non-reflective boundary conditions for acoustic transfer matrix estimation with LES, Proceedings of the Summer Program 2002, Stanford, USA, Centre of Turbulence Research.
- [56] Widenhorn, A., Noll, B., Aigner, A., Accurate Boundary Conditions for the Numerical Calculation of thermoacoustic phenomena in gas-turbine combustion chambers, TURBO EXPO 2006, May 8-11, Barcelona, Spain, GT2006-90441, 2006
- [57] Poinot, T., Lele, S.K., Boundary conditions for direct simulation of compressible viscous flow, *J. Comp. Phys.* 101 (1992), s.104-129
- [58] Kaufmann, A., Nicoud, F., Poinot, T., Flow forcing techniques for numerical simulation of combustion instabilities, *Combustion and Flame* 131 (2002), No.4, pages 371-385
- [59] Kostrzewa, K., Lepers, J., Krebs, W., Noll, B., Huth, M., Prade, B., Aigner, M., Validation of advanced computational methods for determining flame transfer functions in gas turbine combustion systems, ASME Turbo Expo 2007, May 14-17, 2007, Montreal, Canada, GT2007-27267
- [60] Colonius, T., Computational Area-acoustics: Overview and Numerical Methods, VKI Lecture Series, 2006
- [61] Klein, S.A., On the acoustics of turbulent non-premixed flames, PhD Thesis, University of Twente, 2000
- [62] Siewert, P., Flame front characteristics of turbulent lean premixed methane/air flames at high pressure, PhD Thesis, The Swiss Federal Institute of Technology in Zurich (ETHZ), 2006
- [63] Kuo, K.K., Principles of Combustion, John Wiley & Sons, 1986
- [64] Kunz, O., PDF-Simulation von Verbrennungsvorgängen in praxisnahen Brennkammern, Dissertation, TU Stuttgart, 2003

- [65] F.R.Menter, F.R., M.Kuntz, Development and Application of a Zonal DES Turbulence Model for CFX CFX-5 , Ansys-CFX
- [66] Menter, F.R., 1993, "Zonal two-equation k- ϵ turbulence model for aerodynamic flows", AIAA Paper 1993-2906.
- [67] Menter, F.R. and Egorov, Y., A scale adaptive simulation using two equation models, AIAA Paper 2005-1095, Reno 2005
- [68] Peters, N., Turbulent Combustion. Cambridge University Press, 2000
- [69] Warnatz, J., Mass, U., Dibble, R.W., Combustion, 1996:Springer Verlag.
- [70] Spalding, D.B., Mixing and Chemical Reaction in Steady Confined Turbulent Flames, 13th Symposium on Combustion, The Combustion Institute, Pittsburgh, 1971
- [71] Nicol, D.G. , Malte, Ph.C., Hamer, A.J., Roby, R.J, Steele, R.C., Development of a five-step global methane oxidation-no formation mechanism for lean premixed gas turbine combustion, International Gas Turbine & Aeroengine Congress & Exhibition, Stockholm, Sweden – June 2 – June 5, 1998
- [72] Paschereit, C.O., Schuermans, B.B.H., Polifke, W., Mattson, O., Measurement of transfer matrixes and source terms of premixed flames, J.Eng. for Gas Turbines and Power, Vol.124, pp.239-247, 2002
- [73] Pankiewicz, C., Fischer, A., Hirsch, C., Sattelmayer, T., Computation of Transfer Matrices for Gas Turbine Combustors including Acoustics/Flame Interaction, 9th AIAA/CEAS Area-acoustics Conference & Exhibit, Hilton Head, 2003
- [74] Lohrmann, M., Büchner, H., Zarzalis, N., Krebs, W., Flame transfer characteristics of swirl flames for gas turbine applications, ASME TURBO EXPO 2003, June 16-19, Atlanta, Georgia, USA, GT-2003-38113, 2003
- [75] Hettel, M., Habisreuther, P., Bockhorn, H, Unsteady Reynolds-Averaged Navier Stockes (URANS) modeling of flame transfer functions of turbulent premixed jet flames. 12th International Congress on Sound and Vibration, 11-14 July, Lisbon, Portugal, 2005
- [76] Selle, L., Simulation aux grades echelles des couplages acoustique/combustion dans les turbines a gaz, PHD Thesis, INP Toulouse, 2004
- [77] Kopitz, J., Huber, A., Sattelmayer, T., Polifke, W., Thermoacoustic Stability Analysis of an Annular Combustion Chamber with Acoustic Low order Modeling and Validation Against Experiment, ASME TURBO EXPO 2005, June 6-9, Reno-Tahoe, Nevada, USA, GT-2005-68797, 2003
- [78] Stow, S.R., Dowling A.P., Low-Order Modeling of Thermo-acoustic Limit Cycle, ASME TURBO EXPO 2004, June 14-17, Vienna, Austria, GT-2004-54245, 2004
- [79] Hermann, J., Anregungsmechanismen und aktive Dämpfung (AIC) selbsterregte Verbrennungsschwingungen in Flüssigkraftstoffsystemen, Fortschrittberichte VDI, Energietechnik Nr. 364
- [80] Noll, B., Schütz, H., Aigner, M., Numerical simulation of high-frequency flow instabilities near an airblast atomizer, ASME TURBO EXPO 2001, June 4-7, New Orleans, Louisiana, USA, 2001-GT-0041, 2001
- [81] Paschereit, C.O., Schuermans, B., Polifke, W., Mattson, Measurements of transfer matrixes and source terms of premixed Flames .J. of Engineering for Gas Turbines and Power, Vol. 124, 239-247, 2002
- [82] Freitag, E., Konle, H., Lauer, M., Hirsch C, Sattelmayer, T., Pressure influence on the flame transfer function of a premixed swirling flame., ASME TURBO EXPO 2006, May 8-13, Barcelona, Spain, GT-2006-90540, 2006
- [83] Bellows, B.D., Bobba, M.K., Seitzman, J.M, Lieuwen, T., Nonlinear flame transfer function characteristics in a swirl stabilized combustor, ASME Turbo Expo 2006: May 8-11, 2006, Barcelona, Spain, GT2006-91119

-
- [84] Hettel, M., Habisreuther, P., Büchner, H., Bockhorn, H., Zarzalis, N., URANS-modelling of flame transfer functions of turbulent premixed jet flames. ASME TURBO EXPO 2004, June 14-17, Vienna, Austria, 2004-GT-53808, 2004
- [85] Flohr, P., Paschereit, Ch.O., Bart van Roon, Schuermans. B., Using CFD for time-delay modeling of premix flames, June 4-7, New Orleans, Louisiana, USA, 2001-GT-0376, 2001
- [86] Truffin, K., Varoquié, B., Veynante, D., Poinso, T., Lacas., F., Large Eddy Simulations and experimental characterization of the unsteady response of partially premixed flames. Technical Report TR/CFD/04/36, CERFACS, January 2004
- [87] Cook, J., D., Pitsch, H., Peters, N., Numerical simulations of instabilities in a lean premix combustor with finite rate chemistry, Turbo Expo 2003, June 16-19, Atlanta, Georgia, USA, GT2003-38558, 2003
- [88] Brookes, J., S., Stewart Cant, R., Dupere, DJ., I., Dowling A., P., Computational modelling of self excited combustion instabilities, TURBO EXPO 2000, May 8-11, Munich, Germany, 2000-GT-0104, 2000
- [89] Martin, Ch., Benoit, L., Nicoud, F., Poinso, T., Analysis of acoustic energy and modes in a turbulent swirled combustor. In Proceedings of the Summer Program, pages 377-394, Center for Turbulence Research, NASA AMES/Stanford University, USA, 2004
- [90] Young, T., Linear systems and digital signal processing, Prentice-hall, 1985
- [91] Poinso, T., Lele, S., 1992, Boundary Conditions for Direct Simulations of Compressible Viscous Flows, J. of Comput. Phys., Vol. 101, pp. 104-129
- [92] Zwart, P. J., Abshoff, J. Non-reflective Boundary Conditions in CFX5, CFX-VAL01/07042/10/2005
- [93] Widenhorn, A., Noll, B., Aigner, M. Impedance Boundary Conditions for the Numerical Simulation of Gas-Turbine Combustion Systems, ASME Turbo Expo 2008, June 17-20, 2008, Berlin, Germany, GT2008-50445
- [94] Fischer, A., Hybride, thermoakustische Charakterisierung von Drallbrennern, Dissertation, TU München, 2004
- [95] Kostrzewa, K., Widenhorn, A., Krebs, W., Noll, B., Huth, M., Kaufmann, P., Aigner, M., Impact of Boundary Conditions on the Reconstructed Flame Transfer Function for Gas Turbine Combustion Systems, ASME Turbo Expo 2008, June 17-20, 2008, Berlin, Germany, 2008-50446
- [96] Huber, A., Polifke, W., Impact of fuel supply impedance on combustion stability of gas turbines, ASME Turbo Expo 2008, June 17-20, 2008, Berlin, Germany, 2008-51193
- [97] Paschereit, C. O., Weisenstein, W., and Gutmark, E. J., Role of coherent structures in acoustic combustion control, 1998. No. A98-32792 in 29th AIAA Fluid Dynamics Conference
- [98] Dowling, A., A kinematic model of a ducted flame. 1999, *Journal of Fluid Mechanics*, 394, pp. 51-72
- [99] Auer, M. P., Hirsch, C., Sattelmayer, T., Influence of air and fuel mass flow fluctuations in a premix swirl burner on flame dynamics, ASME Turbo Expo 2006, May 8-11, 2006, Barcelona, Spain, GT2006-90127
- [100] Huber, A., Impact of fuel supply impedance and fuel staging on gas turbine combustion stability, Dissertation, TU München, 2009
- [101] Huber, A., Romann, Ph., Polifke, W., Filter-based time-domain impedance boundary conditions, ASME Turbo Expo 2008, June 17-20, 2008, Berlin, Germany, 2008-51195
- [102] Sattelmayer, T., Influence of the Combustor Aerodynamics on Combustion Instabilities From Equivalence Ratio Fluctuations, ASME Turbo Expo 2000, 2000-GT-0082
- [103] Levebvre, A. H., Gas Turbine Combustion, Taylor & Francis Group, 1999

-
- [104] Gruschka, U., Janus. B., Meisl, J., Huth, M., Wasif, S., ULN system for the new SGT5-8000H gas turbine: design and high pressure rig test results, ASME Turbo Expo 2008, June 17-20, 2008, Berlin, Germany, GT2008-51208
- [105] Kato.S, Gas-fired power plant NOx emission controls and related environmental impacts, California Environmental Protection Agency
- [106] Makarewicz.R, Dźwięk I Fale, Wydawnictwo naukowe UAM, Poznan 2004
- [107] Weyna.S, Rozplyw Energii Akustycznych Zrodel Rzeczywistych, Wydawnictwo Naukowe-Techniczne, Warszawa 2005
- [108] Morse, Philip M, Ingard, K. Uno, Theoretical Acoustics, Princeton University Press, 1968
- [109] Martin, C., Benoit, L. Nicoud, F., Poinso, T. , Analysis of acoustic energy and modes in a turbulent swirled combustor, Center for Turbulence Research, Proceedings of the Summer Program 2004
- [110] G. Boudiera, N. Lamarquea, G. Staffelbacha, L.Y.M. Gicquela, T. Poinso, Thermo-acoustic stability of a helicopter gas turbine combustor using Large Eddy Simulation, Aeroacoustics volume 8 · number 1 · 2009 – p. 69 – 94
- [111] A.X, Sengissen. Simulation aux grandes ´echelles des instabilit´es de combustion: vers le couplage fluid/structure, PhD thesis, TH/CFD/06/30, INP Toulouse, France, 2006.
- [112] Fischer, A. Hybride, thermoakustische Charakterisierung von Drallbrennern, Dissertation, TU Mnchen, 2006
- [113] Pla, F.G, An Experimental and Theoretical Study of High -intensity, High-efficiency Sirens, PhD Thesis, The Pennsylvania State University, 1987
- [114] Lepers, J., Krebs, W., Prade, B., Flohr, P., Pollarolo, D., Ferrante,A., Investigation of thermoacoustic stability limits of an annular gas turbine combustor test-rig with and without Helmholtz resonators, ASME Turbo Expo 2005, June 6-9, 2005, Reno-Tahoe, Nevada, USA
- [115] Schuermans, B., Bellucci, V., Paschereit, CH.O., Guethe, F., Meili, F. Flohr, P., A detailed analysis of thermoacoustic interaction mechanisms in a turbulent premixed flame, ASME Turbo Expo 2004, June 14-17, 2004, Vienna, Austria, GT2004-53831
- [116] Menter, F.R., URANS: Applicability, Pitfalls and recent Developments, Hybrid RANS-LES Methods for Industrial CFD, Overview, Guidance and Examples, 2-3June, GE GRC, Munich
- [117] R. Courant, K. Friedrichs and H. Lewy, On the partial difference equations of mathematical physics, IBM Journal, March 1967, pp. 215-234
- [118] Beck, Ch., CFD based NOx Prediction in Stationary Gas Turbine Combustion Systems, Diploma Thesis, Karlsruhe, 2004
- [119] Novick, A.S., Miles, G.A., Lilley, D.G., Modeling Parameter Influences in Gas Combustor Design, J.Energy, 3, 257-264,1979
- [120] Yuen, S. W., Gentemann, A. M. G. and Polifke, W., Investigation of the Influence of Boundary Conditions on System Identifiability using Real Time System Modeling 11th Int. Congress on Sound and Vibration (ICSV11), Saint-Petersburg, Russia, July 5-8, pp. 3501-3508, 2004.
- [121] Schultz, T., Louis, N. Cattafesta III, Nishida, T., Sheplak, M., Uncertainty Analysis of the Two-Microphone Method for Acoustic Impedance Testing, 8th AIAA/CEAS Aeroacoustics Conference & Exhibit, Breckenridge, CO, June 17-19,2002
- [122] Wetzel, F., Habisreuther, P., Zarzalıs, N., Numerical investigation of lean blow out of a model gas turbine combustion chamber using a presumed JPDF- reaction model by taking heat loss processes into account, ASME Turbo Expo 2006, May 8-11, Barcelona, Spain, GT2006-90064
- [123] Poinso, T., Lele, S., Boundary Conditions for Direct Simulations of Compressible Viscous Flows, J. Comp. Phys., Vol. 101, pp. 104-129, 1992
- [124] Martin , Ch. E., Benoit, L., Sommerer, Y., Nicoud, F., Poinso, T., Large-Eddy Simulation and Acoustic Analysis of a Swirled Staged Turbulent Combustor, AIAA JOURNAL Vol. 44, No. 4, April 2006

-
- [125] Widenhorn, A., Noll, B., Aigner, M. Numerical Study of a Non-Reacting Turbulent Flow in a Gas Turbine Model Combustor, 47th AIAA ,5 - 8 January 2009, Orlando, Florida
- [126] Hirsch, C., Fanaca, D., Reddy, P., Polifke, W., Sattelmayer, T., Influence of the swirler design on the flame transfer function of premixed flames, ASME Turbo Expo 2005, June 6-9, 2005, Reno-Tahoe, Nevada, USA, GT2005-68195
- [127] Mockett, Ch., Thiele, F., Solution set-up and post processing, Hybrid RANS-LES Methods for Industrial CFD, Overview, Guidance and Examples, 2-3 June, GE GRC, Munich, 2009
- [128] Bernd, M., Noll, B., Aigner, M., Numerical investigation of entropy noise and its acoustic sources in aero-engines, ASME Turbo Expo 2008, June 9-13, 2008, Berlin, Germany, GT2008-50321
- [129] Zhu, M., Dowling, A.P, Bray, K.N.C , Self-excited oscillations in combustors with spray atomizers , ASME Turbo Expo 2000, May 8-11, 2000, Munich, Germany, 2000-GT-108
- [130] Hantschk, C.C, Vortmeyer, D., Numerical simulation of self-excited combustion oscillations in a non-premixed burner, Combust. Sci. and Tech., 174:189-204, 2002
- [131] Bulat, G., Stopford, Phi., Turrell, M., Frach, D., Buchanan, E., Stoer, M., Prediction of aerodynamic frequencies in a gas turbine combustor using transient CFD, ASME Turbo Expo 2009, June 8-12, 2009, Orlando, Florida, GT2009-59721
- [132] Schoenfeld, T., Poinso, T., Influence of boundary conditions in LES of premixed combustion instabilities, Center for Turbulence Research, Annular Research Brief 1999
- [133] Tanahashi M., Y. Li, Choi G. and Miyauchi T., Direct Numerical Simulation of Combustion-Induced Sound in Turbulent Diffusion Flames, 9th Int. Conf. Numerical Combustion (2002), pp. 201-202
- [134] Reddy Alemela, P., Measurements and scaling of Acoustic Transfer Matrices of Premixed Swirl Flames, Dissertation, TU München, 2009
- [135] Jeong, J., Hussein, F., On the identification of a vortex, J.Fluid Mech. 285, 69-94, 1995

Curriculum Vitae

Name: Krzysztof Kostrzewa
Place of birth: Poznań, Poland
Date of birth: 02 June 1978
Nationality: Polish
Marital status: Married

Education and Work History

2007 - present GE Global Research in Germany
Aerothermal Technologies:
Research Engineer working on combustion and combustion dynamics in gas turbine combustion systems

2004 – 2007 DLR - Institute of Combustion Technology and PhD at Technical University of Stuttgart
Applied Research on Combustion Dynamics in Industrial Applications

2003 – 2004 Von Karman Institute for Fluid Dynamics in Belgium
Turbomachinery and Propulsion Department,
Applied Research on Numerical Optimization

1997 – 2002 Poznań University of Technology in Poland
Machinery and Transportation Department, Chair of Thermal Engineering
MSc in Mechanical Engineering

Publications

Kostrzewa, K., Lepers, J., Krebs, W., Noll, B., Huth, M., Prade, B., Aigner, M., Validation of advanced computational methods for determining flame transfer functions in gas turbine combustion systems, ASME Turbo Expo 2007, May 14-17, 2007, Montreal, Canada, GT2007-27267

Kostrzewa, K., Widenhon, A, Krebs, W., Noll, B., Huth, M., Kaufmann, P., Aigner, M., Impact of Boundary Conditions on the Reconstructed Flame Transfer Function for Gas Turbine Combustion Systems, ASME Turbo Expo 2008, June 17-20, 2008, Berlin, Germany, 2008-5044